

4

SSS-R-88-9844

AFGL-TR-88-0314

**EFFECTS OF DEPTH OF BURIAL
AND TECTONIC STRAIN RELEASE ON
REGIONAL AND TELESEISMIC EXPLOSION WAVEFORMS**

K. L. McLaughlin
T. G. Barker
S. M. Day
B. Shkoller
J. L. Stevens

S-CUBED, A Division of Maxwell Laboratories, Inc.
P.O. Box 1620, La Jolla, California 92038-1620

4 November 1988

SCIENTIFIC REPORT NO. 2

Approved for Public Release; Distribution Unlimited

AIR FORCE GEOPHYSICS LABORATORY
AIR FORCE SYSTEMS COMMAND
UNITED STATES AIR FORCE
HANSCOM AIR FORCE BASE, MA 01731

DTIC
ELECTE
MAY 5 1989
S A D

5 0 0 1

Sponsored by:

Defense Advanced Research Project Agency
Nuclear Monitoring Research Office
5307

DARPA Order No.

Monitored by:

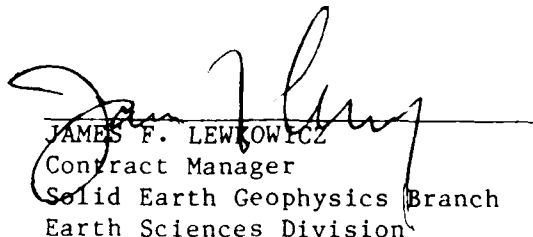
Air Force Geophysics Laboratory

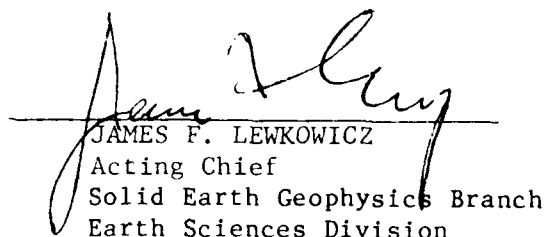
Contract:

F19628-87-C-0093

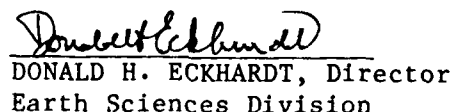
The views and conclusions contained in this document are those of the authors and should not be interpreted as representing the official policies, either expressed or implied, of the Defense Advanced Research Projects Agency or the US Government.

"This technical report has been reviewed and is approved for publication"


JAMES F. LEWKOWICZ
Contract Manager
Solid Earth Geophysics Branch
Earth Sciences Division


JAMES F. LEWKOWICZ
Acting Chief
Solid Earth Geophysics Branch
Earth Sciences Division

FOR THE COMMANDER


DONALD H. ECKHARDT, Director
Earth Sciences Division

This document has been reviewed by the ESD Public Affairs Office (PA) and is releasable to the National Technical Information Service (NTIS).

Qualified requestors may obtain additional copies from the Defense Technical Information Center. All others should apply to the National Technical Information Service.

If your address has changed, or if you wish to be removed from the mailing list, or if the addressee is no longer employed by your organization, please notify AFGL/DAA, Hanscom AFB, MA 01731-5000. This will assist us in maintaining a current mailing list.

Do not return copies of this report unless contractual obligations or notices on a specific document requires that it be returned.

REPORT DOCUMENTATION PAGE

1a REPORT SECURITY CLASSIFICATION UNCLASSIFIED			1b RESTRICTIVE MARKINGS		
2a SECURITY CLASSIFICATION AUTHORITY			3 DISTRIBUTION / AVAILABILITY OF REPORT Approved for Public Release Distribution Unlimited		
2b DECLASSIFICATION / DOWNGRADING SCHEDULE					
4 PERFORMING ORGANIZATION REPORT NUMBER(S) SSS-R-88-9844			5 MONITORING ORGANIZATION REPORT NUMBER(S) AFGL-TR-88-0314		
6a NAME OF PERFORMING ORGANIZATION S-CUBED		6b OFFICE SYMBOL (if applicable)		7a NAME OF MONITORING ORGANIZATION Air Force Geophysics Laboratory	
6c ADDRESS (City, State, and ZIP Code) P.O. Box 1620 La Jolla, California 92038-1620			7b ADDRESS (City, State, and ZIP Code) Hanscom Air Force Base Massachusetts 01731-5000		
8a NAME OF FUNDING / SPONSORING ORGANIZATION Defense Advanced Research Projects Agency		8b OFFICE SYMBOL (if applicable)		9 PROCUREMENT INSTRUMENT IDENTIFICATION NUMBER F19628-87-C-0093	
9c ADDRESS (City, State, and ZIP Code) 1400 Wilson Boulevard Arlington, Virginia 22209			10 SOURCE OF FUNDING NUMBERS		
			PROGRAM ELEMENT NO 62714E	PROJECT NO 7A10	TASK NO DA
			WORK UNIT ACCESSION NO DB		
11 TITLE (Include Security Classification) EFFECTS OF DEPTH OF BURIAL AND TECTONIC STRAIN RELEASE ON REGIONAL AND TELESEISMIC EXPLOSION WAVEFORMS					
12 PERSONAL AUTHOR(S) K.L. McLaughlin, T.G. Barker, S.M. Day, B. Shkoller, and J.L. Stevens					
13a TYPE OF REPORT Scientific No. 2		13b TIME COVERED FROM TO		14 DATE OF REPORT (Year, Month, Day) 1988 November 4	
				15 PAGE COUNT 158	
16 SUPPLEMENTARY NOTATION					
17 COSATI CODES			18 SUBJECT TERMS (Continue on reverse if necessary and identify by block number)		
FIELD	GROUP	SUB-GROUP	Explosions, Finite Differences, Tectonic Release, Seismic Waveforms. Depth of Burial		
19 ABSTRACT (Continue on reverse if necessary and identify by block number)					
<p>The seismic motions from nonlinear two-dimensional (2D) axisymmetric finite difference calculations of underground explosions are propagated to regional and teleseismic distances. Synthetic seismograms are computed and examined to study the effects of depth of burial, medium structure, and prestress on seismic waveforms. The elastodynamic representation theorem is used to couple the results of finite difference source calculations to regional Green's functions computed using a wavenumber integration algorithm. The 2D finite difference source calculations include the nonlinear effects of gravity, spall, bulking, and cracking as well as the finite extent and divergence from spherical symmetry. The results are broadband full wave regional synthetics for explosion sources with cylindrical symmetry. These theoretical seismograms are studied with regard to proposed regional discriminants between explosions and earthquakes.</p>					
20 DISTRIBUTION / AVAILABILITY OF ABSTRACT <input type="checkbox"/> UNCLASSIFIED/UNLIMITED <input checked="" type="checkbox"/> SAME AS RPT <input type="checkbox"/> OTIC USERS			21 ABSTRACT SECURITY CLASSIFICATION UNCLASSIFIED		
22a NAME OF RESPONSIBLE INDIVIDUAL James Lewkowicz			22b TELEPHONE (Include Area Code) 617/377-3028		22c OFFICE SYMBOL LWH

19. Abstract (Continued)

Synthetics for Pahute Mesa tuff are examined for three depths; normal burial, overburied, and cratering. Regional synthetics from axisymmetric explosions are significantly different in the short period band (0.25 to 2 Hz) from simple point source explosion models. Simulation of an overburied explosion shows enhancement of high frequencies relative to a normal buried source. The 2D axisymmetric sources exhibit greater Lg excitation than point sources, and the normal buried source shows enhanced short period fundamental excitation compared to a point source or an overburied source.

Regional synthetics for a simple model of Shagan River explosions also demonstrate that the point source is an inadequate model for regional phase excitation. By contrast, regional synthetics for model explosions in granite with or without prestress differ little from the simple point source model in the short period band. The implications are that the two-dimensional signature for the explosion source depends on medium, and structure in a complicated manner. These calculations demonstrate that the point source explosion model may be inadequate to model discrimination problems in the regional distance range. Higher order models for the explosion source are necessary to understand the effects of depth of burial, medium, and structure, on the high/low frequency discriminant.

Recommendations are made to improve modeling of two-dimensional explosion source effects in short period and high frequency regional waveforms. Improved nonlinear near-source structure interaction and additional calculations for larger ranges of scaled depth of burial and yield will be required to further test the hypothesis that the empirical high/low frequency regional discriminant is related to scaled depth of burial effects.

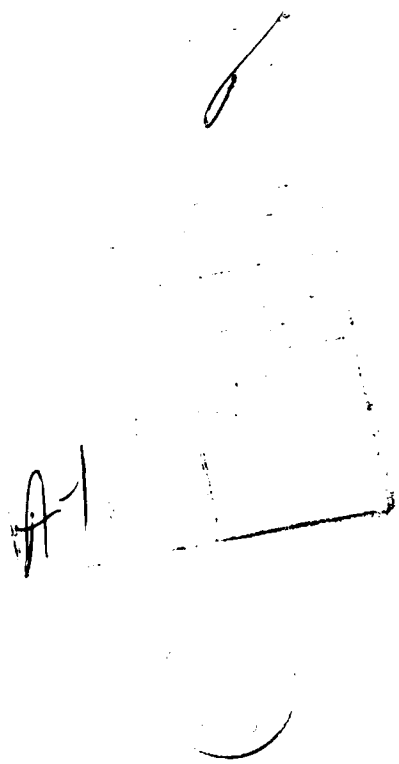


TABLE OF CONTENTS

<u>SECTION</u>	<u>PAGE</u>
I SUMMARY.....	1
II INTRODUCTION.....	2
III POINT SOURCE REGIONAL SYNTHETICS.....	6
3.1 Introduction.....	6
3.2 Basin and Range Model, BR2.....	6
3.3 Amplitude-Distance Relationships.....	13
3.4 Analysis of BR2 Synthetics.....	15
3.4.1 Spectral Domain Measures of Apparent Q.....	15
3.4.2 Time Domain Measures of Apparent Q.....	19
3.5 Conclusions.....	22
IV TWO-DIMENSIONAL SOURCE FAR-FIELD P AND SV WAVEFORMS.....	24
4.1 Introduction.....	24
4.2 Shagan River Simulations.....	24
4.2.1 Waveform Statistics.....	24
4.2.2 Implications for Magnitude:Yield at Shagan River.....	31
4.3 Pahute Mesa Simulations.....	32
4.3.1 Waveform Statistics.....	33
4.3.2 Far-Field P-Wave Spectra and Depth Scaling.....	38
4.3.3 Far-Field P- and SV-Wave Spectra.....	42
4.3.4 Broadband Far-field P Waveforms.....	48
4.4 Effect of Prestress on Far-Field P and SV Waves.....	54
4.6 Conclusions.....	58
V TWO-DIMENSIONAL SOURCE REGIONAL SYNTHETICS.....	67

TABLE OF CONTENTS (Continued)

<u>SECTION</u>	<u>PAGE</u>
5.1 Introduction.....	67
5.2 Pahute Mesa Synthetics.....	68
5.3 Shagan River Synthetics.....	81
5.4 Prestress - PILEDRIIVER Synthetics.....	97
5.5 Conclusions.....	104
VI CONCLUSIONS AND RECOMMENDATIONS.....	105
6.1 Primary Conclusions.....	105
6.2 Ancillary Conclusions.....	107
6.3 Recommendations.....	107
VII REFERENCES.....	109
APPENDIX A: MAGNITUDE-YIELD CALIBRATION USING THE PRESUMED JANUARY 15, 1965 CRATERING EXPLOSIVE.....	A-1
APPENDIX B	B-1
APPENDIX C: APPLICATION OF THE REPRESENTATION THEOREM AND USE OF THE "RING-LOAD" GREEN'S FUNCTION FOR REGIONAL SYNTHETIC CALCULATIONS.....	C-1

LIST OF ILLUSTRATIONS

<u>FIGURE</u>	<u>PAGE</u>
3.1 Basin and Range velocity model BR2.....	7
3.2 Crustal Q_β and Q_{Lg} estimates from the literature as a function of frequency.....	10
3.3 Bandpass filtered point source explosion synthetics for a distance of 325 km (middle) in the BR2 model compared to bandpass filtered recordings of BACKBEACH (left) and MAST (right) at station KNB.....	16
4.1 Definition of Pa, Pb, and Pmax amplitudes read from film records.....	25
4.2 Radiated P waveforms for the 2D Shagan River simulations, attenuation operator ($t^*=0.7s$) and WWSSN instrument responses at 10°, 20°, and 30° takeoff angles.....	27
4.3 Radiated displacement P waveforms for the 2D Shagan River simulations without attenuation or instrument responses at 10°, 20°, and 30° takeoff angles.....	28
4.4 Observed WWSSN waveform statistics Log(Pmax/Pa) and Log(Pmax/Pb) compared to synthetic predictions.....	30
4.5 Radiated displacement P waveforms for the three 2D Pahute Mesa tuff simulations at 10°, 20°, and 30° takeoff angles.....	34
4.6 Radiated displacement P waveforms for the three 2D Pahute Mesa tuff simulations at 10° takeoff angle compared to the 1D elastic source model.....	36

LIST OF ILLUSTRATIONS (Continued)

<u>FIGURE</u>		<u>PAGE</u>
4.7	Same as 4.5a except WWSSN instrument response and attenuation operator ($t^*=0.5s$) applied.....	37
4.8	Same as 4.6a except WWSSN instrument response and attenuation operator ($t^*=0.5s$) applied.....	39
4.9	2D synthetic P-waves at takeoff angle 10° , with WWSSN instrument, and four different attenuation operators.....	40
4.10	Synthetic far-field P-wave power spectra for the Pahute Mesa tuff model, 125 kt. takeoff angle 10° and depths of burial, 200, 680, and 980 meters.....	41
4.11	Spectral ratios of the far-field P-wave (680 meter depth versus 980 meter depth) for three takeoff angles (10° , 20° , and 30°) averaged over several spectral bandwidths.....	43
4.12	Prediction for P-wave spectral ratio between two hypothetical 5 kt sources at 200 and 500 meter depths of burial.....	44
4.13	P (left) and SV (right) displacements at a takeoff angle of 10° for the 2D sources at 200 (top), 680, and 980 meters and the 1D elastic (bottom) source.....	45
4.14	P (left) and SV (right) linear-linear spectra at a takeoff angle of 10° for the 2D sources at 200 (top), 680, and 980 meters and the 1D elastic (bottom) source.....	49
4.15	Deconvolved waveforms from Lyman, et al. for BACKBEACH (top) and PANIR (bottom).....	52
4.16	Deconvolved Pn waveforms from several Pahute Mesa events recorded at KNB and MNV.....	56

LIST OF ILLUSTRATIONS (Continued)

<u>FIGURE</u>	<u>PAGE</u>
4.17 Displacement teleseismic P waveforms (TOA=20°) for the three 2D calculations and the 1D RVP convolved with the Green's function.....	59
4.18 Far-field SV waves (TOA=10°) from the three 2D calculations compared with the 1D elastic point source explosion model.....	61
4.19 Far-field P and SV waveforms are shown to the same scale for comparison.....	64
5.1 Comparison of broadband velocity synthetics for the Pahute Mesa tuffs calculations at 100 km.....	69
5.2 Whole record spectra for the 2D Pahute Mesa tuff synthetics in 5.1a.....	71
5.3 Bandpass filtered seismograms for the 2D 680 meter depth of burial vertical component synthetic.....	73
5.4 Whole record spectral ratio of the 680 and 980 meter depth synthetics.....	75
5.5 Average spectral levels of synthetics for 680 and 980 meter depth sources in three frequency bands.....	77
5.6 Bandpass filtered synthetics and Green's functions in the 0.5 to 1.25 Hz bandwidth.....	78
5.7 Comparison of several velocity models for Eastern Kazakhstan.....	82
5.8 Broadband velocity synthetics for the Shagan River calculations at 200, 680, and 980 meter depths.....	84

LIST OF ILLUSTRATIONS (Continued)

<u>FIGURE</u>		<u>PAGE</u>
5.9	Bandpass filtered Shagan River 2D synthetics (left) and 1D synthetics (right) for depth of 200 meters.....	86
5.10	Whole record narrow band peak amplitudes (top) versus spectral power (bottom) and 2D (left) versus 1D (right).....	89
5.11	Log spectral ratio of 2D to 1D spectra for the whole record, P-wave, and SV-Lg windows.....	93
5.12	Shagan River 680 meter depth of burial 2D synthetic and several Green's functions in the 0.5-1.25 bandwidth.....	94
5.13	RDP estimates from the radial displacements of the finite difference calculations at the working point level.....	98
5.14	2D PILEDRIVER synthetics and Green's functions in the 0.5-1.25 Hz band.....	100
5.15	Fundamental mode excitation for the three 2D PILEDRIVER simulations.....	103

I. SUMMARY

The seismic motions from nonlinear two-dimensional (2D) axisymmetric finite difference calculations of underground explosions are propagated to regional and teleseismic distances. Synthetic seismograms are computed and examined to study the effects of depth of burial, medium, structure, and prestress on seismic waveforms. The elastodynamic representation theorem is used to couple the results of finite difference source calculations to regional Green's functions computed using a wavenumber integration algorithm. The 2D finite difference source calculations include the nonlinear effects of gravity, spall, bulking, and cracking as well as the finite extent and divergence from spherical symmetry. The results are broadband full wave regional synthetics for explosion sources with cylindrical symmetry. These theoretical seismograms are studied with regard to proposed regional discriminants between explosions and earthquakes.

Synthetics for Pahute Mesa tuff are examined for three depths; normal burial, overburied, and cratering. Regional synthetics from axisymmetric explosions are significantly different in the short period band (0.25 to 2 Hz) from simple point source explosion models. Simulation of an overburied explosion shows enhancement of high frequencies relative to a normal buried source. The 2D axisymmetric sources exhibit greater Lg excitation than point sources, and the normal buried source shows enhanced short period fundamental excitation compared to a point source or an overburied source.

Regional synthetics for a simple model of Shagan River explosions also demonstrate that the point source is an inadequate model for regional phase excitation. By contrast, regional synthetics for model explosions in granite with or without prestress differ little from the simple point source model in the short period band. The implications are that the two-dimensional signature for the explosion source depends on medium, and structure in a complicated manner. These calculations demonstrate that the point source explosion model may be inadequate to model discrimination problems in the regional distance range. Higher order models for the explosion source are necessary to understand the effects of depth of burial, medium, and structure, on the high/low frequency discriminant.

Recommendations are made to improve modeling of two-dimensional explosion source effects in short period and high frequency regional waveforms. Improved nonlinear near-source structure interaction and additional calculations for larger ranges of scaled depth of burial and yield will be required to further test the hypothesis that the empirical high/low frequency regional discriminant is related to scaled depth of burial effects.

II. INTRODUCTION

Regional stations or arrays are required for the reliable detection and discrimination of small seismic events. At regional distances, small events are recorded that do not excite sufficient long-period surface waves that the traditional $m_b:M_S$ discriminant can be used. To supplant the teleseismic $m_b:M_S$ discriminant, a variety of regional discriminants have been suggested over the years as reviewed by Pomeroy, *et al.* (1982) and Blandford (1982). Tests of some of these proposed regional discriminants have been made in recent years with western United States earthquakes and explosions. The most successful of the regional discriminants have been regional variants on the $m_b:M_S$ discriminant and a high/low frequency discriminant (Murphy and Bennett, 1982; and recently Taylor, *et al.*, 1988). The empirical results of these high/low frequency discriminants are directly the opposite of the predictions of Evernden, *et al.* (1986). Evernden, *et al.* suggested that explosions at regional distances will appear enriched in "high" frequencies relative to earthquakes. The results from careful studies using Nevada Test Site (NTS) explosions and earthquakes both in the vicinity of NTS (Murphy and Bennett 1982) and earthquakes dispersed across the western United States (Taylor, *et al.* 1988) have shown the opposite to be true. Earthquakes have appeared enriched in high frequencies relative to explosions for Pn, Pg, and Lg phases. Because there is no evidence that there are fundamental differences in the propagation of the earthquake and explosion Pn, Pg, and Lg phases, any observed differences must be due to excitation differences between earthquakes and explosions.

Either these differences reflect fundamental spectral differences in the earthquake and explosion source, or are due to depth and/or excitation differences in the Green's functions. A possibly important clue is the observation that a few overburied explosions at NTS have high frequency enhancement (Taylor, *et al.* 1988) and fail the high/low frequency discriminant. This suggests that scaled depth of burial effects partially control the frequency content of regional phase excitation. Taylor, *et al.* suggest that spall enhances the low frequencies of normal buried explosions and that overburied explosions exhibit less spall and therefore appear enhanced in high frequencies. Other possible explanations are (1) strong attenuation of high frequencies from shallow explosions, or (2) differences between a point explosion source model and a more realistic (2D or 3D) model that incorporates asymmetry in the explosion source.

In this work we explore nonspherically symmetric nonlinear explosion source models as functions of near source structure, burial depth, and prestress. Nonlinear, two-dimensional, axisymmetric finite difference calculations are studied to evaluate the excitation of regional seismic waves from these calculations. We use calculations that serve as explosion models in tuff and granite for fixed yield and different depths. In this way we examine the relative frequency content of waves excited by non-point source models for explosions. These axisymmetric simulations represent the next highest level of complexity above the spherically symmetric explosion point source. Instead of simple linear "pP" and "pS" reflections near the source, the full nonlinear free-surface interaction is simulated including nonlinear yielding, cracking, and spall. The material properties responsible for the containment of the explosion are functions

of hydrostatic pressure and therefore, there is inherent symmetry about the vertical axis for the simplest models that include depth dependent effects.

In addition to a study of the depth of burial effects, we study the excitation of the entire regional waveform by explosions with particular attention to the excitation of the SV component of motion. Bennett, *et al.* (1987) studied variations in excitation of regional phases for point explosion and earthquake sources as functions of depth. Although they found that there are significant variations in the excitation of these phases as functions of depth and focal mechanism, they found no physical mechanisms to explain the empirical high/low frequency discriminant between explosions and earthquakes. Furthermore, they found as others have noted that point explosion sources are poor sources of Lg. Bennett, *et al.* suggested that P-to-SV conversion and "scattering" at interfaces could produce the required SV energy to couple into the Lg waveguide. It is well known that explosion generated Lg is a robust measure of the explosion size (Nuttli, 1986) in contrast to this theoretical difficulty in modeling the phase. Patton (1988) in a detailed study of the HARZER explosion suggests that spall is a significant contributor to regional Lg. Using the nonlinear 2D finite difference simulations we test the hypothesis that axisymmetric explosion models produce more SV than point explosion sources.

We examine the differences between the point explosion source, and explosion models derived from nonlinear, two-dimensional, axisymmetric finite difference calculations. Although these calculations do not simulate azimuthal variability in the source, they do simulate nonlinear free surface interactions including spall, and asymmetries that depend on depth of burial. These models serve as a "first principles" approach that are a step more complicated than spherically symmetric explosions. In the case of cratering simulations, even the physics of crater formation are modeled.

The work reported here is divided into three main sections. These sections, (1) introduce a velocity model for the propagation of regional waves in the basin and range, (2) examine far-field P and SV waves radiated by axisymmetric nonlinear finite difference simulations of explosions, and (3) introduce a new method for the propagation of the nonlinear explosion simulations to regional distances. A brief discussion of the conclusions and recommendations follows.

In Section III, we present a velocity model for purposes of propagation of regional seismic signals, and examine some results of point source synthetics of explosions and earthquakes. These calculations serve two purposes. First, we examine a velocity and Q model for the Basin and Range based on a literature survey and validate the model by examining the distance dependence of Pn, Pg, and Lg. Second, we confirm the conclusions of Bennett, *et al.* (1987) that the regional propagation and excitation differences between earthquakes and explosions does not alone explain the high/low frequency discriminant. As part of a validation and testing process we have examined regional short-period and broad-band seismograms in the Western United States in order to compare their propagation character (spectral and time domain) to predictions from Green's functions produced by the wavenumber integration code. We review results of several authors for the attenuation of regional phases in the western United States. Procedures similar to those applied to real data are then applied to

synthetic Green's functions to validate the velocity and attenuation models for western United States regional wave propagation. Results indicate that frequency dependent Q models may be required for the crust in order to adequately explain the frequency dependence of Pg and Lg as a function of distance. This warrants additional study for the understanding of regional discriminants.

In Section IV, we present far-field P and SV waveforms from axisymmetric nonlinear finite difference calculations for Pahute Mesa and Shagan River structures at various scaled depths of burial. In addition, far-field P and SV from nonlinear models for PILEDRIVER with and without prestress are compared. We have extended the work of Day, *et al.* (1986b) that compared predicted teleseismic P-waveform statistics to observed statistics of $\text{Log}(P_{\text{max}}/P_a)$ and $\text{Log}(P_b/P_{\text{max}})$ of McLaughlin, *et al.* (1985). For comparison with results of Der, *et al.* (1987), McLaughlin, *et al.* (1986) and McLaughlin, *et al.* (1987) we have generated a suite of synthetics based on a number of nonlinear calculations intended to simulate Shagan River and Pahute Mesa contained and cratering explosions as well as contained explosions in granite. These synthetics are compared to observed seismogram statistics. Using adjustments for depth of burial based on synthetic waveforms, the 150 kt limit is estimated for the Shagan River test site.

We conclude, that in general, the 2D nonlinear calculations under predict the short period teleseismic "pP" amplitude. The 2D nonlinear calculations either over predict the amount of attenuation of the "pP" phase or under predict the nonlinear spall contribution to this phase. The P-wave spectral scaling of the 2D nonlinear calculations suggest that overburial enhances high frequencies with respect to normal burial. However, 2D nonlinear SV radiation is enhanced in low frequencies relative to that predicted by a point source model. Taken together, the P-wave and SV-wave radiation predicted by the 2D nonlinear calculations are inconsistent with a simplified 1D point source model for the explosion.

Finally in Section V, we propagate the axisymmetric nonlinear simulations to regional distances using a newly developed interface between the finite difference codes and a wavenumber integration synthetic code. The theoretical justification based on the elastodynamic representation theorem for this interface is contained in an appendix. Finite difference explosion simulations are propagated to regional distances by the use of the wavenumber integration code. This simulates aspects of the source finiteness and directivity not modeled by explosive point sources. In this manner, the two-dimensional aspects of the source models can be properly propagated to regional distances.

We find that enhanced shear wave (Lg) generation is evident in some axisymmetric simulations due to the nonlinear free surface interaction. This addition to the point explosion source model can to first order be seen as a vertically oriented compensated linear vector dipole (CLVD) source.

Although the 2D nonlinear synthetics qualitatively show more explosion generated Lg than the 1D point source model, the Lg excitation is still well below that commonly observed from explosions. The 2D nonlinear synthetics suggest that processes that enhance the CLVD component of the explosion source will contribute to

regional SV energy. Such processes include, but are not limited to, spall and near source scattering. Simulations of explosions in prestressed granite show remarkably little difference between no prestress simulations in the short-period frequency range. These conclusions are in agreement with the lack of correlation of short period (Lg) observations with long period (LR) tectonic release observations.

Day, *et al.* (in preparation) compare two popular methods for the construction of synthetic regional seismograms. The method of modal summation with "locked-modes" as described by Harvey (1981) is compared to a wavenumber integration program based on the work of Apsel (1979). It is found that the two methods produce consistent results for high Q Earth models. However, the perturbation approximation inherent in the modal summation procedure can break down for low Q's appropriate for the western United States. Therefore, the wavenumber integration method for computation of synthetic regional seismograms is the most accurate method if attenuation is to be considered. Also, modal summation computation time rapidly increases with increasing frequency, such that the wavenumber integration procedure is faster and more accurate at frequencies above 1 Hz. Therefore, except where stated, the wavenumber integration method is used for the computation of regional synthetics throughout this report.

III. POINT SOURCE REGIONAL SYNTHETICS

3.1 Introduction

In order to properly model regional seismograms, we require a model for the crust and upper mantle with appropriate velocity and attenuation properties. In this section we introduce a velocity and Q model for the basin and range province and examine the behavior of explosion and earthquake Green's functions for this model. The model is chosen with a frequency independent Q in crust and upper mantle and is validated by comparison of the spatial decay of regional phases for synthetics and observations. These calculations provide a baseline for the evaluation of regional synthetics based on the nonlinear two-dimensional finite difference source simulations.

3.2 Basin and Range Model, BR2

The velocity and Q model, BR2 listed in Table 3.1 (Figures 3.1a,b), was intended to be representative of a number of velocity models that have been proposed for the basin and range province of the western United States. Slight gradients were introduced in the upper crust, lower crust and upper mantle lid in order to turn rays but not produce noticeable triplications. An upper mantle lid P-wave velocity gradient was chosen to be just below that of the CIT100 model series, and the Herrin, *et al.* (1968) P-wave models (0.01215 km/s/km). The velocity model is not intended to represent any single path but to be representative of a typical Basin and Range path. The CIT100 series models of Archambeau, Flinn, and Lambert (1969), as well as the models of Pakiser, (1963), Helmberger (1973), Priestley and Brune (1978), Priestley, *et al.* (1982), Patton and Vergino (1981), Chun (1983), Wallace (1983), Patton and Taylor (1984), Taylor and Patton (1986), and the NTS4 model of Bennett, *et al.* (1987) were all considered. It was decided to suppress the crustal low-velocity zones of the models and retain only the well established low velocity zone of the upper mantle. There is a strong initial velocity gradient at the top of the crust and a lesser gradient throughout the rest of the crust.

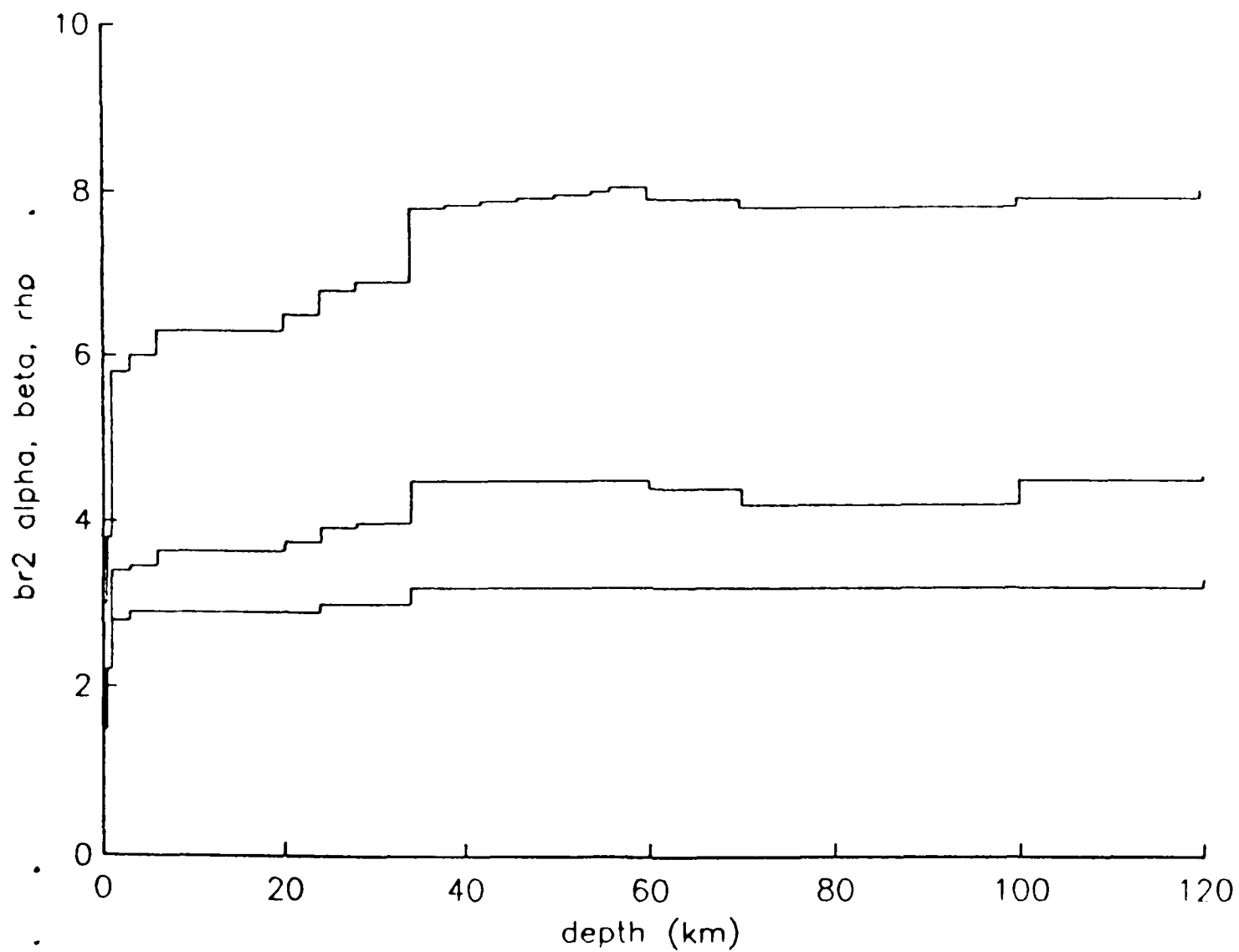


Figure 3.1a. Basin and Range velocity model BR2.

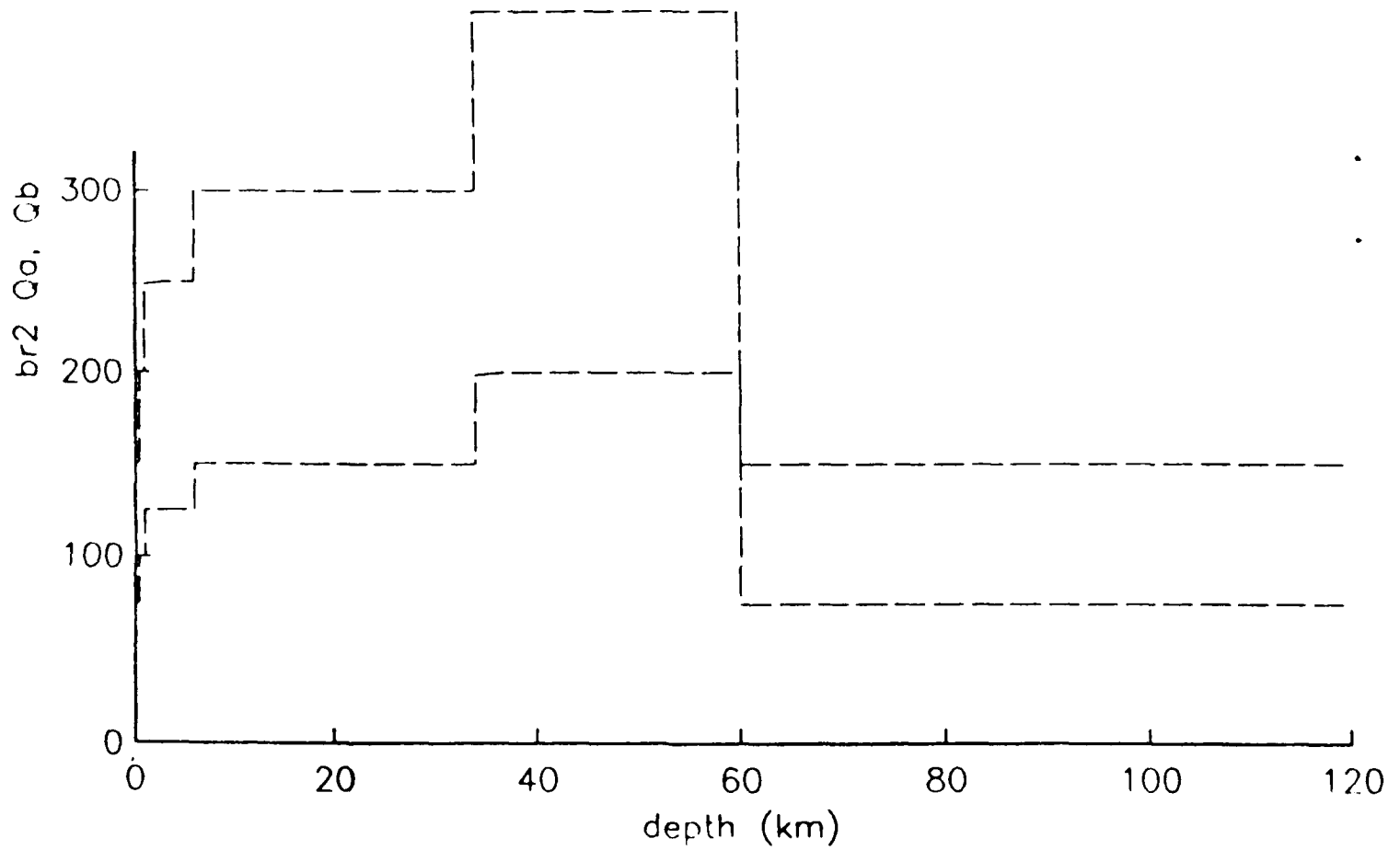


Figure 3.1b. Basin and Range Q model, BR2.

TABLE 3.1 Model BR2

h	α	β	ρ	Q_P	Q_S
(km)	(km/s)	(km/s)	(gm/cc)		
0.50	3.00	1.58	2.00	150.	75.
0.50	3.80	2.20	2.20	200.	100.
2.00	5.80	3.40	2.80	250.	125.
3.00	6.00	3.46	2.90	250.	125.
14.0	6.30	3.64	2.90	300.	150.
4.00	6.50	3.75	2.90	300.	150.
4.00	6.80	3.93	3.00	300.	150.
6.00	6.90	3.98	3.00	300.	150.
4.00	7.80	4.50	3.20	400.	200.
4.00	7.84	4.50	3.20	400.	200.
4.00	7.88	4.50	3.20	400.	200.
4.00	7.92	4.50	3.20	400.	200.
4.00	7.96	4.50	3.20	400.	200.
2.00	8.00	4.50	3.20	400.	200.
4.00	8.05	4.50	3.20	400.	200.
10.0	7.90	4.40	3.20	150.	75.
10.0	7.80	4.20	3.20	150.	75.
20.0	7.80	4.20	3.20	150.	75.
20.0	7.90	4.50	3.20	150.	75.
60.0	8.00	4.55	3.30	150.	75.
20.0	8.10	4.60	3.40	300.	150.

The Q model also was intended to be representative of the basin and range but not to represent any one particular path. Although there may be some recent evidence for deviation from the rule that $\frac{Q_P}{Q_S} \approx 2$, the model was constructed with this con-

straint. Crustal shear-wave Q_β estimates vary quite significantly from author to author and much of the variation may simply be lateral variation in attenuation. Also, frequency dependence of Q is evident in the data and produces differences between authors. Consequently, a median shear-wave average Q value near 1 Hz was chosen for the crust and several depth dependent Q models were used for guidance to choose a depth dependence. Depth dependent Q models for the region include Bache, *et al.* (1980), Chun (1983), Patton and Taylor (1984), and Taylor and Patton (1986). The chosen model features a low surface Q in order to suppress short-period fundamental mode at large regional distances and a low Q zone in the upper mantle low-velocity zone. Q estimates for Pn indicate that there exists a high Q lid to the mantle low-velocity zone. A summary of crustal Q_β and Q_{Lg} estimates from the literature is tabulated below (Table 3.2) and graphically portrayed in Figure 3.2.

In general however, the BR2 model may actually underestimate the total amount of attenuation in the crust and upper mantle at 1 Hz. Model BR2 has a teleseismic P-

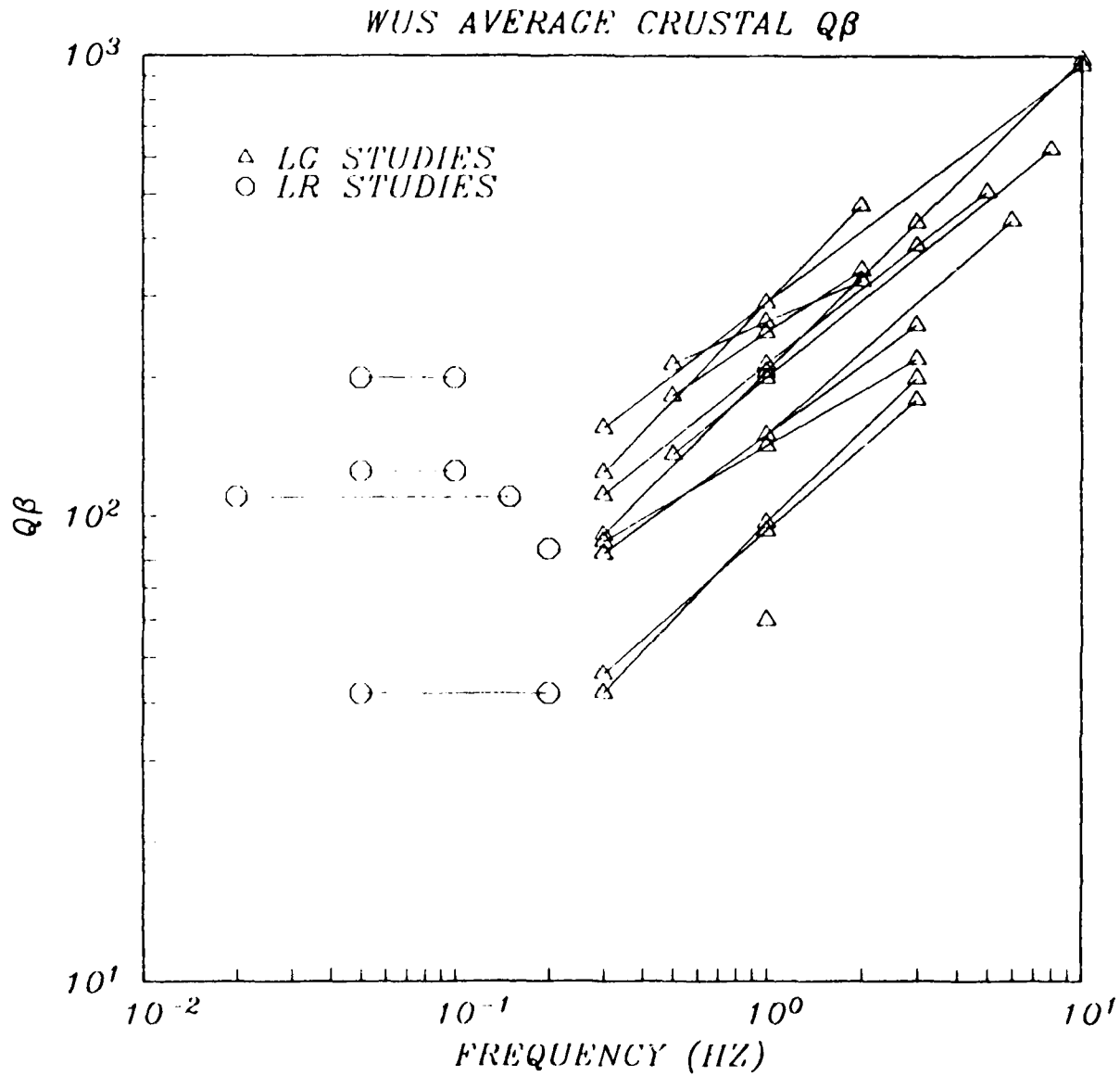


Figure 3.2. Crustal Q_β and Q_{Lg} estimates from the literature as a function of frequency. Lg studies are designated with triangles, LR studies with octagons.

wave t^* of about 0.15 second, and a teleseismic S-wave t^* of 0.50 second down to a depth 200 km. This is 0.20 seconds less than the total \bar{t}_P^* that Der, *et al.* (1985) would attribute to the NTS source region, and would leave the remainder to be accounted for by attenuation along the remainder of the mantle P-wave path to the turning point of the ray.

The average Q's of the BR2 model crust averaged over vertical travel time for P and S waves are 139 and 279, respectively. The average crustal S-wave Q of about 140 was chosen to coincide with the median value for Lg Q's at 1 Hz from a number of researchers working in the Basin and Range.

TABLE 3.2 SUMMARY OF AVERAGE CRUSTAL Q_β ESTIMATES

REFERENCE	Q	RANGE (Hz)
Press (1964)	$Q_{Lg} = 450$	0.7-1.3
Mitchell (1975)	$Q_\beta = 125$	0.05 to 0.1
Lee and Solomon (1975)	$Q_\beta = 200$	0.05 to 0.1
Braile (1977)	$Q_\beta \approx 60$	≈ 1
Bache <i>et al.</i> (1978)(NTS-ALQ)	$Q_\beta = 125$	0.05 to 0.1
Cheng and Mitchell (1981)	$Q_\beta = 85$	0.2
Der <i>et al.</i> (1981)(OB2NV)	$Q_{Lg} = 200 f^{0.5-0.6}$	0.5 to 8
Chun (1983)	$Q_\beta \approx 42$	0.05 to 0.2
Singh and Herrmann (1983)	$Q_{Lg} = 250 f^{0.45}$	0.5 to 2
Pesceckis and Pomeroy (1984)	$Q_{Lg} = 264 f^{0.3}$	0.5 to 2
Patton and Taylor (1984)	$Q_\beta \approx 110$	0.02 to 0.15
Nuttli (1981)	$Q_{Lg} = 290 f^{0.7}$	1 to 5
Nuttli (1986)(NTS-TUC-DUG-BKS)	$Q_{Lg} = 290 f^{0.7}$	0.3 to 2
Chavez and Priestley (1986)(EXP)	$Q_{Lg} = 206 f^{0.68}$	0.3 to 10
Chavez and Priestley (1986)(EQKS)	$Q_{Lg} = 214 f^{0.54}$	0.3 to 5
Taylor <i>et al.</i> (1988)	$Q_{Lg} = 150 f^{0.6}$	1 to 6
Patton (1987)(NTS-ELK)	$Q_{Lg} = 150 f^{0.5}$	0.3 to 3.0
Patton (1987)(NTS-KNB)	$Q_{Lg} = 142 f^{0.4}$	0.3 to 3.0
Patton (1987)(NTS-LAC)	$Q_{Lg} = 97 f^{0.7}$	0.3 to 3.0
Patton (1987)(NTS-MNV)	$Q_{Lg} = 93 f^{0.6}$	0.3 to 3.0

The upper mantle Q model was chosen to strike a balance between relatively high Q's observed for Pn and the surface wave models that have less resolution as to the location of the low-Q region in the upper mantle. Estimates of the average Q for Pn are often dependent on the geometrical spreading assumed and hence are velocity model dependent. A model that assumes a half-space upper mantle will predict a frequency dependent Pn propagation with the classical head-wave nature. Observations

of Pn, however, show that it is an impulsive high-frequency arrival and that the Pn spectrum corrected for the source spectrum does not fall-off faster than proportional to f^{-1} .

In order to demonstrate this, we correct explosion Pn spectra for instrument and source and then estimate a t^*_{Pn} from the spectral slope. Estimates of t^*_{Pn} for a number of paths are listed below (Table 3-3) for the HARDHAT explosion (Climax Stock, NTS) to several regional LRSM (Long Range Seismic Measurement) stations. The t^*_{Pn} estimates would indicate a mean Q of about 600 with a standard error of the mean of 100 and a standard error of the observations of 400. This large scatter implies that individual event-receiver paths exhibit large variations in attenuation. Apart from the large scatter in these estimates the mean value is in general agreement with an apparent Q_α around 500 in the upper mantle lid if we account for the average attenuation of the crust.

TABLE 3.3 HARDHAT TO LRSM t^*_{Pn} (0.5 to 7 Hz)

$\Delta(\text{deg})$	$t^*_{Pn}(\text{sec})$	STATION
1.4	0.06	DV-CL
2.6	0.05	KN-UT
3.0	0.05	TN-CL
3.6	0.14	WM-AZ
3.6	0.05	FM-UT
4.3	0.05	WI-NV
4.4	0.14	FS-AZ
4.5	0.40	CP-CL
5.3	0.05	SF-AZ
6.6	0.10	DR-CO
6.6	0.20	HL-ID
8.7	0.40	PT-OR
9.2	0.85	LC-NM
9.4	0.40	RT-NM

All of the CIT100 series models of Archambeau, Flinn, and Lambert (1969) had very high Q lids. Werth, Herbst, and Springer (1962) estimated $Q_{Pn} = 300$ to 400 in the 96 to 714 km distance range based on observations of Ranier Mesa events recorded on Benioff seismograph systems. At the high end of Q_{Pn} estimates from the literature, Evernden, *et al.* (1986) suggest that Pn has a Q between 1000 and 2000 in tectonic regions.

As far as frequency dependence for model Q's are concerned, we have chosen to make the synthetic computations (at least at first) with a frequency independent attenuation structure. However, numerous authors have reported frequency dependent Q models for Lg as listed above, fewer authors have reported frequency dependence

for Pn and Pg attenuation. Taylor, *et al.* (1988) estimate frequency dependence for Pn and Pg apparent Q's as $Q_{Pn} = 250 f^{0.6}$ and $Q_{Pg} = 300 f^{0.1}$. These correspond to a 1 Hz t^*_{Pn} at 300 km of 0.15 sec and a $\bar{t}^*_{Pn} = t^*_{Pn} + f \frac{dt^*}{df} = 0.06$ sec. The effect of the power law frequency dependence is to lower \bar{t}^*_{Pn} which controls the spectral shape of the phase and if interpreted as a constant Q model would imply a Q_{Pn} in excess of 600. Similarly at 300 km and 1 Hz, Taylor, *et al.* would predict $t^*_{Pg} = 0.14$ sec.

We have assumed that $\frac{Q_\alpha}{Q_\beta} = 2$. Both analysis presented later in this section and the results of the Q estimates of Taylor, *et al.* (1988) suggest that for frequencies above 1 Hz, the crustal P- and S-wave Q's may have different frequency dependence and that at high frequencies, Q_β may be higher than Q_α . Similar results were found by Goncz, *et al.* (1986) for the eastern United States for a comparison of apparent Pn and Sn Q's. Also, Soreno and Orcutt (1987) claim similar results for oceanic Pn and Sn phases. It is not known at this time if this is due to propagation effects in layered media, intrinsic bulk-attenuation, or whether this is due to scattering by lateral variations in crustal structure producing different effects on P type and S type modes of propagation. From our numerical experiments, it appears that this phenomenon is not due to one-dimensional (1D) layered structure effects, which leaves intrinsic bulk-attenuation and/or scattering. Extensions to the wavenumber integration procedure are easily implemented that will introduce separate frequency dependence into the attenuation of P and S waves in the medium.

3.3 Amplitude-Distance Relationships

We also wish to represent the average observed amplitude-distance relationships for Pn, Pg, and Lg. In the following, we review some of the sometimes conflicting reports from the literature. These differences often reflect the difference between using Log(amplitude/period), versus Log(amplitude), or maximum amplitude versus a specified cycle, or differences in instrumental bandwidths.

As far as empirical distance relationships are concerned, the Pn amplitudes from explosions or shallow earthquakes in the western U.S. are generally proportional to R^{-3} to $R^{-3.5}$ according to a review by Blandford, *et al.* (1981). The Werth, *et al.* (1962) data can be regressed to a relationship for three events (10 data points) as $\text{Log}(Pn) = \text{Log}(\text{Yield}) + 9.3(0.6) - 3.05(0.24) * \text{Log}(R)$, for the amplitude of the first half cycle of the Pn (amplitude in nm, R in km). Cases for attenuation less than R^{-3} may be found, such as the Veith and Clawsen (1972) B values for Log(amplitude/period) zero to peak P-wave magnitude which correspond to a linear formula for m_b from $\Delta = 2$ to 10 degrees,

$$m_b = -1.55(0.08) + 2.1(0.1)\text{Log}(\Delta).$$

Evernden (1967) derived a formula for m_b from Pn peak to peak amplitude (in nm) of

$$m_b = -7.55 + 1.21\text{Log}(A/T) + 3.04\text{Log}(R).$$

The Evernden study was based on LRSM records for NTS explosions. Taylor, Denny, and Vergino (1986) found using broadband velocity seismograms that $Lg(A/T)$ was proportional to R^{-3} for earthquakes and explosions in the 300 to 1000 km range. However Denny, Taylor and Vergino (1987) arrived at a preferred formula of

$$m_b = -3.95 + \text{Log}(A) + 2.42\text{Log}(R)$$

and a distance coefficient of 2.79 for $\text{Log}(A/T)$. They argued that m_b based on $\text{Log}(A)$ was more stable than that based on $\text{Log}(A/T)$ and that better $m_b:M_S$ discrimination of earthquakes and explosions resulted from their choice for the m_b distance correction formula. Clearly, we see that instrumental bandwidths, and the choice of $\text{Log}(A)$ versus $\text{Log}(A/T)$ are important factors in the published amplitude distance decays for Pn.

These differences in instrumental bandwidth impact the use of other phases as well as Pn. Blandford, *et al.* (1981) report that Pg or Pmax as measured on LRSM stations decays as $R^{-3.0}$ in the western U.S. Similarly, they found that Lg decayed as $R^{-3.0}$. Based on these distance corrections they reported that the distance corrected Pg/Lg ratio could be used to discriminate between earthquakes and explosions. Barker (1981) using raw ANMO records of NTS explosions and various WUS earthquakes also reported separation of earthquake and explosion populations using the Pg/Lg ratio. Barker's explosions were of varying size but at nearly the same distance range. Barker also reported success using Pg/Pn on the raw records and Pn(0.625Hz)/Pn(2.5Hz) ratios in conjunction with the Pg/Lg ratio. Murphy and Bennett (1982) using earthquakes and explosions in southern Nevada recorded at TFO found the Pg/Lg ratios from the raw records did not discriminate earthquake and explosion populations. However, they found that Lg(2-4Hz)/Lg(0.5-1Hz) ratios successfully separated explosions and earthquakes. Gupta, *et al.* (1984) reported that high-frequency to low-frequency ratios for Lg were a useful discriminant, but that a spectral measure of Pg/Lg could also be used to increase the discrimination power of the two combined statistics. Since these studies were conducted with different instrumental bandwidths (LRSM, SRO, Johnson-Matheson, and Halls-Sears), the frequency and distance dependence of raw record Pg/Lg ratios may have contributed to discrepancies between some of the workers. The combination of two or more measures of the regional phases in a discriminant function may overcome some of the variations in a single discriminant measure. Clearly, if these difficulties are to be overcome, then these phase ratio and spectral discriminants must take into account the distance dependence of the phases in order to make frequency and distance corrections.

Taylor, *et al.* (1988) extended the Murphy and Bennett discriminant to higher frequencies and found that the (6-8Hz)/(1-2Hz) works even better than the (2-4Hz)/(0.5-1Hz) measure. In order to accomplish this, they introduced distance and frequency dependent corrections for each phase. However, they did find exceptions for some overburied explosions. The overburied explosions appear to have higher frequency Lg than normally contained explosions.

In conclusion, we see that in order to make a portable discriminant based on the spectra of single phases or combinations of phases, will require an understanding of

the basic propagation characteristics for the regional wavepackets. In the next section, we show that the full waveform synthetics can simulate these characteristics and then discuss some characteristics of the model required to achieve this.

3.4 Analysis of BR2 Synthetics

Figures 3.3a, b, and c show synthetics at 325 km and 400 km distance compared to records from the broadband stations KNB (~320), LAC (~320), and ELK (~400) for BACKBEACH and MAST. The synthetics are velocity in nm/sec for a Heavyside step explosion point source (moment of 10^{14} Nt-M) at a depth of 1 km for the BR2 model. The data is recorded on the LLNL broadband systems with a flat response to velocity in the bandwidth of interest. The data and synthetics have been bandpassed in four bands 0.05-0.16 Hz, 0.16-0.50 Hz, 0.50-1.58 Hz, and 1.58-5.0Hz. The general character of the Pn and Pg phases at high frequencies and the low-frequency surface waves are similar to the real data. The primary differences can be seen in the coda of the deterministic wavepackets and in the amplitudes of the Lg at intermediate frequencies and above 1 Hz. BACKBEACH can be seen to have generated relatively more Lg than MAST at ELK and KNB. However, in general the Lg amplitudes are not more than a factor of two above the Pg coda. Clearly, the explosion point source does not excite enough Lg relative to other phases to agree with observations. Also, the relative amplitude of the synthetic Lg signals between the 0.50-1.58Hz and the 1.58-5.0Hz bandwidths is not right. The explosion Lg that is excited in the 1D layered models by a point source does not contain enough energy above 1 Hz. We will return to this later after a more detailed analysis of the synthetics using both spectral and time domain bandpass analysis..

In order to test that the velocity and Q model represents propagation in the western U.S. we have used the synthetics as data is often used to infer the spatial decay of regional phases and estimate Q. Using broadband velocity records that represent the velocity response to a step function source we find that for a deviatoric source (average between strike-slip and dip-slip at 45° azimuth) at 8 km depth the peak amplitudes (velocity) of the three phases can be characterized as:

$$\text{Log}(Pn_{\text{max}}) \propto -2.84 * \text{Log}(R/100), \sigma = 0.14$$

$$\text{Log}(Pg_{\text{max}}) \propto -2.40 * \text{Log}(R/100), \sigma = 0.13$$

$$\text{Log}(Lg_{\text{max}}) \propto -2.44 * \text{Log}(R/100), \sigma = 0.10$$

The power law decay of these phases between R^{-2} and R^{-3} are in rough agreement with other broadband velocity decays observed in the region. Since the amplitude-distance relationship is frequency dependent, and therefore will also be dependent on instrumental bandwidth, we applied two different techniques to estimate the apparent spatial Q from the synthetics.

3.4.1 Spectral Domain Measures of Apparent Q

We assume that the amplitude of a phase is proportional to a geometrical spreading factor R^{-g} where $0.5 \leq g \leq 1$, and an anelastic factor $\exp(-\pi f R / c / Q)$ where R is distance, c is the group velocity, and Q is the apparent quality factor. Therefore, we may estimate Q by either assuming a geometrical spreading exponent and fit the

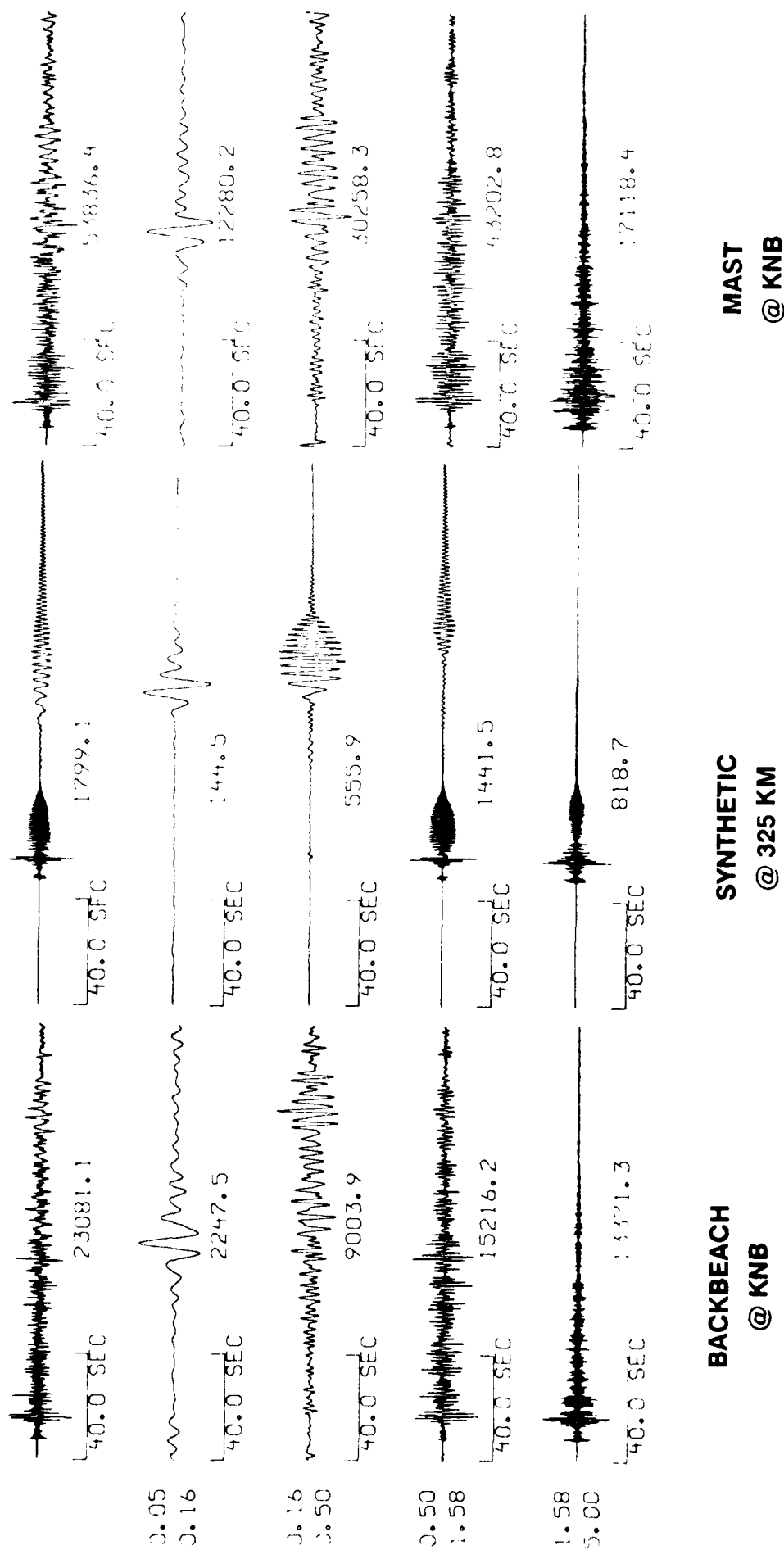


Figure 3.3a. Bandpass filtered point source explosion synthetics for a distance of 325 km (middle) in the BR2 model compared to bandpass filtered recordings of BACKBEACH (left) and MAST (right) at station KNB. Broadband velocity seismograms and bandpass filters 0.05-0.16 Hz, 0.16-0.5 Hz, 0.5-1.58 Hz, and 1.58-5.0 Hz from top to bottom. Relative excitation of Pn and Pg at high frequencies and P and Rayleigh at intermediate frequencies are about right. Synthetic Lg excitation relative to Pg is a poor match with observations.

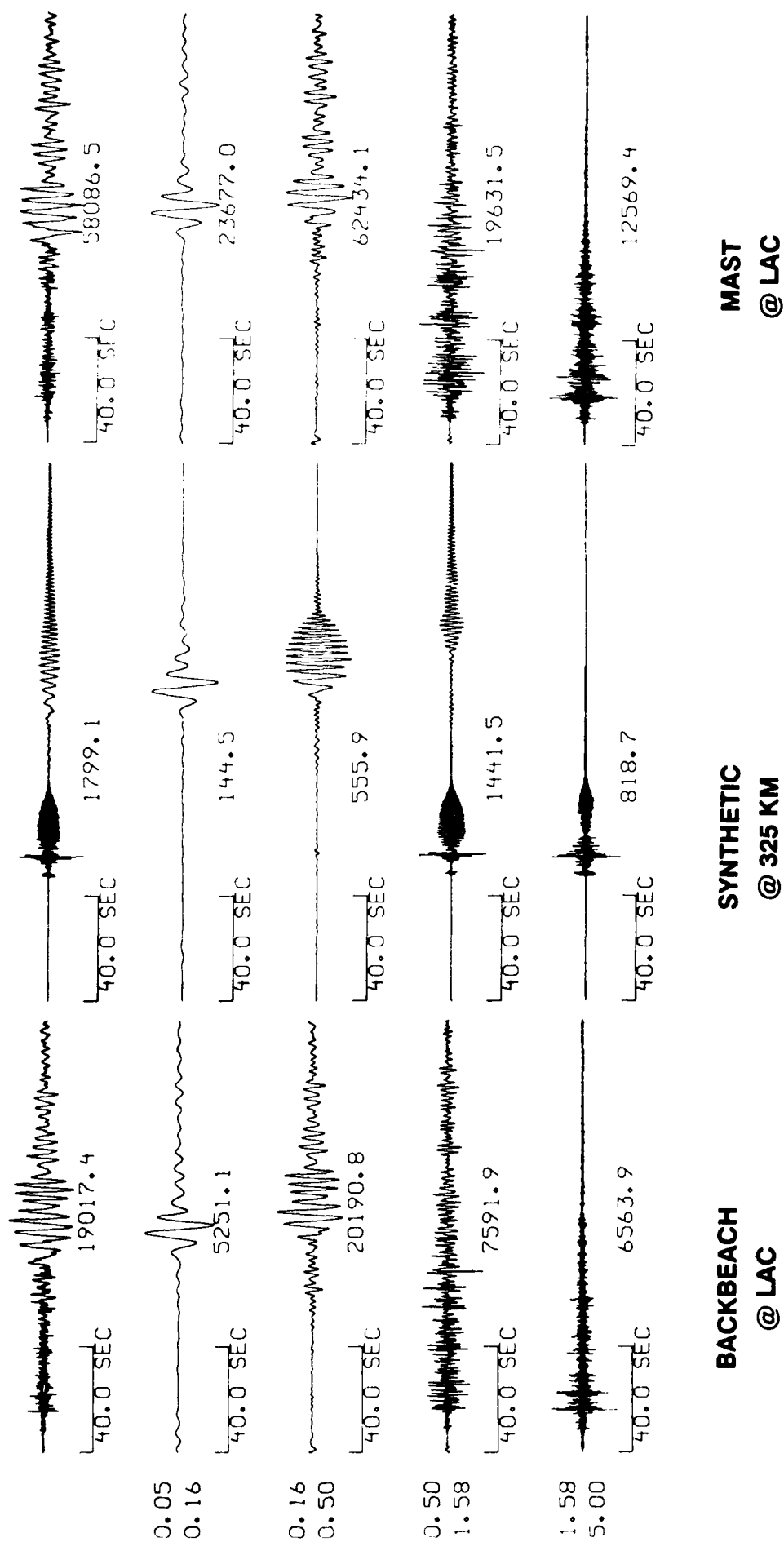


Figure 3.3b. Comparison of bandpass filtered synthetics at 325 km with observations at station LAC: BACKBEACH (right), synthetic (center), and MAST (left).

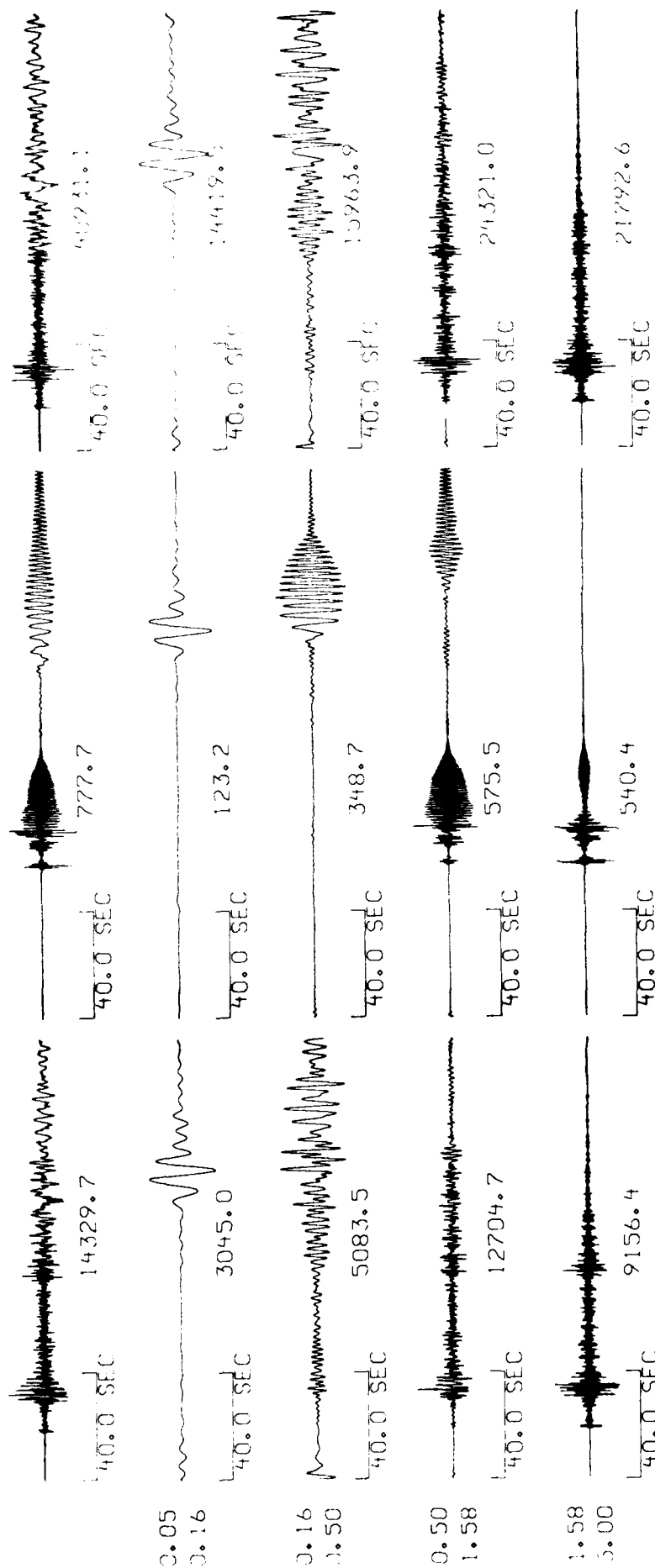


Figure 3.3c. Comparison of bandpass filtered synthetics at 400 km with observations at station ELK: BACKBEACH (right), synthetic (center), and MAST (left).

amplitude decay with distance, or we may compute ratios of spectra at different distances and estimate Q from the slope of the spectral ratio: $\text{Log}(A_1/A_2) = -g \text{Log}(R_1/R_2) - \pi f \text{Log}(e)(R_1 - R_2)/c/Q$.

Using spectral ratios of vertical components between different distances (200km/600km, 300km/700km, etc...) for synthetic Pg ($c = 6$ km/s) we find no distance dependence for the apparent spectral Q and only insignificant differences between the Pg excited by an explosion and that by a deeper "earthquake" (All "earthquake" results quoted here are an average between the response of strike-slip and dip-slip sources at 45° azimuth). We find $Q_{Pg} = 256(32)$ mean, 270 rms, 231 median, and 244(11%) geometrical mean for the 8 km deep earthquake source. Similarly for the 1 km explosion source, we find $Q_{Pg} = 306(50)$ mean, 335 rms, and 276(17%) geometrical mean. The spread in Q by either determination is about ± 140 . So even with synthetic data, it is clear that such a determination is subject to considerable variance. For comparison, the BR2 model has an average Q_P of about 270 in the crust which compares favorably with the spectral Q observed in the synthetic Pg's. We see no distance dependence on the apparent spectral Q to suggest for example that ratios between 200 km and 400 km are any different than ratios between 400 km and 600 km.

Similar results for Pn apparent Q ($c = 7.8$ km/s) from spectral ratios show a very large spread with $Q_{Pn} = 607(150)$ mean, 743 rms, 370 median, and 506(22%) geometrical mean. The large uncertainty from synthetic data indicate that the prospects of determining Q in this manner from real data will encounter even larger scatter. The values are roughly consistent with the Q_P value of 400 in BR2 for the upper mantle lid, but suggest that the estimates are biased on the high side.

For Lg ($c = 3.5$ km/s) we find $Q_{Lg} = 242(20)$ mean, 250 rms, 253 median, and 240(9%) geometrical mean, for the 8 km deep earthquake, $Q_{Lg} = 144(13)$, 150 rms, 142 median, 140(10%) geometrical mean, for a 0.5 km deep earthquake source, and $Q_{Lg} = 106(7)$ mean, 108 rms, 102 median, and 104(4%) geometrical mean for a 1 km deep earthquake source. We find no apparent distance dependence on the apparent Lg attenuation. The estimates from the shallow earthquake synthetics are consistent with the average Q for the model crust of BR2 of 139. The deep earthquake Lg spectra are contaminated by Sn which arrives within the Lg window and accounts for the higher Q estimate. The shallow earthquake Lg is better excited and the Q is more consistent with the average crustal Q_β .

3.4.2 Time Domain Measures of Apparent Q

The time domain measures for attenuation are estimated by bandpass filtering the records and then fitting a functional form to the Log-peak-amplitude in each band as a function of distance. Trade-off between the geometrical spreading assumed and the apparent Q is unavoidable in this procedure. However, bounds can be placed on the geometrical effects that can be expected for waveguide phases such as Pg and Lg. Geometrical effects can be bounded by cylindrical spreading, $R^{-1/2}$, and spherical spreading, R^{-1} . The Airy phase approximation often used for Lg results in $R^{-5/6}$ (Nuttli, 1986). Since regional attenuation is often described simply as a power law, we will first simply give the best fit exponents for each bandwidth of interest. We

have used Butterworth bandpass filters of one octave width and 48 db/octave roll-offs outside the bandwidth specified by -3 db corner frequencies.

Using the 1 km deep explosion and the 8 km deep earthquake vertical velocity records, we can summarize the data in the following tables. For the three bandwidths, 0.625 to 1.25, 1.25 to 2.5 and 2.5 to 5 Hz, Q 's are inferred assuming the center frequencies of 0.9, 1.8 and 3.7 Hz.

The $R^{-1/2}$ and $R^{-5/6}$ assumptions bracket the average crustal Q_P of 270 for this model. There is no real significant difference between the earthquake and explosion determinations of Q with this procedure.

Pg BEST FIT EXPONENTS		
	EXPLOSION	EARTHQUAKE
0.625-1.25 Hz	-1.3	-1.4
1.25-2.5 Hz	-2.5	-2.6
2.5-5.0 Hz	-4.6	-3.7

APPARENT Q_{Pg}						
	EXPLOSION			EARTHQUAKEh=8km		
EXPONENT	f= 0.9	1.8	3.7	f=0.9	1.8	3.7
-1	660	317	255	507	276	338
-5/6	447	280	242	378	248	317
-1/2	273	233	223	245	209	280

Contrary to the suggestion by Haskell (1966) that P_g will exhibit a leakage attenuation, we find that the apparent Q 's for the synthetics are indistinguishable from the average compressional Q of the crust. Haskell pointed out that P_g may be interpreted as a superposition of crustal leaking modes, and therefore would have an apparent spatial attenuation greater than the intrinsic attenuation of the crust. It would seem that at least for models such as BR2, that the leakage attenuation of P_g is small. Haskell's analysis was motivated in part by the Press's (1966) observation's of $Q_{Pg} = 260$ while $Q_{Lg} = 450$. Press's observations for Q_{Lg} are clearly out of line with the majority of other estimates listed in Table 3.2, although his Q_{Pg} observations are consistent with those of Taylor, *et al.* (1988). It is unclear why Press's estimate for crustal shear Q is high with respect to the other estimates listed in Table 3.2.

The same approach as used with P_g is now used to analyze the bandpass filtered P_n waveforms and leads to the following tabulated results.

Pn BEST FIT EXPONENTS		
	EXPLOSION	EARTHQUAKEh=8km
0.625-1.25 Hz	-2.9	-2.8
1.25-2.50 Hz	-1.9	-2.4
2.50-5.0 Hz	-3.4	-3.2

APPARENT Q_{Pn}						
	EXPLOSION			EARTHQUAKE		
EXPONENT	f=0.9	1.8	3.7Hz	f=0.9	1.8	3.7Hz
-1	91	385	327	97	221	338
-5/6	86	327	298	88	201	317
-1/2	75	252	262	77	167	275

There are obviously frequency dependent effects in the Pn Green's functions. The Q estimates correspond to a Q proportional to $f^{0.92}$, $f^{0.93}$, and $f^{0.91}$, for exponents -1, -5/6, and -1/2 respectively, if a power law were chosen as the parameterization, $Q = Q_0 f^\eta$. The effect of an apparent Q_{Pn} nearly proportional to frequency is profound for the parameter that determines the shape of the spectrum, $\bar{t}^* = t^* + f \frac{dt^*}{df} = \frac{R}{cQ_0} (1-\eta)f^{-\eta}$. For the spread of values quoted above we find that the predicted \bar{t}^* at 500 km would be in the 0.05 to 0.1 second range. This is within the wide range of values determined from LRSM stations recording HARDHAT Pn listed in Table 3-3. If such a \bar{t}^* were interpreted as an apparently frequency independent Q, it would imply an apparent Q of between 650 and 1300 for Pn. The estimates are also consistent with the results from spectral ratios of the synthetics presented above. The values in the 1 to 2 Hz range are roughly in agreement with Taylor, *et al.*'s (1988) estimate for Pn Q's of 250 in this range. The best fit exponential decays for all bands are in the R^{-2} to $R^{-3.5}$ range consistent with observations of recordings with similar bandwidths.

Finally, the analysis for Lg was performed on two earthquake sources at depths of 0.5 and 8 km since the explosion synthetics had weak Lg amplitudes at distances greater than 400 km. For the 1.25 to 2.5 and 2.5 to 5.0 Hz bandwidths the Lg amplitudes at large distances were too small to see above the numerical noise and Pg coda. In these cases, we could only determine upper limits to the exponents and to the apparent Q. In the case of the 8 km deep earthquake, the Lg signal is contaminated by Sn and the Q is higher than the crustal Q of the model. Lg was difficult to measure at high-frequencies since the synthetic signal is too small at distances greater than 400 km. The Lg excitation for the explosion is weak. Lg excitation even for a shallow earthquake (h = 0.5km) is weak and the attenuation imposes a severe limitation on the observed Lg at distance. The Lg is often contaminated by Pg coda. Since spatial attenuation near 1 Hz is within reasonable agreement with observations we are faced with the conclusion that crustal Q must increase with frequency in the basin and range or we would not be able to see Lg at distances greater than 300 km at frequencies above 1 Hz.

Lg BEST FIT EXPONENTS

	EARTHQUAKE(h=8km)	EARTHQUAKE(h=0.5km)
0.625-1.25Hz	-2.8	-3.5
1.25 -2.5 Hz	<-2.4	-
2.5 - 5.0 Hz	<-3.2	-

APPARENT Q_{Lg}

	EARTHQUAKE(h=8km)			EARTHQUAKE(h=0.5km)
EXPONENT	f=0.9	1.8	3.7Hz	f=0.9 Hz
-1	263	<304	<530	156
-5/6	241	<288	<503	145
-1/2	187	<256	<454	129

3.5 Conclusions

Using a realistic crust and upper mantle model for the Basin and Range, we have demonstrated that spatial attenuation of regional phases can be properly modeled near 1 Hz consistent with the literature. Synthetics in this model predict no significant differences between the apparent spatial attenuation rates between earthquakes and explosions. The velocity and Q model will be used in a subsequent section of this report to propagate seismic waves from more complicated explosion models to regional distances. Although our main goal was to validate a model to be used to simulate regional propagation suitable for discrimination studies, we have found several interesting ancillary results.

First, the Airy phase cylindrical spreading approximation at 1 Hz should yield an excellent measure of the "average" shear Q in the crust. Similar results were found for the apparent attenuation and geometrical spreading of synthetic Pg.

Second, the frequency dependence of synthetic Pn mimics a Q that increases with increasing frequency. This was found despite the use of a frequency independent attenuation in the model. The functional dependence of this Pn propagation will surely depend on the fine points of the velocity model and should be more closely investigated.

Third, the explosion point source is a very poor source of Lg. This has been noted before, and various mechanisms have been proposed for the generation of SV, including P to SV conversion at interfaces (Bennett, *et al.* 1987), more general scattering (Gupta and Blandford, 1983), and spall (Patton, 1988). It is clear that, the problem becomes even worse when realistic attenuation is introduced into the regional Green's function.

For both the earthquake and the explosion generated synthetic Lg, the high frequency amplitudes are too low to match observations if a frequency independent attenuation operator is used. Clearly, this suggests that the empirical frequency dependence of the Lg Q between $f^{0.5}$ and $f^{0.7}$ actually reflect the frequency dependence of

the average shear Q of the crust. Additional study is required to determine if $Q(f)$ models with more complicated depth dependence will require that the entire crust reflect such a dependence or whether the phenomenon is isolated to some specific depth range.

IV. TWO-DIMENSIONAL SOURCE FAR-FIELD P AND SV WAVEFORMS

4.1 Introduction

In this section we examine the far-field P- and SV-waves radiated by several non-linear axisymmetric finite difference simulations. There are "Shagan River" simulations at four different depths of burial and constant yield. Simulations for a Pahute Mesa tuff model were conducted at three different depths of burial and constant yield. And finally, there are three simulations intended to model explosions in prestressed granite.

Although our principle aim is to compute regional synthetics, there are several reasons for studying the far-field body waves from these simulations. The body waves are simpler and can be compared directly to observed waveforms. The simpler Green's function facilitates a more direct study of the physics of the source.

The Shagan River simulations have been previously discussed by Day, *et al.* (1986b) in order to derive magnitude corrections for the January 15, 1965 presumed cratering explosion at Shagan River. The predicted waveform statistics of "a", "b", and "c" phase were compared to observations in order to correct the presumed cratering WWSSN mb to an equivalent contained explosion. We re-examine this analysis and estimate the 150 kt mb magnitude limit at this test site.

Similarly, we examine the P waveform statistics for the Pahute Mesa tuff model. In light of the observations of Taylor, *et al.* (1988) that normal buried events at NTS are relatively low-frequency with respect to overburied events, we examine the P and SV waves radiated by the Pahute Mesa tuff models three depths of burial.

Finally, the body waves from three calculations of explosions in prestressed granite are examined. These "PILEDRIIVER" simulations are examined to observe the effects of tectonic release (prestress) on the short-period P-SV waveforms. These simulations were previously used by Day, *et al.* (1986a) to demonstrate the effects of tectonic release on long-period Rayleigh waves. We extend the seismic analysis to the effects of tectonic release on far-field broadband P and SV body waves from explosions in granite.

4.2 Shagan River Simulations

4.2.1 Waveform Statistics

McLaughlin, *et al.* (1985 and 1986) presented evidence that statistical differences could be seen in teleseismic P-waves from Shagan River explosions diagnostic of the depth of burial. The statistics of the relative amplitudes of the first positive swing, "a", the first negative swing, "b", and the second positive swing, "c", or "max" of the WWSSN P-wave were examined (see Figure 4.1). It was found that the network statistics for $\text{Log}(P_{\text{max}}/P_a)$, $\text{Log}(P_b/P_a)$, and $\text{Log}(P_{\text{max}}/P_b)$ showed that the January 15, 1965 presumed cratering explosion at Shagan River had an m_b magnitude 0.10 to 0.30 units less than contained explosions with comparable "a" phase amplitude. The yield of the January 15, 1965 event is presumed to be 125 kt (Marshall, *et al.*, 1979; Rodean, 1979). Therefore, this suggests an alternative manner by which the Shagan River test site could be calibrated. Day, *et al.* (1986b) used axisymmetric nonlinear

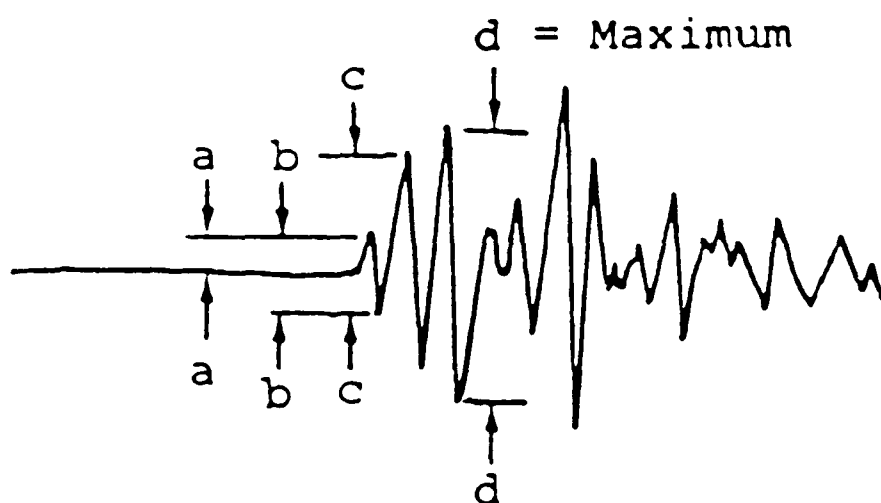


Figure 4.1.

Definition of P_a , P_b , and P_{max} amplitudes read from film records. P_b and P_{max} are $1/2$ the peak-to-peak b and max measurements while P_a is the zero-to-peak amplitude measurement.

finite difference simulations to predict teleseismic P-waveforms for Shagan River events of 125 kt at several depths of burial. Their results were in apparent agreement with McLaughlin, *et al.* However, as we will see, the predicted $\text{Log}(P_{\text{max}}/P_a)$ from the synthetics is not in agreement with observations for contained shots.

In an effort to understand this discrepancy, we have re-examined the waveform statistics for the S-CUBED nonlinear simulations. Furthermore, we have performed the analysis on simulations for the Pahute Mesa tuff model. The analyses have been repeated with different attenuation models, with both constant t^* and frequency dependent $t^*(f)$. The effects of typical crustal layering at the receiver have also been examined for the Pahute Mesa synthetics.

Figure 4.2 shows predicted teleseismic P-wave WWSSN waveforms for the Shagan River simulations of 125 kt, at depths of 200 meters (optimal cratering depth), 680 meters (normal containment depth) and 980 meters (overburied). The seismograms include the effects of attenuation (constant $t^* = 0.7$ sec) and instrument response for three take off angles of 10, 20 and 30 degrees. We are concerned here with the equivalent teleseismic signals represented by the synthetics for a takeoff angle of 10 degrees. We see that the waveform changes morphology as depth is increased; the "c" phase becomes larger relative to the "a" phase as depth is increased. The "a" phase amplitude is largely determined by the amplitude of the direct P wave, the attenuation operator and the instrument response. The later "b" and "c" amplitudes are affected by the constructive and destructive interference of the direct and later portions of the P-wave as well as the attenuation and instrument operators.

Figure 4.3a shows the far-field displacement pulses without the attenuation and instrument operators included in Figure 4.2. From these waveforms we see that the simulations all produce a negative polarity "pP" but that the amplitude and timing is a function of depth. The deeper explosions show negative pulses somewhat attenuated with respect to the direct P wave and perhaps distorted by propagation through the nonlinear region above the explosion. The negative phase for the cratering simulation is related to crater formation and is only referred to as a "pP" to simplify terminology. These pulses are compared in Figure 4.3b with deconvolutions from Der, *et al.* (1987) for the January 15, 1965 event and several other Shagan River explosions of similar magnitude. We see that the cratering simulation is in fair agreement with the deconvolution of the January 15, 1965 event while the 680 meter simulation does not have the large negative polarity pulse prominent in the deconvolutions of each of the m_b 5.8 or 5.9 events. The 680 meter simulation appears to show a smaller and delayed "pP" when compared to the deconvolutions.

Figure 4.4 shows the predicted statistics for $\text{Log}(P_{\text{max}}/P_a)$ versus $\text{Log}(P_{\text{max}}/P_b)$ from the simulations shown in Figure 4.2 compared to some observed values (McLaughlin, *et al.*, 1986). The observed data is only for events with $m_b(P_{\text{max}}) > 5.5$. The simulations predict $\text{Log}(P_b/P_a)$ to be about 0.3 which is in general agreement with observations which range from 0.25 to 0.50. The observations show a distribution of $\text{Log}(P_{\text{max}}/P_a)$ and $\text{Log}(P_{\text{max}}/P_b)$ with the presumed cratering shot with minimum P_{max} amplitude relative to "a" or "b" amplitude. The simulations predict $\text{Log}(P_{\text{max}}/P_a)$ and $\text{Log}(P_{\text{max}}/P_b)$ for the "normal" contained shot nearly identical with

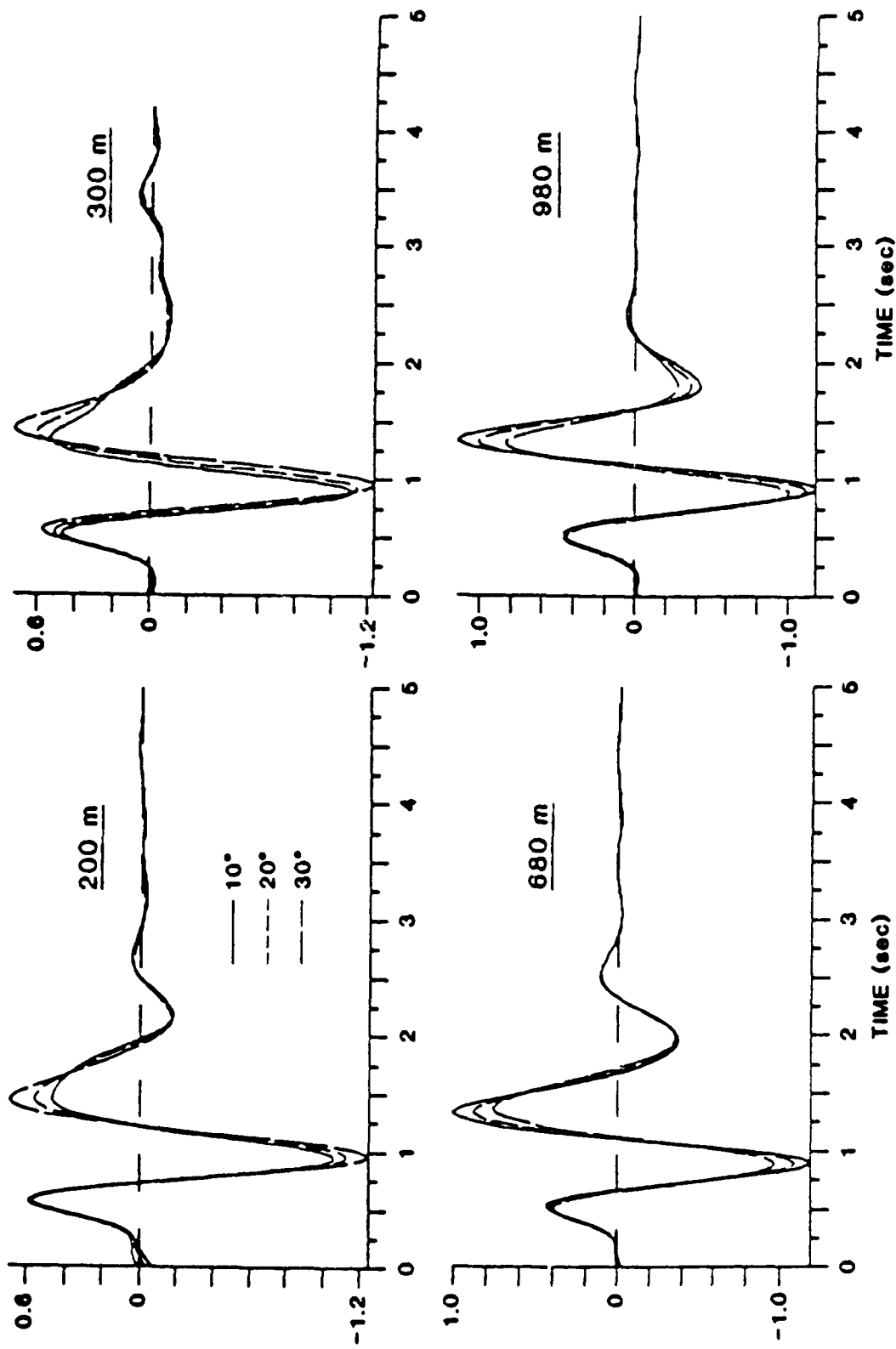


Figure 4.2. Radiated P waveforms for the 2D Shagan River simulations, attenuation operator ($t^* = 0.7$ s) and WWSSN instrument responses at 10°, 20°, and 30° takeoff angles.

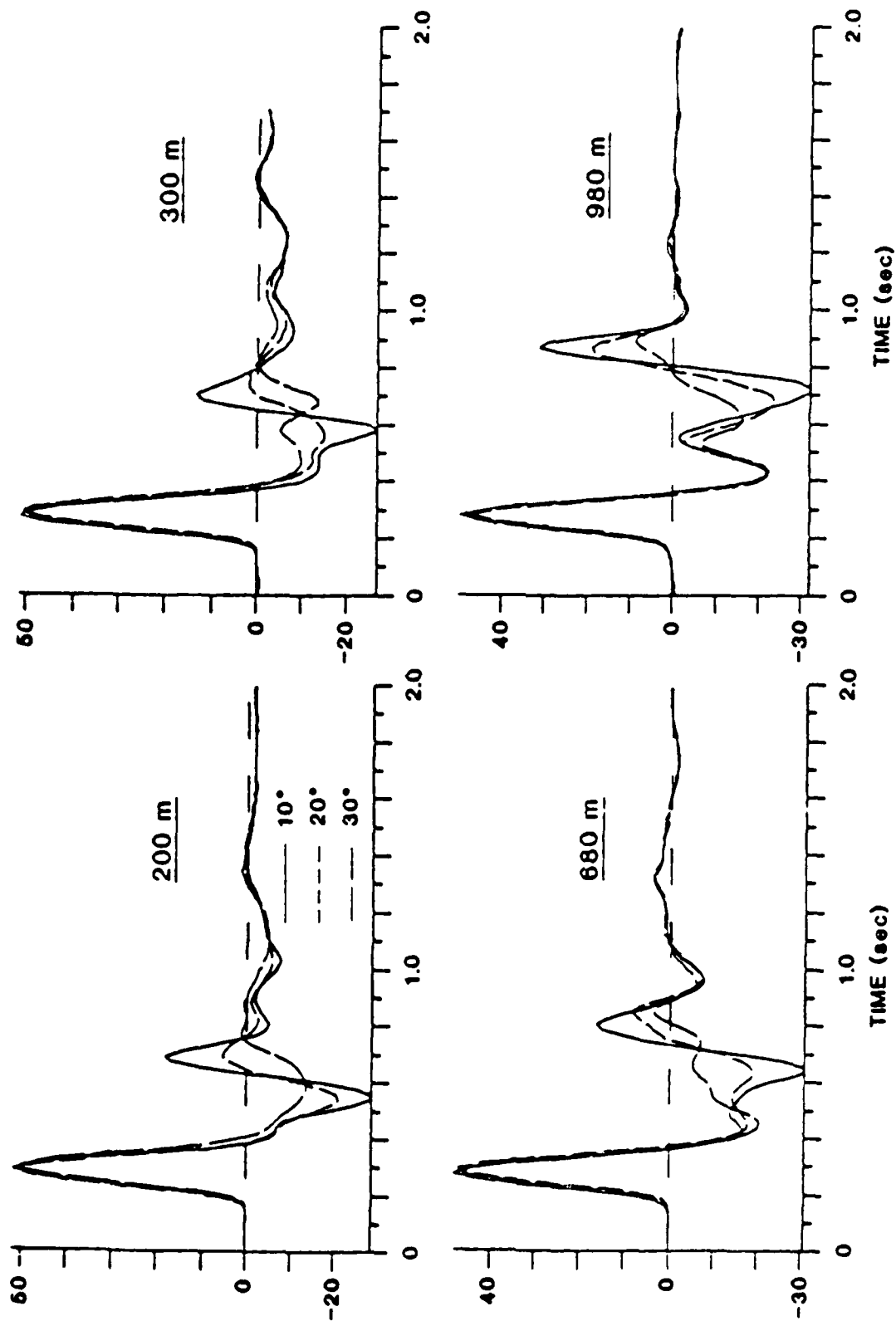


Figure 4.3a. Radiated displacement P waveforms for the 2D Shagan River simulations without attenuation or instrument responses at 10°, 20°, and 30° takeoff angles.

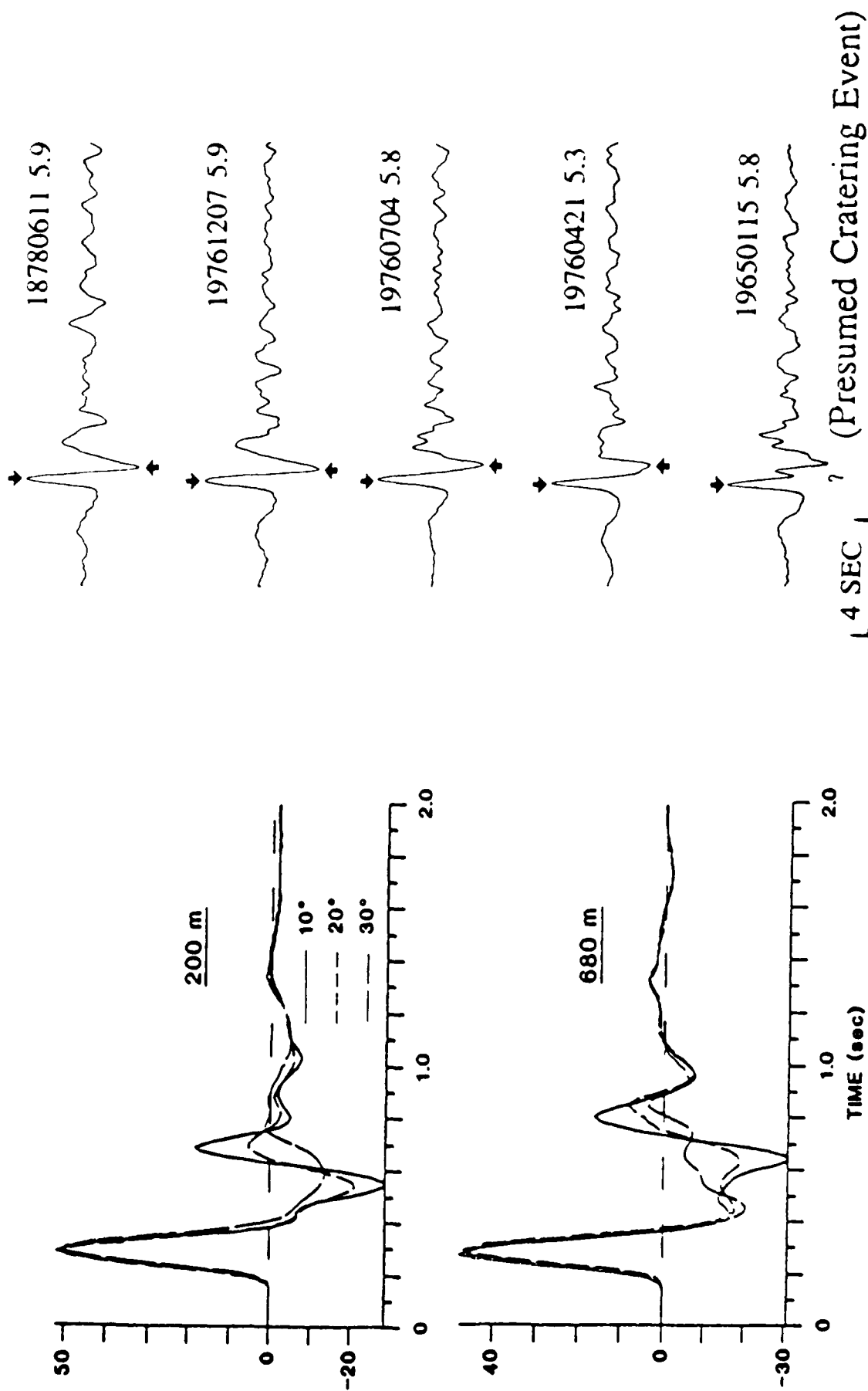


Figure 4.3b.

A comparison of deconvolved Shagan River far-field P-waves (right) with synthetic far-field P waveforms for depths of 200 and 680 meters. The 200 meter cratering synthetic shows good qualitative agreement with the 19650115 event at Shagan River, while other events of similar magnitude appear to have larger "pP" arrivals than predicted by the synthetics.

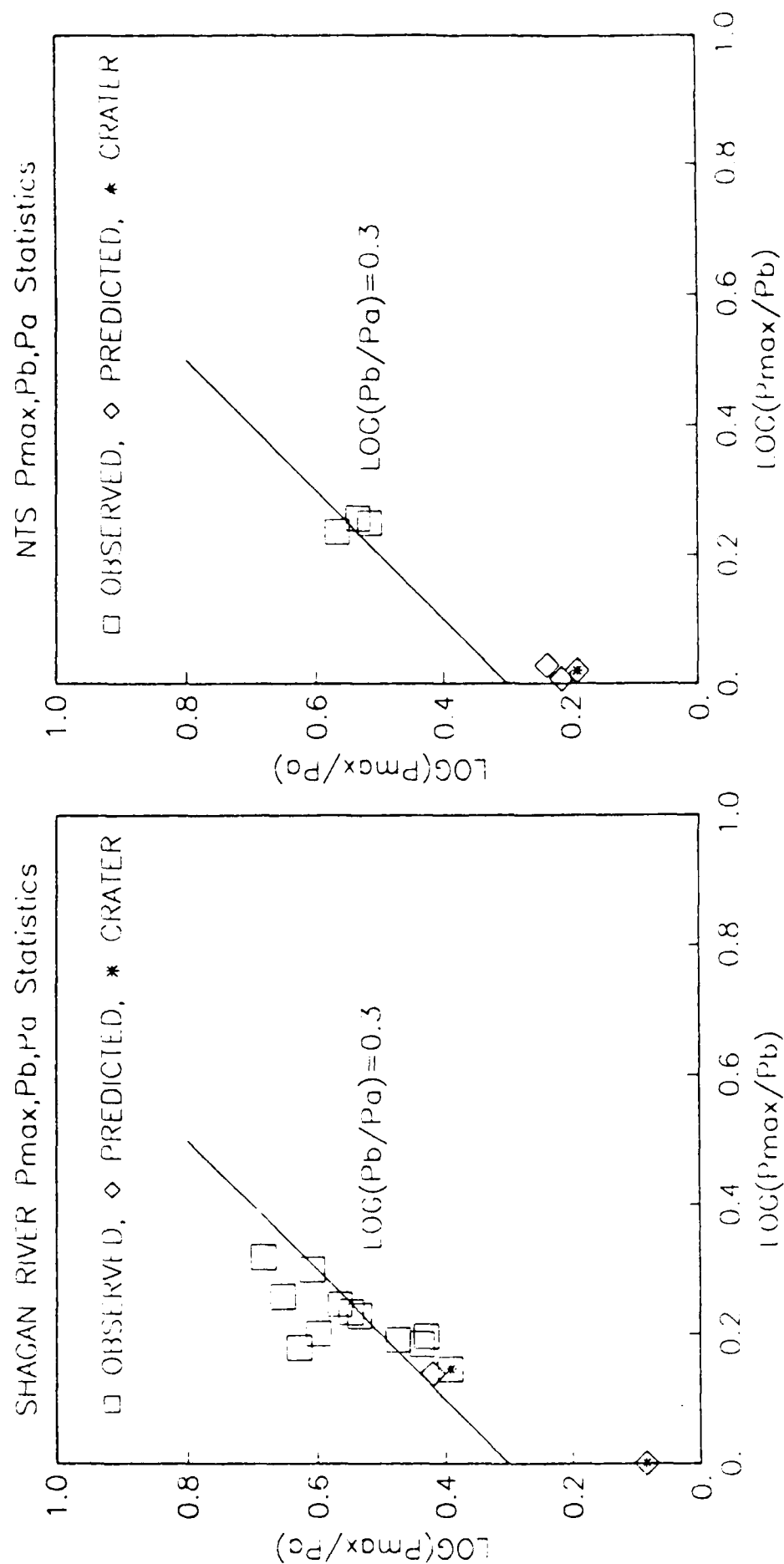


Figure 4.4. Observed WWSSN waveform statistics $\text{Log}(P_{\text{max}}/P_a)$ and $\text{Log}(P_{\text{max}}/P_b)$ compared to synthetic predictions. The synthetic $\text{Log}(P_b/P_a)$ predictions are approximately correct but the synthetics under predicted P_{max} amplitudes relative to the P_a and P_b amplitudes.

the observed values for the cratering shot. Furthermore, they predict that $\text{Log}(P_{\text{max}}/P_b) = 0.0$ for the 200 meter depth shot, in contrast to observations for the cratering shot of about 0.15. Clearly, the simulations are under predicting the P_{max} in all cases although they do an acceptable job of predicting the relative amplitudes of P_a and P_b .

We are left with the conclusion that the nonlinear contained simulations under predict the "pP" amplitude that is responsible for the interference effect that produces the large "c" phase amplitude. This is based on the relative Log-amplitude statistics as well as the deconvolution results that generally show distinct pP arrivals for Shagan River explosions in the m_b 5.5 to 6.2 range.

We see that this problem also exists for the Pahute Mesa tuff model. Figure 4.4 shows the $\text{Log}(P_{\text{max}}/P_a)$ and $\text{Log}(P_{\text{max}}/P_b)$ predictions for NTS based on the Pahute Mesa tuff calculations compared to observations for three Pahute Mesa events. Again, the value of $\text{Log}(P_b/P_a) = 0.2$ is roughly in agreement with the data (about 0.3), but the P_{max} amplitude is under predicted by about a factor of 2 relative to the P_a and P_b amplitudes. We will come back to this in a later section.

4.2.2 Implications for Magnitude:Yield at Shagan River

Given that the simulations incorrectly predict the P_{max} phase, but appear to give agreement on P_a and P_b , we re-examine the calibration of the Shagan River test site using the presumed cratering event as a 125 kt reference event. From the simulations, we have that $\text{Log}(P_a)_{\text{contained}} - \text{Log}(P_a)_{\text{cratering}} = -0.128$, and $\text{Log}(P_b)_{\text{contained}} - \text{Log}(P_b)_{\text{cratering}} = 0.0$. As pointed out by Day, *et al.*, the 2D synthetics predict an "a" phase coupling scaling with depth nearly equal to that predicted by Murphy (1977); coupling inversely proportional to the cube-root of depth. Such scaling would predict the shallower event to have a larger RDP by $\text{Log}(680/200)/3 = 0.177$ units. Since the event cratered in the first few tenths of a second, the simple depth scaling should only be expected to give a qualitative estimate of the depth scaling for the initial phase and is expected to progressively fail for later times in the P-waveform. From the synthetics, we expect that a contained explosion with a yield of 125 kt would have had an $m_b(P_a)$ 0.128 less than the January 15, 1965 event but with the same $m_b(P_b)$. Indeed, if we examine the magnitudes from in Table 4.1, we see that the events of November 30, 1969 and September, 15, 1978 have $m_b(P_b)$ values close to the presumed cratering explosion and that their $m_b(P_b) - m_b(P_a)$ differences ($5.77 - 5.38 = 0.39$, and $5.67 - 5.35 = 0.32$) are close to what is predicted from an adjustment of the January 15, 1965 cratering explosion $m_b(P_a) - m_b(P_a)$, $5.72 - 5.48 + 0.128 = 0.37$. Consequently, we estimate that for the WWSSN magnitude estimation procedure used by McLaughlin, *et al.* (1986) that a normally contained 125 kt explosion corresponds to $m_b(P_a) = 5.48(0.05) - 0.13 = 5.35(0.05)$ and $m_b(P_b) = 5.72(0.05)$. In Appendix A we use these corrected magnitudes to estimate the 150 kt limit at the Shagan River test site.

TABLE 4.1 MLE MAGNITUDES (McLaughlin *et al.* (1986))

YY/MM/DD	m_b (Pa)	m_b (Pb)	m_b (Pmax)
65/01/15	5.48(0.05)	5.72(0.05)	5.87(0.04)
68/06/19	4.59(0.05)	5.02(0.04)	5.27(0.04)
69/11/30	5.38(0.04)	5.77(0.03)	5.97(0.03)
73/07/23	5.76(0.05)	6.02(0.05)	6.20(0.04)
73/12/14	5.16(0.05)	5.49(0.05)	5.74(0.05)
75/04/27	4.99(0.12)	5.32(0.10)	5.53(0.10)
76/07/04	5.24(0.08)	5.61(0.05)	4.91(0.06)
76/12/07	4.93(0.15)	5.42(0.12)	5.61(0.13)
78/06/11	5.25(0.05)	5.57(0.05)	5.85(0.05)
78/09/15	5.35(0.06)	5.67(0.05)	5.86(0.06)
79/06/23	5.72(0.06)	5.96(0.06)	6.18(0.06)
80/09/14	5.58(0.09)	5.90(0.08)	6.14(0.08)

4.3 Pahute Mesa Simulations

In the following section, we describe seismic waveforms from simulations done in a layered medium which models explosion emplacement at Pahute Mesa. The model has three layers representing a very low velocity surface layer, and a strong velocity increase at the water table. As with the Shagan River calculations, the simulations for Pahute Mesa were done for a yield of 125 kt, and at a cratering depth (200 m), an optimal depth (680 m), and an overburied depth (980 m). The 2D calculations include the full nonlinear response of the material as well as the effects of gravity, cracking, spall, and the ballistic material response in the case of the cratering calculation (200 m). A "generic" Pahute Mesa structure was constructed based on properties from a number of drill holes in the area. The seismic velocity model at the source is given in Table 4.2. Other material properties of the model are given by Day, *et al.* (1986).

TABLE 4.2 PAHUTE MESA TUFF MODEL

layer thickness (km)	β (km/s)	α (km/s)	ρ (gm/cc)	depth (km)
0.122	0.661	1.204	1.00	0.0-0.122
0.460	1.109	2.025	1.95	0.122-0.582
∞	1.581	2.887	2.00	0.582- ∞

The contained calculations were constrained so as to match the cavity sizes for events of these depths and yield. It is interesting to note that the calculations for the 125 kt, 980 meter depth simulation were subsequently found to match the surface ground-zero peak vertical velocity and the free-fall (spall) observed time for SCOTCH to within 10%. Tensile failure occurred in the simulations at a number of horizons above the working point, but the actual spall in the calculations, defined as a period of free-fall (-1 g), was found to be confined to the weak surface layer (upper 122 m). Events of this size and depth at Pahute Mesa, for which data is available, show spall

reaching to depths as much as 1/3 the depth of burial (H. Patton, personal communication). Detailed ground motion records above the working point could serve as important constraints for future modeling efforts, particularly if spall openings and closures are important to regional phase excitation.

4.3.1 Waveform Statistics

We have computed the far-field signal along rays leaving the bottom of the source structure for three take-off angles (10, 20 and 30 degrees). These three angles correspond to a teleseismic P wave at 60 degrees (17 km/s), Pn apparent velocity in the 9 to 10 degree range (8.5 km/s), and a crustal Pg apparent velocity (5.8 km/s). In addition, for comparison with the waveforms of observed seismograms, the signals were convolved with various attenuation operators and a WWSSN instrument response.

The dependence of the unfiltered signals on take-off angle and depth of burial is shown in Figures 4.5a and b, respectively. The first peak, the direct arrival P, is unaffected within this range of take-off angles, but the trailing signal, the free surface interaction phase pP, is affected. At each depth, pP is largest and is delayed most at the steepest take-off angle (10^0). This is predicted by elastic theory. The increase in pP amplitude is greatest at the deepest depth. The direct arrivals at depths of 200 and 680 m are nearly the same amplitude, but the amplitude from a depth of 980 m is diminished to about 40% of the others. This is due to differences in material properties with depth. The amplitude of pP relative to P is largest for the deeper shots, showing the effect of containing the explosion.

To isolate the effects of nonlinear interactions with the free surface, we have compared the 2D simulations discussed above with comparable 1D source simulations. The 1D solutions were obtained by first performing a nonlinear calculation in a whole space whose material properties were the same as those at the depth of burial in the 2D calculation, and then extracting the reduced velocity potential (RVP). The RVP was convolved with the elastic source structure transfer function to obtain the far-field wave leaving the source structure, which can be compared directly to the comparable 2D results. The 2D and 1D waveforms are overlain in Figure 4.6.

As might be expected, the difference between the 1D and 2D free surface interaction is most apparent at the shallowest depth (200m), where cratering occurred. The direct waves are the same, but the large negative peak predicted by an elastic free surface reflection is almost absent in the 2D simulation. This is the case for all three take-off angles. At deeper depths, the nonlinear pP is generally delayed by 0.2 seconds relative to the elastic pP. The reduction in amplitude of pP due to the nonlinear free surface interaction is greatest ($\sim 1/3$) at the shallowest take-off angle (30^0), and least (25 %) at the steepest take-off angle (10^0).

To compare these waveforms with features of observed seismograms, we convolved the time series discussed above with an attenuation operator and an instrument response. Although we examine the effects of other attenuation operators later in this paper, we begin with a frequency-independent operator with $t^* = 0.5$. A short-period WWSSN instrument response was used. The synthetic seismograms for the three take-off angles are overlain at the three depth of burials in Figure 4.7. The first two peaks, the "a" and "b" phases are the same for each take-off angle at all depth of

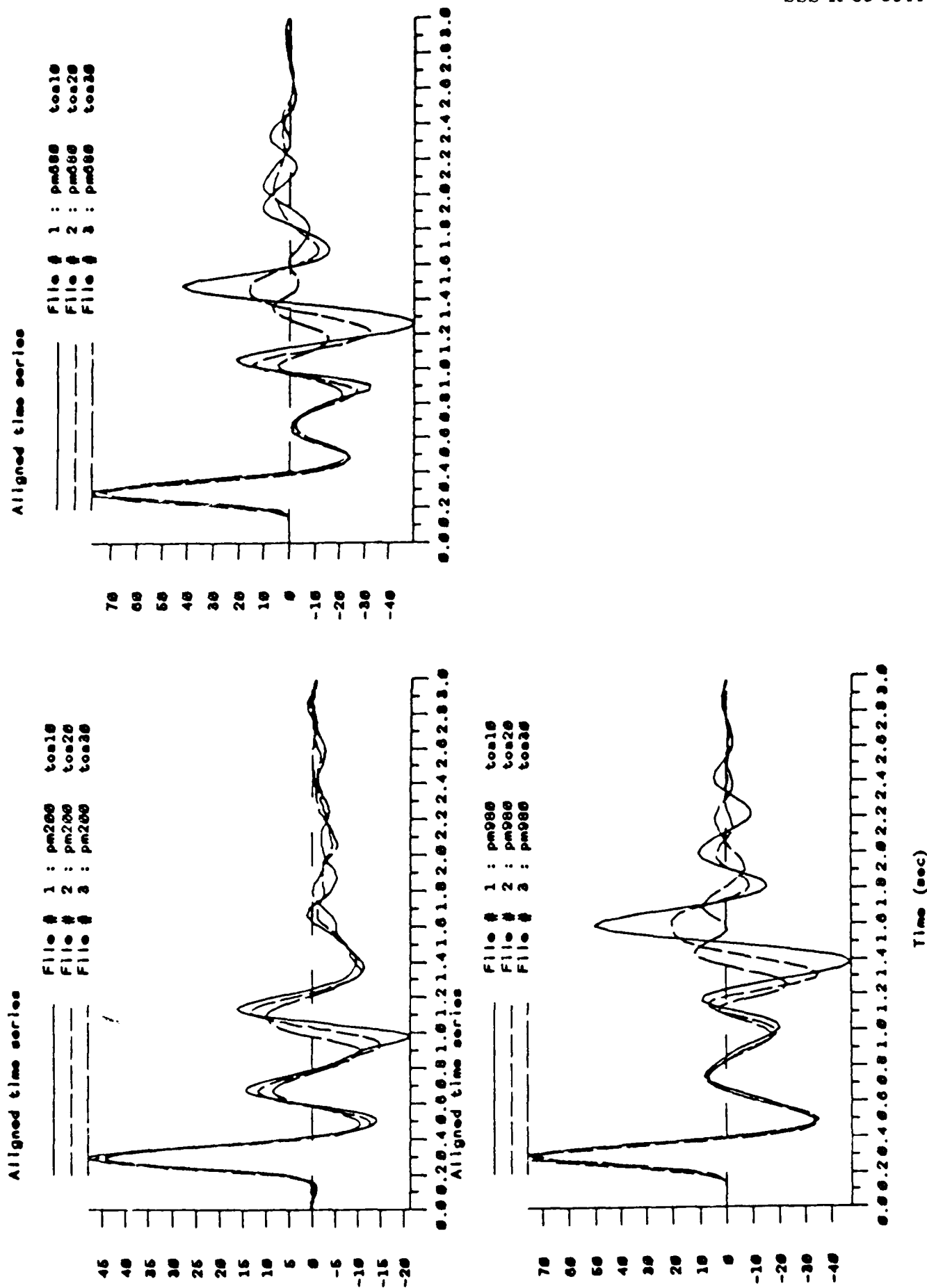


Figure 4.5a. Radiated displacement P waveforms for the three 2D Pahute Mesa tuff simulations at 10°, 20°, and 30° takeoff angles.

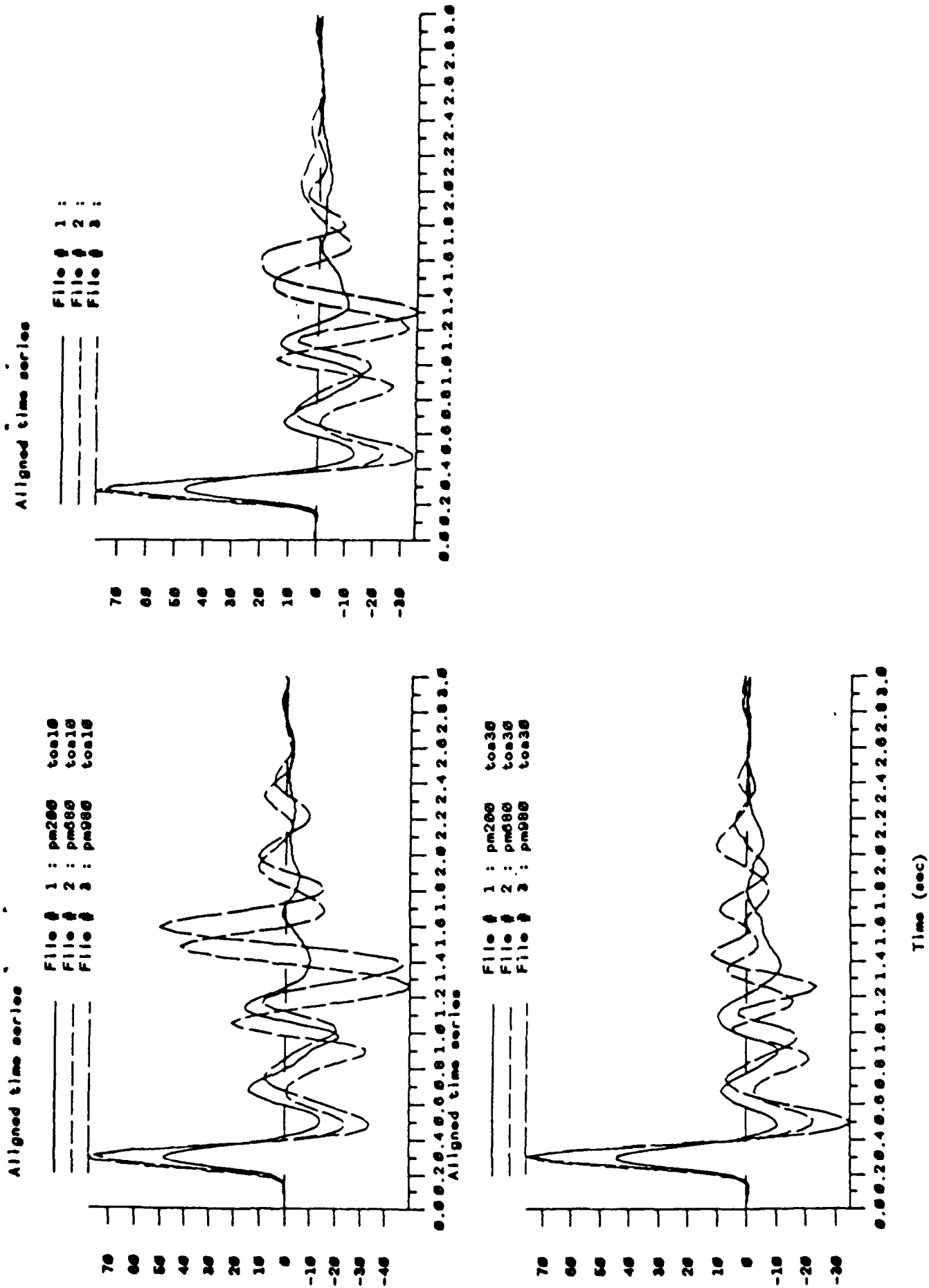


Figure 4.5b. Radiated displacement P waveforms for the three 2D Pahute Mesa tuff simulations at 10°, 20°, and 30° takeoff angles.

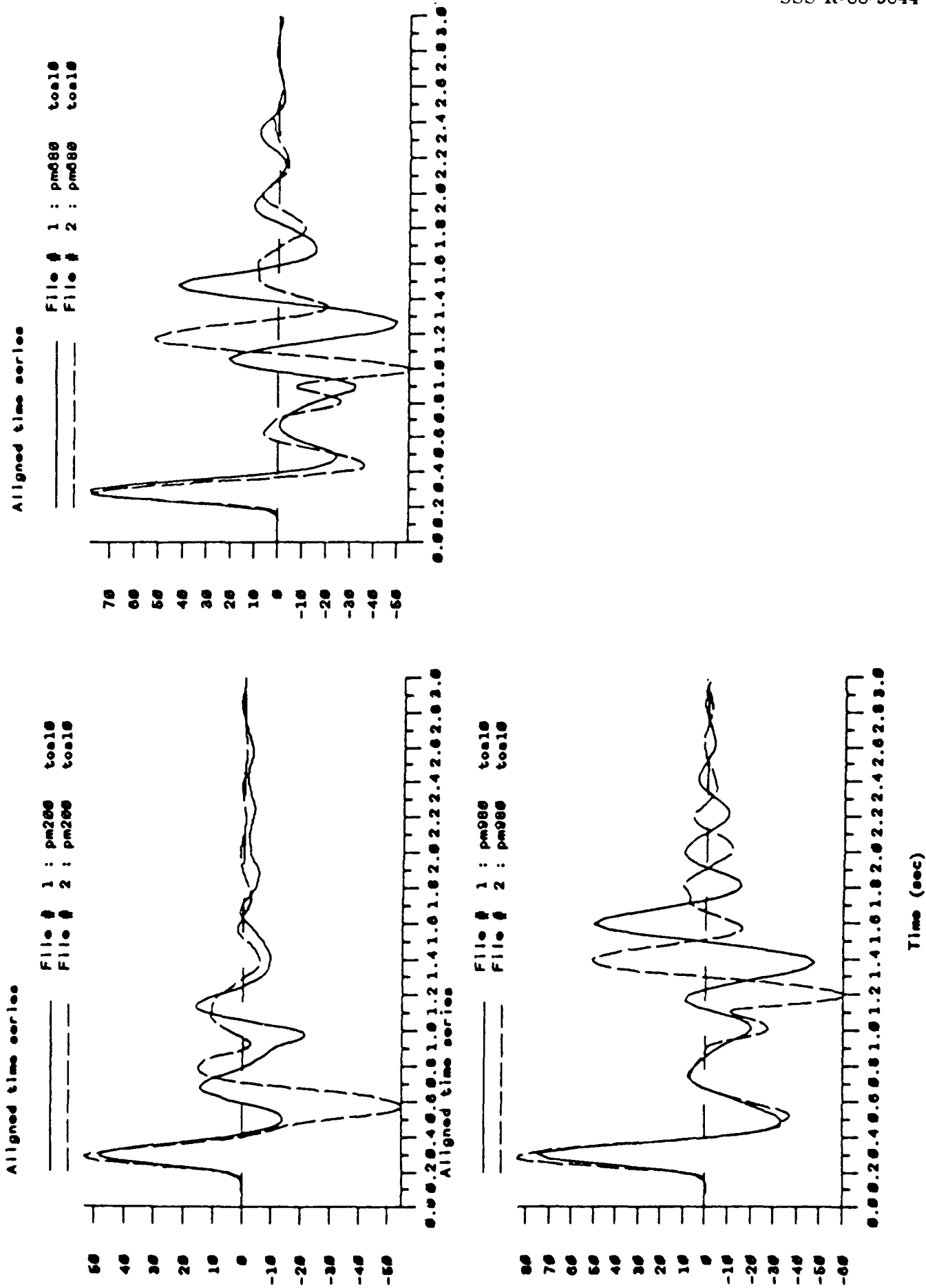


Figure 4.6. Radiated displacement P waveforms for the three 2D Pahute Mesa tuff simulations at 10° takeoff angle compared to the 1D elastic source model.

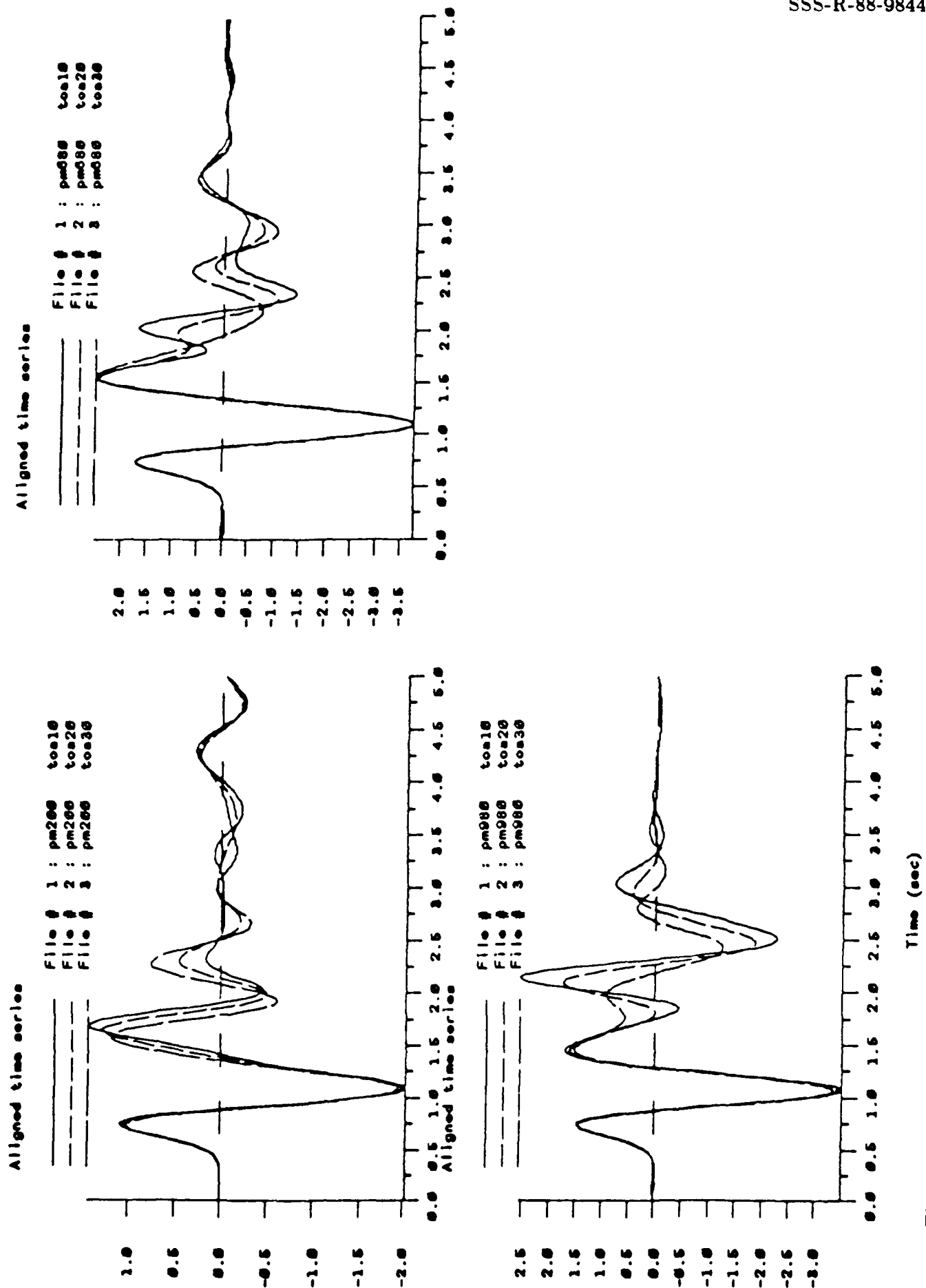


Figure 4.7. Same as 4.5a except WWSSN instrument response and attenuation operator ($t^* = 0.5$ s) applied.

burials, while the "c" phase changes slightly in amplitude and period as a function of take-off angle for the cratering shot. The increase in the ratio of pP to P is most apparent at the steepest take-off angle (10°). Note that the effect on the ratio of "c" to "b" amplitude is small at all take-off angles. The effects of a WWSSN instrument response and $t^* = 0.5$ sec are shown in Figure 4.8.

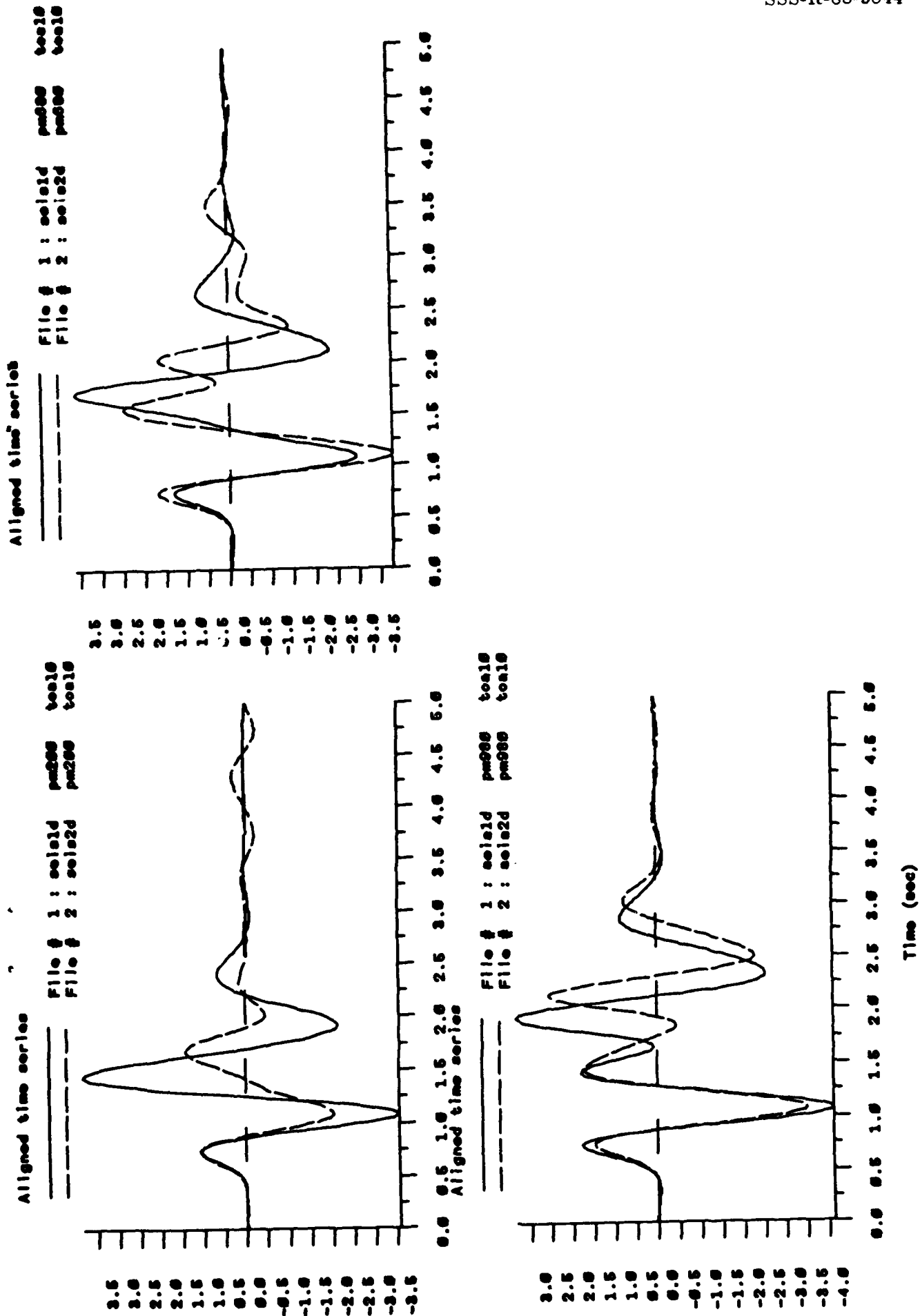
For the seismograms discussed above, a frequency-independent Q model with $t^* = 0.5$ was used. The effects of using the frequency dependent Q models of Der and Lees (1985) can be seen in Figures 4.9. The models are designated TT for a tectonic-to-tectonic path, TS for a tectonic-to-shield path, and SS for a shield-to-shield path. Model TT is most attenuative, SS is least attenuative and TS is intermediate. The t^* at 1 Hz for the three models are 0.35 0.55 and 0.75 sec for SS, TS, and TT respectively. We expect that the paths from NTS to the WWSSN stations are a mix of paths bracketing the TS and TT models.

In Figure 4.9, the waveform plots are scaled by the largest of the traces, so that the relative amplitudes are apparent. As expected, the SS model is largest. The seismograms for the TS model and the frequency-independent model track each other closely. The differences between the SS model and the others is apparent in the seismograms for the cratering shot, where the inflection in the "c" phase, due to separation of P and pP, can be seen for SS but shows up as a widened peak for the other Q models. The separation of P and pP is apparent to different degrees for the four Q models in the optimally buried (680 m) shot.

As was done in Day, *et al.* (1986b), measurements of the "a", "b" and "c" phases and their relative values were made for the synthetic seismograms. Their values are listed in Tables B.1a through B.1e of Appendix B. Several additional figures are shown in Appendix B. The ratios of the "b" and "c" phases ($\frac{1}{2}$ peak-to-peak) to the "a" (zero-to-peak) are shown. These measurements are referred to as P_{ab} , P_{bc} , and P_a , respectively. These ratios, $\frac{P_{ab}}{P_a}$ and $\frac{P_{bc}}{P_a}$, are generally less than 0.25 (a factor of 1.8) for the various models for both the contained and optimally buried shots, with the contained somewhat larger. Observations are typically about 0.6 (a factor of 4), indicating that the simulated pP is delayed and/or is too small compared to observations. As can be seen from Figure 4.9, and examination of Tables B.1a through B.1e, the $\text{Log}(P_a/P_b)$ and $\text{Log}(P_c/P_a)$ are little affected by the choice of attenuation model. The scatter due to the most divergent attenuation models is less than 0.05 log units.

4.3.2 Far-Field P-Wave Spectra and Depth Scaling

Figure 4.10 shows the P-wave power spectra for the three simulations appropriate for a 10 degree takeoff angle. Note that the 200 meter, cratering simulation, has an over all lower level above 0.5 Hz. Because we are interested in discrimination problems associated with over burial, we will concentrate on the two 680 and 980 meter depth of burial simulations. The 680 and 980 meter simulations are rather similar although the 980 meter spectrum has deeper spectral nulls. In order to bring out the differences between the two sets of spectra, we computed spectral ratios for the three different take-off angles averaged over several bandwidths (Figure 4.11). We see that



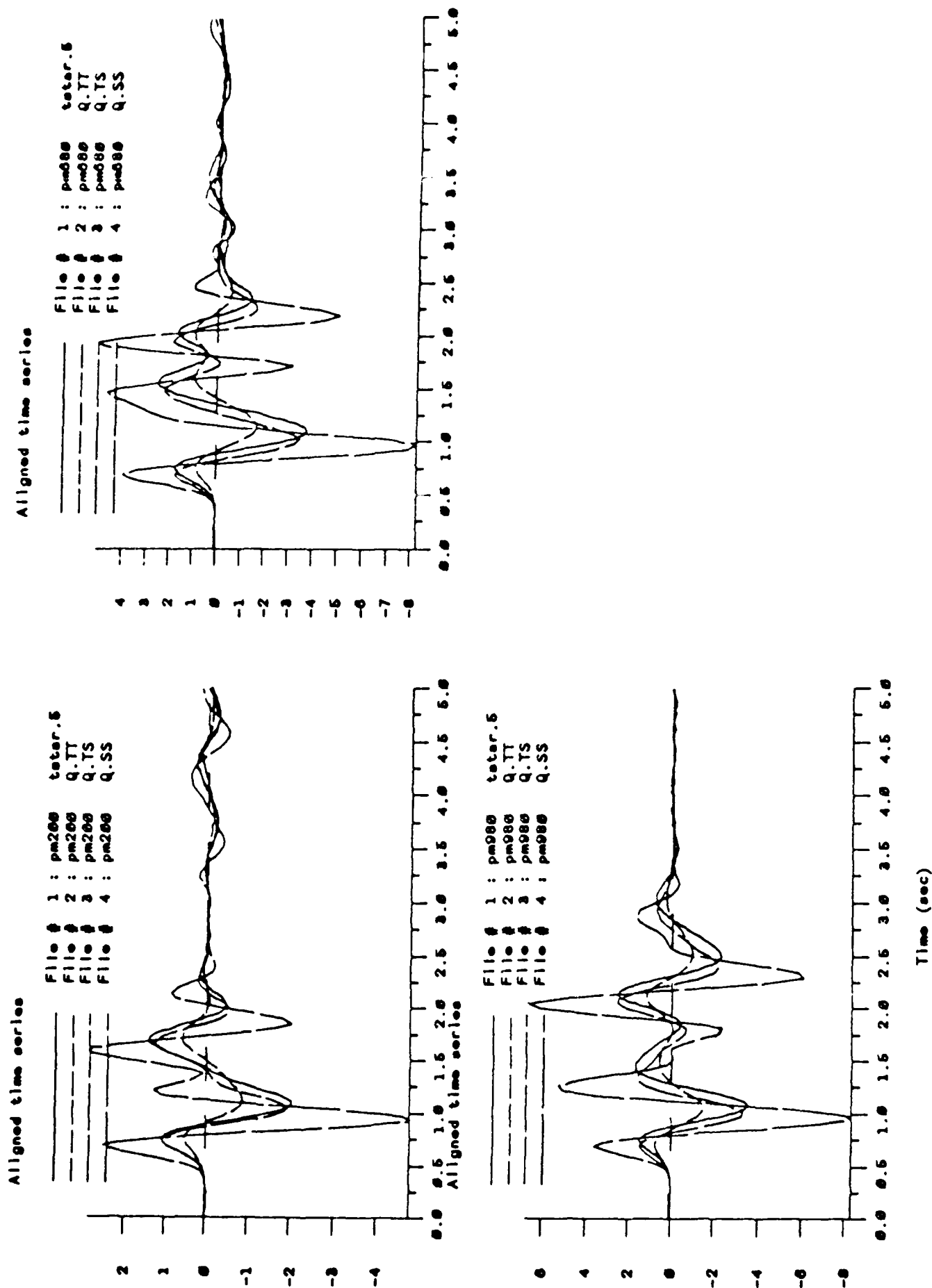


Figure 4.9. 2D synthetic P-waves at takeoff angle 10° , with WWSSN instrument, and four different attenuation operators. All traces shown at same scale.

SYNTHETIC TELESEISMIC P-WAVE SPECTRA
PAHUTE MESA TUFF MODEL, 125 Kt, TAKEOFF ANGLE 10°

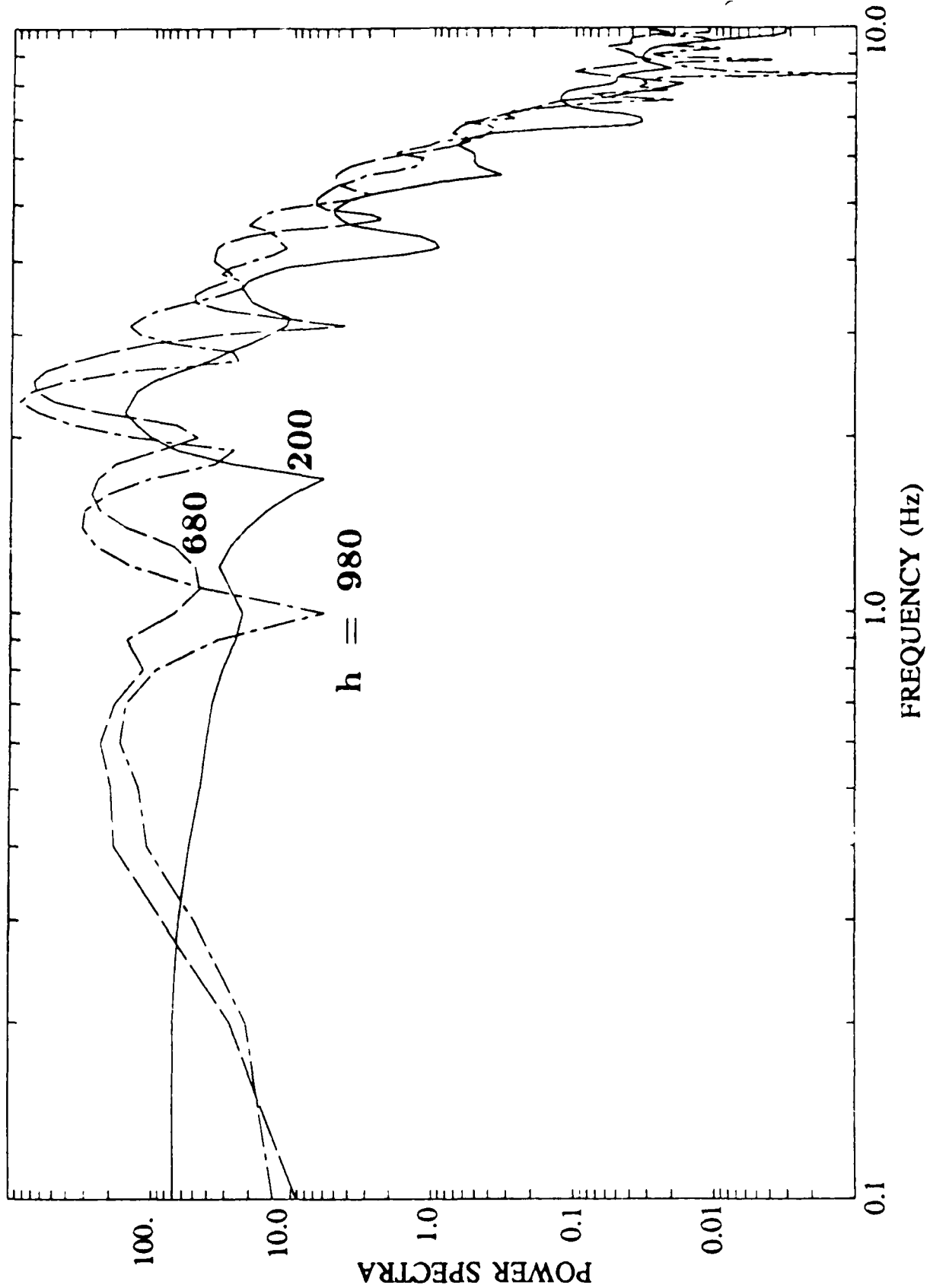


Figure 4.10. Synthetic far-field P-wave power spectra for the Pahute Mesa tuff model, 125 kt, takeoff angle 10° and depths of burial, 200, 680, and 980 meters.

all three takeoff angles show a net enhancement of the 680 meter spectra below 1 Hz, and a net enhancement of the 980 meter spectra above 1 Hz. The net difference in $\text{Log}(680/980)$ below 1 Hz and above 2 Hz is about 0.15 log units or a factor of 40%. This low/high frequency difference for the two scaled depths is only visible with the spectral averaging. The difference is in agreement with what is predicted by Murphy (1977) depth scaling in tuff. Figure 4.11 shows the predicted spectral ratio for these two scaled depths with the appropriate material properties. The simple depth scaling theory predicts the low/high frequency difference properly but not the actual level of the ratio.

Taylor, *et al.* (1988) have observed that overburied explosions at NTS are relatively enriched in high frequencies with respect to adjacent normal buried explosions. In fact they have found that these overburied events fail the high/low frequency discriminant and appear to look like earthquakes. However, the small explosions in their data base ($m_b < 4$) that fail the high/low frequency discriminant are 100% or more overburied. It is clear however, that the nonlinear simulations and the simple depth scaling theory are in qualitative agreement with the observations.

To illustrate the consequences of the depth scaling, we use Murphy's (1977) depth scaling theory with a velocity model of Leonard and Johnson (1987). The predicted spectral ratio between two 5 kt explosions at depths of burial 200 and 500 meters are shown in Figure 4.12. A factor of 3 enhancement is predicted for the high frequency spectrum of the overburied explosion. Roughly half of this shift in spectrum is produced by the shift in corner frequency due to the increase in overburden pressure with depth, and the remaining difference is due to the differences in material properties associated with the increase in compressional velocity with depth. The relative high frequency enhancement with respect to normal depth of burial increases with decreasing yield and with increasing overburial such that factors of 10 are predicted for 1 kt explosions overburied 100% or more in tuff with the Leonard and Johnson velocity model.

4.3.3 Far-Field P- and SV-Wave Spectra

One important way in which two-dimensional sources may differ from one-dimensional point sources is the radiation of direct SV energy. A complete set of P and SV far-field displacement waveforms are shown in Figures 4.13a, b, and c for take-off angles of 10, 20, and 30 degrees respectively. In each case, the 2D simulations for 200, 680, and 980 meter depth are shown along with the elastic response of the model convolved with a 1D RDP that was computed for the 680 meter depth. Note that there is a small SV arrival on the nonlinear 2D synthetics that does not appear in the 1D model. This is the direct SV produced by the axisymmetric explosion model. Upon visual inspection, one can see that the 2D SV pulses appear broader (lower frequency) than the 1D elastic model. Also the peak amplitude of the 2D 680 meter SV synthetic is delayed with respect to the elastic propagator model. However, the general features of the 2D and 1D model are similar and the peaks and troughs of the 2D SV pulses can be correlated with similar peaks and troughs of the 1D elastic model. Consequently, we can qualitatively describe the differences between the 2D nonlinear synthetics and the 1D linear model as if the elastic P-SV conversions above

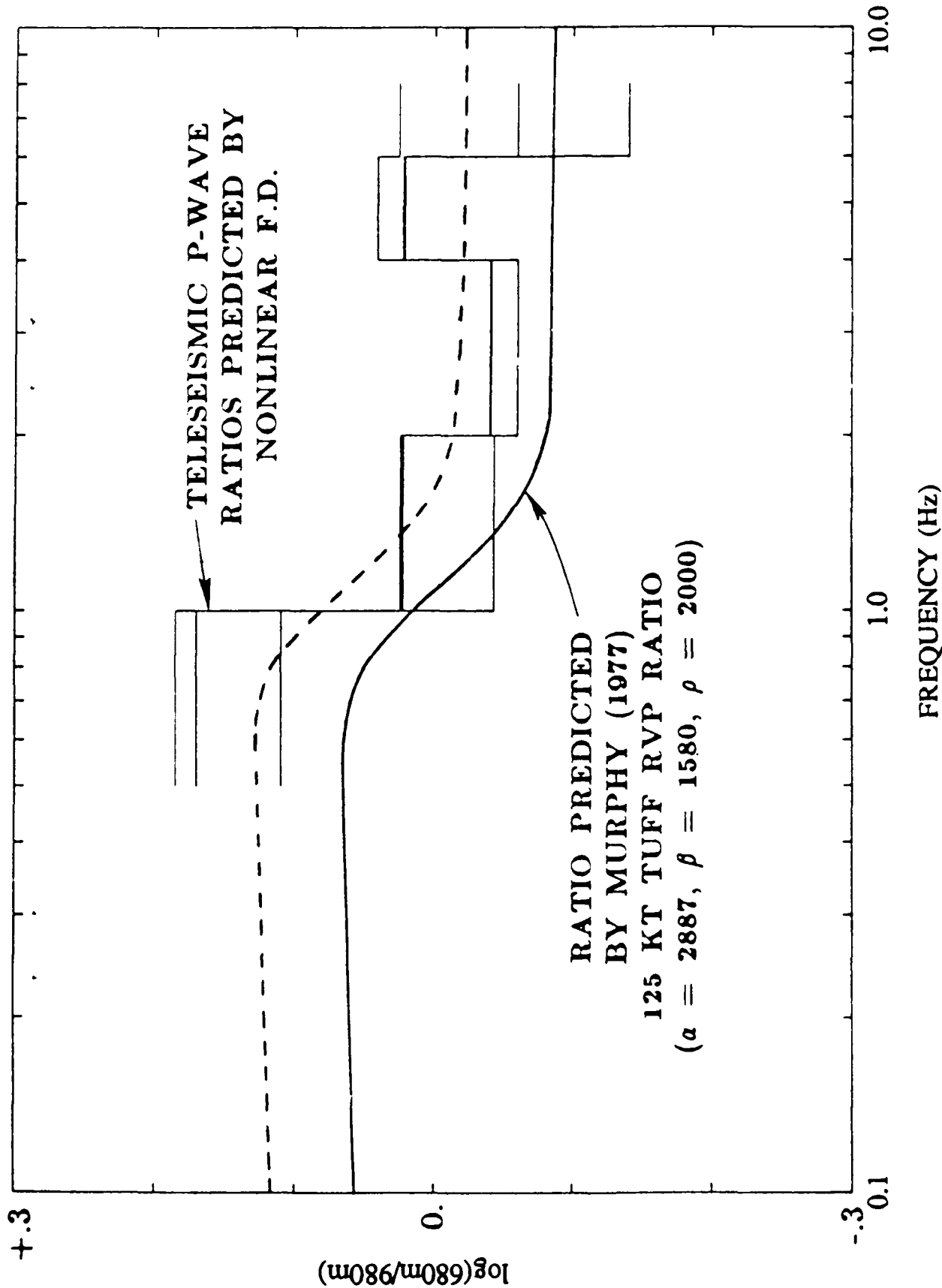


Figure 4.11.

Spectral ratios of the far-field P-wave (680 meter depth versus 980 meter depth) for three takeoff angles (10° , 20° , and 30°) averaged over several spectral bandwidths. The ratios show a low frequency enhancement of the 680 meter synthetic and a high frequency enhancement of the 980 meter synthetic P-waves. A spectral ratio based on Murphy (1977) scaling is shown for comparison (solid line) and also the same theoretical prediction shifted upward (dashed line) to agree with the finite difference synthetics.

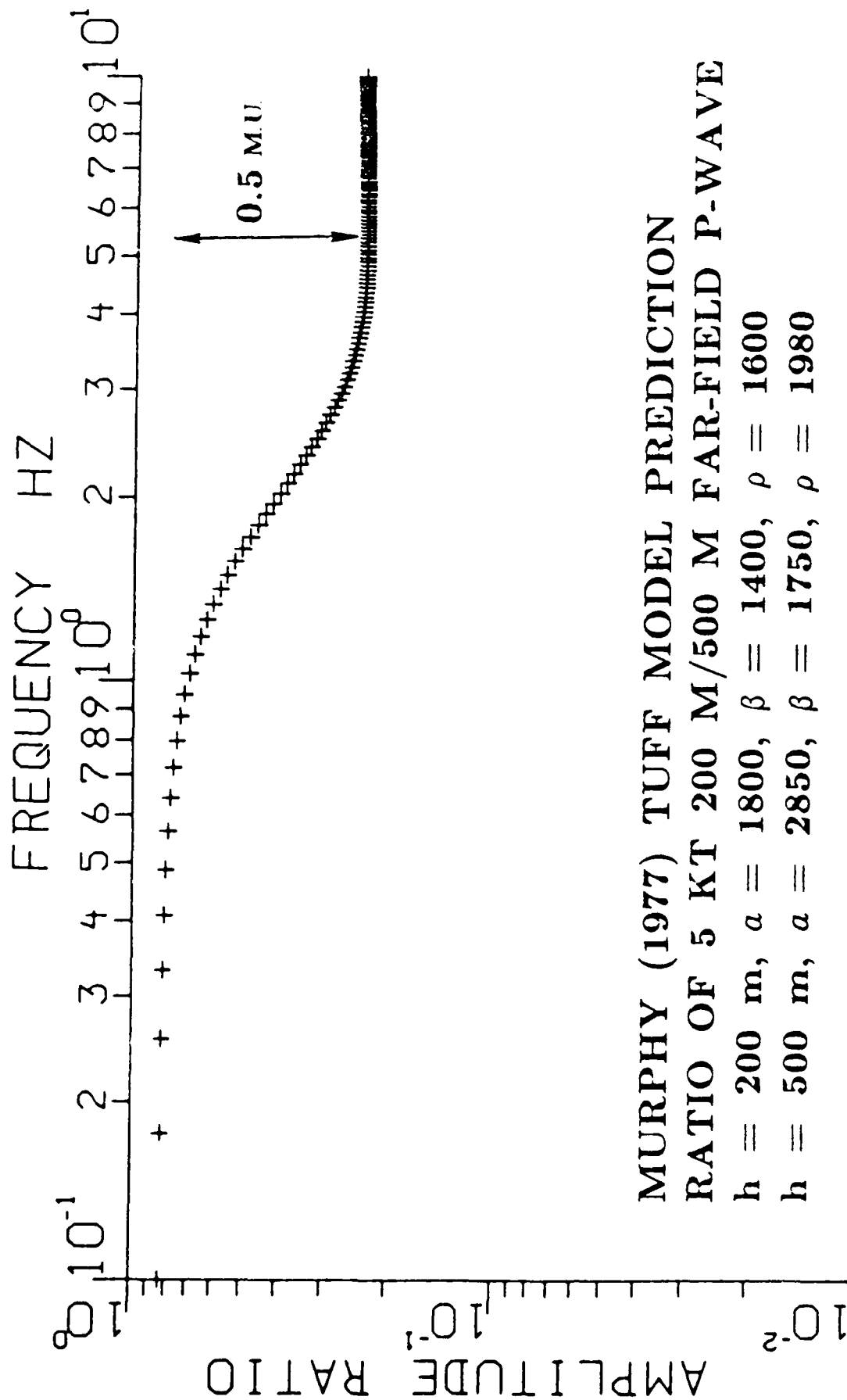


Figure 4.12. Prediction for P-wave spectral ratio between two hypothetical 5 kt sources at 200 and 500 meter depths of burial. A factor of 3 high/low frequency difference is predicted based on cube root depth scaling and a typical NTS velocity/density model.

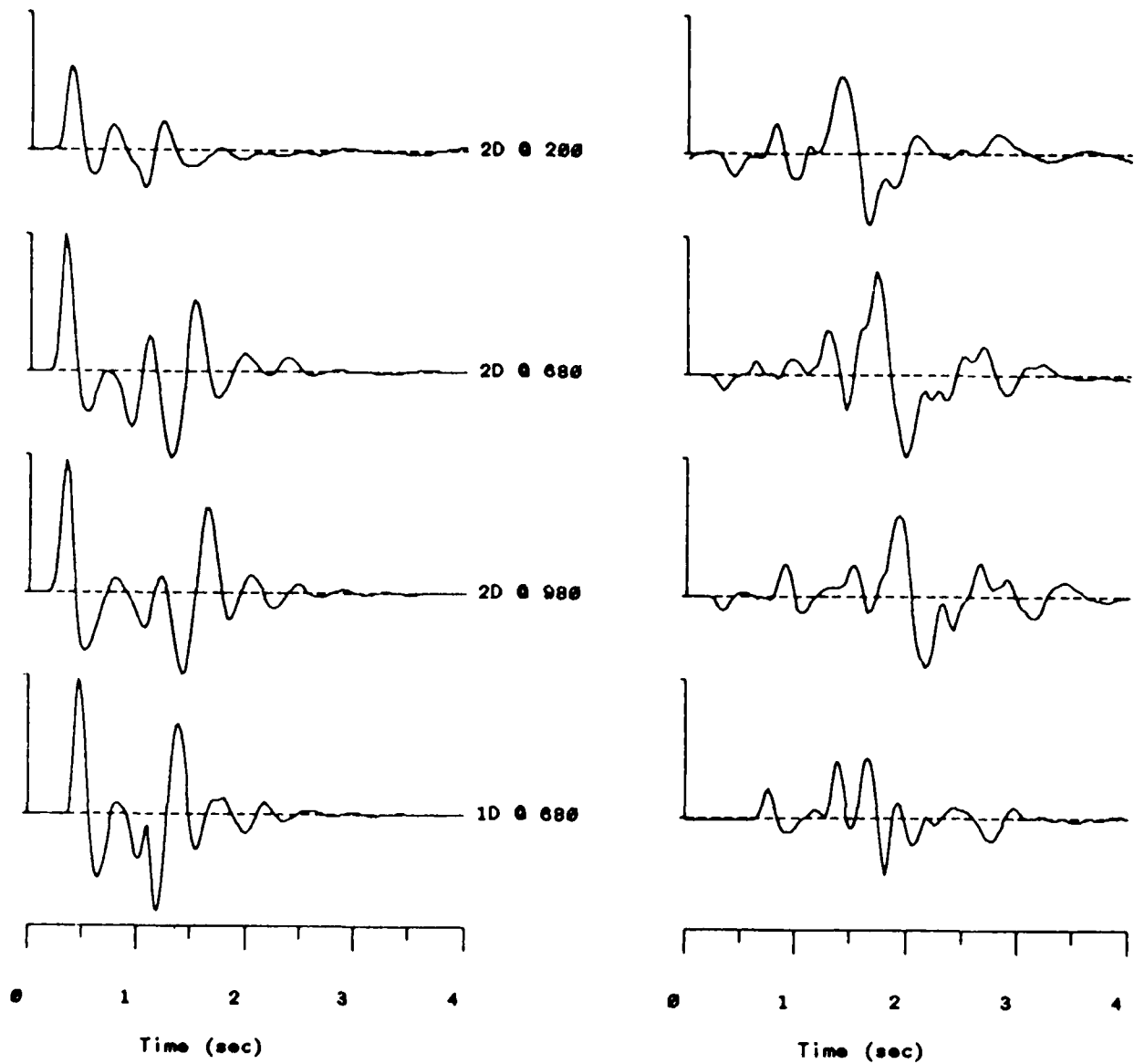


Figure 4.13a. P (left) and SV (right) displacements at a takeoff angle of 10° for the 2D sources at 200 (top), 680, and 980 meters and the 1D elastic (bottom) source. All traces shown to same scale. Note the direct SV in the 2D sources.

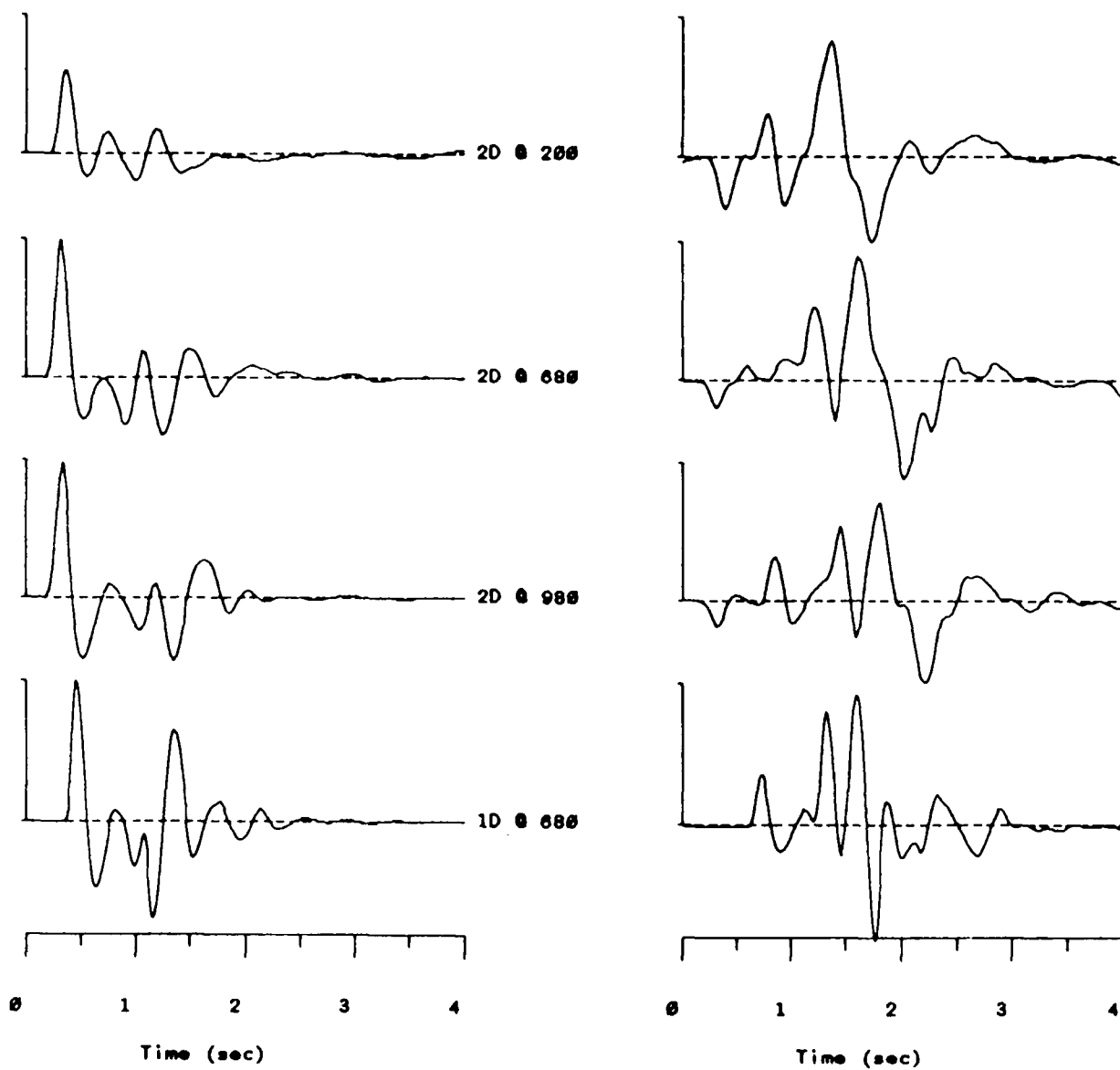


Figure 4.13b. P (left) and SV (right) displacements at a takeoff angle of 20° for the 2D sources at 200 (top), 680, and 980 meters and the 1D elastic (bottom) source. All traces shown to same scale. Note the direct SV in the 2D sources.

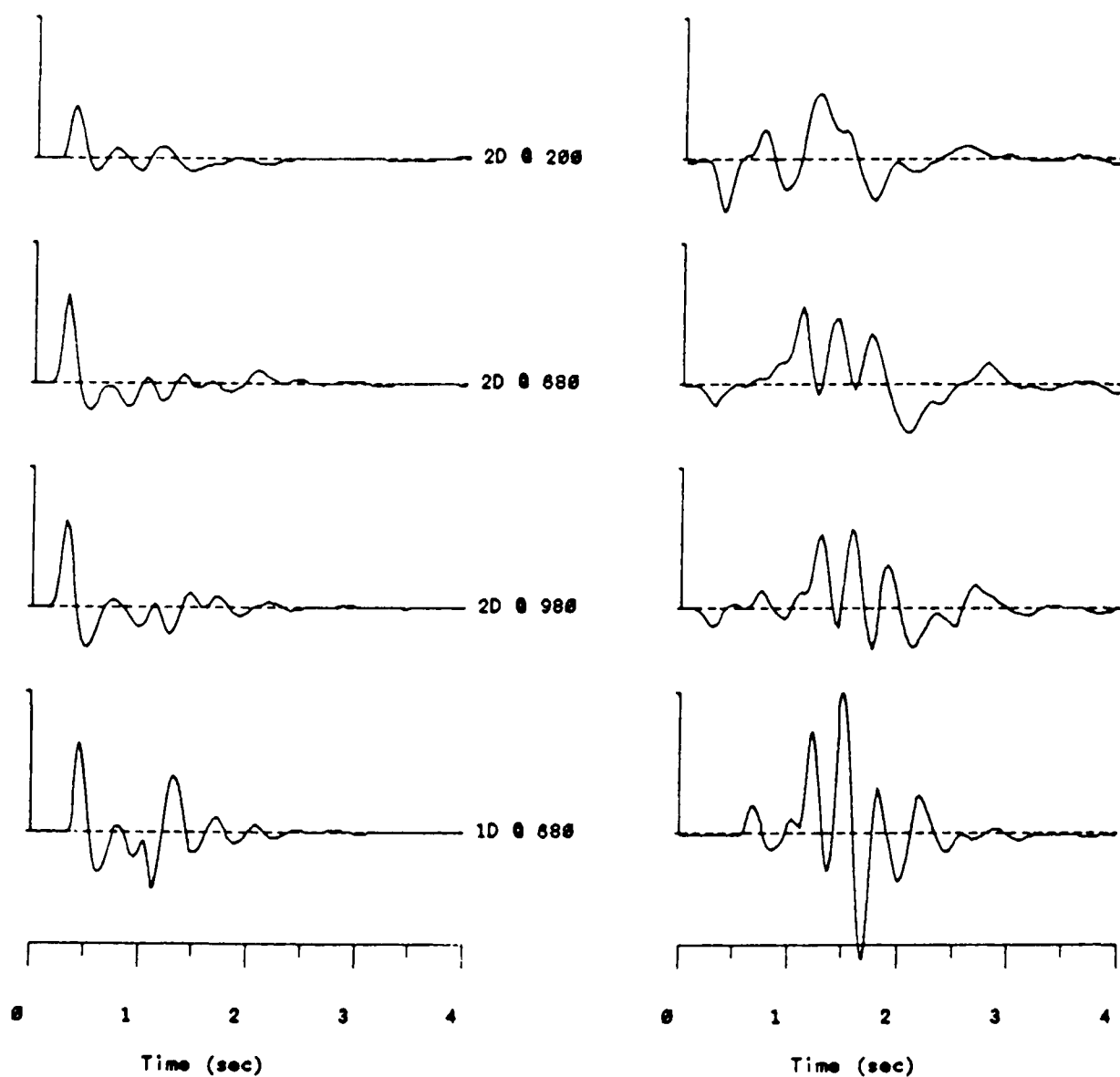


Figure 4.13c. P (left) and SV (right) displacements at a takeoff angle of 30° for the 2D sources at 200 (top), 680, and 980 meters and the 1D elastic (bottom) source. All traces shown to same scale. Note the direct SV in the 2D sources.

the working point were attenuated and delayed. The 2D 980 meter depth synthetic is the most like the elastic 680 meter depth synthetic in appearance. Judging from the timing of the secondary P and SV pulses it appears that the major SV source from the 2D nonlinear axisymmetric simulations remains the conversion of P to SV at the free surface (pS). The attenuation of the high frequency SV above the source increases with increasing take-off angle and is greatest for the 30 degree take-off angle.

Figures 4.14a, b, and c. show the linear-linear spectra corresponding to the time functions of Figures 4.13a, b, and c respectively. Note that the 2D nonlinear sources have greater low frequency amplitude and less high frequency amplitude than the elastic simulation. Also, note that the spectral nulls clearly visible in the 1D elastic P and SV spectra are not as apparent in the 2D nonlinear spectra. Clearly, the qualitative explanation that pP and pS are attenuated and delayed is inadequate to explain the spectral character of the nonlinear simulations. If the pP and pS were simply linearly attenuated, the spectral nulls would remain. Furthermore, the low frequency amplitudes have been increased as well as the high frequency amplitudes reduced. The nonlinear interactions with the free surface and the interfaces above the 680 and 980 meter sources are responsible for phases that appear in the time domain like pP and pS but have spectral character unlike the direct explosion source.

4.3.4 Broadband Far-Field P Waveforms

Figures 4.15a and b compare broadband teleseismic synthetics for the Pahute Mesa simulations with deconvolutions by Lyman, *et al.* (1986) and Der, *et al.* (1987). Recordings from the EKA array were deconvolved of instrument and an attenuation operator using either the array sum (Lyman, *et al.*) or a multichannel deconvolution estimator (Der, *et al.*). Lyman, *et al.* removed an attenuation operator with $t^* = 0.35$ sec, while Der, *et al.* used a $t^* = 0.45$ sec. By comparing the two deconvolutions of PURSE, one can see that the major characteristics of the waveform are robust with respect to variations in attenuation operator and deconvolution method.

The events chosen for comparison are all announced by DOE to be in the 20 to 200 or 20-150 kt ranges. Their maximum-likelihood m_b 's (Lyman, *et al.*, 1986) are greater than 5.5 and depths of burial between 599 meters (PURSE) and 978 meters (SCOTCH). According to Springer and Kinneman (1971), SCOTCH has a yield of 150 kt and therefore a scaled depth of burial of $180 \text{ meters/kt}^{1/3}$.

The broadband seismograms (from Lyman, *et al.*) are labeled with "ApP" indicating the inferred pP arrival, and "As" a sometimes significant positive arrival following the "ApP". In the case of PURSE there is a phase labeled "Aq" which Lyman, *et al.* suggest may be aftershock activity. Hamilton, *et al.* (1972) report that PURSE reactivated the aftershock zone of BENHAM that was detonated 4.5 months earlier. Lay (1987) and Lay and Welc (1987) observe no more significant coda complexity for PURSE than for other Pahute Mesa explosions as measured across the WWSSN network. Lay (1987) however, claims that SCOTCH exhibited anomalous P-coda complexity on average across the WWSSN and yet shows little unusual coda in Figure 4.15b. The Der, *et al.* deconvolution for the somewhat larger explosion (mle- m_b 6.24), FONTINA, shows coda levels similar to PURSE. FONTINA and PURSE were

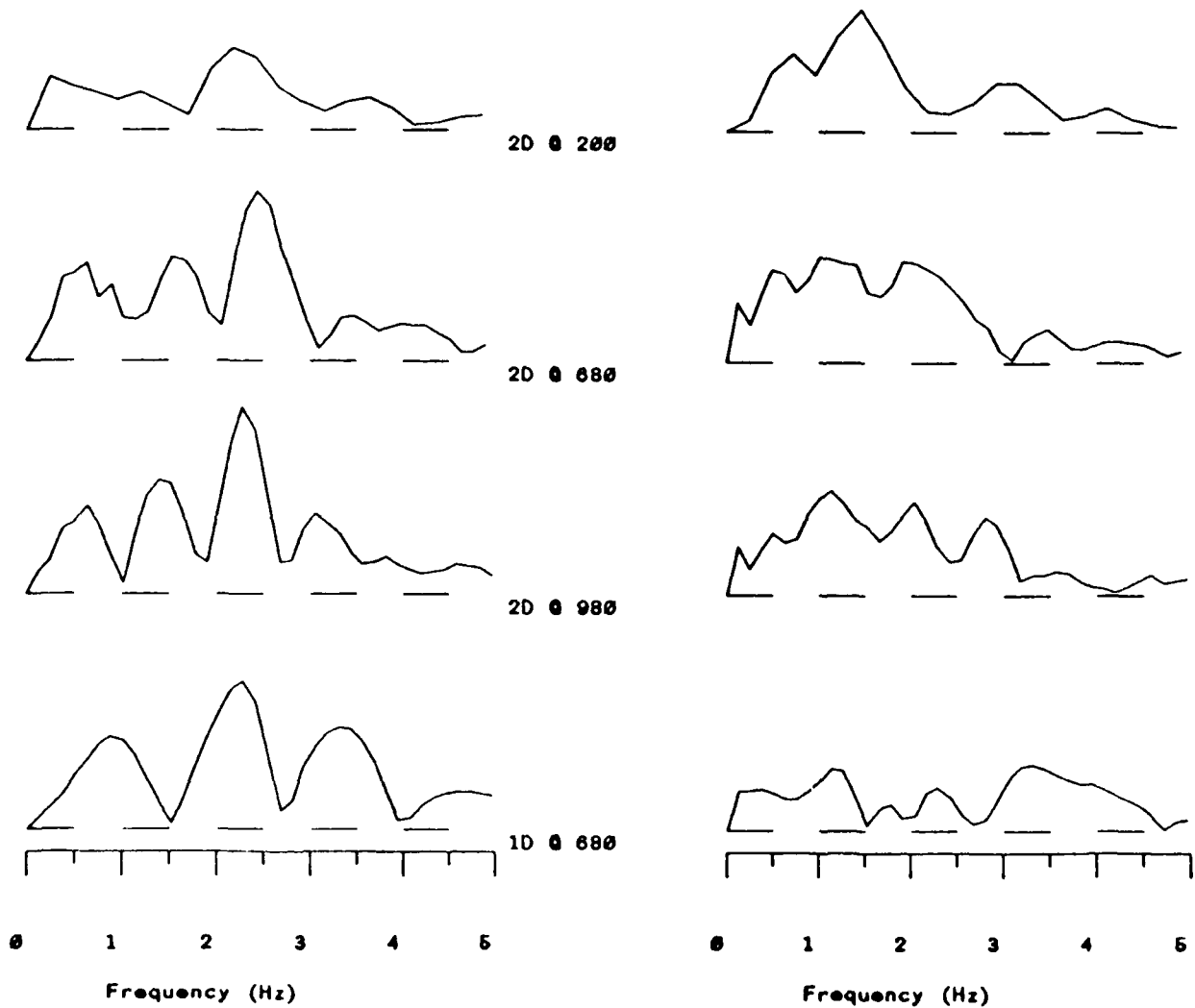


Figure 4.14a. P (left) and SV (right) linear-linear spectra at a takeoff angle of 10° for the 2D sources at 200 (top), 680, and 980 meters and the 1D elastic (bottom) source. All spectra shown to same scale. Note the spectral scalloping in the 1D source and the depletion of high frequencies in the 2D SV spectra.

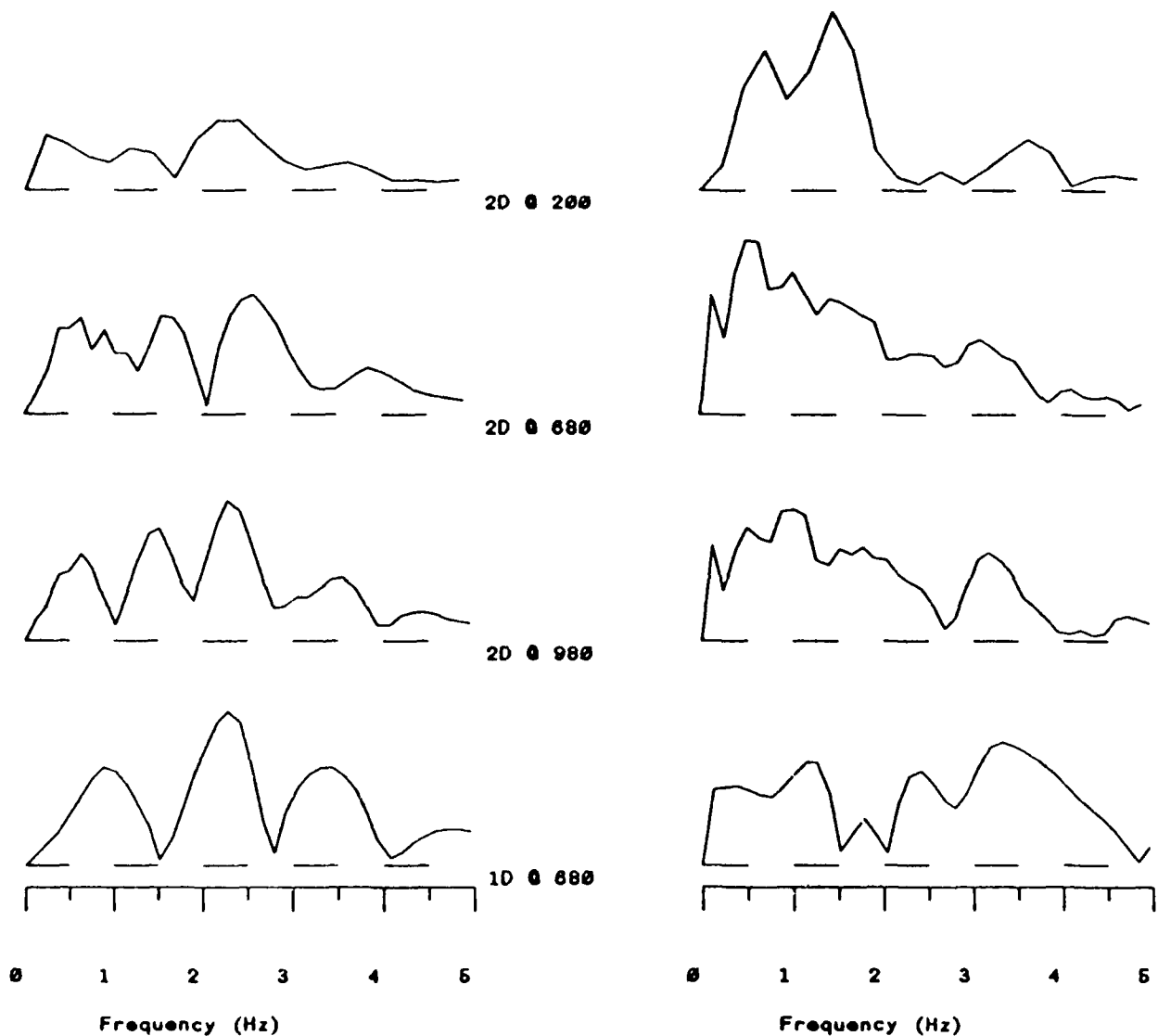


Figure 4.14b. P (left) and SV (right) linear-linear spectra at a takeoff angle of 20° for the 2D sources at 200 (top), 680, and 980 meters and the 1D elastic (bottom) source. All spectra shown to same scale. Note the spectral scalloping in the 1D source and the depletion of high frequencies in the 2D SV spectra.

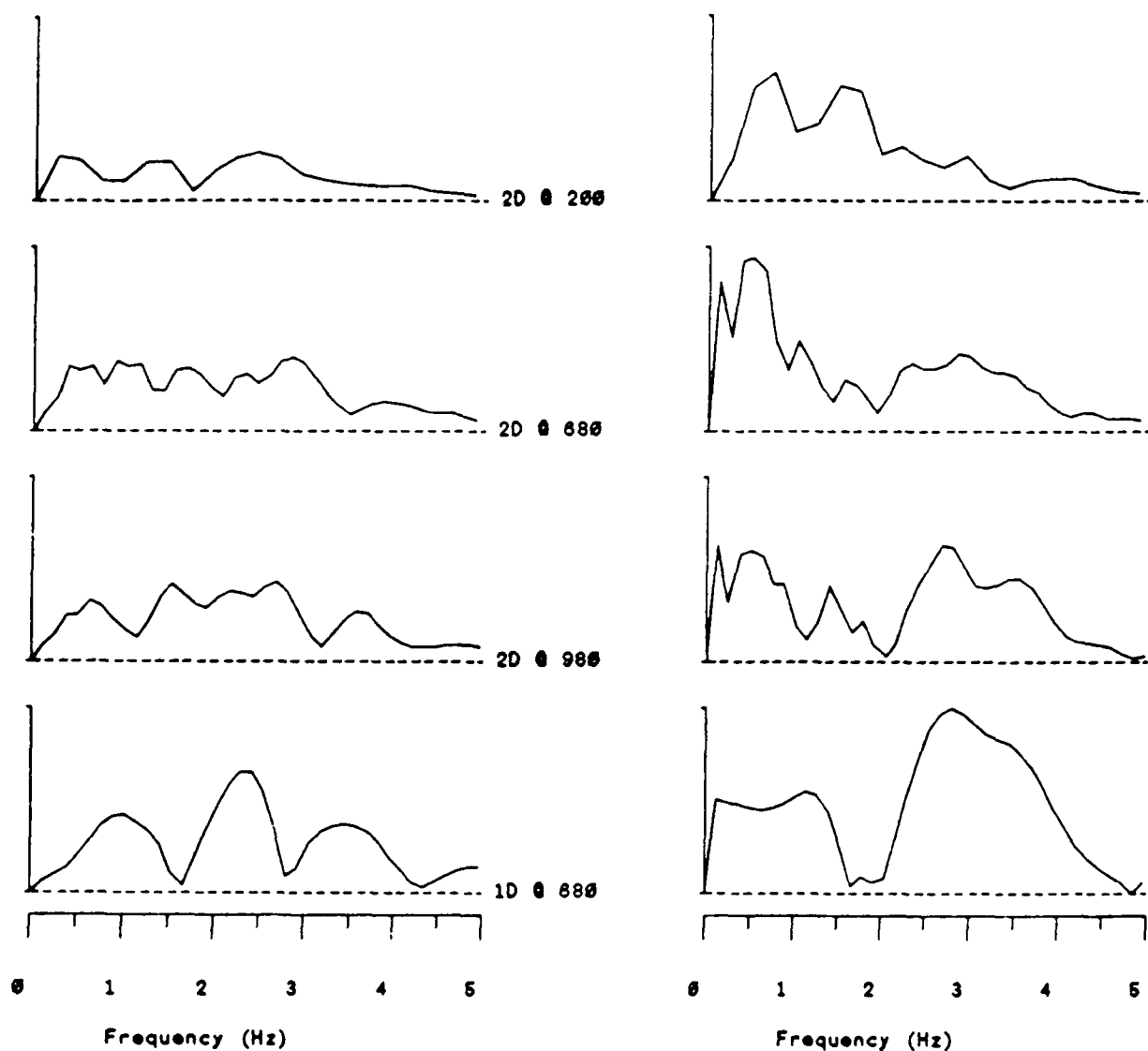


Figure 4.14c. P (left) and SV (right) linear-linear spectra at a takeoff angle of 30° for the 2D sources at 200 (top), 680, and 980 meters and the 1D elastic (bottom) source. All spectra shown to same scale. Note the spectral scalloping in the 1D source and the depletion of high frequencies in the 2D SV spectra.

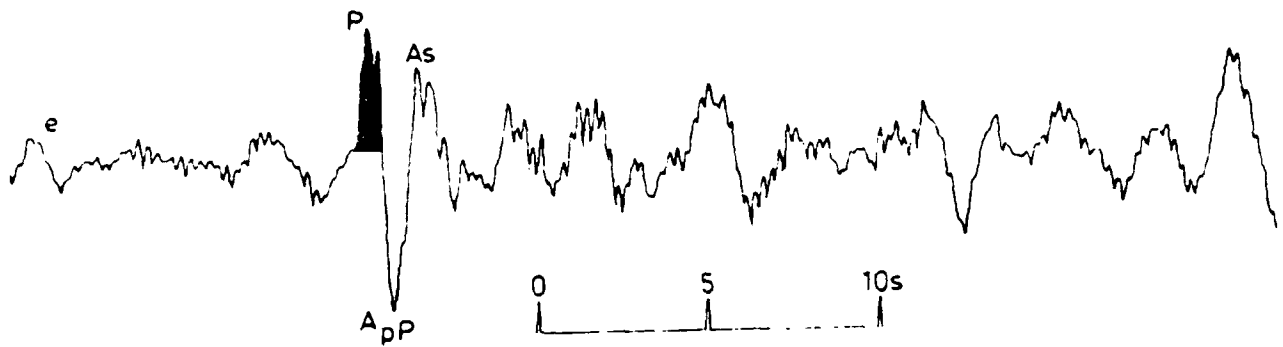


FIGURE 41. P SEISMOGRAMS RECORDED AT ESKDALEMUIR, SCOTLAND FROM NTS
EXPLOSION BACKBEACH

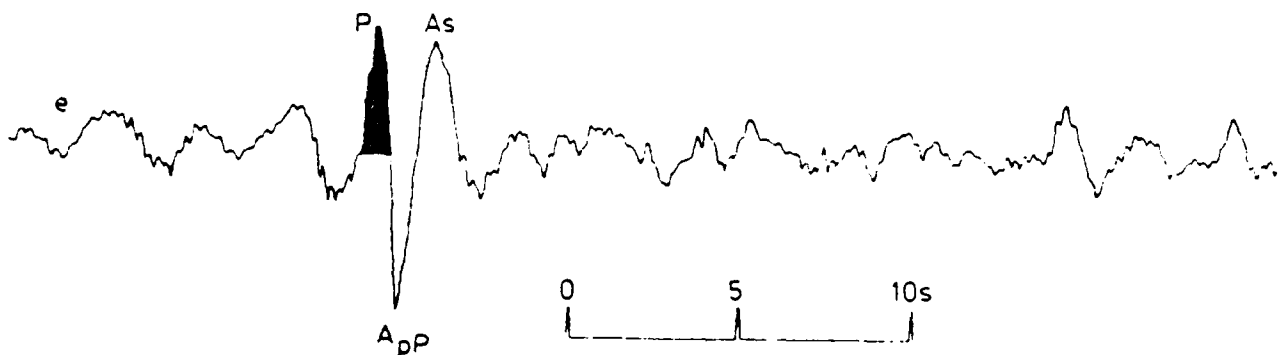
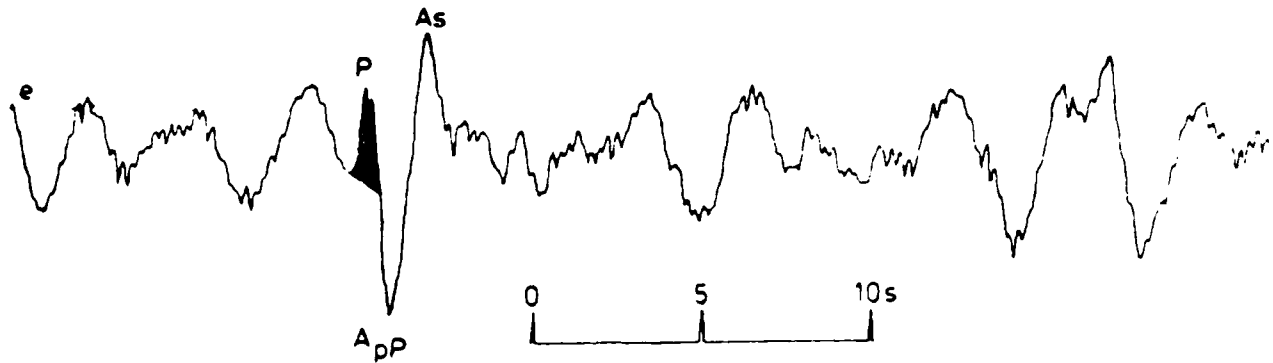
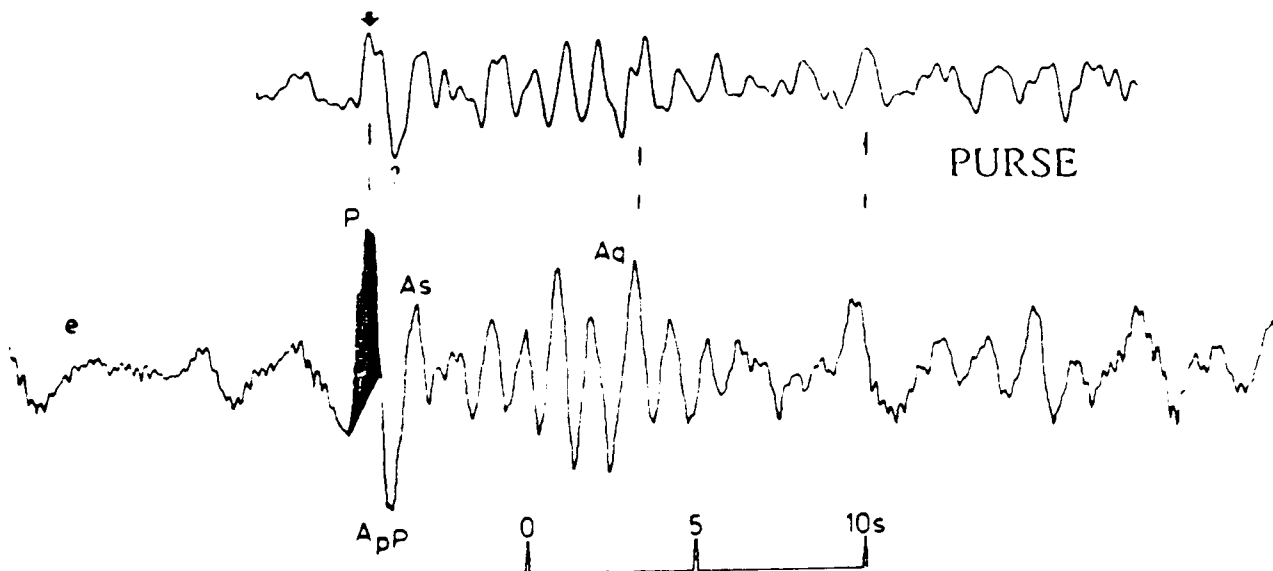


FIGURE 42. P SEISMOGRAMS RECORDED AT ESKDALEMUIR, SCOTLAND FROM NTS
EXPLOSION PANIR

Figure 4.15a. Deconvolved waveforms from Lyman, *et al.* for BACKBEACH (top) and PANIR (bottom).



**FIGURE 21. P SEISMOGRAMS RECORDED AT ESKDALEMUIR, SCOTLAND FROM NTS
EXPLOSION SCOTCH**



**FIGURE 25. P SEISMOGRAMS RECORDED AT ESKDALEMUIR, SCOTLAND FROM NTS
EXPLOSION PURSE**

Figure 4.15b. Deconvolved waveforms from Lyman, *et al.* for SCOTCH (top) PURSE (bottom), and from Der, *et al.* for PURSE (middle). The two deconvolved waveforms for PURSE used different procedures and different t^* 's.

located within 2 km of each other and may have illuminated some nearby scatterer or FONTINA may also have re-activated a cluster of activity that was observed by Hamilton, *et al.* 4 km east of PURSE and would have been within 2 km of FONTINA.

The 980 meter deep 2D synthetic waveform (Figure 4.15c) exhibits a 1.1 sec pP-P and the largest positive swing in the "coda" is at 1.3 seconds after the P and less than 1/2 the amplitude seen in the deconvolutions. The apparent pP amplitude of the overburied synthetic is substantially less than most of the observations.

With these small "pP" signals and without the large "As" phases in the synthetics it is not possible to properly simulate the Pmax/Pa amplitude ratios observed on teleseismic WWSSN seismograms. These secondary arrivals in the very early coda of teleseismic P have been noted by Frasier (1972) and many others. Given that this "phase" is so prevalent on explosions from NTS it is unlikely that it is a scattered phase but rather related to nonlinear interaction of the explosion with the free surface. Springer (1974) has suggested spall closure is a significant mechanism for the generation of this phase. Although the 2D axisymmetric nonlinear calculations include spall and nonlinear behavior above the explosion, they may underestimate the contribution of spall if it is not uniform.

For comparison with the synthetics at shallower take off angles, Figure 4.16a shows deconvolved Pn signals from a set of events at the broadband stations KNB and MNV. A comparison of the observations with synthetics is made in Figure 4.16b. The agreement between synthetics and the observations is acceptable given the observed variation between the two stations MNV and KNB. The most striking aspect of both the observations and the 2D synthetics, is the lack of any noticeable "pP" phase. This is in contrast to the elastic Green's function with a point explosion source which predicts a prominent pP phase (dashed line in Figure 4.16b).

TABLE 4.3 PAHUTE MESA EVENTS USED FOR COMPARISON
-ORDERED BY DEPTH OF BURIAL (DOB)-

EVENT	m_b	M_s	DOB(m)	YIELD(kt)	SCALED-DEPTH
PURSE	5.66	4.74	599	20-200	≥ 102
BACKBEACH	5.54	-	611	20-150	≥ 115
FONDUTTA	5.49	-	633	20-150	≥ 119
PANIR	5.66	-	681	20-150	≥ 128
FARM	5.63	-	689	20-150	≥ 130
SCOTCH	5.59	4.45	978	150	180

4.4 Effect of Prestress on Far-Field P and SV Waves

Day, *et al.* (1986) presented nonlinear models of tectonic release from underground explosions. They illustrated their analysis with synthetic long period Rayleigh waves from a suite of granite source calculations. One of these three 2D calculations modeled PILEDRIVER (61 kt, 463 meter depth of burial) in granite. The remaining two calculations were performed with horizontal prestress (7.5 MPa and 15Mpa) to

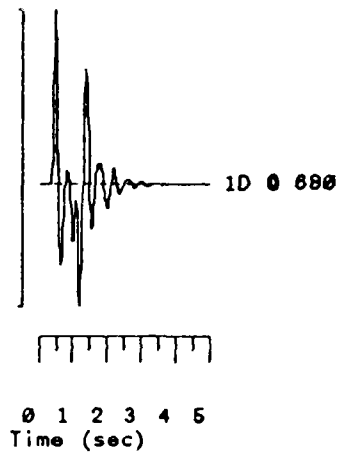
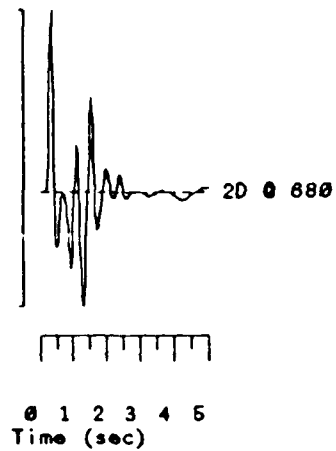
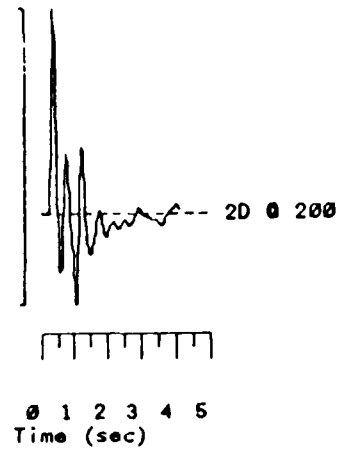


Figure 4.15c. Far-field teleseismic P-waves (takeoff angle of 10°) from the 2D sources at 200, 680, and 980 meter depths of burial and the 1D RVP at 680 meters. Same scale as Figures 4.15a and b.

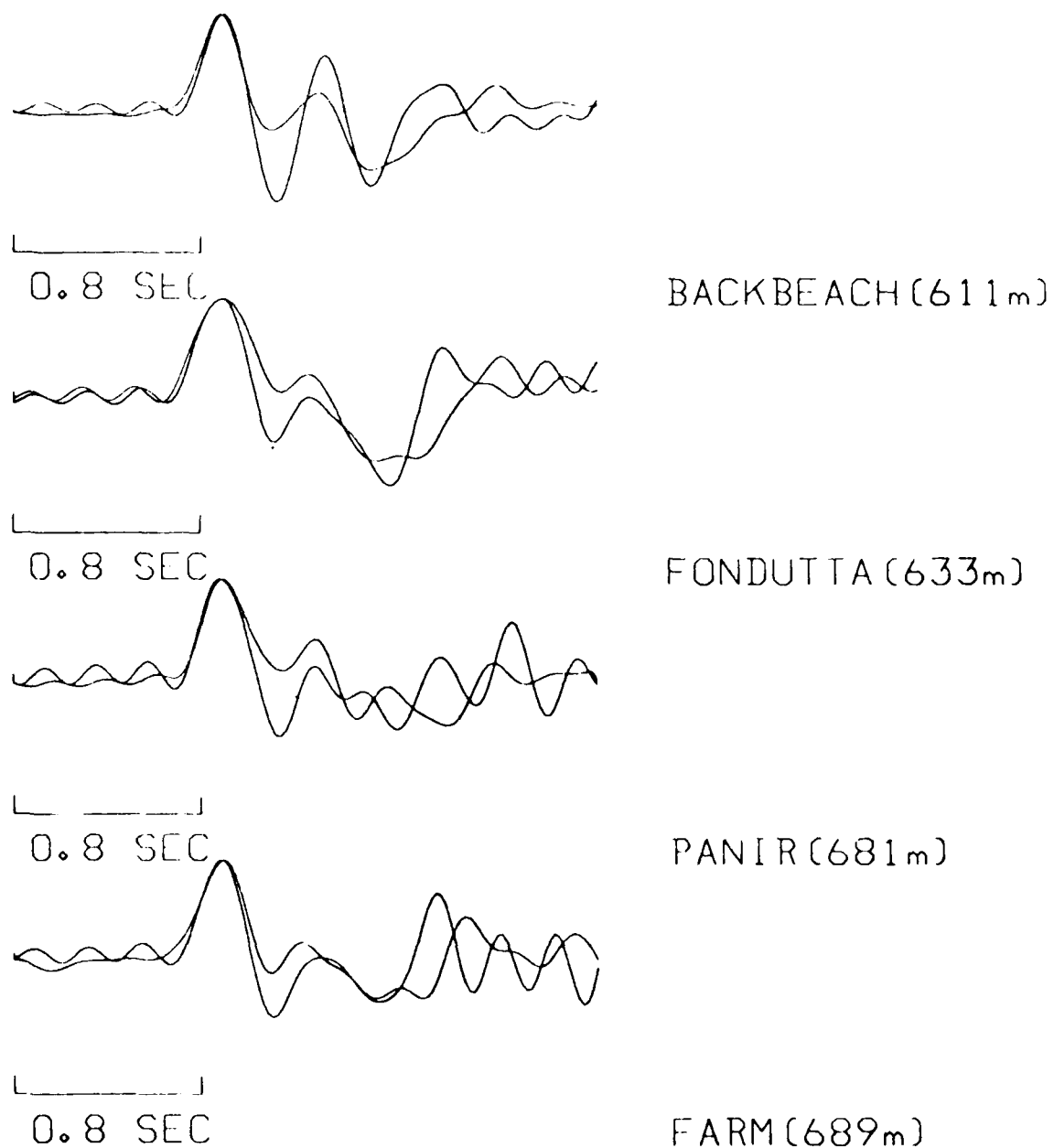


Figure 4.16a. Deconvolved Pn waveforms from several Pahute Mesa events recorded at KNB and MNV. A "pPn" arrival is not generally apparent on the displacement waveforms.

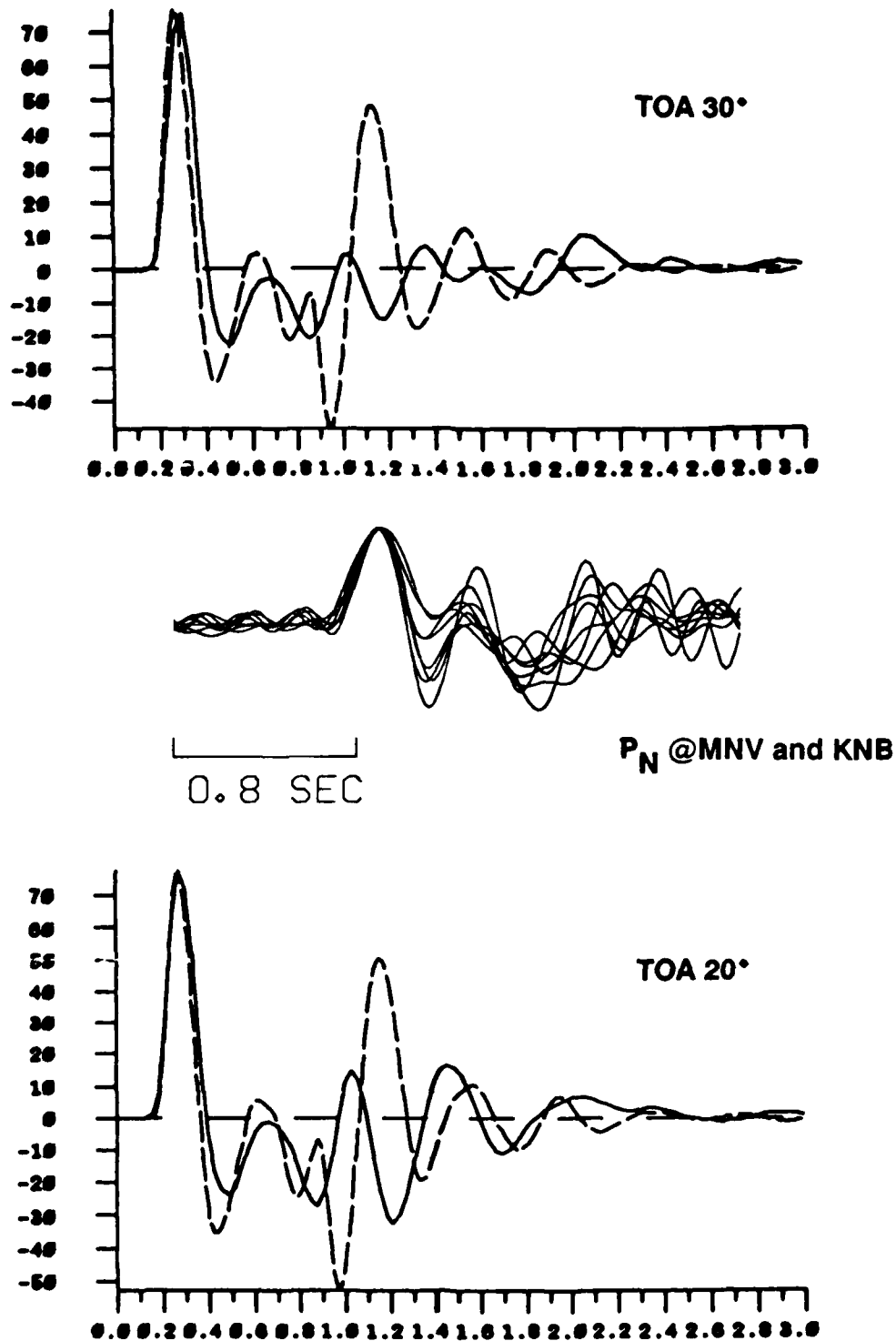


Figure 4.16b. A comparison of deconvolved P_n at MNV and KNB compared to 1D (dashed line) and 2D (solid line) synthetics for takeoff angles of 20° and 30°. Note that the 2D synthetics have little or no "pP" signal while the 1D synthetics predict a detectable "pP" arrival.

examine the effects of tectonic release. In this section, we examine the short-period far-field body waves from these simulations and compare the no prestress and prestress explosion sources with a 1D point source model for the explosion.

Figure 4.17a shows the far-field displacement waveforms for the three 2D non-linear calculations and a 1D source convolved with the elastic Green's function for a point source with 20° takeoff angle. We see that the three 2D calculations are very similar with an apparent "pP" about 50% the amplitude of the initial P. The 1D source apparent "pP" is larger than the initial positive P by about 10%, because the 1D RDP has considerable overshoot. These waveforms are convolved with an instrument response and an attenuation operator ($t^* = 0.8$ sec) in Figure 4.17b. We see again that the three 2D P waveforms are very similar. All sources give the same P_a amplitude and that the 1D waveform has a distinctively larger P_c swing. As with the Pahute Mesa and Shagan River synthetics, the relative amplitude of the P_c phase to the P_b and P_a phase is smaller than the typical short-period waveform. In order to increase the P_c phase amplitude, the 2D simulations would be required to have larger "pP" arrivals.

The far-field SV waveforms for three takeoff angles (10° , 20° , and 30°) are shown in Figures 4.18a, b, and c. The 1D source has the largest broadband peak SV amplitude at all takeoff angles. The 2D simulations generate a small direct SV wave that precedes the P to S conversion in the elastic Green's function. The differences between the 2D sources are smallest for 10° takeoff angle and greatest for 30° takeoff angle. The direct SV is largest for the largest prestress.

The broadband displacement waveforms are summarized (takeoff angle 30°) in Figure 4.19a. They are shown all at the same scale and we can see that the 2D SV pulses are generally broader than the 2D P pulses unlike the 1D SV and P pulses which have similar pulse widths. The spectra of these broadband signals are shown in Figure 4.19b. We see that the 2D P spectra are broader than the 1D P spectrum, and that the 2D SV spectra are more sharply peaked than the 1D SV spectrum. As is evident in the time domain pulses, the 2D SV spectra have a dominant peak at lower frequency than the 2D P spectra.

We can see from the 2D body waves that the horizontal prestress has little effect on the amplitudes and waveforms of the far-field short period P and SV signals. The 2D P waveforms are quite different than the 1D waveforms, but as with the Pahute Mesa and Shagan River simulations, the P_c phase relative to the P_a and P_b phases appears to be smaller than observed.

4.6 Conclusions

The discrepancies between the Pahute Mesa and Shagan River synthetic and observed teleseismic waveform statistics, together with the deconvolution results indicate that the nonlinear free-surface interaction phase, "pP" is too small in the synthetics. It is possible that this is related to the fact that spall was observed in the synthetics only at very shallow depths (less than 122 m for the Pahute Mesa calculations). Given that the tuff model was chosen to be a simple "ensemble" average of structures from a number of shots in the Pahute Mesa area, this may reflect the possibility that

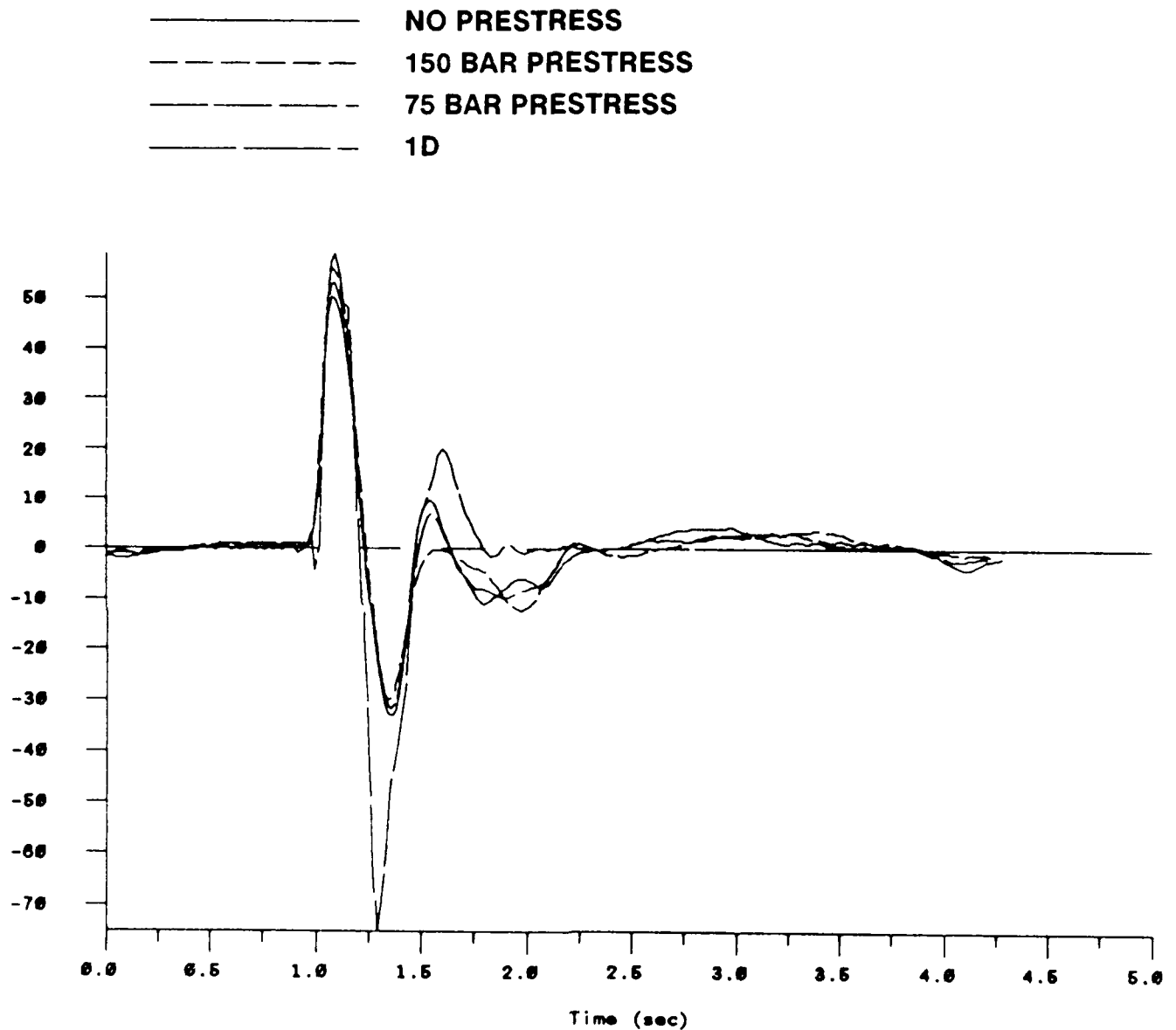


Figure 4.17a. Displacement teleseismic P waveforms ($\text{TOA}=20^\circ$) for the three 2D calculations and the 1D RVP convolved with the Green's function. Note the three 2D calculations predict very similar P-waves while the 1D synthetic predicts a large pP arrival. Takeoff angle 20°

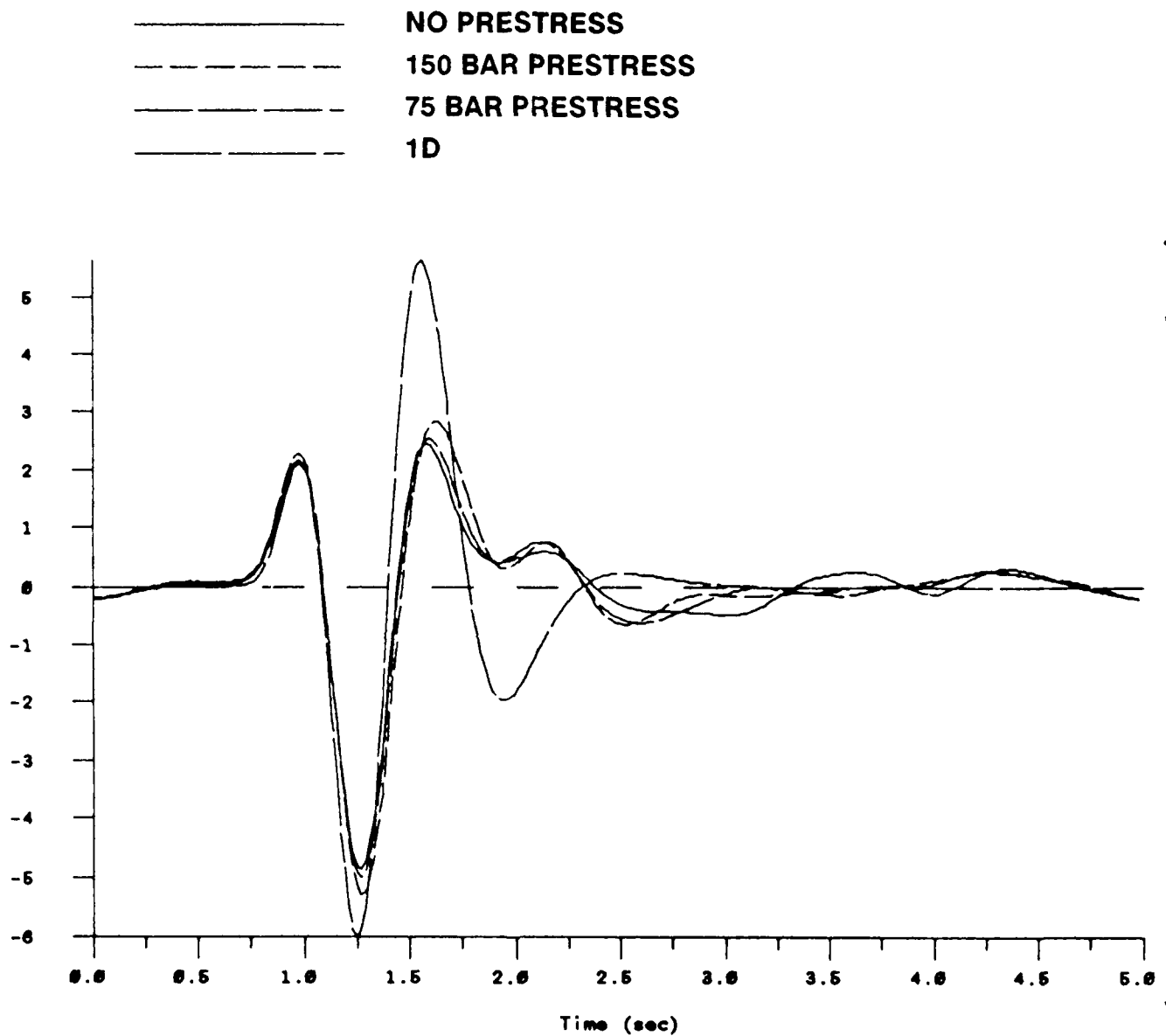


Figure 4.17b. P waveforms (TOA=20°) from 4.17a convolved with KS36000 and attenuation operator ($t^* = 0.8$ sec). 2D synthetics all predict very similar P-waves, while the 1D synthetic predicts a much larger "c" phase.

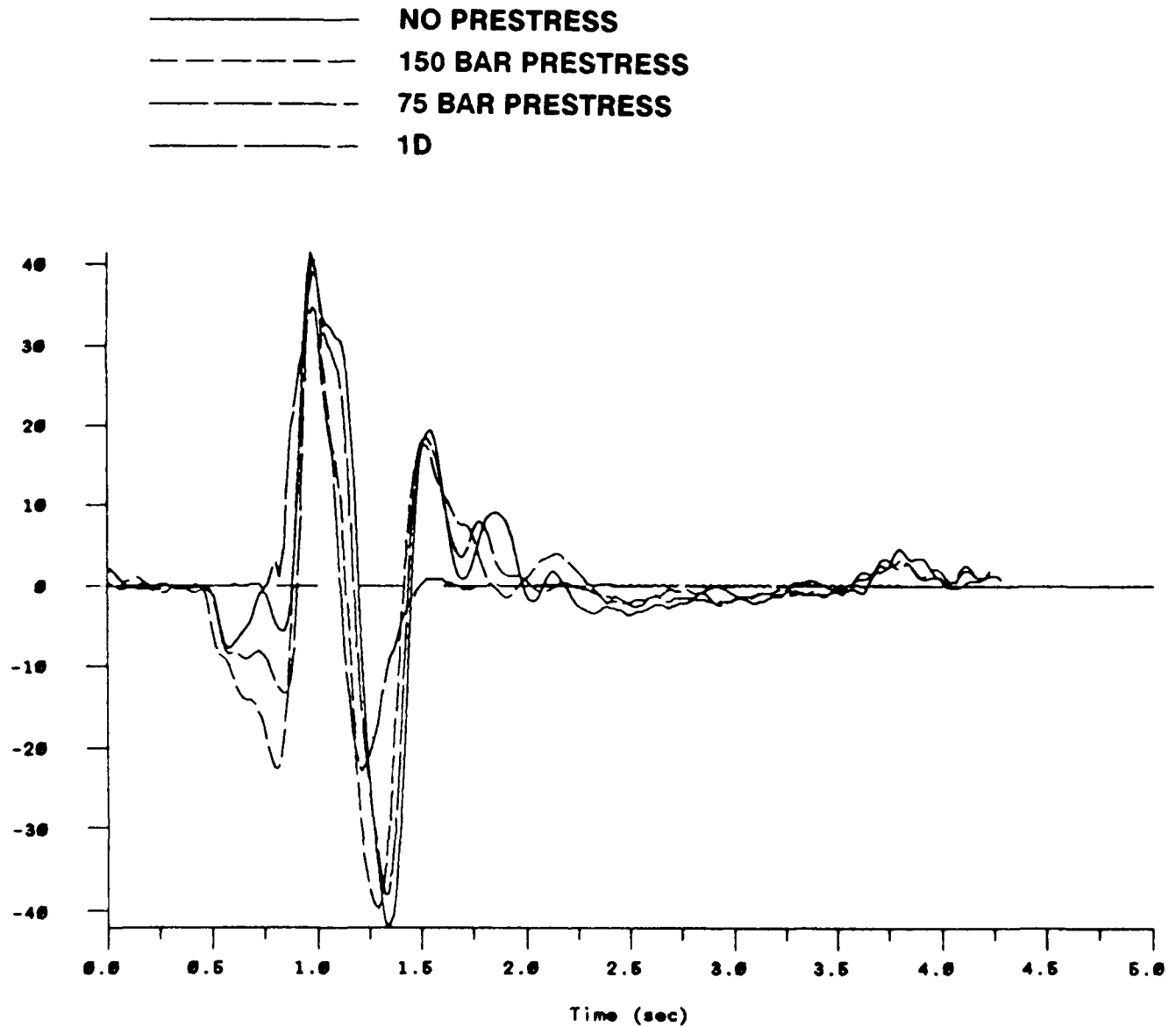


Figure 4.18a. Far-field SV waves ($\text{TOA}=10^\circ$) from the three 2D calculations compared with the 1D elastic point source explosion model. Takeoff angle 10° . Note the direct SV wave (at 0.4 sec) in the 2D calculations that is absent in the 1D synthetic. 2D synthetics are largely alike except for the amplitude of the direct SV wave.

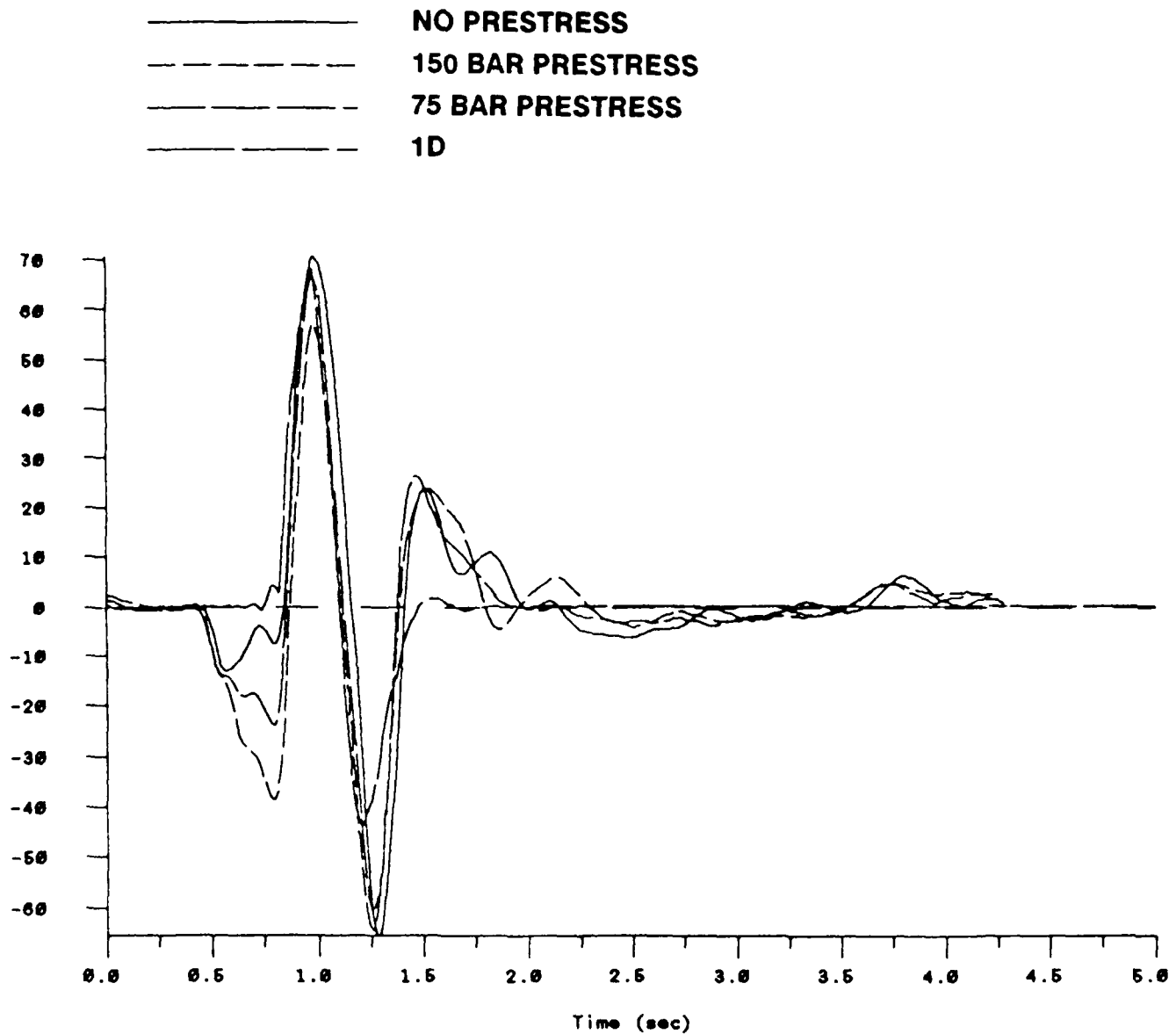


Figure 4.18b. Far-field SV waves ($\text{TOA}=20^\circ$) from the three 2D calculations compared with the 1D elastic point source explosion model. Takeoff angle 20° . Note the direct SV wave (at 0.4 sec) in the 2D calculations that is absent in the 1D synthetic. 2D synthetics are largely alike except for the amplitude of the direct SV wave.

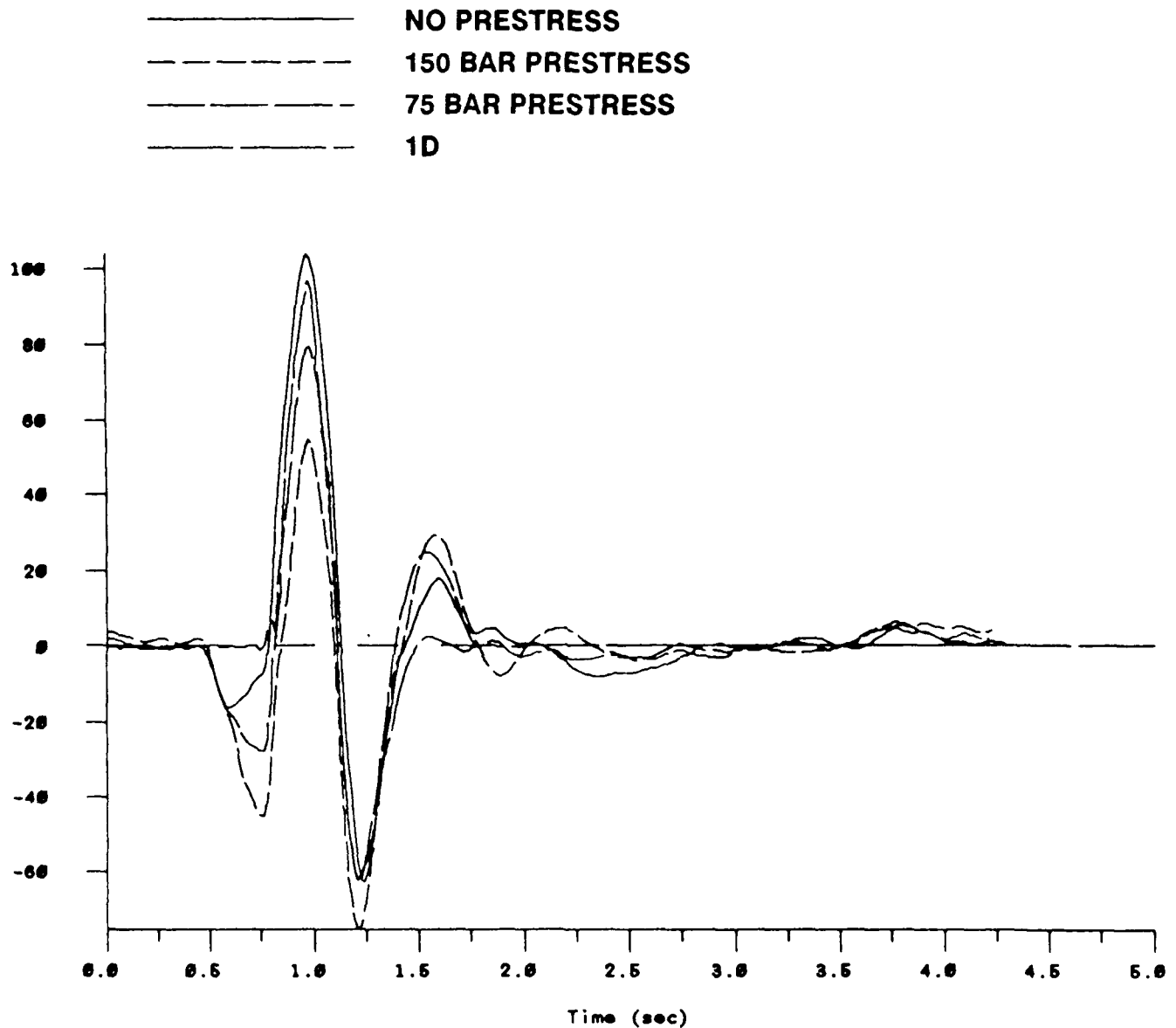


Figure 4.18c. Far-field SV waves ($\text{TOA}=30^\circ$) from the three 2D calculations compared with the 1D elastic point source explosion model. Takeoff angle 30° . Note the direct SV wave (at 0.4 sec) in the 2D calculations that is absent in the 1D synthetic. The 15 MPa prestress case exhibits the smallest SV amplitude, the no prestress has the greatest largest SV amplitude, and the 7.5 MPa prestress and 1D elastic synthetics are intermediate.

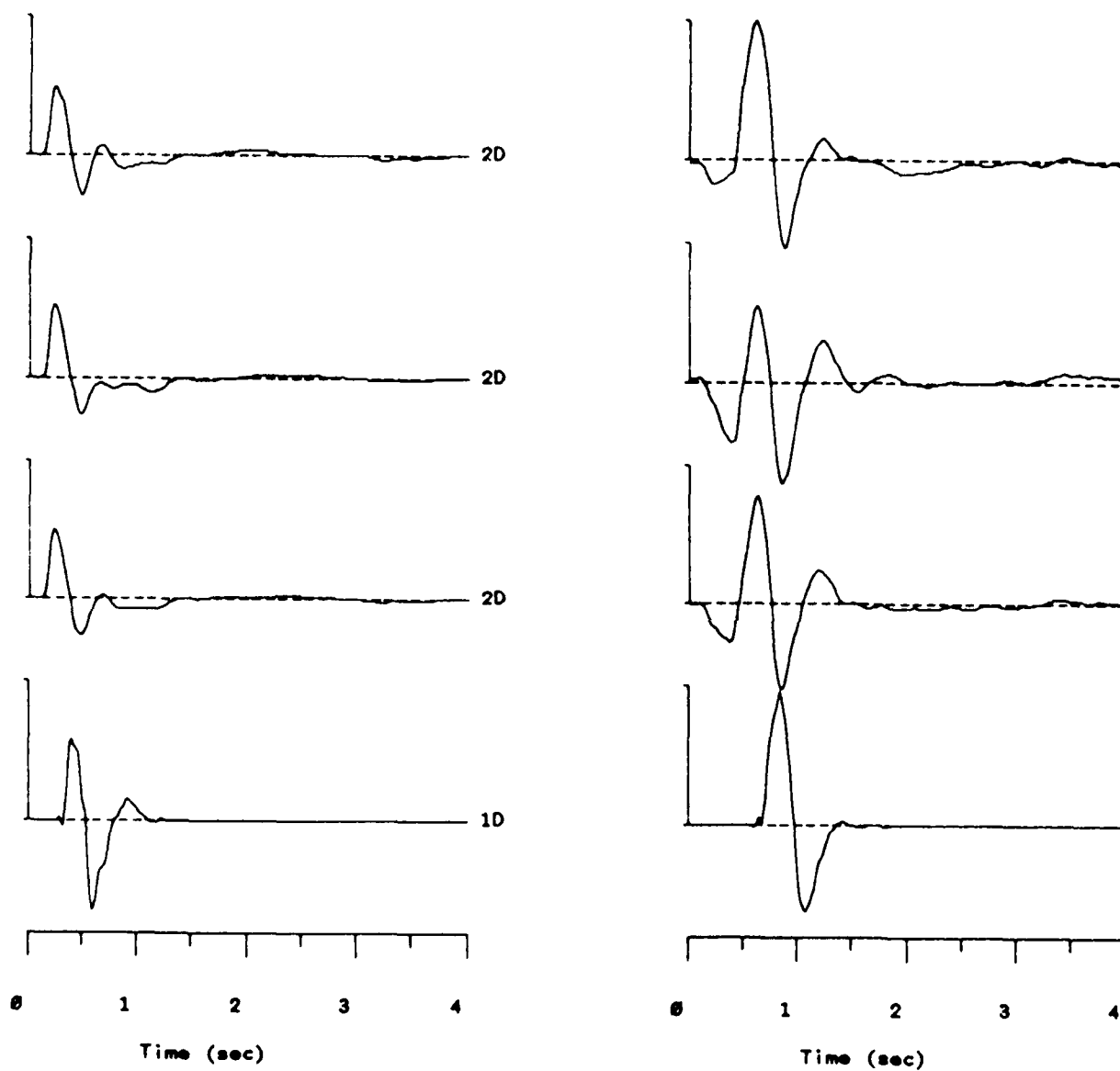


Figure 4.19a. Far-field P and SV waveforms are shown to the same scale for comparison. Takeoff angle 30° . Top to bottom: 2D no prestress, 150 bar prestress, 75 bar prestress, 1D.

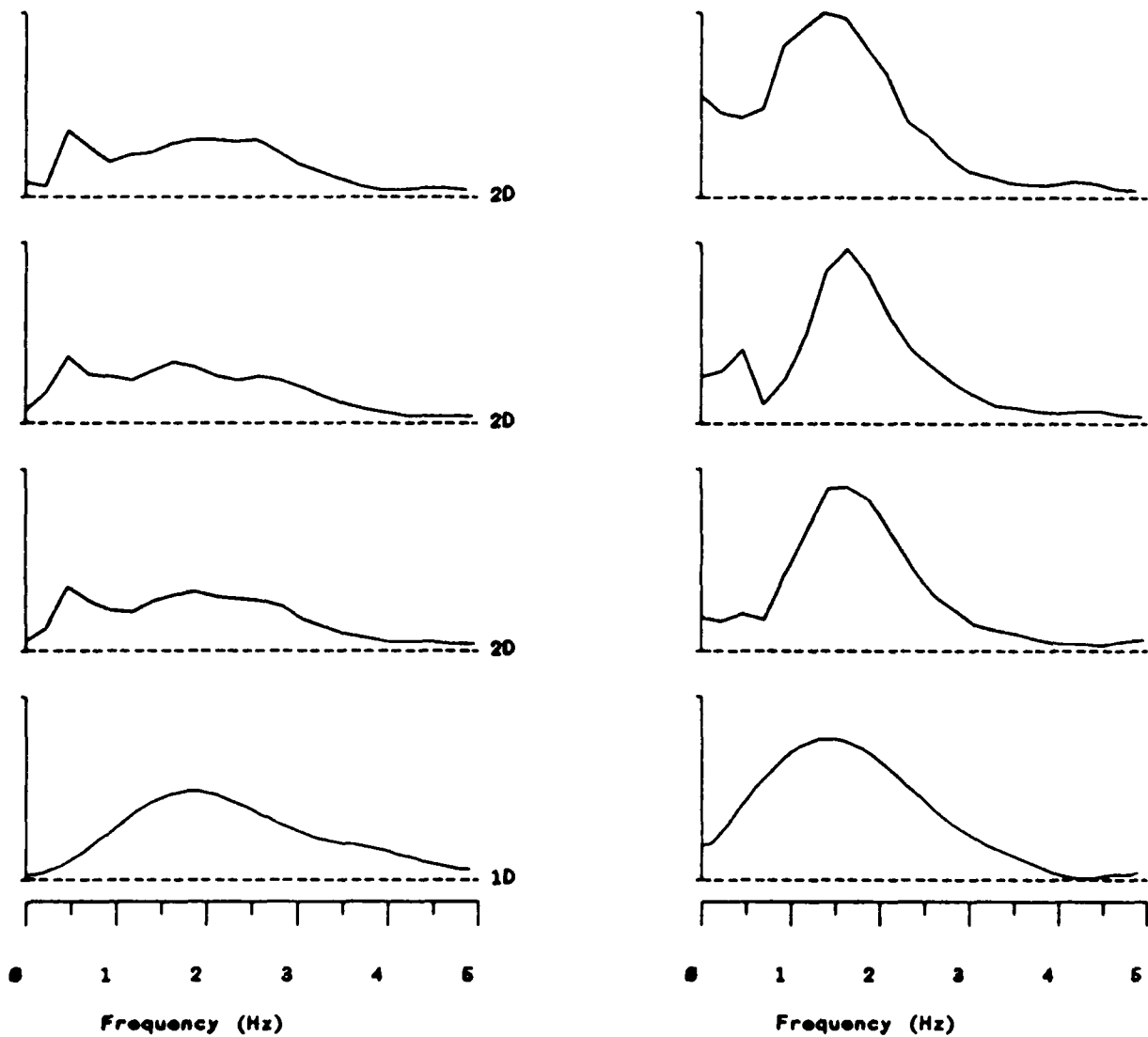


Figure 4.19b. Linear-linear spectra of waveforms shown in 4.19a. Note that the P and SV spectra are different shapes for the 2D calculations, unlike the 1D elastic point source model.

there is no "average" structure when nonlinear calculations are concerned. We suggest four possible explanations. 1) The material between 122 meters and the water table is weaker than that used in the model such that spall would extend to greater depth. 2) The presence of weak thin beds of ash fall tuff, or other thin layers of weak material may act as regions for localized tensile failure. 3) Lateral heterogeneities in the material above the shot may initiate instabilities that localize spall and produce non-uniform spalling. 4) The nonlinear properties of the materials above the shot attenuated too much energy from the free-surface reflection. In each case, detailed ground motion observations and numerical experiments would help to test the hypothesis. In particular, the detailed modeling of the inter-bedded nature of the Pahute Mesa geologic environment would test whether the weak beds can localize tensile failure along specific horizons and extend spall to greater depth. There are a few limited data sets of surface and buried accelerometer records available to help control such simulations.

The regional Pn observations at KNB and MNV show that the pPn is largely absent for Pahute Mesa tuff. This is in contrast to the prediction from elastic theory but in agreement with the nonlinear simulations. This indicates that the simulations are properly modeling the nonlinear effects at least for the regional Pn waveform.

In the spectral domain, the synthetics demonstrate that the overburied explosion is enriched in high frequencies, and depleted in low-frequencies with respect to the normal containment depth. The observations for the far-field direct P wave are consistent with cube-root depth scaling of the corner frequency. The nonlinear far-field P-wave spectra demonstrate that the pP is not a spectral replica of the direct P, and that the nulls predicted by linear propagation from a point source are not at the same locations and are much less prominent.

For the 2D axisymmetric simulations, the bulk (but not all) of the SV energy appears to originate with the free-surface interaction as with the elastic 1D explosion model. However, the two-dimensional far-field SV radiation is enhanced in low frequencies relative to the 1D explosion model and deficient in high frequencies. The same high/low frequency effect is true of the P-wave radiation but much less pronounced. Therefore, we can not explain the high/low frequency change in the SV radiation by a simple corner frequency shift in an explosive point source radiator. A more complicated model of the explosion source is required to explain the frequency content of the far-field SV.

V. TWO-DIMENSIONAL SOURCE REGIONAL SYNTHETICS

5.1 Introduction

Regional wave-guide phases such as Pg and Lg may be interpreted in three basic ways; integration over modes, integration over generalized rays, or integration in the frequency wavenumber domain. In the modal domain, the phases are viewed as a superposition of modes with similar group velocity and cover a band of phase velocities. Because the excitation of each mode has a complicated depth dependence and because the number of modes grows with increasing frequency, we can not simply synthesize the high frequency regional seismogram with a few well chosen modes excited by a point source at a chosen depth. Furthermore, as is demonstrated by Day, *et al.* (in preparation) the locked mode approximation to modal summation synthesis is shown to fail for regional seismograms with attenuation. Asymptotically, we can view the Pg and Lg arrivals as bundles of critically reflected rays making multiple reflections (rays) in the crustal waveguide. Haskell (1966) showed that the Pg modes are asymptotic to the phase and group velocities predicted from such a ray-theoretic approach. Furthermore, Haskell argued that because of conversion at interfaces Pg constitutes a set of leaky modes that suffers from loss of SV energy into the mantle. Finally, in the frequency-wavenumber domain we can view Pg and Lg as slowness bands of the layer response that constructively interfere to produce arrivals with a nearly constant group velocity as a function of distance. Consequently, we can not synthesize the Pg and Lg waveforms with a single slowness or take off angle as was done to produce the far-field P and S waveforms.

Although the modal and ray-theoretic methods add a sense of intuition to the process of generating synthetics, the wavenumber integration synthesis is the most exact method of analysis under the approximation that the Earth consists of laterally homogeneous layers. Because, intuition can often be fooled by complex wave phenomena, we have used the more exact method of wave synthesis to test the hypothesis that non-linear 2D explosion effects will produce a signature in regional phases and their spectra.

The method used in the following section to generate regional synthetics is based upon an application of the elastodynamic representation theorem (see Aki and Richards, 1980) and is exact under the layered structure approximation. The mathematical details are contained in an appendix. In essence, the displacements and tractions are propagated from the finite difference grid to regional distances using a surface boundary integral containing the wavenumber integration Green's functions. For the Pahute Mesa synthetics, the regional velocity model BR2 is used with the upper most layers altered to exactly replicate the model used in the simulations (Table 4.4). In the case of the Shagan River simulations, a structure for Eastern Kazakh from Stevens (1986) was used to compute Green's functions. The calculations were performed on a CRAY-2 supercomputer. A typical synthetic at 100 km distance, with a bandwidth of 0 to 2 Hz, required approximately 90 minutes of CPU time. This is largely due to the large number of Green's functions that must be computed at the depths and distances required for the boundary integral method of seismogram

synthesis. The code makes partial use of the vector processing capability of the supercomputer. Calculations for broadband seismograms scale quadratically with distance and linearly with bandwidth. For example, a doubling of range increases computation time by a factor of four while doubling the bandwidth simply doubles computation time. The nonlinear finite difference calculations are considered valid up to 5 Hz.

5.2 Pahute Mesa Synthetics

The simulations described in Section 4.3 were propagated as broadband seismograms to a distance of 100 km for frequencies up to 2 Hz. Figures 5.1a and b show regional synthetics for 2D axisymmetric calculations compared to those for point source explosion responses convolved with an RVP. We see that the 1D point source peak amplitude is larger than the 2D amplitude in all three depths of burial. However, the general character of the seismograms is similar for the 1D point sources and the 2D distributed sources. The 2D cratering synthetic has a more prominent fundamental Rayleigh wave arrival at 55-65 seconds than the 1D synthetic. Somewhat surprisingly, the 680 and 980 meter 2D synthetics show more impulsive initial P waves than the 1D point sources.

The surface low velocity layers in the model are responsible for two very slow Airy phases at 80-90 seconds and 100-110 seconds. These slow arrivals show the largest differences between the 2D and 1D synthetics and illustrate that the 2D sources have nonlinear phenomena extending up to the near surface to excite waves in these layers. The low velocity surface layers responsible for these Airy phases are rarely continuous in the Basin and Range for more than 50 km so we would not expect these parts of the seismogram to be robust features of the propagation. However, the energy of these modal waves must be scattered into other portions of the seismic field and contribute energy to other portions of the seismogram such as Lg or teleseismic P coda.

The whole record spectra for the 2D synthetics are shown in Figures 5.2a and b. The 680 and 980 spectra are virtually indistinguishable between 0.6 and 2 Hz. Below 0.6 Hz, the 680 simulation is enhanced in low frequencies with respect to the overburied simulation. The spectra for the cratering synthetics are displaced from the other spectra for clarity and are clearly different from the contained synthetics above 0.5 Hz.

Figures 5.3a and 5.3b show multiple bandpass filtered seismograms of the 2D vertical simulated seismograms from Figure 5.1a. The 1 octave bandpasses demonstrate that the 680 meter deep source's surface waves between 0.03 and 0.5 Hz are 70 to 100% larger than the 980 meter synthetics. Murphy's (1977) cube-root depth scaling would predict 12%. The Pg and Lg amplitudes in the 0.5 to 2.0 Hz bandwidth are much the same amplitudes between the two depths of burial. The multiple bandpass filters therefore show that the low frequency enhancement of the normal buried explosion is primarily in the slow surface waves. Simple point source explosion scaling can not account for these excitation differences.

Spectra of the synthetic Pg show no systematic differences between the two depths of burial, while a spectrum of the Lg window shown in Figure 5.4 indicates that the normal depth of burial synthetic is enriched in low frequencies (below 1 Hz)

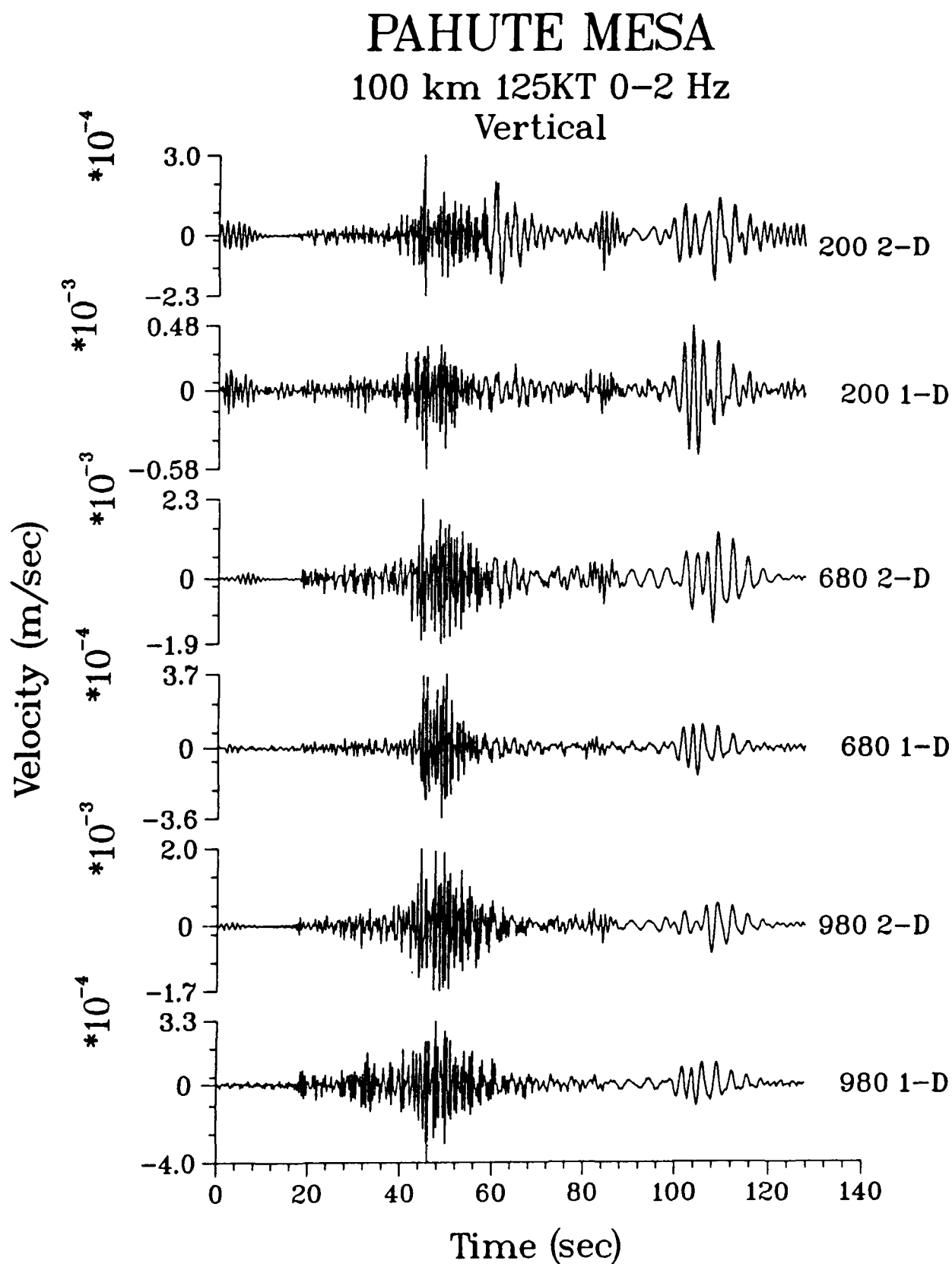


Figure 5.1a.

Comparison of broadband velocity synthetics for the Pahute Mesa tuffs calculations at 100 km. Vertical component, 0 to 2 Hz bandwidth.

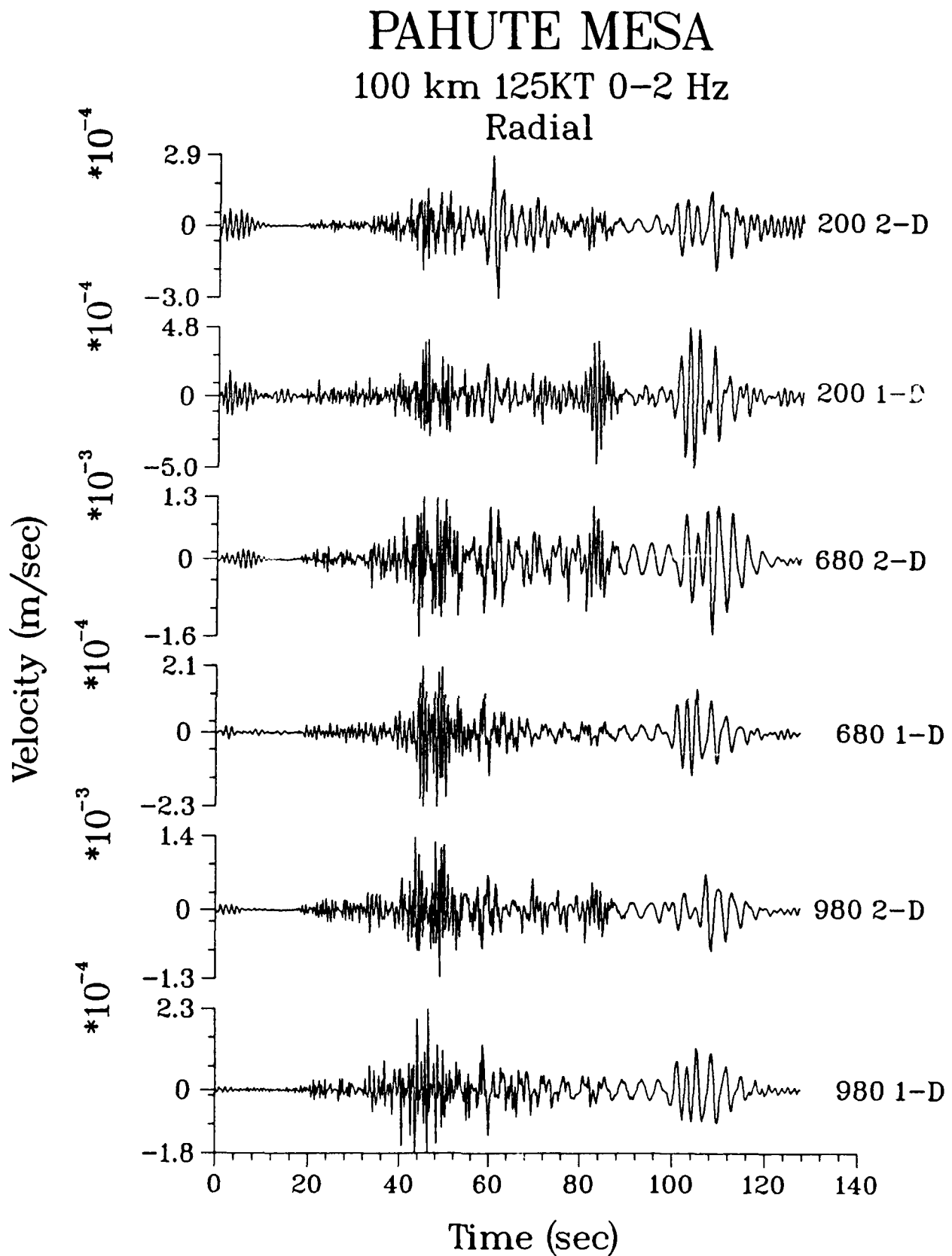


Figure 5.1b. Comparison of broadband velocity synthetics for the Pahute Mesa tuffs calculations at 100 km. Radial component, 0 to 2 Hz bandwidth.

PAHUTE MESA
100 km 125KT 0-2 Hz
2-D Vertical

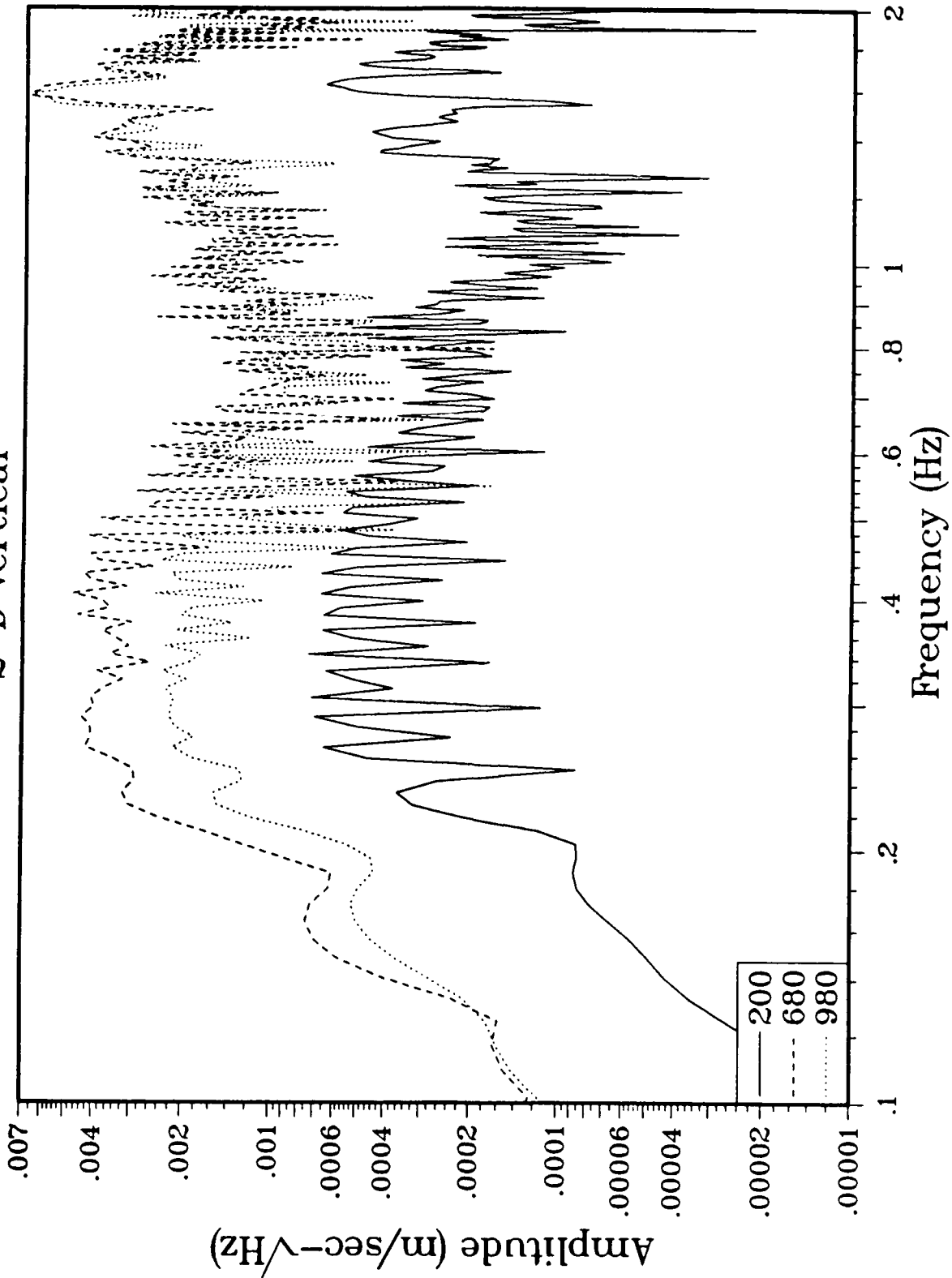


Figure 5.2a. Whole record spectra for the 2D Pahute Mesa tuff synthetics in 5.1a. Note the low-frequency difference between the 680 and 980 meter depth synthetics.

PAHUTE MESA
100 km 125KT 0-2 Hz
2-D Radial

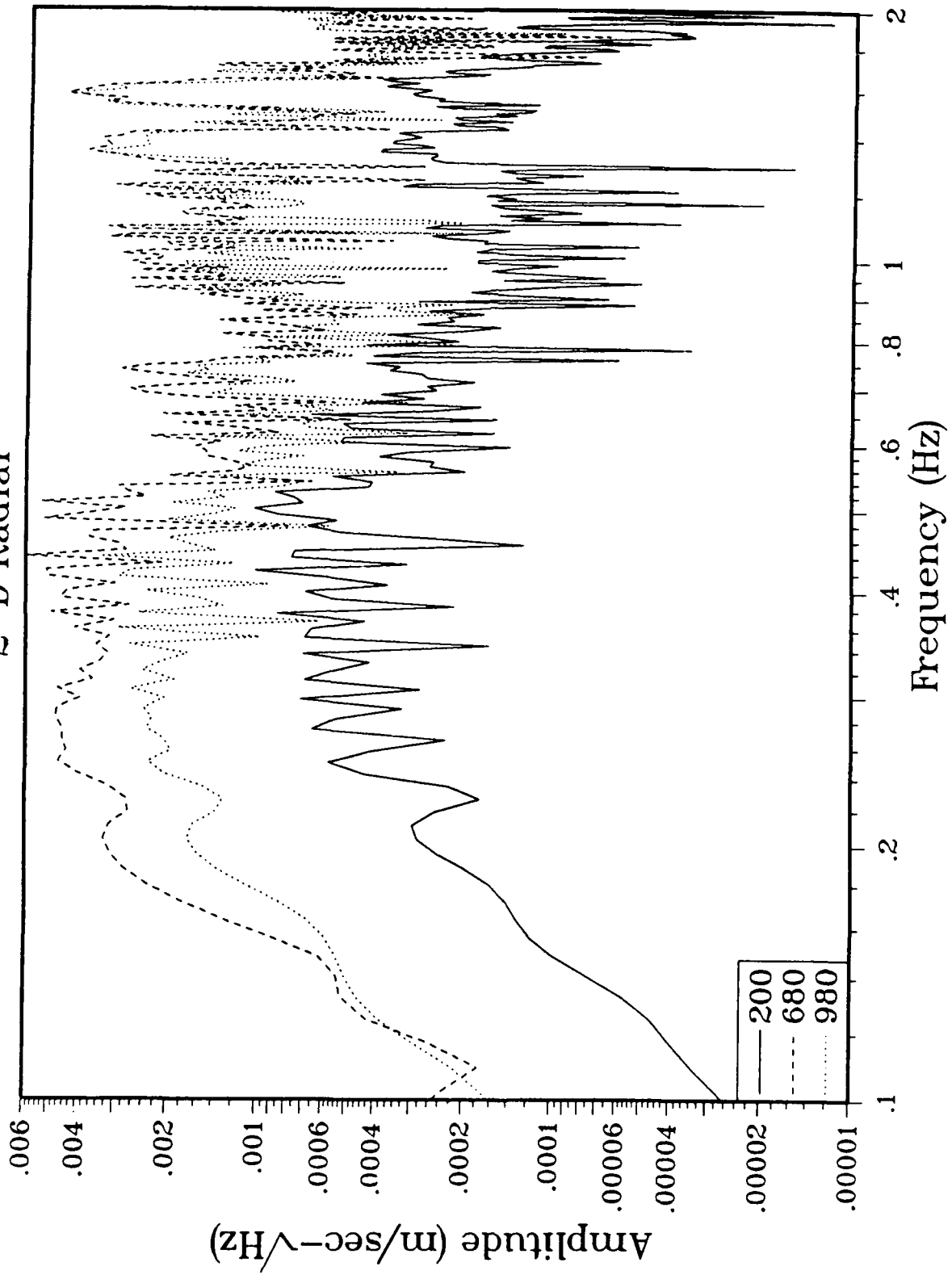


Figure 5.2b. Whole record spectra for the 2D Pahute Mesa tuff synthetics in 5.1b. Note the low-frequency difference between the 680 and 980 meter depth synthetics.

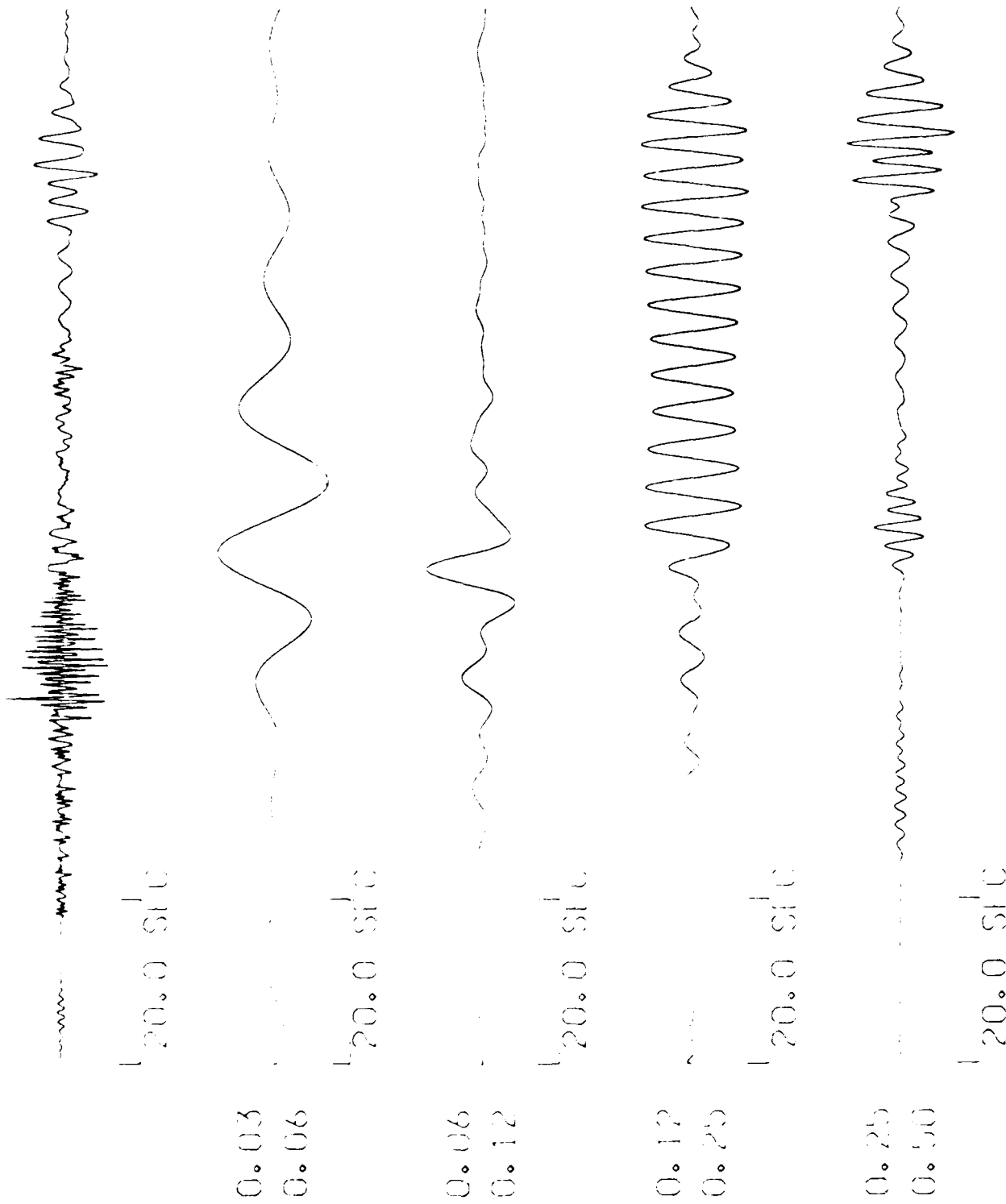


Figure 5.3a. Bandpass filtered seismograms for the 2D 680 meter depth of burial vertical component synthetic. Traces are from top to bottom, broadband velocity, 0.03-0.06 Hz, 0.06-0.12 Hz, 0.12-0.25, and 0.25-0.5 Hz.

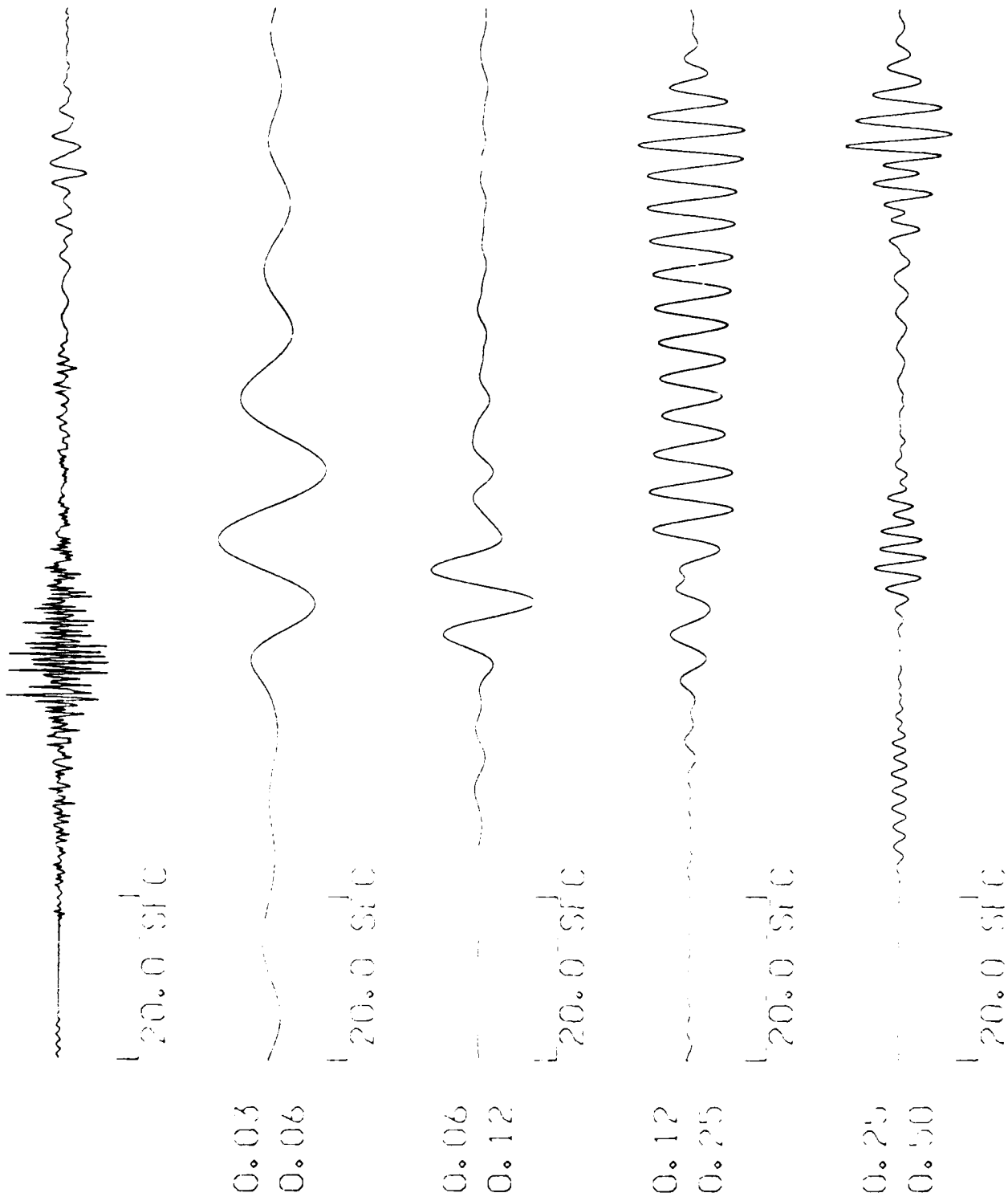


Figure 5.3b. Bandpass filtered seismograms for the 2D 980 meter depth of burial vertical component synthetic. Traces are from top to bottom, broadband velocity, 0.03-0.06 Hz, 0.06-0.12 Hz, 0.12-0.25, and 0.25-0.5 Hz.

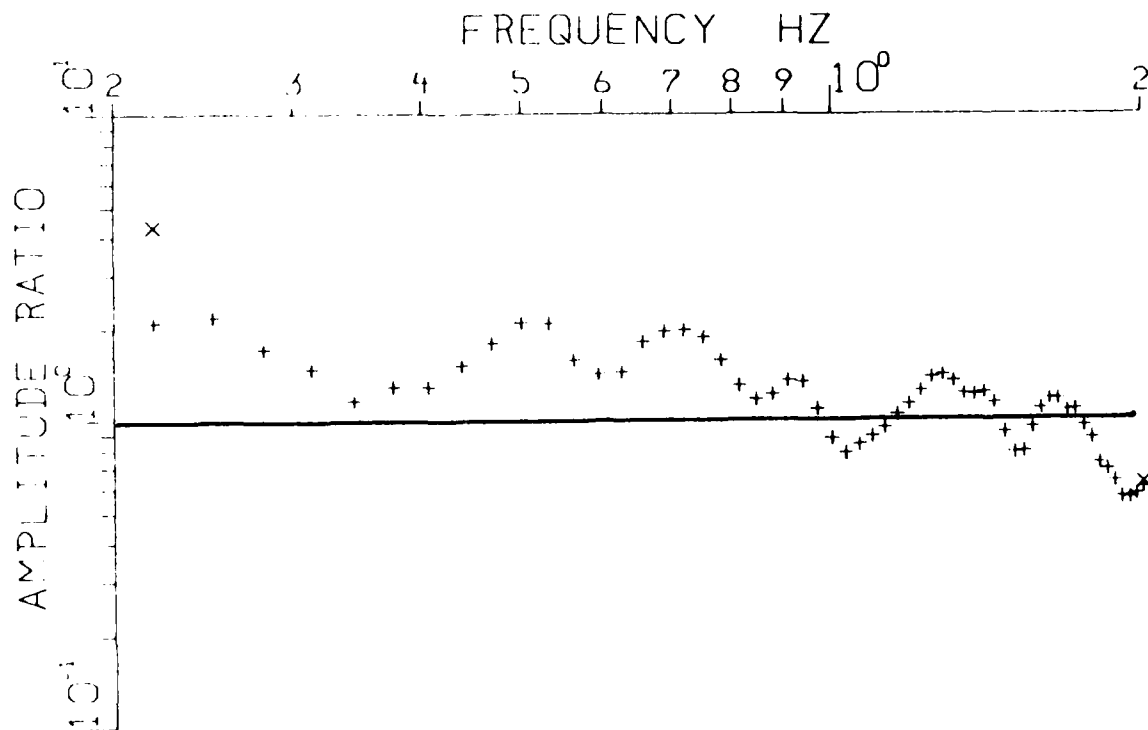


Figure 5.4. Whole record spectral ratio of the 680 and 980 meter depth synthetics. The 680 meter depth source is enhanced in frequencies below 1 Hz.

and depleted in high frequencies (above 1 Hz) with respect to the overburied synthetic.

In order to examine this frequency dependence above 2 Hz and to test the frequency dependence upon distance, three additional narrow bandwidths were examined, 1.25-1.56, 2.50-2.81, and 4.69-5.0 Hz at a distance of 320 km. A comparison of the whole record spectra are shown in Figure 5.5. The average log-amplitudes for the three bandwidths show that for the two 0.31 Hz bands centered on 1.41 and 2.66 Hz, the two depths of burial are indistinguishable. However, at the highest band centered at 4.85 Hz, the 680 meter depth of burial synthetic is depleted by a factor of 2 with respect to the 980 meter depth synthetic. The two spectral averages are distinct at the 2 σ confidence level. The time domain seismogram limited to the 4.69 to 5 Hz bandwidth indicates that the energy is predominately P with high group velocities. This result is qualitatively consistent with the far-field P spectra of Section 4.3.2 that demonstrated that the far-field P wave from the over buried simulation was enriched in high frequencies in accordance with cube-root depth scaling.

In order to examine the excitation differences below 2 Hz that can not be explained by cube-root depth scaling of point explosion sources, we computed point explosion Green's functions for a range of depths. From symmetry arguments, we can argue that the 2D axisymmetric source may to lowest order be represented by a vertical force, F_z , and a moment tensor with three non-zero elements, M_{xx} , M_{yy} , and M_{zz} . The axisymmetric source has $M_{xx}=M_{yy}$. The explosion part is given by $M_I = (M_{xx} + M_{yy} + M_{zz})/3 = 2/3 M_{xx} + 1/3 M_{zz}$. The non-isotropic part is given by $M_{CLVD} = M_{xx} - M_{zz}$, and is termed the compensated linear vector dipole (CLVD). It is equivalent to vertical tension compensated by horizontal compression. Alternatively, the CLVD source is equivalent to the superposition of two 45° thrust faults with fault strikes oriented at 90° to each other. It should be emphasized that these three "canonical" sources, F_z , explosion, and CLVD, are only the first three terms in an infinite expansion that is guaranteed to converge only at low frequencies (wavelengths longer than the source dimensions).

Conservation of linear momentum guarantees that F_z has no net value (low frequency). Day, *et al.* (1983) have argued that in the long wavelength limit, spall can be described by a point force model with negligible low-frequency amplitude. However, the vertical point force and CLVD source from spall may radiate short period waves. The vertical point force arises in the simulations from the gravitational attraction that keeps the grid from flying off into space. This force can be computed directly from the monitored tractions and displacements on the cylindrical surface and is found to be small compared to the net first order moments. A detailed analysis in terms of these moments will be examined in a future report, so we do not elaborate further on the details of the expansion except to show the Green's functions for the CLVD source as a function of depth compared to the complete 2D axisymmetric synthetics.

Figures 5.6a, b, and c show the complete 2D synthetics (680 meter) compared to the explosion and CLVD Green's functions in three bandwidths of interest. In the 0.5 to 1.25 Hz bandwidth, we see that the 2D synthetic (at bottom) is similar to the explosion Green's function convolved with an RDP except for the slow arriving surface

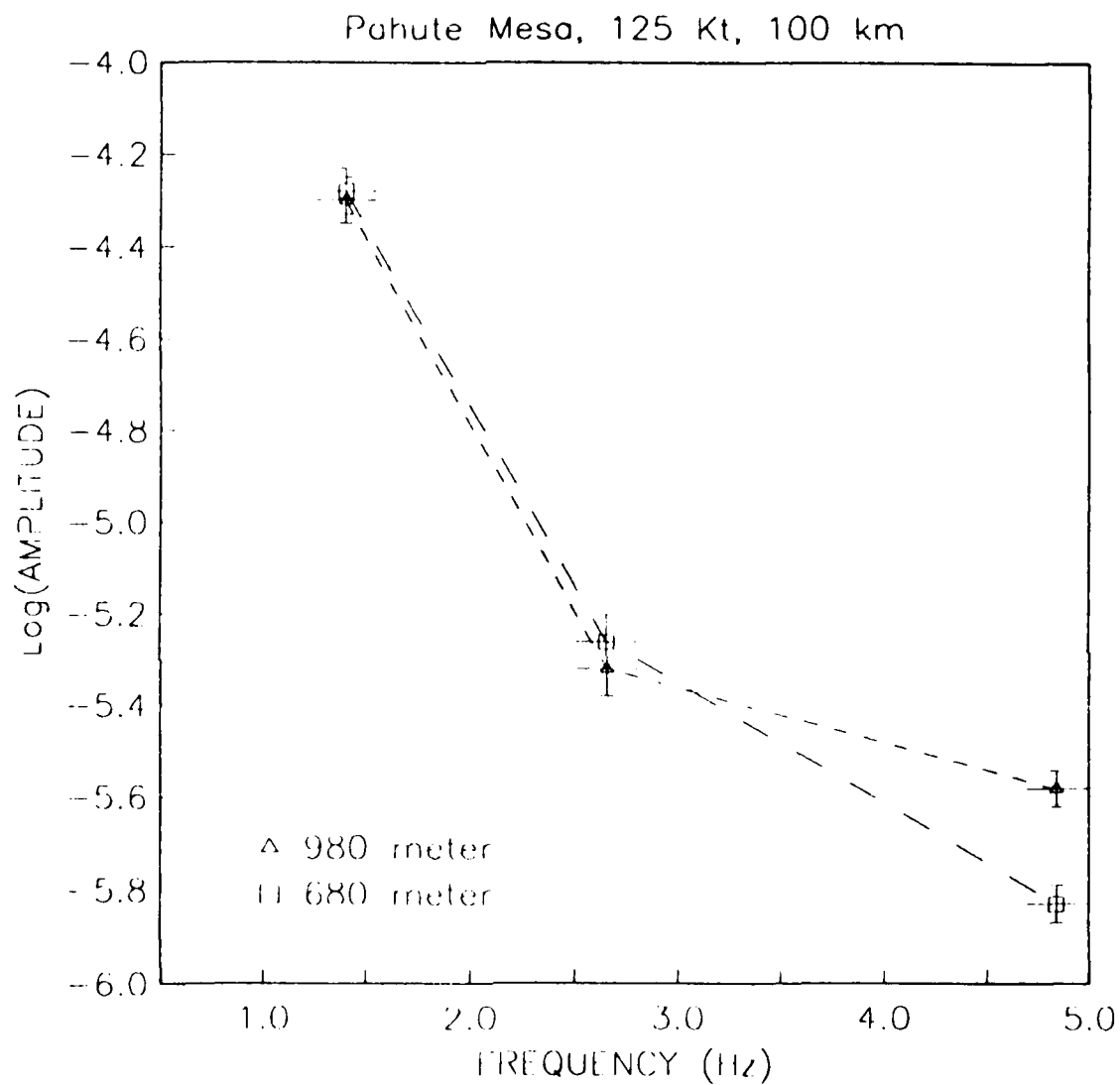


Figure 5.5.

Average spectral levels of synthetics for 680 and 980 meter depth sources in three frequency bands. The two depths of burial are indistinguishable at 1.4 or 2.5 Hz. The 980 meter synthetic is enriched for frequencies above 4.5 Hz with respect to the 680 meter synthetic.

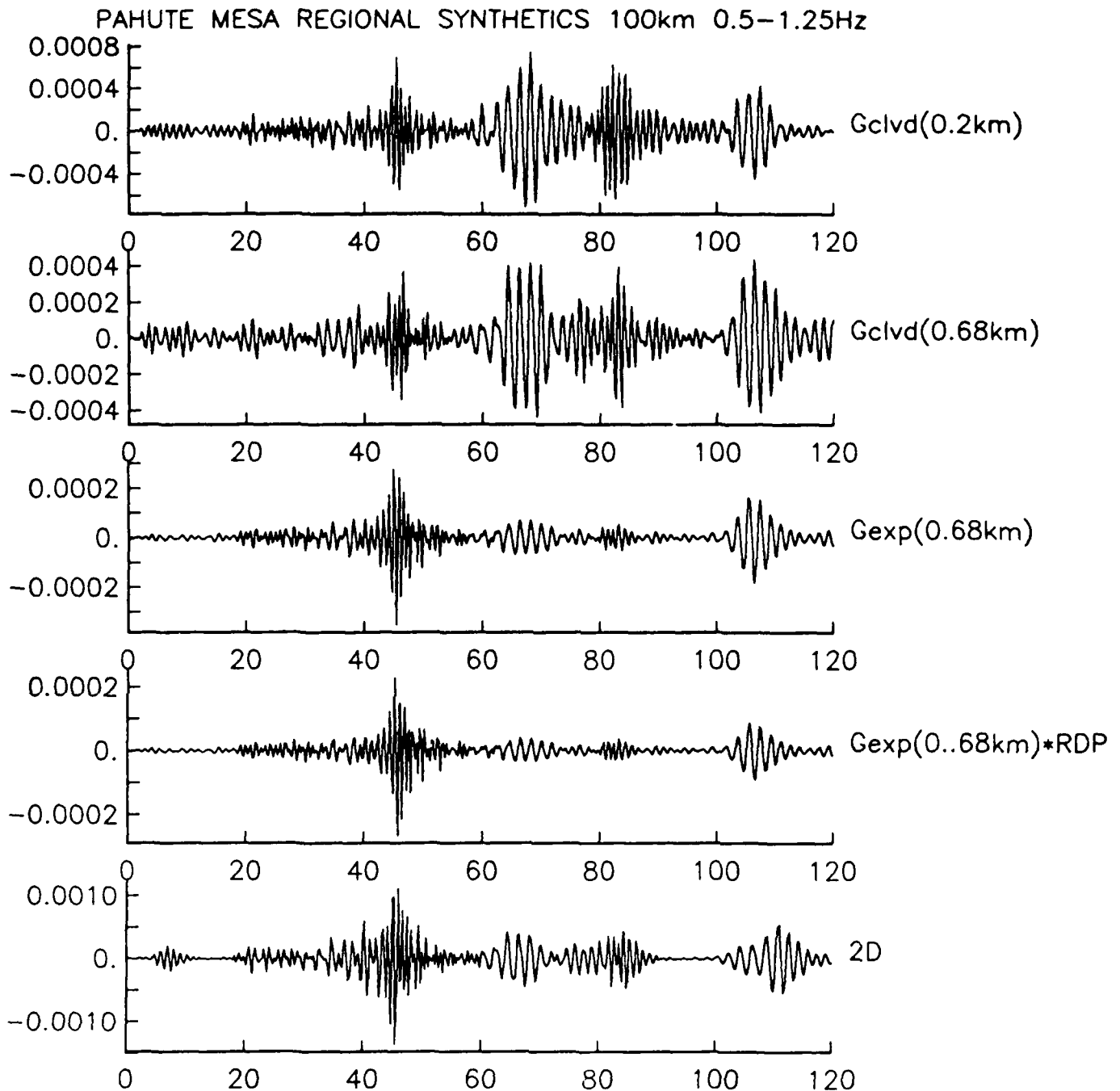


Figure 5.6a. Bandpass filtered synthetics and Green's functions in the 0.5 to 1.25 Hz bandwidth. From bottom to top; 2D 680 meter depth synthetic, the 1D synthetic at 680 meters, the explosion Green's function for a source at 680 meters, the CLVD Green's function for a source at 680 meters, and a CLVD Green's function for a source at 200 meters depth. Note, that the late arriving surface waves are best excited by a CLVD source and are not adequately excited by an explosive source at the working point.

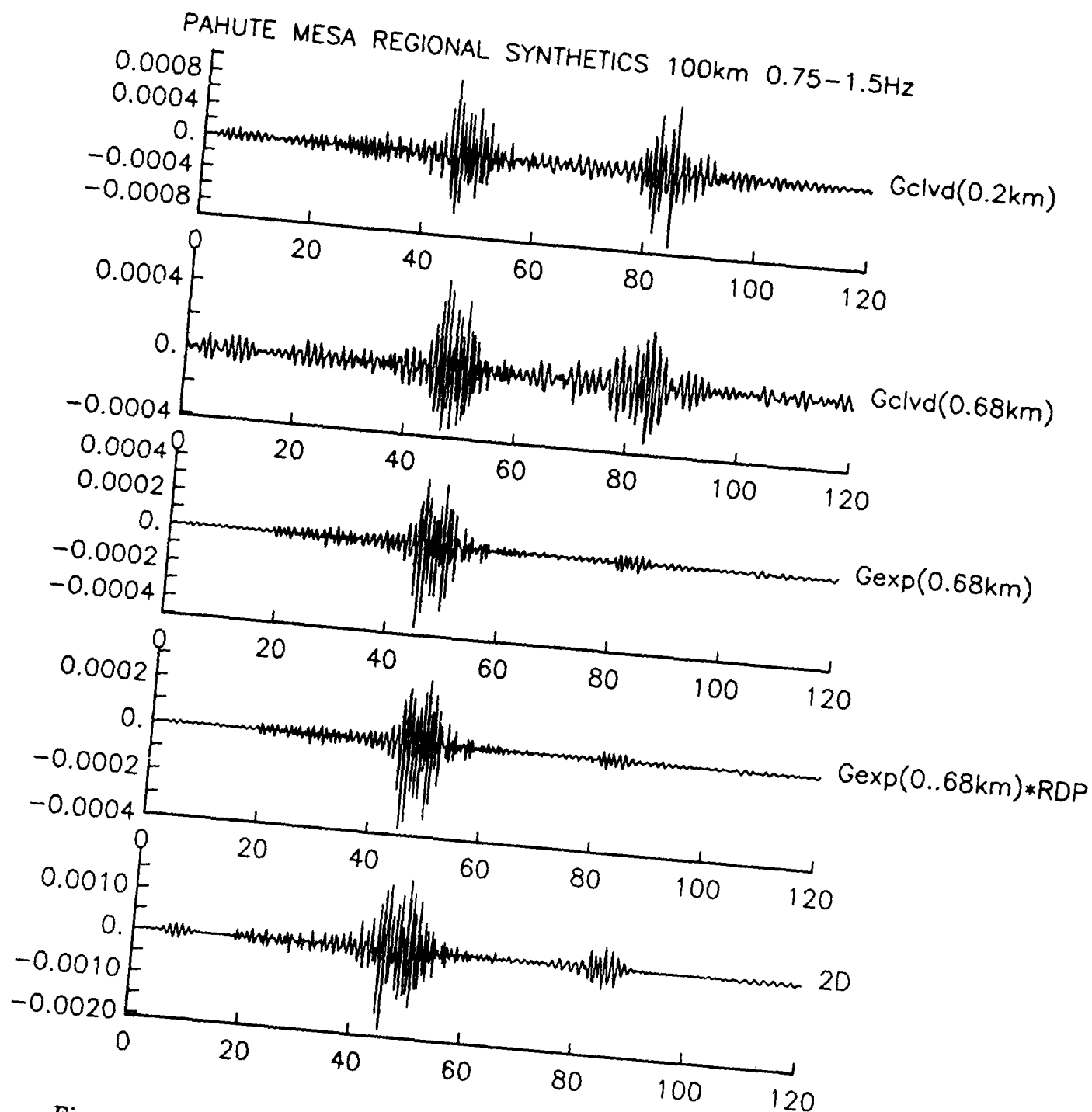


Figure 5.6b.

Bandpass filtered synthetics and Green's functions in the 0.75 to 1.50 Hz bandwidth. From bottom to top; 2D 680 meter depth synthetic, the 1D synthetic at 680 meters, the explosion Green's function for a source at 680 meters, the CLVD Green's function for a source at 680 meters, and a CLVD Green's function for a source at 200 meters depth. Note, that the late arriving surface waves are best excited by a CLVD source and are not adequately excited by an explosive source at the working point.

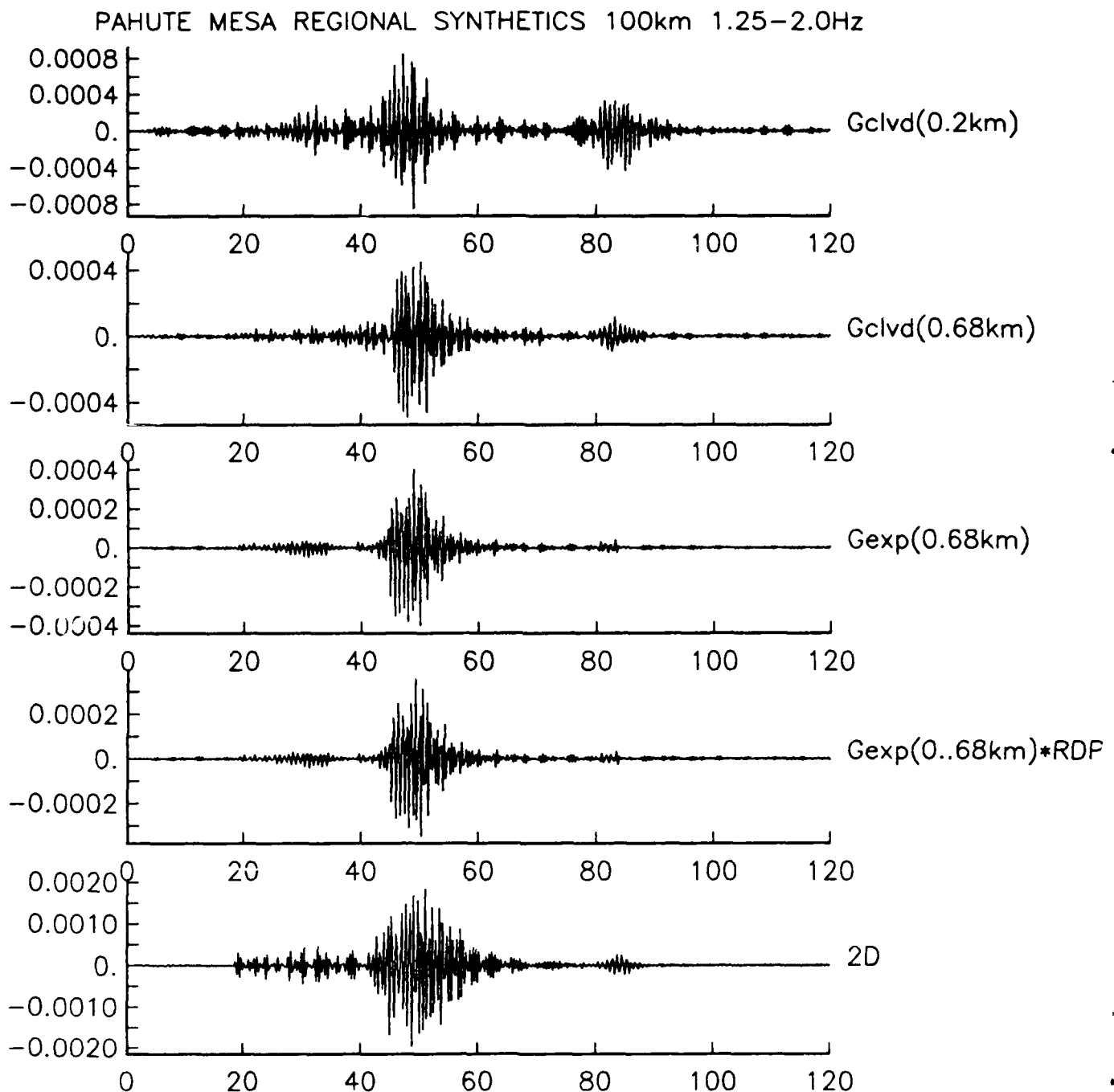


Figure 5.6c. Bandpass filtered synthetics and Green's functions in the 1.25 to 2.0 Hz bandwidth. From bottom to top; 2D 680 meter depth synthetic, the 1D synthetic at 680 meters, the explosion Green's function for a source at 680 meters, the CLVD Green's function for a source at 680 meters, and a CLVD Green's function for a source at 200 meters depth. Note that neither the point explosion nor the CLVD's excite the Pg wavetrain observed in the 2D synthetic. The Lg wavetrain is also longer than either the point explosion or the CLVD Green's function.

waves and some energy at 40 seconds. The CLVD Green's functions for depths of 680 and 200 meters are rich in energy at these times and weak at other arrival times. Clearly the CLVD source is an efficient low phase velocity SV radiator without producing substantial Pg waves or the surface waves that arrive at 45 to 50 seconds. In the 0.75 to 1.5 Hz and 1.25 to 2.0 Hz bandwidths we see that the explosion Green's function can account for the majority of the 2D synthetic except for the surface wave that arrives at 80 seconds and some of the high frequency impulsive arrivals in the Pg coda (20 to 40 seconds). The CLVD source is an efficient radiator for the surface wave arriving at 80 seconds. A shallow CLVD source (200 meters) is an even better radiator than a deeper source (680 meters).

Consequently, we can see that the 2D synthetics differ from a simple explosion point source. It is not possible to model the 2D explosion source with a single explosion Green's function convolved with an RDP. The relative excitation of Pg, Lg, and surface modal waves as a function of frequency demonstrate that a higher order description of the source beyond a point explosion is necessary. The normal buried source is enriched in shallow modal excitation at low frequencies (below 12 Hz) relative to either a point source or the overburied source. The deeper source is enriched in high frequencies in the Lg (above 1 Hz) and Pg (above 4 Hz). The enrichment of high frequency P waves for overburial is consistent with cube-root depth scaling.

The very simple examination of the CLVD Green's functions compared to the 2D synthetics indicates that a superposition of CLVD and explosion sources may model much of the observed excitation behavior of the 2D synthetics. The CLVD source would have a different spectral content (and therefore time function) that provides the enhancement of the shallow source with respect to the deeper source in the 0.5 to 1.5 Hz bandwidth. An obvious physical mechanism for this "signal" is the spall behavior of the sources as a function of scaled depth. The deeper source has less spall; the spall signal is weaker and shorter in duration. Asymmetrical expansion of the source such as less (or more) expansion in the horizontal direction than the vertical direction could also result in a net CLVD component to the source.

As was pointed out earlier, the Pahute Mesa simulations exhibited spall, but it was confined to a weak shallow surface layer. Observations indicate that spall typically occurs at greater depths than in the simulations, therefore, we would expect that the spall signal would be larger in reality than was predicted by the 2D calculations. The CLVD source is an efficient radiator of P waves at steep angles of incidence and a weak P-wave radiator at shallow angles of incidence. Therefore, a larger CLVD may be the source component needed to improve the teleseismic P waveform simulations and provide a mechanism that can explain the high/low frequency observations of Murphy and Bennett (1982) and Taylor, *et al.* (1988).

5.3 Shagan River Synthetics

The model used to compute regional synthetics for the Shagan River calculations is listed in Table 5.3, and is taken from Stevens (1986) with the minor addition of a 2 km thick layer identical to that used in the finite difference calculations. For comparison, Figure 5.7 compares the Eastern Kazakhstan P-velocity models of Leith

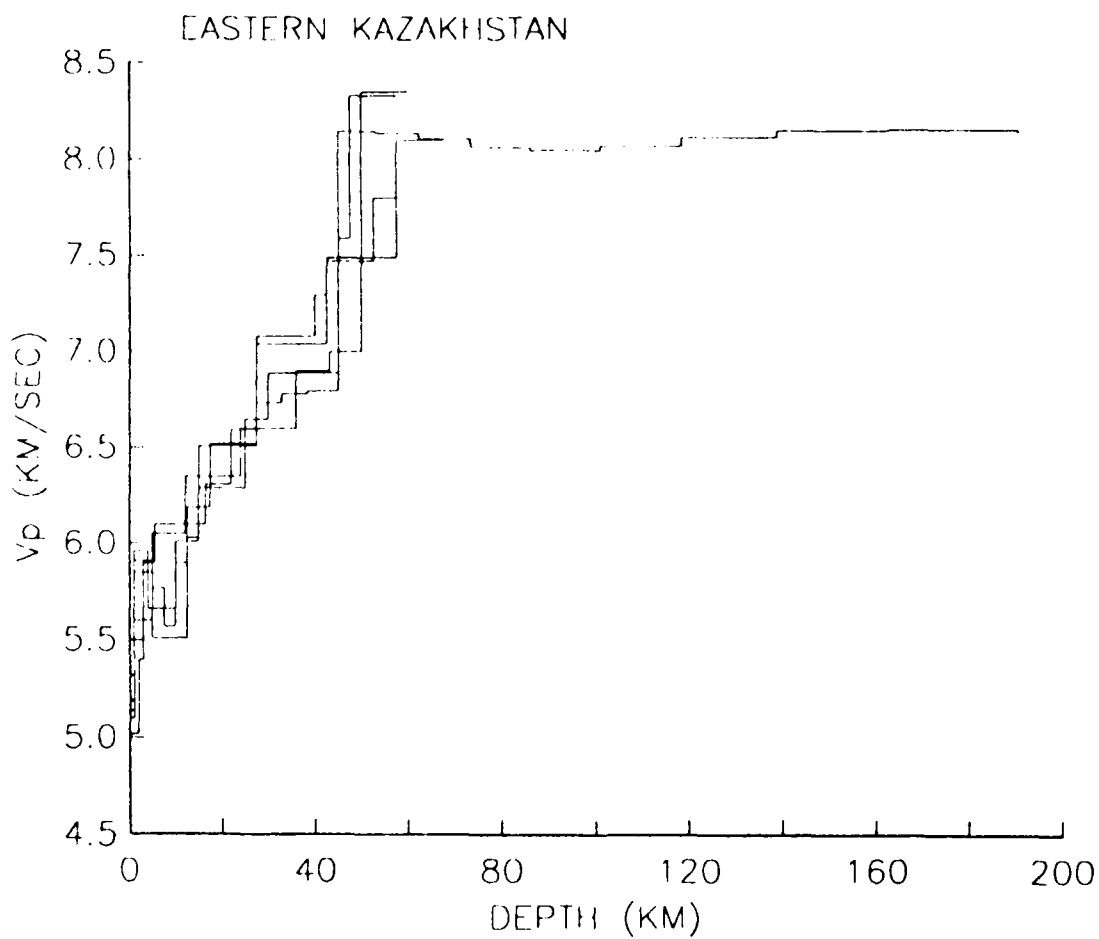


Figure 5.7. Comparison of several velocity models for Eastern Kazakhstan.

(1987), and Priestley, *et al.* (1988) with the Stevens (1986) model. These models are characterized by a thick high velocity crust and a high velocity sub-Moho velocity. The Priestley, *et al.* crustal models, based on vertical-to-radial teleseismic P-wave transfer functions, are characterized by nearly continuous crustal velocity gradients. Leith's model, based on Soviet published regional refraction profiles, is similar to the Priestley, *et al.* models with no prominent "Conrad" discontinuity. Stevens' model based on inversion of explosion generated waves recorded at MAIO, and other published Soviet profiles places most of the crustal velocity increase in a mid-crustal transition zone.

TABLE 5.3 Eastern Kazakhstan Structure
Modified from Stevens (1986)

h(km)	α (km/s)	β (km/s)	ρ (gm/cc)	Q_μ	depth
2.	5.02	2.79	2.7	100.	0
1.	5.4	3.0	2.7	150.	2
2.488	5.9	3.3	2.7	200.	3
10.976	6.1	3.4	2.7	600.	5.488
5.488	6.308	3.541	2.702	525.9	16.464
5.488	6.597	3.703	2.807	500.	21.952
5.488	6.736	3.781	2.858	450.	27.44
5.564	6.782	3.807	2.875	400.	32.928
6.504	6.795	3.814	2.879	350.	38.492
8.006	8.147	4.573	3.372	179.5	44.996
9.359	8.138	4.568	3.369	167.5	53.002
10.94	8.106	4.55	3.358	159.4	62.361
12.78	8.065	4.527	3.343	153.8	73.301
14.95	8.047	4.517	3.336	150.3	86.081
17.47	8.07	4.53	3.345	148.7	101.031
20.42	8.117	4.556	3.361	148.1	118.501
23.88	8.154	4.577	3.375	147.9	138.921
27.91	8.161	4.581	3.378	147.4	162.801
32.63	8.145	4.572	3.372	146.8	190.711
38.14	8.12	4.558	3.363	146.2	223.341
∞	8.101	4.547	3.356	145.8	261.481

The synthetics for an epicentral distance of 100 km are shown in Figures 5.8a and b. As with the Pahute Mesa synthetics of the previous section, each 2D calculation is paired with a 1D calculation. The largest amplitude phase on the broadband as well as bandpass filtered seismograms (Figures 5.9a, b, and c) up to about 1.2-1.4 Hz, is a fundamental mode (LR long-period or Rg short-period) Airy phases with group velocities between 2.7 and 3.0 km/s. The impulsive direct crustal P (Pg) wave is followed by SV arrivals with "group" velocities between 3.5 and 2.7 km/s. Maximum amplitudes from the bandpass filtered seismograms of Figures 5.9 and Fourier spectra are compared in Figures 5.10a, b, and c.

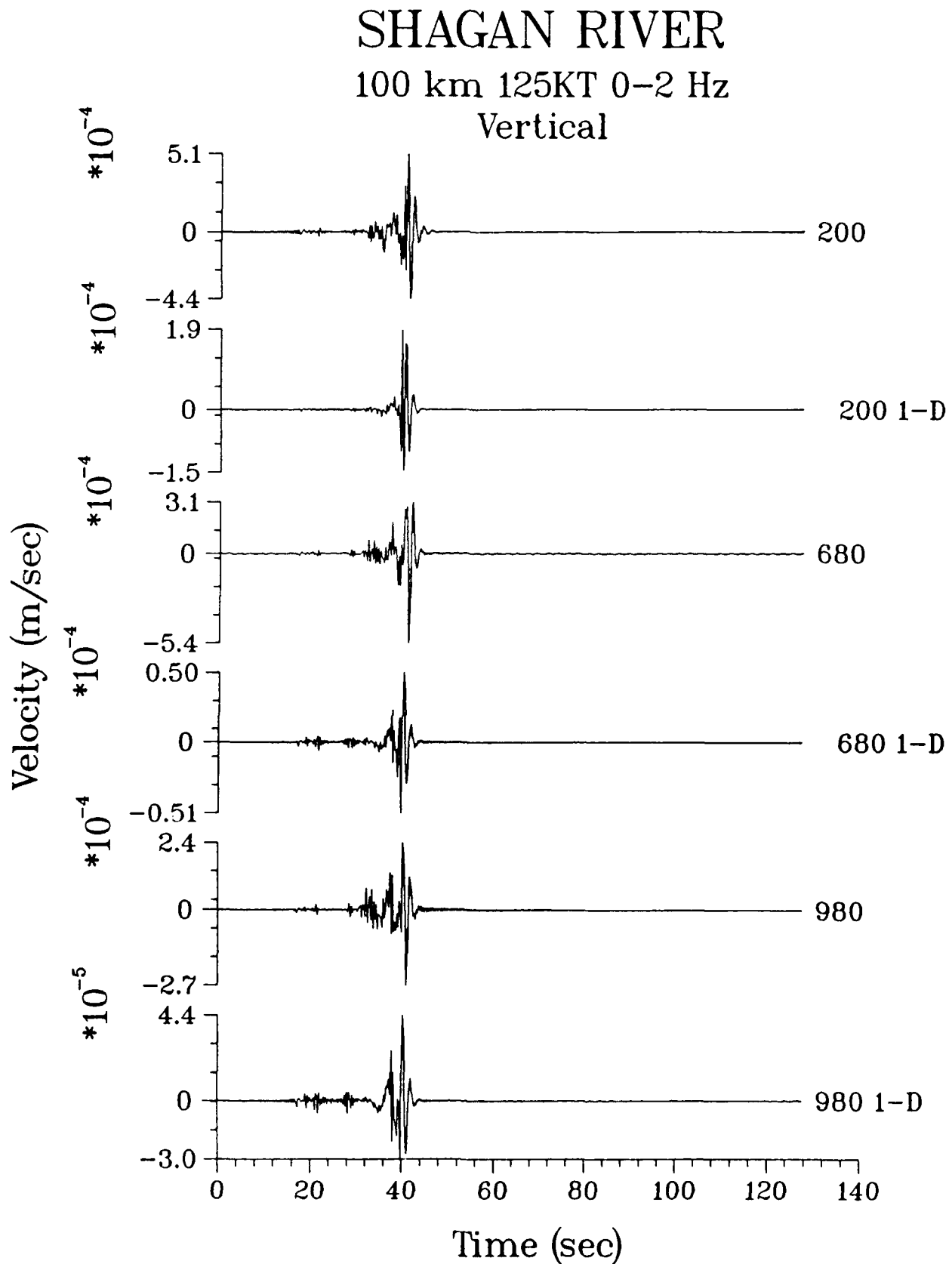


Figure 5.8a.

Broadband velocity synthetics for the Shagan River calculations at 200, 680, and 980 meter depths. 2D and 1D synthetics are displayed together for comparison. Vertical component, 100 km, 0 to 2 Hz bandwidth.

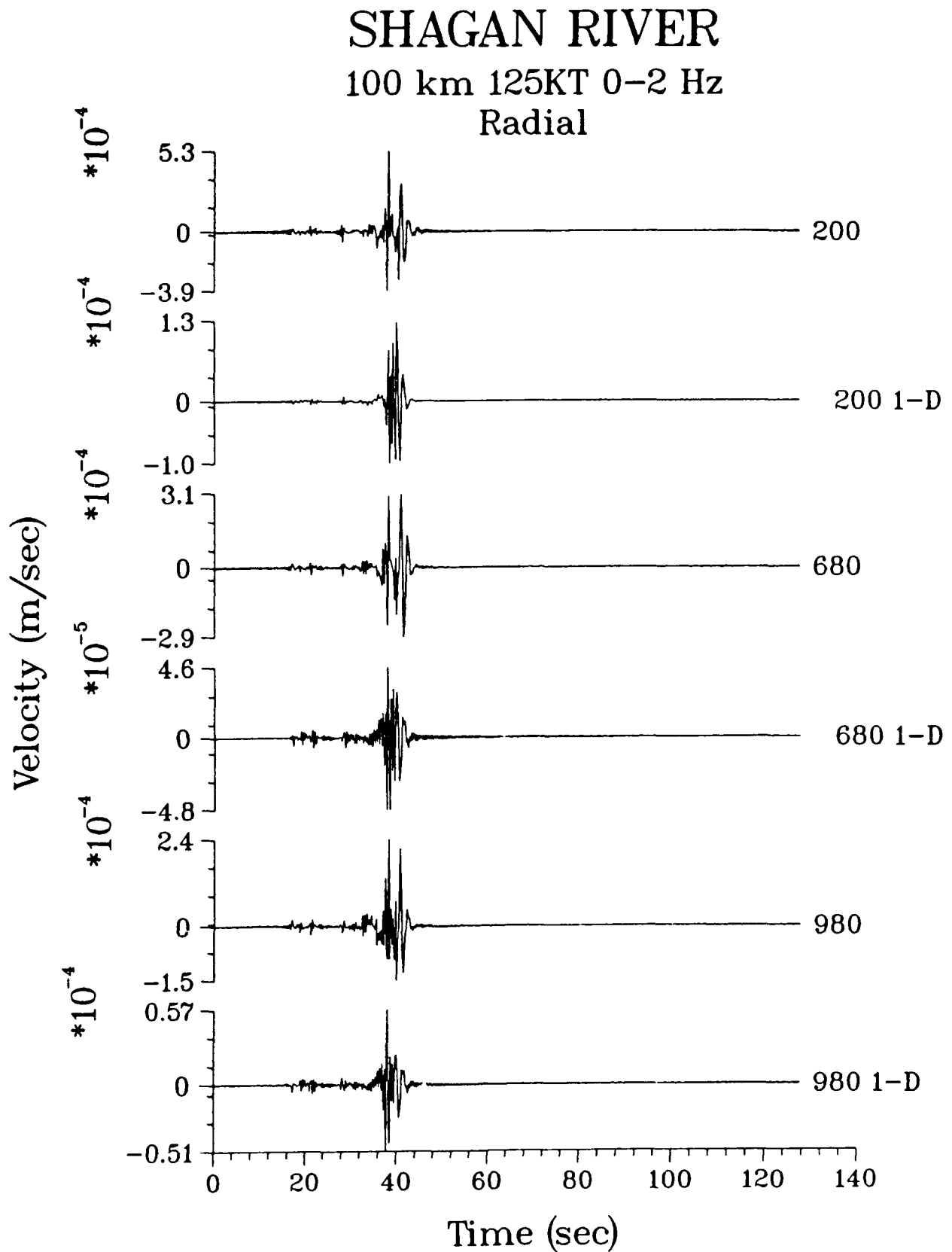


Figure 5.8b.

Broadband velocity synthetics for the Shagan River calculations at 200, 680, and 980 meter depths. 2D and 1D synthetics are displayed together for comparison. Radial component, 100 km, 0 to 2 Hz bandwidth.

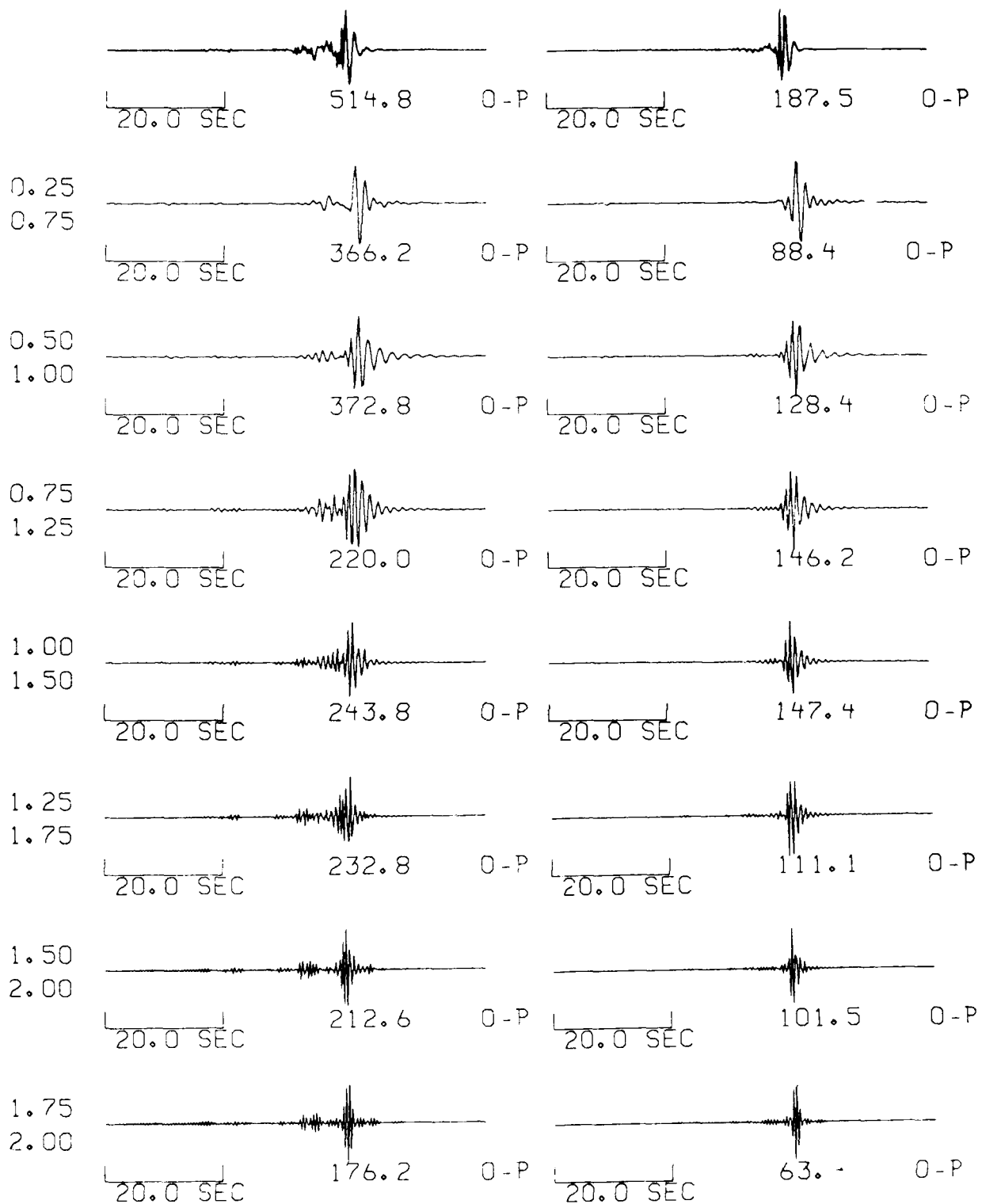


Figure 5.9a. Bandpass filtered Shagan River 2D synthetics (left) and 1D synthetics (right) for depth of 200 meters. Bandwidths are indicated to the left.

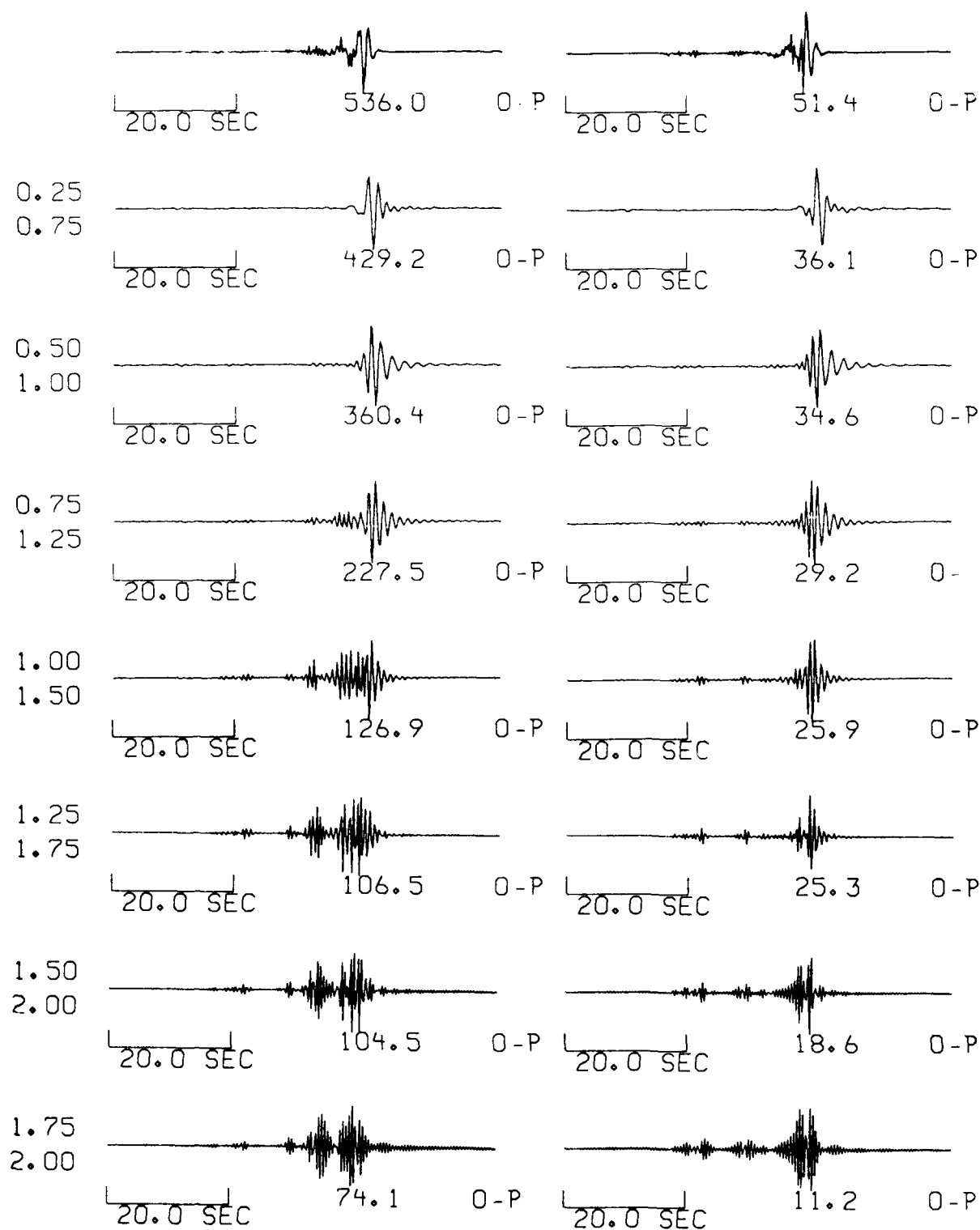


Figure 5.9b. Bandpass filtered Shagan River 2D synthetics (left) and 1D synthetics (right) for depth of 680 meters. Bandwidths are indicated to the left.

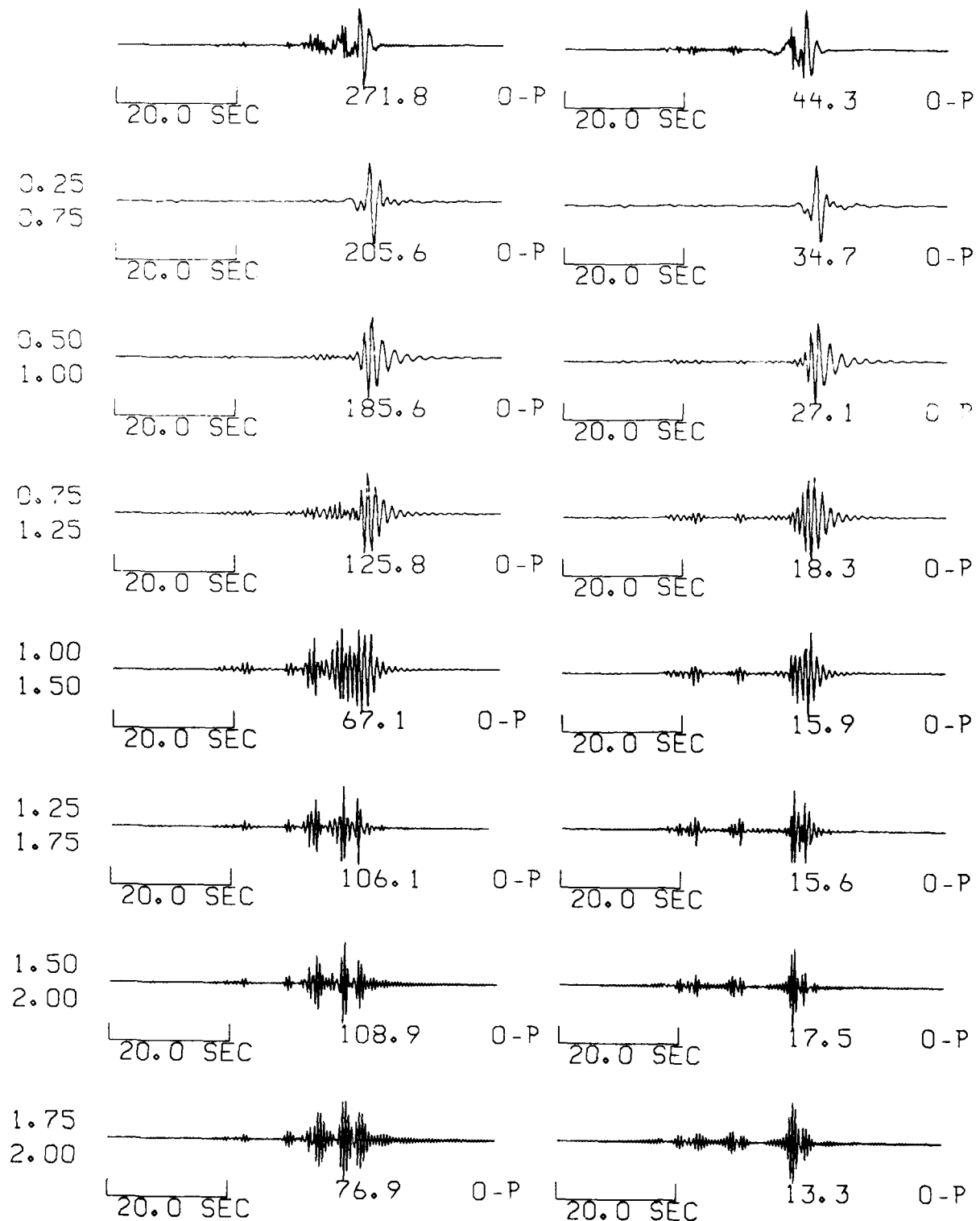


Figure 5.9c. Bandpass filtered Shagan River 2D synthetics (left) and 1D synthetics (right) for depth of 980 meters. Bandwidths are indicated to the left.

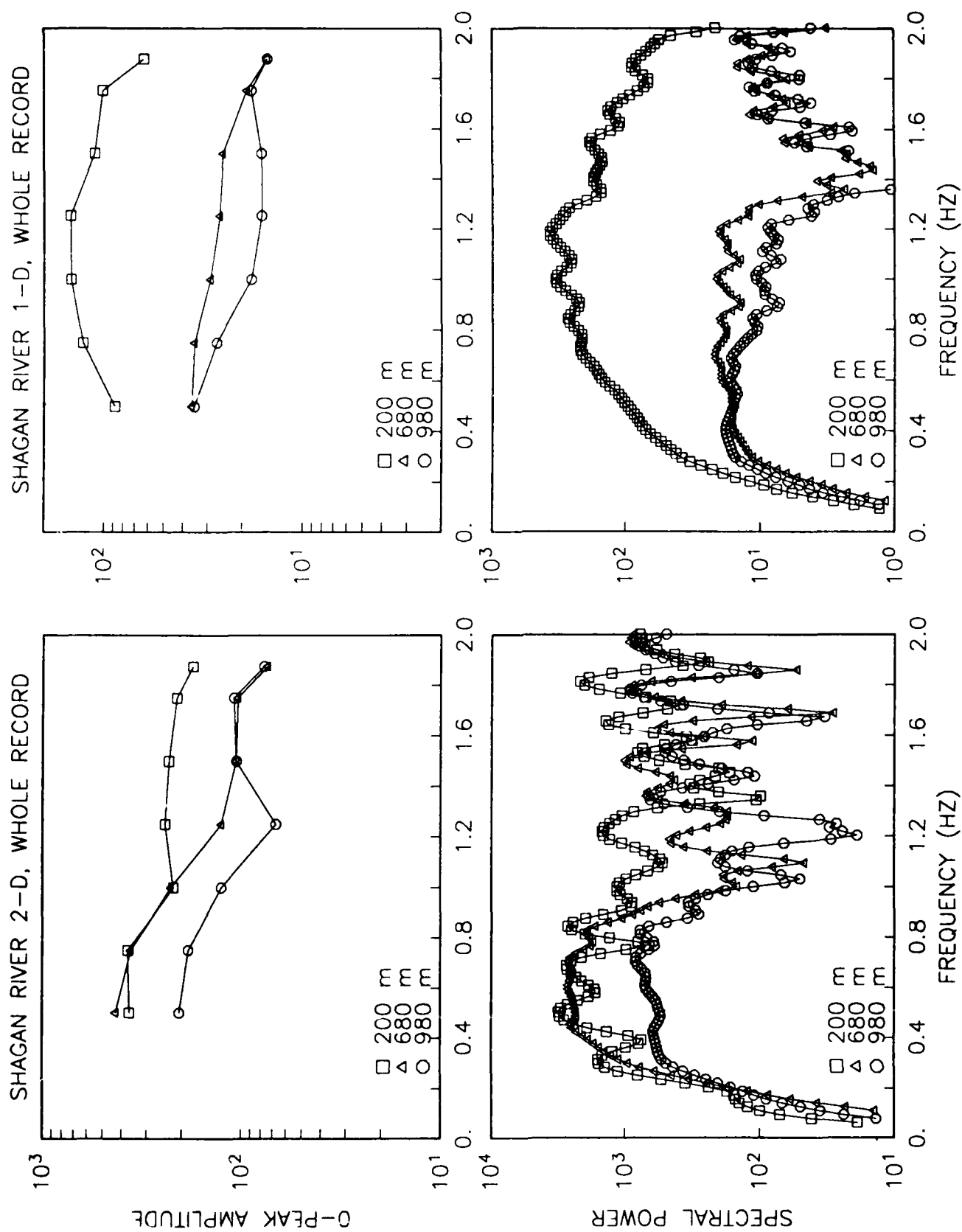


Figure 5.10a. Whole record narrow band peak amplitudes (top) versus spectral power (bottom) and 2D (left) versus 1D (right).

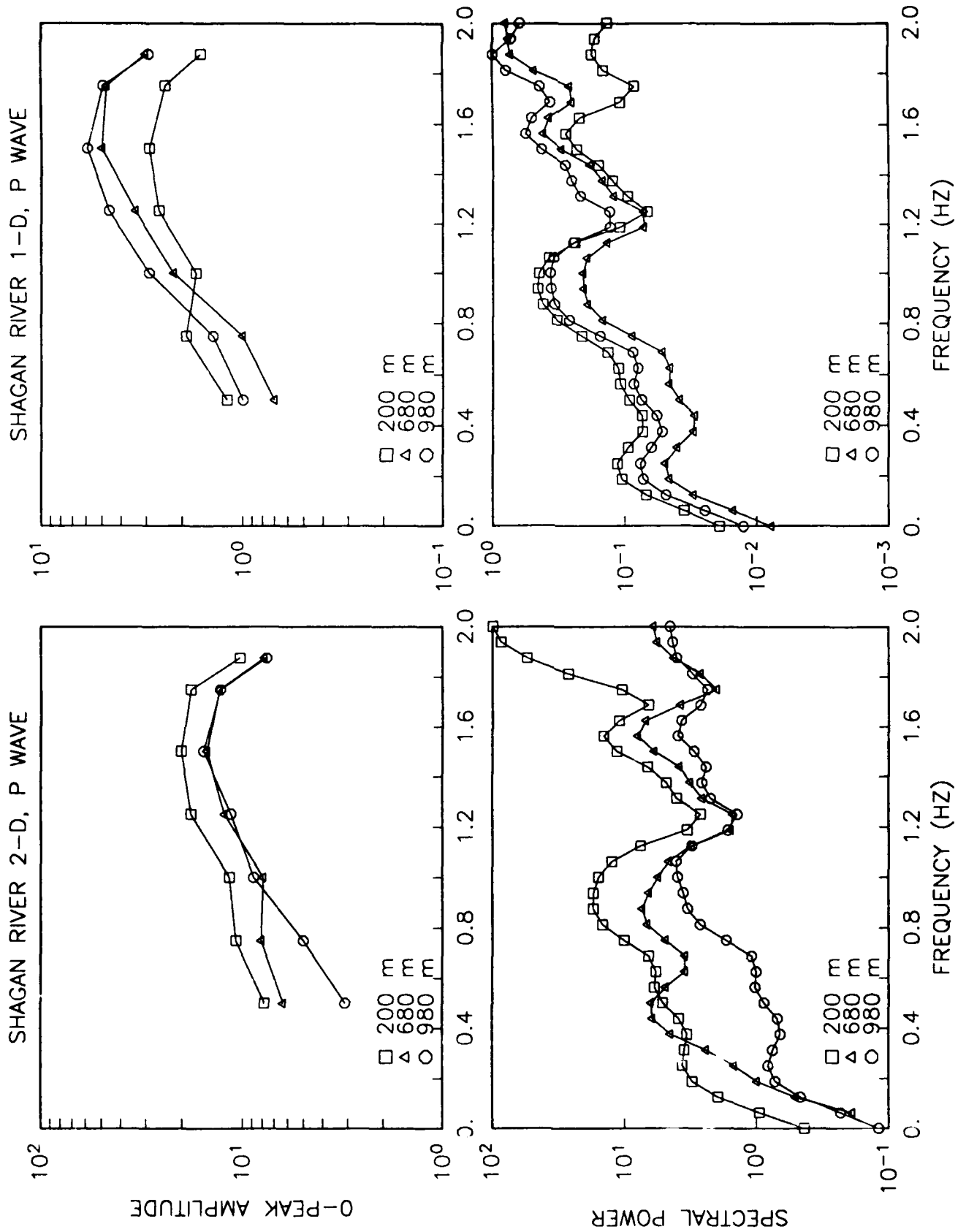


Figure 5.10b. P-wave narrow band peak amplitudes (top) versus spectral power (bottom) and 2D (left) versus 1D (right).

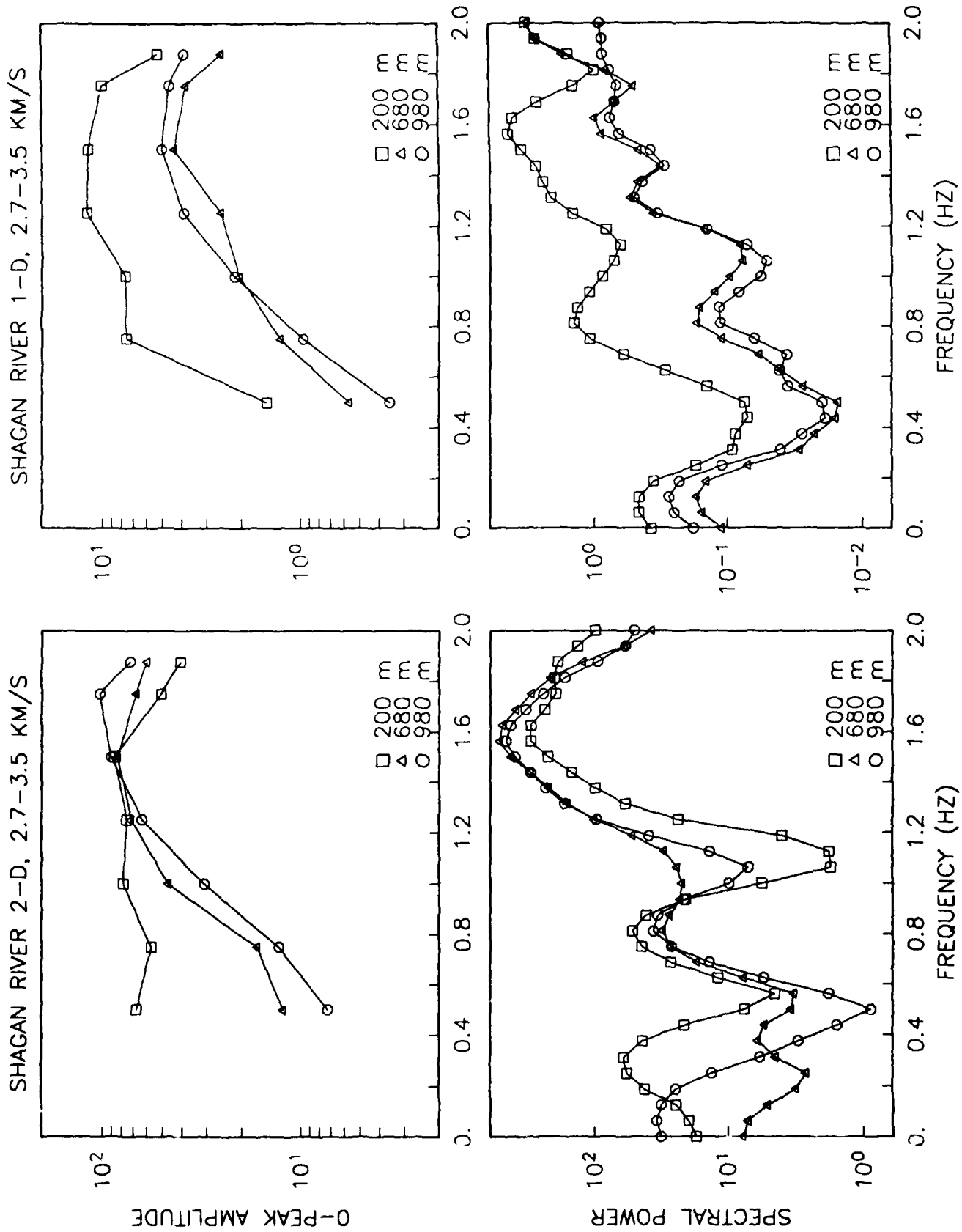


Figure 5.10c. SV-Lg window (2.7-3.5 km/s) narrow band peak amplitudes (top) versus spectral power (bottom) and 2D (left) versus 1D (right).

The whole record spectra largely reflect the time-domain peak amplitudes and are dominated by the fundamental mode Rayleigh up to 1.0 Hz for the 2D or 1.2 Hz for the 1D synthetics at depths of 680 and 980 meters. The 200 meter depth synthetics are dominated by the fundamental up to 1.5 Hz for the 2D synthetic and up to the 2 Hz Nyquist frequency for the 1D synthetic. The large amplitude of the 1D 200 meter depth synthetic is a product of a large 1D moment (a factor of 2 over the 980 meter synthetic) and strong depth dependence for the excitation function of the fundamental mode elastic Green's function. Clearly, the 1D synthetic demonstrates the short comings of the point explosion source model for the cratering explosion in this structure. The differences between the 2D and 1D contained synthetics (680 and 980 meters) are more subtle. The prominent "notch" in the whole record spectra about 1.0 Hz in the 2D synthetics is at 1.4 Hz in the 1D synthetics. This notch occurs where the fundamental mode amplitude decreases as a function of increasing frequency and declines below the level of the higher modes and SV body waves which are increasing with frequency. Obviously this "notch" will be a complicated function of burial depth, event size (hence corner frequency), and distance (hence differential attenuation of modes and body waves). The peak amplitudes taken from the whole record do not show this spectral "notch" nearly as well as the power spectrum because the signal power spectra is dispersed in the time domain as several arrivals.

The P and SV window spectra and amplitudes are shown in Figures 5.10b and c. The 2D P-wave spectra and time domain peak amplitudes illustrate that the 680 meter depth synthetics have an enhancement (about a factor of 2) in the 0.4 to 0.8 Hz bandwidth with respect to the 980 meter depth synthetics. This is not the case for the 1D elastic synthetics which show a nearly constant amplitude offset between the two source depths of about 40% up to 1.6 Hz. The 1D spectra simply reflect the cube-root depth scaling of the 1D RVP's. This is clearer when we plot the 2D spectra referenced to the 1D spectra in Figure 5.11. Only the two depths, 680 and 980 meters, are shown. First, note that the P-wave low frequencies for the 680 meter depth event are enhanced with respect to the 980 meter depth event. Both contained P-waves show a tendency for there to be a loss of high frequencies above 1.6 Hz. Second, note that the 680 meter depth event whole record spectra show an enhancement in the 0.2 to 0.8 Hz frequency bandwidth. There is little systematic difference between the two whole record spectra above 1.0 Hz. Third, the SV wavetrain (2.7-3.5 km/s) spectra show little difference between the two depths of burial. The 2D synthetics are enhanced in the 1.2 to 1.6 Hz frequency bandwidth with respect to the 1D explosion source model.

As with the Pahute Mesa synthetics, we present in Figures 5.12a, b, and c, a comparison at three bandwidths of the 2D synthetic with the explosion and CLVD Green's functions. In the 0.5 to 1.25 Hz bandwidth, there is an apparent delay in the fundamental Rayleigh wave of the 2D source with respect to the explosion or CLVD Green's functions. Actually this represents the lower frequency nature of the 2D fundamental relative to the 1D point source model. There can not be much CLVD in the 2D synthetic in this frequency band. In the 0.75 to 1.5 Hz bandwidth, the 2D synthetic has arriving energy in the 30 to 40 second time window that is absent in the explosion Green's function and easily accounted for by a CLVD source. In the 1.25 to 2.0 Hz bandwidth, the arrivals in the 30 to 40 second window can easily be explained

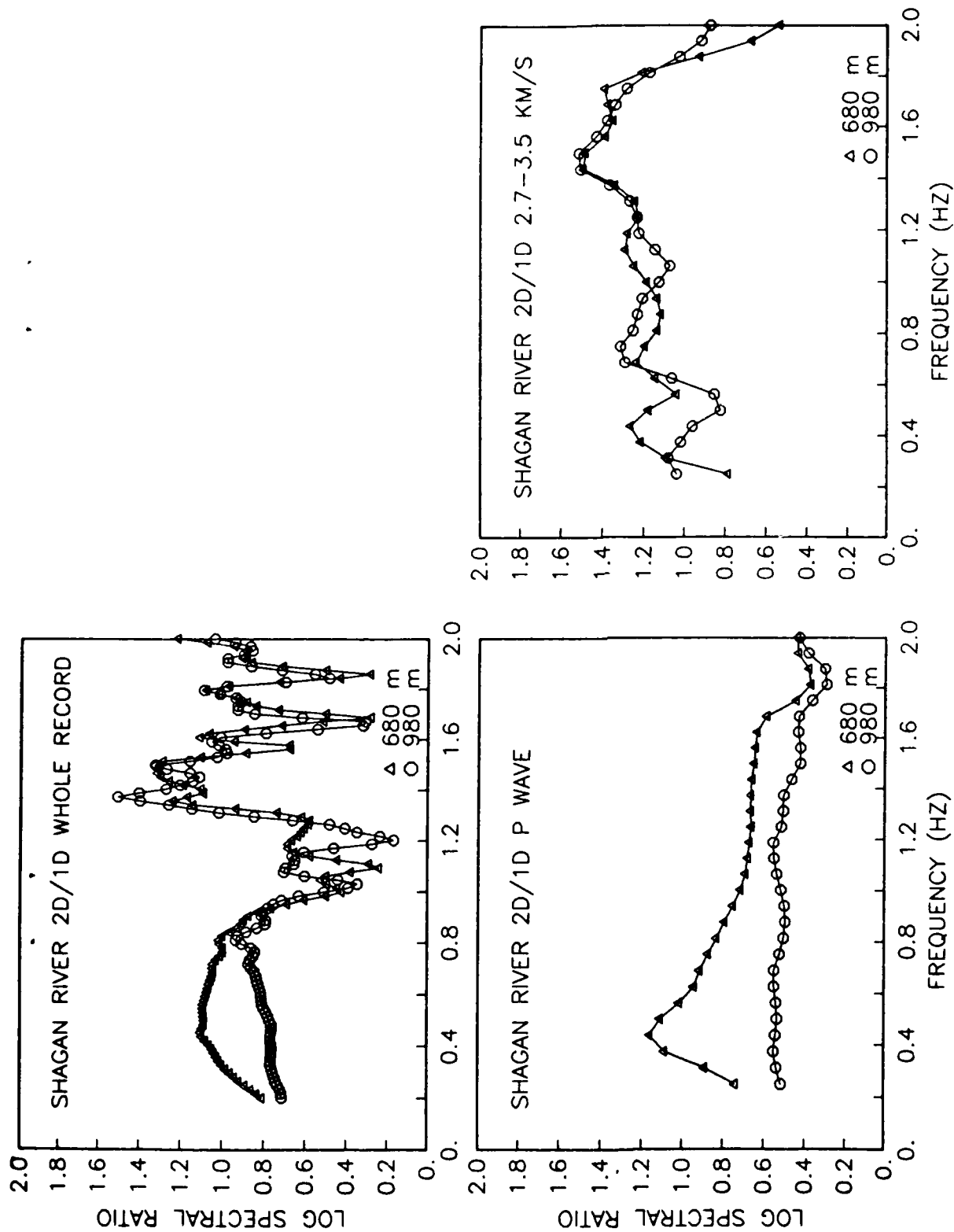


Figure 5.11.

Log spectral ratio of 2D to 1D spectra for the whole record, P-wave, and SV-Lg windows. The whole record spectral ratios are dominated by the fundamental excitation of the 2D and 1D synthetics. The P-wave shows the low frequency enhancement of the 680 versus the 980 2D synthetic. The SV-Lg window shows little difference between the two depths of burial, although the frequency dependence of the SV-Lg excitation of the 2D versus the 1D sources are apparent.

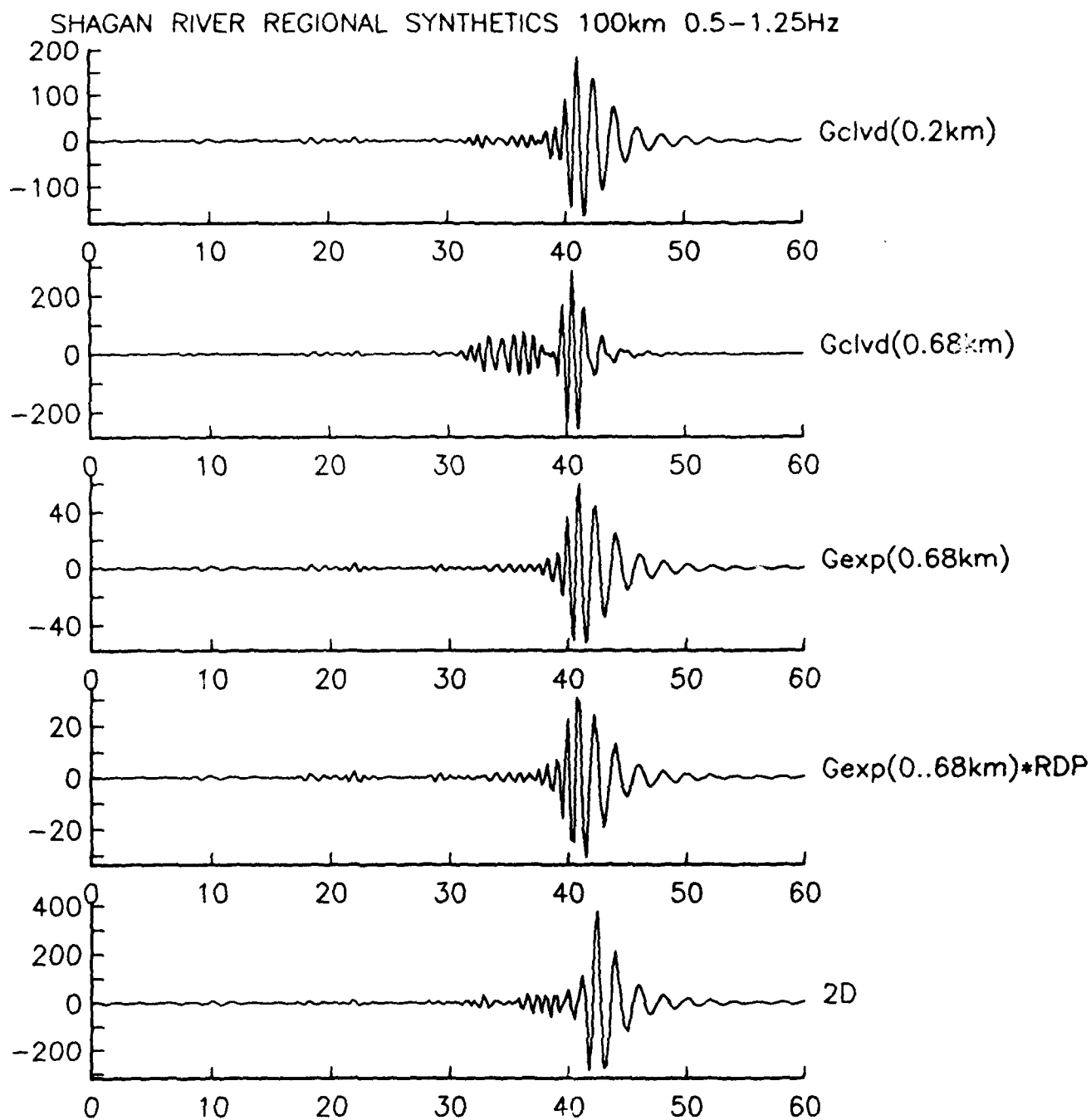


Figure 5.12a. Shagan River 680 meter depth of burial 2D synthetic and several Green's functions in the 0.5-1.25 bandwidth. From bottom to top are: the 680 meter depth 2D synthetic, the 680 meter depth explosion Green's function convolved with the 1D RDP, the 680 meter depth explosion Green's function, the CLVD Green's function at 680 meters depth, and the CLVD Green's function at 200 meters.

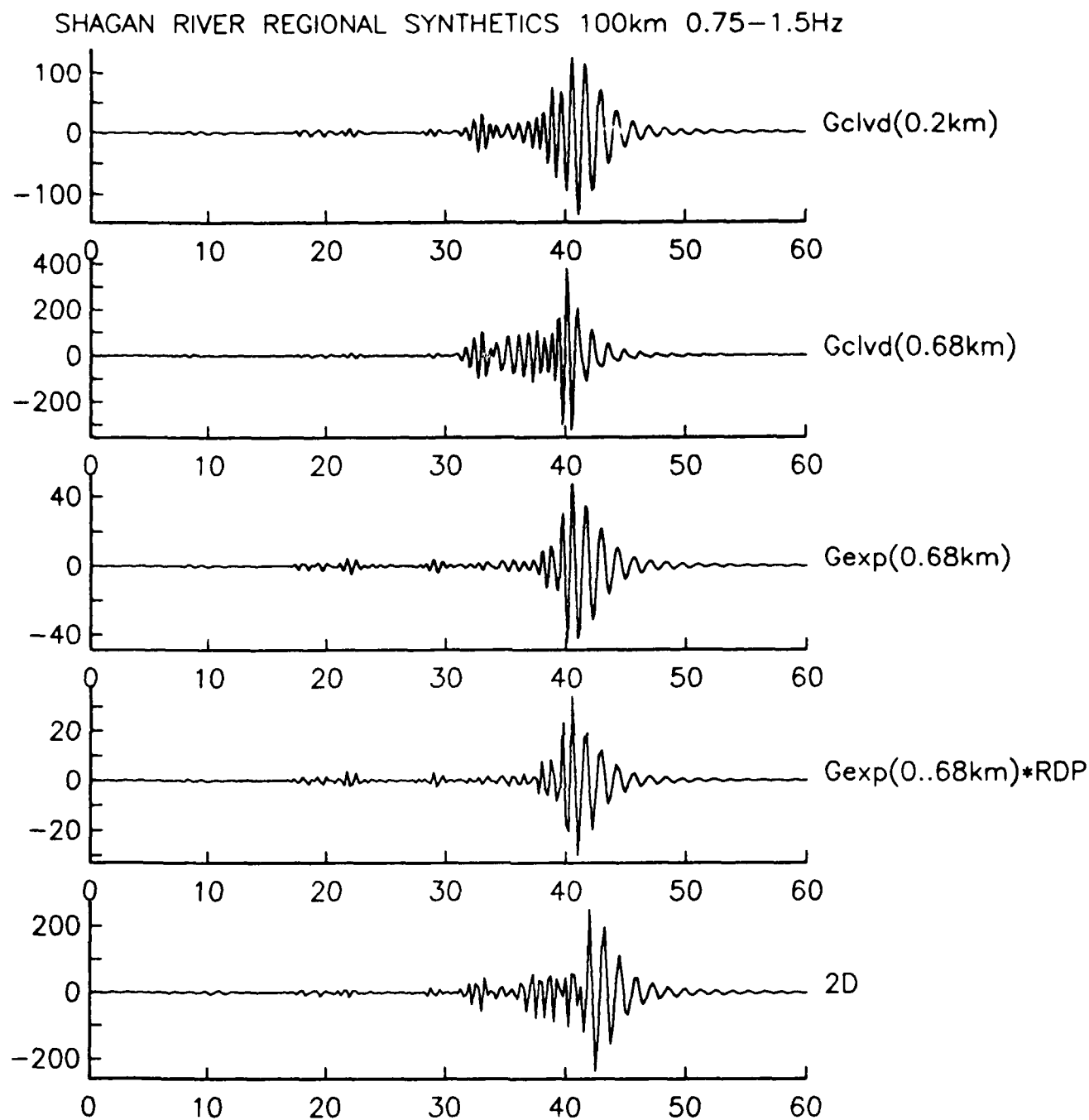


Figure 5.12b. Shagan River 680 meter depth of burial 2D synthetic and several Green's functions in the 0.75-1.5 bandwidth. From bottom to top are: the 680 meter depth 2D synthetic, the 680 meter depth explosion Green's function convolved with the 1D RDP, the 680 meter depth explosion Green's function, the CLVD Green's function at 680 meters depth, and the CLVD Green's function at 200 meters. Note the SV-Lg arrival on the 2D trace that resembles the CLVD Green's function.

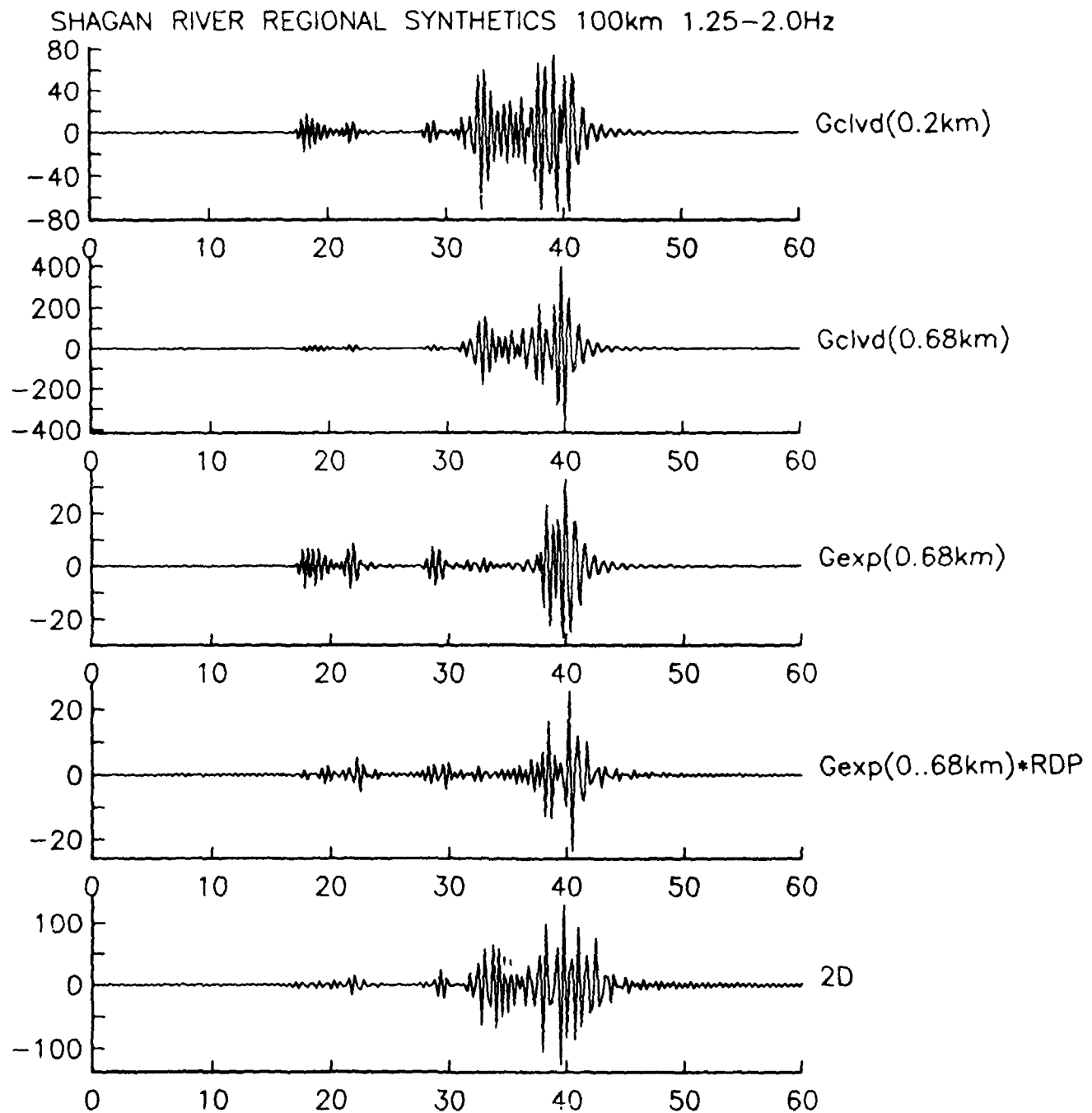


Figure 5.12c. Shagan River 680 meter depth of burial 2D synthetic and several Green's functions in the 1.25-2.0 bandwidth. From bottom to top are: the 680 meter depth 2D synthetic, the 680 meter depth explosion Green's function convolved with the 1D RDP, the 680 meter depth explosion Green's function, the CLVD Green's function at 680 meters depth, and the CLVD Green's function at 200 meters. Note the SV-Lg arrival on the 2D trace that resembles the CLVD Green's function.

with a CLVD source.

To satisfy these observations, the CLVD source must be peaked in the 1 to 2 Hz bandwidth to explain the 2D Shagan River synthetics rather than in the 0.5 to 1 Hz bandwidth as with the Pahute Mesa synthetics. However, the situation is not as simple as with the Pahute Mesa synthetics. There is a need to either reduce the 0.5 to 1 Hz explosion energy relative to the point source or to provide some sort of interference between the point explosion and the CLVD (or higher order moments) in this frequency band. The fundamental energy arriving at 40 seconds is obviously missing in the 2D synthetic relative to the point explosion or the CLVD Green's functions.

In summation, we see that the Shagan River simulations indicate that even a simple source structure may yield a 2D seismogram that can not be properly modeled by a point explosion. The Pg, Lg, and fundamental all show evidence of a complex source. The Lg amplitudes are enhanced relative to the point explosion source, and the Pg and fundamental waveforms show a frequency dependence that suggests interference between multiple sources.

5.4 Prestress - PILEDRIIVER Synthetics

The granite calculations presented here, with and without prestress, have been previously discussed by Day, *et al.* (1986). They synthesized long period teleseismic Rayleigh waves from the results of the finite difference equations and demonstrated that prestress could effectively reduce or reverse Rayleigh waves from an explosion. These finite difference calculations were in effect simulations of the PILEDRIIVER event (61 kt) located in Climax Stock (depth of 463 m) at NTS. Near-field motion was used to constrain the 2D calculations for the non prestress simulations and the results are a set of well constrained calculations that properly model spall as well as the observed near-field RDP estimates.

In addition to the PILEDRIIVER calculation, two calculations were performed corresponding to horizontal non hydrostatic prestresses of 7.5 and 15 MPa (75 and 150 bars). These prestress conditions correspond to a diagonal stress tensor with $\sigma_{xx} = \sigma_{yy} = 7.5$ or 15 MPa, $\sigma_{zz} = 0$, superimposed on the hydrostatic pressure field. Subsequent tectonic stress release due to relaxation in the nonlinear zone of the explosion results in an "explosion" source plus a "tectonic" source. In the long period limit, this composite source is composed of a point explosion with moment tensor proportional to the identity tensor, and a tectonic source with moment tensor proportional to a CLVD. The two sources have different time functions and therefore introduce an interference pattern that is manifested as reversed and phase shifted long period Rayleigh waves.

The near field effects of prestress are readily seen in RDP's estimated from the monitored displacements of the finite difference calculations. Figure 5.13 shows the estimated RDP's from the radial displacement synthetic record at a range of 1090 meters at the working point level. The zero prestress RDP has a peak near 50,000 m^3 and a static value near 20,000 m^3 (2×10^{16} Nt-M). The 7.5 MPa prestress case shows that the static explosion "estimated RDP" at this location is very nearly canceled by the tectonic stress release. The 15 MPa prestress case shows a complete reversal of the "estimated RDP".

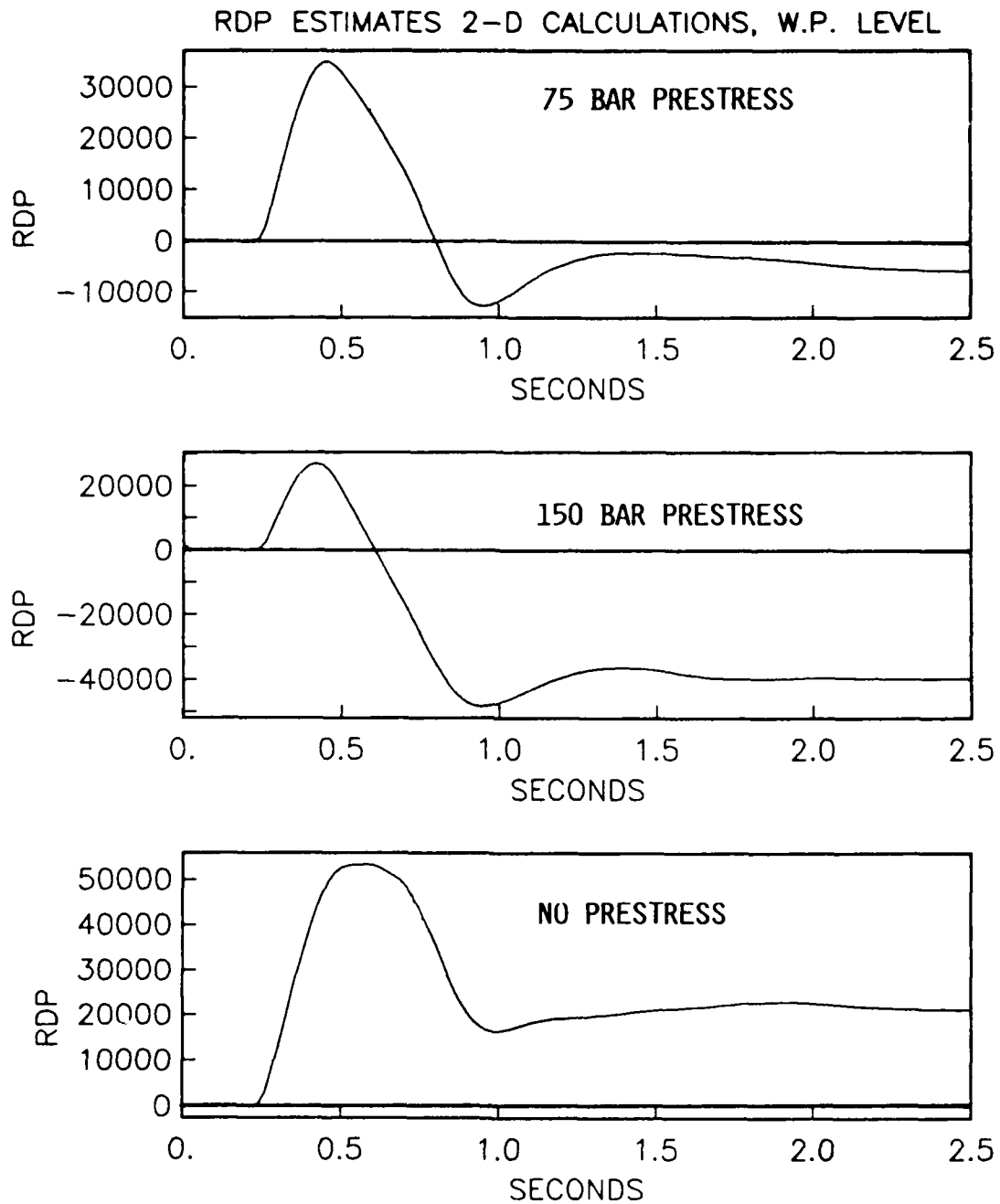


Figure 5.13.

RDP estimates from the radial displacements of the finite difference calculations at the working point level. No prestress (bottom) shows a typical granite RDP with static level near 20,000 m^3 . 7.5 MPa prestress (top) shows a static level near zero, while the 15 MPa prestress (middle) shows a complete reversal.

In contrast to the long period teleseismic seismogram the short period regional seismogram simulations show little effects of prestress. Synthetics for the three cases are shown in Figures 5.14a, b, and c for three bandwidths, 0.5 to 1.25, 0.75 to 1.5 and 1.25 to 2 Hz, respectively. Along with these synthetics are Green's functions for the explosion and the CLVD source for comparison. The structure used to compute the synthetics is the BR2 model with the Climax Stock structure replacing the upper 3.95 km with the granite structure used in the finite difference calculations..

The three 2D synthetics are remarkably like the explosion Green's function in the short period band. The relative amplitudes of the Pg, Lg, and Rayleigh waves are quite similar to a point explosion model. Unlike the Pahute Mesa and Shagan River simulations, the 2D granite calculations are modeled fairly well by the point explosion and require little or no CLVD source to match the Pg/Lg ratio.

In order to demonstrate that the prestress does produce effects at longer periods, we show in Figure 5.15, the fundamental mode excited by the three sources. Note that periods longer than 10 seconds are reversed. There is significant miss-match between the three seismograms in the 10 to 2 sec bandwidth, but that the seismograms become more similar with increasing frequency. In the 1 to 2 Hz band the regional seismogram is dominated by the explosion and shows little evidence of the tectonic release.

Modified BR2 Structure				
h	α	β	ρ	Q_α
0.05	1.440	0.752	2.65	150.0
0.13	4.692	2.457	2.65	150.0
3.77	5.350	2.79	2.65	150.0
1.0	5.8	3.4	2.8	250.0
3.0	6.0	3.46	2.9	250.0
12.0	6.3	3.64	2.9	300.0
4.0	6.5	3.75	2.9	300.0
4.0	6.8	3.93	3.0	300.0
6.0	6.9	3.98	3.0	300.0
4.0	7.8	4.5	3.2	400.0
4.0	7.84	4.5	3.2	400.0
4.0	7.88	4.5	3.2	400.0
4.0	7.92	4.5	3.2	400.0
4.0	7.96	4.5	3.2	400.0
4.0	8.00	4.5	3.2	400.0
2.0	7.95	4.5	3.2	400.0
10.0	7.9	4.4	3.2	150.0
10.0	7.8	4.2	3.2	150.0
20.0	7.8	4.2	3.2	150.0
20.0	7.9	4.5	3.2	150.0
60.0	8.0	4.55	3.3	150.0
20.0	8.1	4.6	3.4	300.0

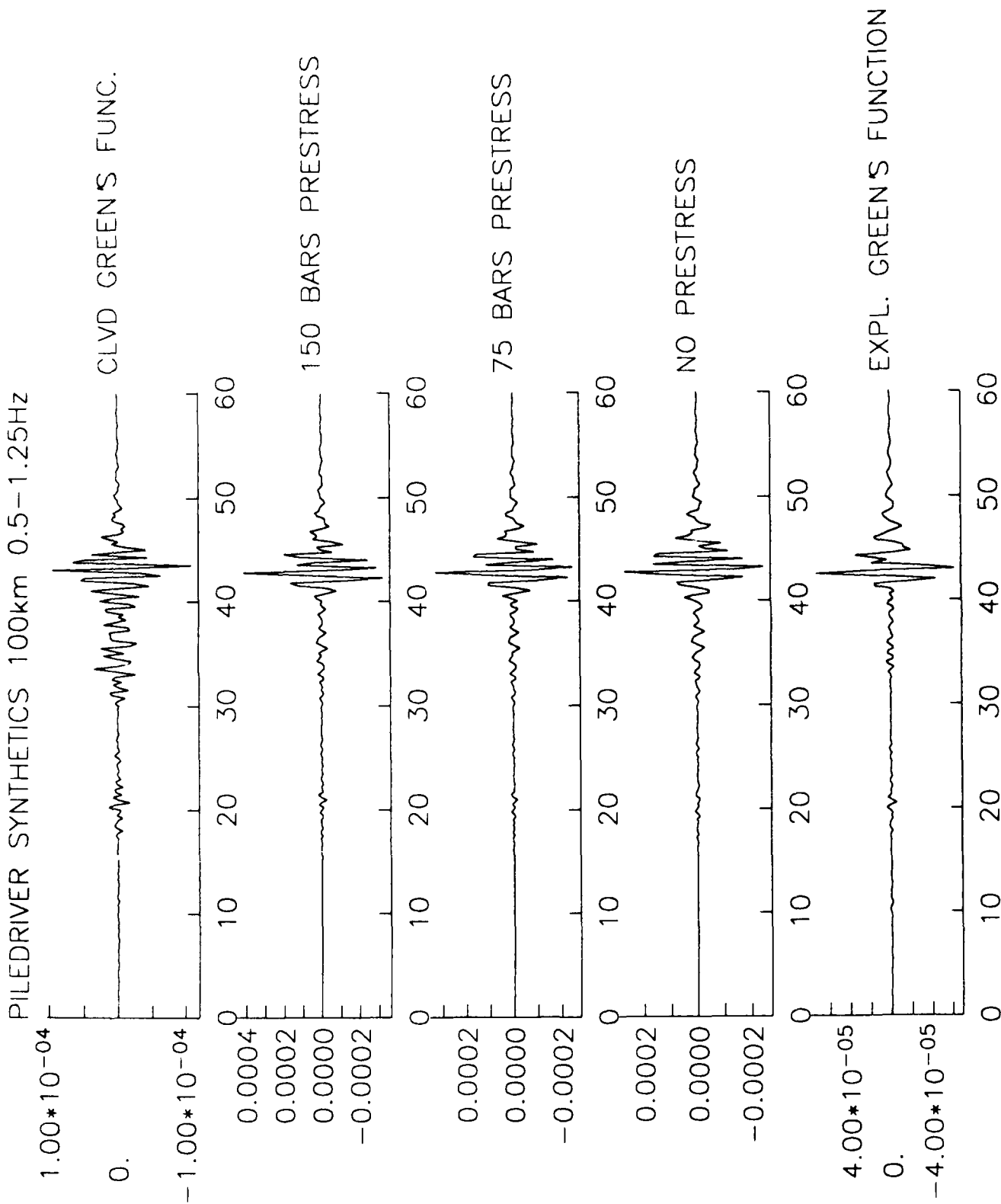


Figure 5.14a. 2D PILEDRIVER synthetics and Green's functions in the 0.5-1.25 Hz band.
 Bottom to top: the explosion Green's function, no prestress, 7.5 MPa prestress, 15 MPa prestress, and the CLVD Green's function.

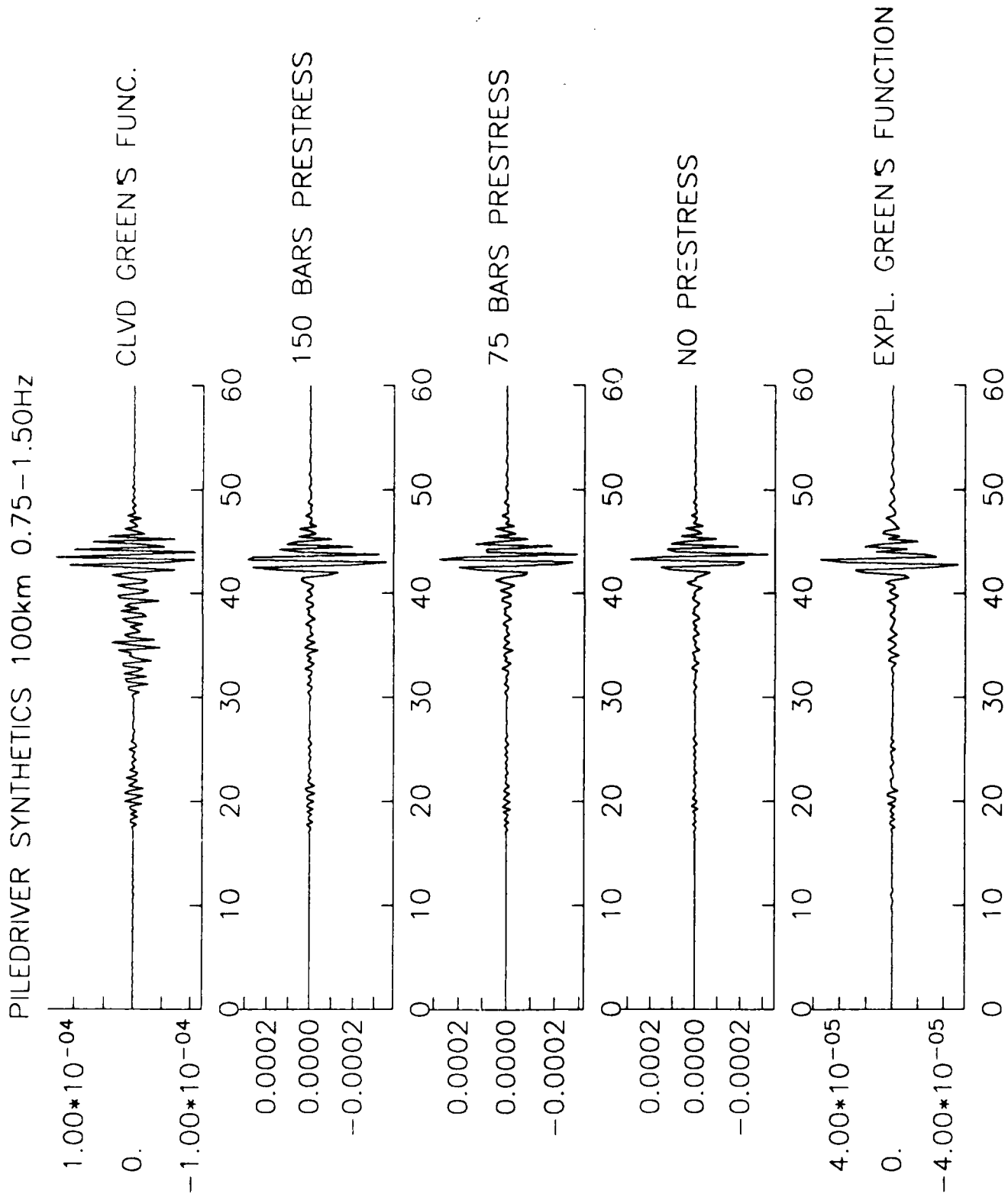


Figure 5.14b. 2D PILEDRIIVER synthetics and Green's functions in the 0.75-1.5 Hz band. Bottom to top: the explosion Green's function, no prestress, 7.5 MPa prestress, 15 MPa prestress, and the CLVD Green's function.

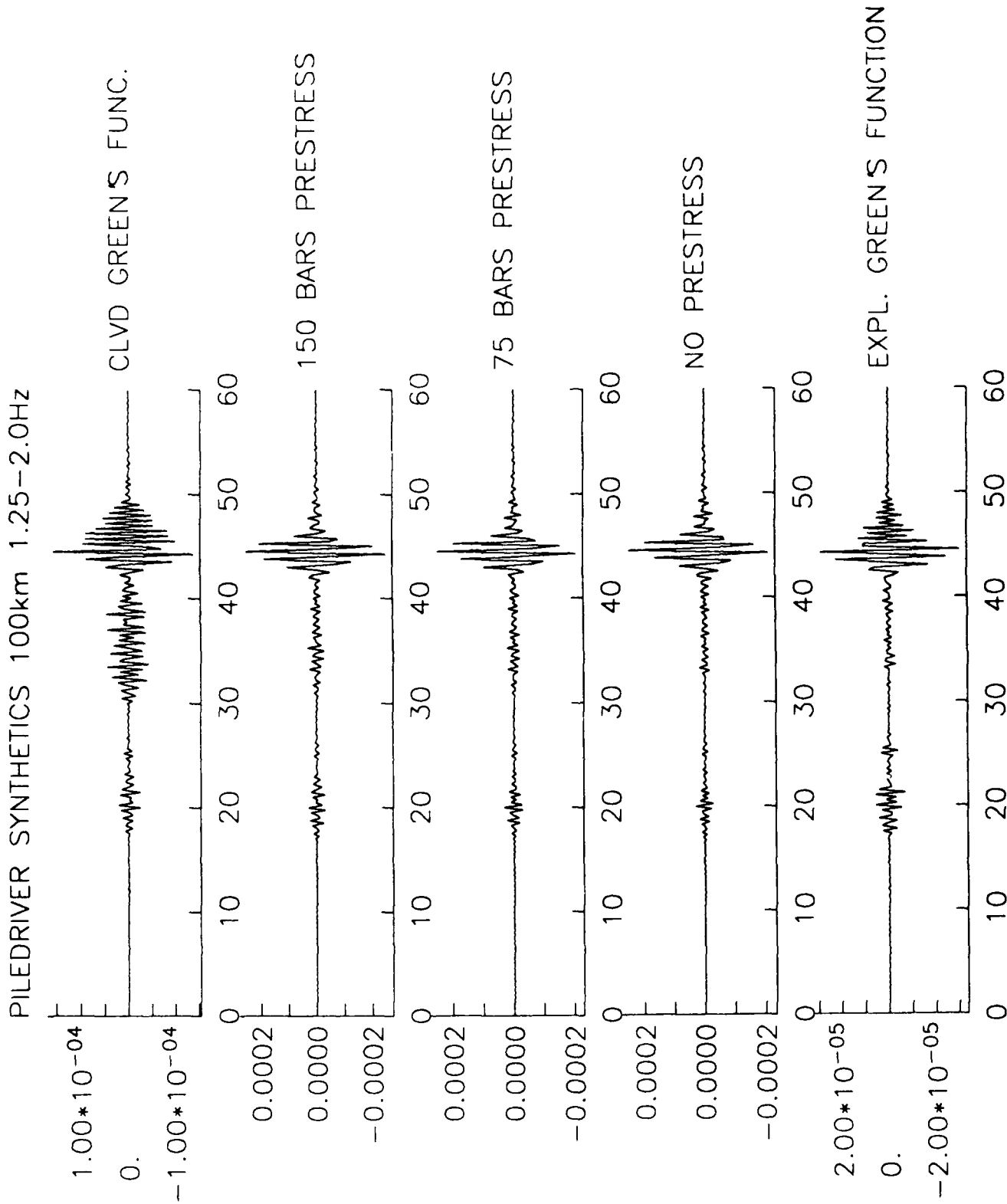


Figure 5.14c. 2D PILEDRIIVER synthetics and Green's functions in the 1.25-2.0 Hz band.
 Bottom to top: the explosion Green's function, no prestress, 7.5 MPa prestress, 15 MPa prestress, and the CLVD Green's function.

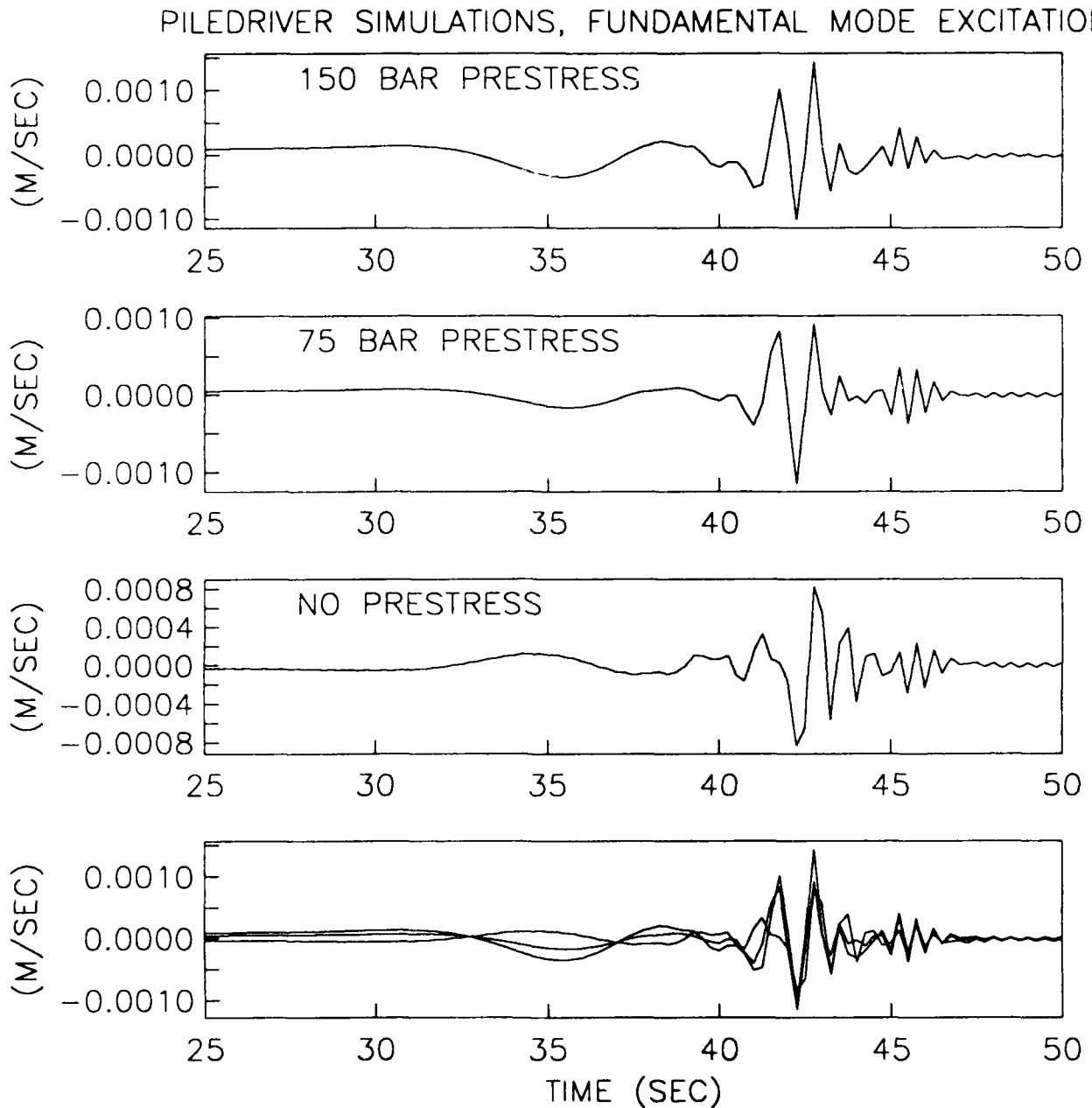


Figure 5.15. Fundamental mode excitation for the three 2D PILEDRIER simulations. Vertical component, 100 km, 0 to 2 Hz bandwidth. Note that although the 10 second surface waves are reversed for the prestressed cases, the Rayleigh waves are progressively alike with increasing frequency (increasing group velocity).

5.5 Conclusions

We see from the three sets of simulations, Pahute Mesa tuff, Shagan River, and prestressed granite, that structure, medium, depth of burial, and prestress all have distinctly different effects on the regional seismogram. However, in all of the 2D synthetics except for granite, the CLVD component of the source is a significant contributor to SV radiation. This secondary source modulates P radiation, and interferes with the fundamental mode in the 0.25 to 2 Hz band. We note that for each of the three sets of synthetics, the effects occur at different frequencies and are apparent on different phases. A conclusion common to all the synthetic simulations, except granite, is that a point explosive source is not an adequate model for regional explosion seismograms in the 0.25 to 2 Hz bandwidth.

We saw in Section III that the 1D point source explosion model does not adequately excite regional Lg (Figures 3.3a, b, and c). Both the Pahute Mesa and Shagan River 2D synthetics show enhanced Lg excitation over the 1D synthetics. It appears that to first order introduction of a CLVD term may explain some of the 2D Lg excitation. However, it is clear that the amount of Lg excitation in the 0.5 - 2 Hz bandwidth even for the 2D synthetics falls far short of the observations. It is possible that increased spall in the 2D simulations could contribute to an increase in the CLVD component of the short period source and hence increase Lg excitation without increasing the Pn and Pg excitation.

As for the simulations of explosions in prestressed granite, we see that the "tectonic release" has negligible short period signature. This is in agreement with the lack of correlation between short period (Lg) and long period (LR) observations, where the long period observations clearly indicate that tectonic release can significantly effect the amplitude and phase of fundamental Rayleigh waves. The 2D simulations suggest that the coherent tectonic release has a gradual onset longer than two seconds such that waves with period shorter than two seconds are virtually unaffected.

VI. CONCLUSIONS AND RECOMMENDATIONS

6.1 Primary Conclusions

The main thrust of the effort has been to examine the nature of explosion depth dependence on the excitation of regional phases. Several observations have been made over the last few years beginning with Murphy and Bennett (1982) that regional phases from explosions at NTS are lacking in high frequencies relative to earthquakes. We have examined several possible causes of such a phenomenon. First, we have examined the depth dependence of explosion and earthquake Green's functions. This work follows in the wake of work by Bennett, *et al.* (1987) and uses a more accurate technique to model regional propagation, namely wavenumber integration as opposed to modal summation. We find that although there are depth dependent trends in the Green's functions for explosions and earthquakes, 1D layered propagation with simple point explosion sources can not explain the observations.

Point source explosions in simple 1D layered crustal models can not excite adequate amplitudes of Lg to match observations. The nonlinear 2D axisymmetric finite difference source simulations that have been examined begin to remedy this deficiency. Although it is clear from the far-field SV waveforms that the 2D source does not directly radiate more energy than the 1D source. Bennett, *et al.* (1987) suggested that with introduction of near-source layering, P-SV conversion could be increased and increase Lg amplitudes. However, even with substantial layering near the source, a point explosion source does not generate sufficient SV energy in a layered structure within the necessary phase velocity range of 3 to 4.0 km/s. When intrinsic attenuation is added to the crust (in order to model the spatial decay of Lg at 1 Hz) the explosion point source synthetic Lg amplitude is practically non-existent beyond 300 km. The "two-dimensional" axisymmetric nonlinear finite difference simulations examined in this study also suffer from this deficiency at frequencies below 1 Hz. Above 1 Hz, we found that 2D synthetics exhibited relative Lg excitation that required a component of CLVD to the source. This part of the source does not have the same time function as the explosion, and if it is caused by spall then it has no low frequency moment. Therefore, we should expect the CLVD component of the source to be peaked with respect to the explosion source. The dominant frequency of the CLVD component will be determined by the time history of the nonlinear free surface interaction including spall. Although the 2D simulations excite more Lg than the 1D point source, they still are not adequate radiators of regional SV energy to agree with observations. The regional Green's functions suggest that processes that enhance the CLVD component of the source will generally increase the Lg/Pn and Lg/Pg ratios. These physical processes would include, but not be limited to, spall closure, bed separation and anisotropic cavity formation.

The Pahute Mesa simulations show that the primary depth of burial effects on the regional seismogram excitations are manifested in the shallow modal content of the seismogram. These shallow Rayleigh waves (Rg) cannot be expected to propagate to large distances in a region such as the Basin and Range, but must be scattered into other phases (perhaps Lg and P-coda). The 2D simulations show that the depth of

burial strongly affects the excitation of these shallow modes over and above that predicted by a point explosive source at the working point depth. Presumably, the nonlinear effects of the source extend to shallow depths and give the event the appearance of being shallower than the working point. The overburied simulations showed less of this trend and therefore we expect that this mechanism would contribute to the enhancement of low frequencies of normal burial with respect to over burial.

Clearly, the short period excitation of Lg by explosions requires some mechanism(s) that has(have) not been properly modeled. Alternative mechanisms include scattering, tectonic release, and non-isotropic nonlinear effects. One promising linear scattering mechanism is the conversion of short-period Rayleigh waves into Lg by shallow heterogeneity and topography (McLaughlin and Jih, 1987). Detailed calculations to verify the efficacy of this model have not yet been carried out. Although long-period tectonic release has not been shown to correlate well with short-period signals, there are observations of well developed short-period SV and SH waves in the 3 to 10 km range (Stump and Johnson, 1984; McLaughlin, *et al.* 1983). These shear waves may be produced by some incoherent release of tectonic strain or they may be due to some nonlinear interaction of the explosion with near-source heterogeneity.

The axisymmetric finite difference simulations model nonlinear effects of pore crush-up, cracking, and spall assuming a simple layered structure. The simulations predict observable direct far-field SV from the explosion as well as from conversion at interfaces and spall formation. Simulations have in the past stressed simple layered models of the near-source in order to simplify the interpretation of the physics involved. Introduction of additional layering may produce more spall above the explosion. Furthermore, addition of lateral heterogeneity around the explosion may introduce non-uniform spall and generate SV and SH motion not predicted by the laterally homogeneous layering. Such a mechanism is nonlinear and can only be explored using more elaborate nonlinear models with presently available nonlinear codes.

The CLVD component to the 2D synthetics is the principal difference between the 2D and the 1D models. This component of the source is largely responsible for the differences in regional synthetics between the 2D full-wave synthetics and the simple point explosion model. Since this source component radiates P energy largely in the vertical direction it could be responsible for increasing the apparent "pP" in teleseismic signals while contributing little "pP" to regional Pn. Furthermore, since it radiates SV primarily in the horizontal direction, this source component can be responsible for excitation of regional Lg.

Several lines of evidence suggest that the Pahute Mesa tuff simulations underestimated the amount of spall observed for "typical" events of their size and scaled depth. Spall has been observed to occur to 1/3 the depth of burial for events in the 20 to 150 kt range with scaled depths of burial between 120 and 180 $m \cdot Y^{(-1/3)}$ (Howard Patton, personal communication). Spall only occurred in the upper most layer (122 m) for tuff simulations examined in this report. Presumably, the low tensile yield strength of the upper most weak layer served to confine the spall to such a shallow layer. Analysis of the Pahute Mesa tuff simulations indicates that the explosion moments (or RDP's) are somewhat small compared to observational estimates for Pahute Mesa

events. If the yield strength of the tuffs were to be reduced above the shots, the explosion moments would increase, and amplitudes above the shots would increase as well as encourage spall at greater depth. Increased spall would increase the CLVD component of the source and therefore increase the amount of SV-Lg excitation. Increased spall may contribute to the "pP" signal at steep take off angles and better simulate the teleseismic P waveform. At the same time, the CLVD component to "pPn" would not be greatly affected, and the Pn waveform would be modeled as before.

6.2 Ancillary Conclusions

From our examination of synthetic methods, we have found that "full-wave" wavenumber integration techniques are required to properly model the entire seismogram at regional distances in the western United States. Modal summation methods can lead to erroneous results if applied for high frequency synthetics in the presence of attenuation.

A crustal shear Q that increases with increasing frequency is required in order to properly model the spectral and temporal character of Lg as a function of distance in the basin and range. The relative amplitudes of Lg for synthetic earthquake and explosion sources at 3 Hz can not be properly simulated with a frequency independent crustal Q .

Lg synthetics indicate that the spatial Lg attenuation corrected for Airy-phase and cylindrical geometrical spreading should be an excellent measure of the "average" shear Q of the crust. Similar results are found for synthetic Pg attenuation and geometrical spreading. For the model examined, the leakage of Pg energy was minimal and the synthetic Pg Q closely approximated the average crustal compressional Q .

The frequency dependence of Pn attenuation is found to be sensitive to the gradient in the upper mantle lid just below the Moho. A slight velocity gradient below the Moho will introduce an apparent Pn Q that increases with increasing frequency even though a constant Q intrinsic attenuation is assumed.

6.3 Recommendations

The results of this work suggest that nonlinear scaled depth of burial effects should be observable in regional seismograms. However, the nonlinear calculations analyzed in this report only cover a limited range of scaled depths and yields. In order to confirm the conjecture that the high-frequency/low-frequency (HF/LF) discriminant is a depth of burial effect will require calculations for greater overburial and smaller yields. Those explosions that Taylor, *et al.* (1988) found to fail the discriminant, were low-yield explosions overburied by 100% or more. Calculations presented in this report indicate that both a low-frequency enhancement is seen in the normal buried shot relative to the overburied shot, but that high frequency enhancement is also evident in the overburied source. Calculations should be repeated to simulate smaller explosions with substantial overburial in a refined tuff model.

The extent of the nonlinear attenuation that affects the radiation of "pP" and SV from the nonlinear simulations should be addressed. Clearly, the tuff models can be improved by introduction of additional layering to simulate the low yield strength interbedded tuff and ash fall layers in the geologic sections. Analysis indicates that spall should be an important contributor to regional seismograms and in particular could be an effective Lg radiator. Introduction of lower yield strength tuffs above the working point should increase the predicted explosion moments and increase the depth to which spall occurs in the simulations. This will increase the spall momentum and increase the CLVD component of the seismic source. Additionally, the introduction of thin weak layers into the model may encourage multiple spall separations and increase SV radiation.

Competing linear scattering mechanisms for the generation of Lg by explosions should be investigated. It is evident that the biggest differences in the 2D and 1D synthetics are present in the lowest group velocity modes of propagation. Since the low velocity near surface layers of the crust are responsible for these modes, it is unclear where this energy ultimately goes since these surface layers are rarely continuous and highly heterogeneous. Therefore, scattering must play an important part in the energy budget of these modes and the ultimate fate of this energy radiated by the shallow explosion. It has been proposed that this energy is coupled into the Lg wavetrain.

Care should be taken in assuming that geometrical spreading for Pn (and probably Sn) is frequency independent at high frequencies. The velocity gradient (in any region of the world) below the Moho is poorly constrained by either *refraction or reflection* data and therefore, only poorly known. The sensitivity of the frequency dependence of the Pn apparent attenuation to this gradient implies that strong trade-offs can exist between source models and attenuation models for Pn unless the source models are independently constrained. The spectral shape is insufficient to constrain the frequency dependence of Q and spatial decay information is required at multiple frequencies.

The Shagan River simulations discussed in this report demonstrate that explosions in a simple high velocity brittle material may exhibit substantial differences at regional distances from a point source model. However, it is clear that this simple model for the Eastern Kazakhstan test site can and should be improved in the light of new information about the testing locality. Information about rock types, velocities, layering information, and testing depths should be incorporated into the nonlinear explosion models for comparison with 1D models for explosions and earthquakes.

VII REFERENCES

- Aki, K., and P. Richards, (1980), "Quantitative Seismology, Freeman, San Francisco. 557 pages.
- Archambeau, C. B., E. A. Flinn, and D. G. Lambert (1969), "Fine Structure of the Upper Mantle," *J. Geophys. Res.*, 74, 5825.
- Apsel, R. J. (1979), "Dynamic Green's Functions for Layered Media and Applications to Boundary-Value Problems," Phd Thesis, U. C. San Diego, 349 pages.
- Barker, B. W. (1981), "Regional Phases from Explosions and Earthquakes in the Southwest US as Recorded by Station ANMO" (Presented AFOSR Conference May 1981, Las Vegas, Nevada).
- Barker, B. W. and J. R. Murphy (1988), "Further Studies of Seismic Variability at the Shagan River Test Site, SSS-R-88-9213, submitted to U.S. Arms Control and Disarmament Agency, Washington, D. C. 20451.
- Bache, T. C., W. L. Rodi, and D. G. Harkrider (1978), "Crustal Structures Inferred from Rayleigh-Wave Signatures of NTS Explosions," *Bull. Seism. Soc. Am.*, 68, 1399-1413.
- Bache, T. C., J. M. Savino, S. M. Day, J. T. Cherry, H. J. Swanger, N. Rimer (1979), "Summary of Seismic Discrimination and Explosion Yield Estimation Research, SSS-R-79-3847 Final Report submitted to AFTAC/VSC, Patrick Air Force Base, Florida 32925.
- Bache, T. C., J. R. Murphy, S. M. Day, T. J. Bennett, and B. Shkoller (1980), "Regional Detection of Decoupled Explosions, Yield Estimation, from Surface Waves, Two-Dimensional Earthquake Modeling and Automated Magnitude Measures," VSC-TR-81-27, S-CUBED Semiannual Report Submitted Vela Seismological Center, Alexandria, Virginia 22314.
- Bache, T. C., S. M. Day and H. J. Swanger (1982), "Rayleigh Wave Synthetic Seismograms from Multi-Dimensional Simulations of Underground Explosions, *Bull. Seism. Soc. Am.*, 54, 1875-1888.
- Bache, T. C., H. J. Swanger, B. Shkoller and S. M. Day (1981), "Simulation of Short Period Lg, Expansion of Three-Dimensional Source Simulation Capabilities and Simulation of Near-Field Ground Motion from the 1971 San Fernando, California, Earthquake," Systems, Science and Software Final Report submitted to AFOSR, SSS-R-81-5081, July.
- Bennett, T. J., J. R. Murphy, and H. K. Shah (1987), Theoretical Analyses of Regional Phase Behavior," S-CUBED Report SSS-R-87-8113.

- Blandford, R. (1976), "Experimental Determination of Scaling Laws for Contained and Cratering Explosions," Teledyne Geotech Technical Report, SCAD-TR-76-3.
- Blandford, R. R., M. Tillman (1977), "Summary of Short-Period Explosion and Earthquake Coda Shapes with Implications for Regional Discrimination," Teledyne Geotech Report SDAC-TR-77-2, Alexandria, Virginia 22314.
- Blandford, R. R., R. Hartenberger, and R. Naylor (1981), "Regional Amplitude-Distance Relations, Discrimination and Detection," VSC-TR-81-15, Vela Seismological Center, Alexandria, Virginia 22314.
- Braile, L.W. (1977), "Interpretation of Crustal Velocity Gradients and Q Structure Using Amplitude-Corrected Refraction profiles, in *The Earth's Crust*, J. G. Heacock (ed.), *Am. Geophys. Union Geophys. Monogram*, 20, 427-439.
- Chun, K. Y. (1983), "Crustal Shear Velocity Modeling in Nevada: A Study of Broadband Multi-Mode Surface Waves," Phd Thesis, U. C. Berkeley, 149 pages.
- Chavez, D. E. and K. F. Priestley (1986), "Measurement of Frequency Dependent Lg Attenuation in the Great Basin, *Geophysical Res. Let.*, 13, 551-554.
- Cheng, C. C. and B. J. Mitchell (1981), "Crustal Q in the United States from Multimode Surface Waves," *Bull. Seism. Soc. Am.*, 71, 161-181.
- Day, S. M., J. T. Cherry, N. Rimer and J. L. Stevens (1982), "Nonlinear Modeling of Tectonic Release from Underground Explosions," S-CUBED Topical Report to VELA Seismological Center, SSS-R-82-5555, August.
- Day, S. M., N. Rimer and J. T. Cherry (1983), "Surface Waves from Underground Explosions with Spall: Analysis of Elastic and Nonlinear Source Models," *Bull. Seism. Soc. Am.*, 73, 247-264.
- Day, S. M., N. Rimer and T. G. Barker (1985), "Numerical Study of Source Effects on Explosion Magnitudes," in DARPA/AFTAC Nuclear Monitoring Seismic Research Review for FY85, Patrick Air Force Base, December.
- Day, S.M., N. Rimer, T. G. Barker, E. J. Halda, and B. Shkoller, (1986), "Numerical Study of Depth of Burial Effects on the Seismic Signature of Underground Explosions," S-CUBED Report to DNA, DNA-TR-86-114.
- Day, S. M., J. T. Cherry, N. Rimer, and J. L. Stevens (1986a), "Nonlinear Model of Tectonic Release from Underground Explosions," *Bull. Seism. Soc. Am.*, 77, 996-1016.

- Day, S. M., N. Rimer, and T. G. Barker (1986b), "Numerical Study of Depth of Burial Effects on the Seismic Signature of Underground Explosions," SSS-R-86-7398, DNA-TR-86-114, S-CUBED, La Jolla, California 92038.
- Denny, M. D., S. R. Taylor, and E. S. Vergino, (1987), "Investigation of m_b and M_S Formulas for the Western U.S. and Their Impact on the m_b - M_S Discriminant, *Bull. Seism. Soc. Am.*, 77, 987-995.
- Der, Z. A., K. L. McLaughlin, I. N. Gupta and W. Helterbran (1985), "Finite Difference Cratering Support," Final Technical Report, Teledyne Geotech Report No. TGAL-85-7, November.
- Der, Z. A., A. C. Lees, K. L. McLaughlin, R. H. Shumway, E. Smart, T. W. McElfresh, and M. E. Marshall (1987), "Maximum-Likelihood Multichannel Deconvolution of P-waves at Seismic Arrays," Teledyne Geotech Report TGAL-87-3, Alexandria, Virginia 22314-1581.
- Der, Z. A., P. Charmaine, P. Mrazek, E. Smart, and B. W. Barker (1978), "Some Aspects of Lg and Pg Propagation," Teledyne Geotech Report SDAC-TR-78-11, Alexandria, Virginia 22314.
- Der, Z. A., A. O'Donnell, P. J. Klouda (1981), "An Investigation of Attenuation, Scattering and Site Effects on Regional Phases," Teledyne Geotech Report, VSC-TR-81-11, Alexandria, Virginia 22314.
- Der, Z. A., and A. C. Lees (1985), "Methodologies for Estimating $t^*(f)$ from Short-Period Body Waves and Regional Variations of $t^*(f)$ in the United States," *Geophys. J. R. astr. Soc.*, 82, 125-140.
- Dwyer, J. J., R. B. Herrmann and O. W. Nuttli (1983), "Spatial Attenuation of the Lg Wave in the Central United States," *Bull. Seism. Soc. Am.*, 73, 781-796.
- Evernden, J. F., C. Archambeau, and E. Cranswick (1986), "An Evaluation of Seismic Decoupling and Underground Nuclear Test Monitoring Using High Frequency Seismic Data, *Reviews of Geophysics*, 24, 143-215.
- Goncz, J. H., W. C. Dean, Z. A. Der, A. C. Lees, K. L. McLaughlin, T. W. McElfresh, and M. E. Marshall (1986), "Propagation and Excitation of Lg, Sn, and P-Pn Waves from Eastern United States Earthquakes by Regression Analysis of RSTN Data, Teledyne Geotech Report TGAL-86-7, Alexandria, Virginia 22314-1581.
- Haskell, N. A. (1966), "The Leakage Attenuation of Continental Crustal P Waves," *J. Geophys. Res.*, 71, 3955-3967.
- Harvey, D. J. (1981), "Seismogram Synthesis Using Normal Mode Superposition, the Locked Mode Approximation, *Geophys. J. R. astr. Soc.*, 66, 37-70.

- Herrmann, R. B. and A. Kijko (1983), "Modeling Some Empirical Vertical Component Lg Relations, *Bull. Seism. Soc. Am.*, 73, 157-171.
- Kennett, B. L. N. (1972), "Seismic Waves in Laterally Inhomogeneous Media," *Geophys. J. R. astr. Soc.*, 27, 301-325.
- Given, J. W., and G. R. Mellman (1986), Personal Communication.
- Gupta, I. N. and J. A. Burnetti (1981), "An Investigation of Discriminants for Events in Western USSR Based on Regional Phases Recorded at Station KABUL," *Bull. Seism. Soc. Am.*, 71, 263-274.
- Gupta, I. N., and R. R. Blandford (1983), "A Mechanism for Generation of Short-Period Transverse Motion from Explosions," *Bull. Seism. Soc. Am.*, 73, 571-591.
- Gupta, I. N., J. A. Burnetti, R. A. Wagner, and M. Marshall (1984) Discrimination Between Quarry Blasts, Nuclear Explosions, and Earthquakes," Teledyne Geotech Report TGAL-TR-84-1, Teledyne Geotech, Alexandria, VA.
- Gupta, I. N., R. R. Blandford, R. A. Wagner, J. A. Burnetti and T. W. McElfresh (1986), Use of P coda for Determination of Yield of Nuclear Explosions, *Geophys. J. R. astr. Soc.* 83, 541-554.
- Hamilton, R. M., B. E. Smith, F. G. Fischer, and P. J. Papanek (1972), "Earthquakes Caused by Underground Nuclear Explosions on Pahute Mesa, Nevada Test Site," *Bull. Seism. Soc. Am.*, 62, 1319-1342.
- Haskell, N. A. (1966), "The Leakage Attenuation of Continental Crustal P Waves," *J. Geophys. Res.*, 71, 3955-3967.
- Helmberger, D. V. (1973), "On the Structure of the Low Velocity Zone," *Geophys. J. R. astr. Soc.*, 34, 251-263.
- Herrin, E., E. P. Arnold, B. A. Bolt, G. E. Clawson, E. R. Engdahl, H. W. Freedman, D. W. Gordon, A. L. Hales, J. L. Lobdell, O. Nuttli, C. Romney, J. Taggart, and W. Tucker (1968), "1968 Seismological Tables for P Phases," *Bull. Seism. Soc. Am.*, 58, 1193-1241.
- Lay, T. (1987), "Analysis of Near-Source Contributions to Early P-Wave Coda for Underground Explosions: 2, Frequency Dependence," *Bull. Seism. Soc. Am.*, 77, 1252.
- Lay, T. and J. L. Welc (1987), "Analysis of Near-Source Contributions to Early P-Wave Coda for Underground Explosions: 1) Waveform Complexity," *Bull. Seism. Soc. Am.*, 77, 1017.
- Leith, W. (1987), "Geology of NRDC Seismic Station Sites in Eastern Kazakhstan," Memo to DARPA/NMRO.

- Lee W.B. and S.C. Solomon (1975), "Inversion Schemes for Surface Wave Attenuation and Q in the Crust and the Mantle," *Geophys. J. R. astr. Soc.*, 43, 47-71.
- Leonard M. A and L. R. Johnson (1987), "Velocity Structure of Silent Canyon Caldera, Nevada Test Site," *Bull. Seism. Soc. Am.*, 77, 597-613.
- Luco, J. E., and R. J. Apsel (1983), "On the Green's Functions for A Layered Half-Space. Part I," *Bull. Seism. Soc. Am.*, 73, 909-929.
- Lyman, N. S., A. Douglas, P. D. Marshall, and J. B. Young (1986), "P Seismograms Recorded at Eskdalemuir, Scotland from Explosions in Nevada, USA," AWRE Report No. O 10/86. AWRE, MOD(PE), Aldermasten, Berks. U.K.
- Mackenzie, K. and J. Orcutt (1984), "The Fine Structure of the Oceanic Moho," *J. Geophys. Res.*, in press.
- Malin, P. (1978), "A First Order Scattering Solution for Modeling Lunar and Terrestrial Seismic Coda," Princeton University Ph.D. Thesis.
- Marshall, P. D., D. L. Springer, and H. C. Rodean (1979), "Magnitude Corrections for Attenuation in the Upper Mantle," *Geophys. J. R. astr. Soc.*, 57, 609-638.
- Marshall, P. D., T. C. Bache, and R. C. Lilwall (1984), "Body Wave Magnitudes and Locations of Soviet Underground Explosions at the Semipalatinsk Test Site," AWRE Report No. O 16/84.
- McLaughlin, K. L., I. N. Gupta and R. Wagner (1985), "Finite Difference Cratering Support Task 1," Final Report, Teledyne Geotech Report No. TGAL-85-3, May.
- McLaughlin, K. L., R. O. Ahner, R. Wagner, and M. Marshall (1986), "Maximum Likelihood Magnitudes and $\log(P_{\max}/P_a)$ at Novaya Zemlya and Eastern Kazakh Test Sites," TGAL-86-02, Teledyne Geotech, Alexandria, Virginia 22314.
- McLaughlin, K. L. and R. S. Jih (1987), "Finite Difference Simulations of Rayleigh-Wave Scattering by Shallow Heterogeneity," AFGL-TR-87-0322, TGAL-87-02, Teledyne Geotech, Alexandria, Virginia 22314.
- McLaughlin, K. L., M. E. Marshall, R. Wagner, W. Chan, A. C. Lees, and R. S. Jih (1987) "A Maximum Likelihood General Linear Model (GLM87) for Test-Site Magnitude:Yield Estimation and P-Wave Measures of Yield at Novaya Zemlya and Sinkiang Test Sites," Teledyne Geotech Report TGAL-87-05.
- Mitchell, B. J. (1975), "Regional Rayleigh Wave Attenuation in North America," *J. Geophys. Res.*, 80, 4904-4916.

- Mueller, R. A. and J. R. Murphy (1971), "Seismic Characteristics of Underground Nuclear Detonations," *Bull. Seism. Soc. Am.*, 61, 1675-1692.
- Murphy, J. R., C. B. Archambeau and H. K. Shah (1983), "Magnitude/Yield Variability in the Western United States: Analysis of the Rulison/Gasbuggy Anomaly," S-CUBED Final Report submitted to AFOSR, SSS-R-83-5978, January.
- Murphy, J. R., and T. J. Bennett (1982), "A Discrimination Analysis of Short-Period Regional Seismic Data Recorded at Tonto Forest Observatory," *Bull. Seism. Soc. Am.*, 72, 1351-1366.
- Murphy, J. R. (1977), "Seismic Source Functions and Magnitude Determinations for Underground Nuclear Detonations," *Bull. Seism. Soc. Am.*, 57, 135-158.
- Nuttli, O. (1981), "Similarities and Differences Between Western and Eastern United States Earthquakes, and Their Consequences for Earthquake Engineering," in *Earthquakes and Earthquake Engineering: the Eastern United States*, J. E. Beavers, Ed., Ann Arbor Publishers, Michigan, 25-51.
- Nuttli, O. (1986), "Yield Estimates of Nevada Test Site Explosions Obtained from Seismic Lg Waves," *J. Geophys. Res.*, 91, 2137-2151.
- Nuttli, O. (1986), "Lg Magnitudes of Selected East Kazakhstan Underground Explosions," *Bull. Seism. Soc. Am.*, 76, 1241-1251.
- Pakiser, L. C. (1963), "Structure of the Crust and Upper Mantle in the Western U.S.," *J. Geophys. Res.*, 68, 5754-5756.
- Patton, H. J. (1982), "Measurements of Rayleigh-Wave Phase Velocities in Nevada: Implications for Explosion Sources and the Massachusetts Mountain Earthquake," *Bull. Seism. Soc. Am.*, 72, 1329-1349.
- Patton, H. J., and E. S. Vergino (1981), "Source Effects on Surface Waves From Nevada Test Site Explosions," Report UCRL-53247, Lawrence Livermore National Laboratory.
- Patton, H. J. and S. R. Taylor (1984), "Q Structure of the Basin and Range From Surface Waves," *J. Geophys. Res.*, 89, 6929-6940.
- Patton, H. J. (1987), "Application of Nuttli's Method to Estimate Yield of NTS Explosions Recorded on LLNL's Digital Seismic System," LLNL Report UCRL-97628.
- Priestley, K. and J. N. Brune (1978), "Surface Waves and the Structure of the Great Basin of Nevada and Western Utah," *J. Geophys. Res.*, 83, 2265-2272.

- Priestley, K. J. A. Orcutt, and J. N. Brune (1980), "Higher Order Surface Waves and Structure of the Great Basin of Nevada and Western Utah," *J. Geophys. Res.*, 85, 7166-7174.
- Press, F. (1964), "Seismic Wave Attenuation in the Crust," *J. Geophys. Res.*, 69, 4417-4418.
- Peseckis, L. L. and P. W. Pomeroy (1984), "Determination of Q using Lg Waves and Its Implications for Nuclear Yield Estimation," *EOS*, 65, 995.
- Richards, P. G. and W. Menke (1983), "The Apparent Attenuation of A Scattering Medium," *Bull. Seism. Soc. Am.*, 73, 1005-1021.
- Rimer, N., S. M. Day, G. A. Hegemier, H. E. Read, S. K. Garg and S. Peyton (1984), "Effects of Pore Fluid Pressure on Explosive Ground Motions in Low Porosity Brittle Rocks," S-CUBED Final Report (Draft) submitted to the Defense Nuclear Agency, SSS-R-84-6766, DNA-TR-85-245.
- Rimer, N., J. T. Cherry, S. M. Day, T. C. Bache, J. R. Murphy and A. Maewal (1979), "Two-Dimensional Calculation of PILEDIVER, Analytic Continuation of Finite Difference Source Calculations, Analysis of Free-Field Data from MERLIN and Summary of Current Research," Systems, Science and Software Quarterly Technical Report submitted to VSC/ARPA, SSS-R-79-4121, August.
- Ringdal, F. (1987), "Magnitudes of Large Semipalatinsk Explosions Using P Coda and Lg Measurements at NORSAR," NORSAR Report.
- Rodean, H. C. (1979), "ISC Events from 1964 to 1976 at and Near the Nuclear Testing Ground in Eastern Kazakhstan," UCRL-52856, Lawrence Livermore Laboratory.
- Rodi, W. L., J. M. Savino, T. G. Barker, S. M. Day and T. C. Bache (1978), "Analysis of Explosion Generated Surface Waves in Africa, Results from the Discrimination Experiment and Summary of Current Research," Systems, Science and Software Quarterly Technical Report, SSS-R-78-3653, April.
- Singh, S. and R. B. Herrmann (1983), "Regionalization of Crustal Coda Q in the Continental United States," *J. Geophys. Res.*, 88, 527-538.
- Springer, D. L. (1974), "Secondary Sources of Seismic Waves from Underground Nuclear Explosions," *Bull. Seism. Soc. Am.*, 64, 581-594.
- Stevens, J. L. and S. M. Day (1985), "The Physical Basis for mb:Ms and Variable Frequency Magnitude Methods for Earthquake/Explosion Discrimination," *J. Geophys. Res.*, 90, 3009-3020.
- Stevens, J. L. (1986), "Estimation of Scalar Moments from Explosion-Generated Surface Waves," *Bull. Seism. Soc. Am.*, 76, 123-151.

- Stevens, J. L. and K. L. McLaughlin (1988), "Analysis of Surface Waves from the Novaya Zemlya, Mururoa, and Amchitka Test Sites, and Maximum Likelihood Estimation of Scalar Moments from Earthquakes and Explosions," S-CUBED Technical Report (Draft) SSS-R-89-9953 submitted to DARPA/AFTAC, September.
- Stump, B., and L. R. Johnson (1984), "Near-Field Characterization of Contained Nuclear Explosions in Tuff," *Bull. Seism. Soc. Am.*, 74, 1-26.
- Swanger, H. J. (1982), "Simulation of Regional Phases," S-CUBED Final Report SSS-R-82-5481, submitted to AFOSR, Bolling Air Force Base, Washington, D.C. 20322.
- Sykes, L. R. and S. Ruggi (1986), "Soviet Underground Nuclear Testing: Inferences from Seismic Observations and Historical Perspective," NWD-86-4, Natural Resources Defense Council, Washington, D. C. 20005.
- Taylor, S. R. and H. J. Patton (1986), "Shear-Velocity Structure from Regionalized Surface-Wave Dispersion in the Basin and Range," *GRL*, 13, 30-33.
- Taylor, S. R., N. W. Sherman, M. D. Denny (1988), "Spectral Discrimination Between NTS Explosions and Western U.S. Earthquakes at Regional Distances," *Bull. Seism. Soc. Am.*, 78, 1563-1579.
- Veith, K. F., and G. E. Clawsen (1972), "Magnitude from Short-Period P-Wave Data," *Bull. Seism. Soc. Am.*, 62, 435-452.
- Wallace, T. C. (1983), "Long Period Regional Body Waves," Phd. Thesis, California Institute of Technology, Pasadena, California
- Werth G. C., R. F. Herbst, and D. L. Springer (1962), "Amplitudes of Seismic Arrivals from the M Discontinuity," *J. Geophys. Res.* 67, 1587-1610.

APPENDIX A

**MAGNITUDE:YIELD CALIBRATION USING THE PRESUMED
JANUARY 15, 1965 CRATERING EXPLOSIVE**

Since, most magnitudes or other yield estimators for the Shagan River test site are based on $m_b(\text{Pmax})$, $m_b(\text{Lg})$, M_S , or M_I , we have to relate the $m_b(\text{Pa})$ and $m_b(\text{Pb})$ estimates of Section 4.2.2 to other measures that have been made for a great deal more events. It is generally thought that if various independent seismic "magnitudes" are used, then better yield estimates result due to the cancellation of random errors on an event by event basis. We do this by forming a general linear model for the estimation of a "GLM" unified magnitude. We assume that the slope between M_S and M_0 or M_I with body-wave magnitude is 0.9, and we use the relationship, $M_S = \log(M_0) - 11.86$, from Stevens (1986) to make a first approximation of converting moments to M_S . M_0 are taken from Stevens (1986), M_I are taken from Stevens (personal communication) and Given and Mellman (1986). M_S are taken from Sykes and Ruggi (1986). We also use the $m_b(\text{Lg})$ estimates of Nuttli (1986), the P coda estimates of Gupta (1986), and the P coda and rms Lg estimates of Ringdal (1987). Gupta's P coda measurements were corrected for an estimated source spectrum and are theoretically proportional to moment, therefore we correct them to m_b assuming a 0.9 slope. We use two sets of m_b estimates. 12 events (less the cratering event) for which McLaughlin, *et al.* (1986) estimated maximum likelihood WWSSN magnitudes for $m_b(\text{a})$, $m_b(\text{b})$, and $m_b(\text{max})$, and the ISC m_b estimates of Marshall, *et al.* (1984). Since fewer than 15% of the ISC stations used by Marshall *et al.* are WWSSN stations, the two sources of m_b are largely based on independent data sets. We expect that the $m_b(\text{Pa})$, $m_b(\text{Pb})$ and $m_b(\text{Pmax})$ estimates are all highly correlated.

In order to use the general linear model, we ignore correlation that surely exists between the various P measures, Lg measures, and LR measures of yield. Since the correlations are unknown at this time, and the full general linear model with correlation is numerically intractable, we are forced at this stage to assume independence. Some care has been taken to balance the data sets so that this should not be an overly important consideration. Given this consideration, we are probably underestimating the standard errors of the correction terms and the event GLM magnitude.

The results are shown below in Tables A.1 and A.2. The baseline corrections for the different source measures have been adjusted so that the $m_b(\text{ISC})$ estimates of Marshall, *et al.* (1984) have no net correction. For comparison with another set of magnitudes, the average difference between these magnitude estimates and those of Barker and Murphy (1988) is 0.00(0.03) with an rms value of 0.11.

From this data, we can now estimate the GLM magnitude for the January 15, 1965 event based on the available $m_b(\text{Pa})$, $m_b(\text{Pb})$, M_S , and $m_b(\text{Lg})$ estimates. We have estimated uncertainties for the $m_b(\text{Lg})$ of 0.05, and M_S of 0.07. Stevens and McLaughlin (1988) have estimated moments for the NTS cratering shots SEDAN and SCHOONER. They found that these events had $\log(M_0)$'s 0.6 log units lower than comparable contained shots of the same yield. We estimate an additional uncertainty in this correction of 0.1 log units because of various factors concerning the differences between explosion coupling in different media. Therefore, the Sykes and Ruggi M_S for the January 15, 1965 event should be corrected to $3.9(0.07) + 0.6(0.1)$. Nuttli's data for SEDAN show no evidence that cratering made a difference in $m_b(\text{Lg})$. The results are summarized as follows,

$$m_b(Pa) = 5.48(0.05) - 0.128 + 0.661(0.034) = 6.013(0.060)$$

$$m_b(Pb) = 5.72(0.05) + 0.000 + 0.312(0.030) = 6.032(0.058)$$

$$M_S = 0.9 * (3.9(0.07) + 0.06(0.1)) + 2.262(0.047) = 6.31(0.12)$$

$$m_b(Lg) = 5.87(0.05) + 0.089(0.034) = 5.959(0.060)$$

We are faced with forming some sort of weighted average of the estimates, based on their reliability. If we include the M_S estimate in a weighted average then we have $m_b(125\text{kt}) = 6.025(0.03)$. The variance of the M_S estimate is probably under estimated as it is the most uncertain data point. Given that we prefer the weighted average of the P and Lg estimates, $m_b(125\text{kt}) = 6.00(0.03)$. Assuming an m_b :Log(yield) slope of 0.9, this infers a GLM unified $m_b(150\text{kt}) = 6.07(0.03)$.

It should be noted that systematic variations in magnitude differences (see Barker and Murphy 1988; Ringdal, 1987) have been observed across the Shagan River test site, and that the January 15, 1965 event was located in the southeast corner of the test site (Rodean, 1979; Marshall, *et al.* 1984). This introduces an additional systematic uncertainty to the estimated 150 kt level due to spatial variability. These rms variations are typically about 0.1 magnitude units across the test site based on the rms error in the GLM. Therefore, 6.07(0.11) is a conservative estimate of the 150 kt GLM unified magnitude and its uncertainty. As can be seen in Table A.2, a number of the largest events are within the 97.7% upper bound (two sigma) of the inferred 150 kt limit.

We have used the nonlinear calculations to infer $m_b(a)$ and $m_b(b)$ corrections for the January 15, 1965 presumed cratering explosion at the Shagan River test site. In order to relate these corrected magnitudes to more recent events of interest, we have developed a GLM unified magnitude based on m_b , $m_b(Lg)$, P coda, M_S , M_0 , and M_I . The results are subject to two sources of systematic error. The focusing defocusing of m_b signals at Shagan could be responsible for a baseline error in the cratering event m_b . We have estimated this uncertainty to lie in the 0.11 magnitude range. Finally, the corrections to the $m_b(a)$ and $m_b(b)$ magnitudes derived from the nonlinear calculations are subject to model assumptions and our knowledge of the geophysical parameters of the Shagan River test site. The fact that the corrections imply the correct differences between $m_b(a)$ and $m_b(b)$ for contained and cratering events of comparable magnitude suggest that the simulations are properly modeling the early portion of the waveform.

TABLE A.1 GLM MAGNITUDE CORRECTIONS

MAGNITUDE	INTERCEPT	σ	SLOPE	#EVENTS
m_b (ISC)	0.0	0.024	1.0	13
m_b (Pmax)	+0.084	0.018	1.0	11
m_b (Pb)	+0.312	0.018	1.0	11
m_b (Pa)	+0.661	0.022	1.0	11
m_b (Lg)	+0.089	0.024	1.0	15
m_b (Lgl)	+0.103	0.022	1.0	14
P coda	+4.589	0.024	0.9	7
P coda1	+0.003	0.018	1.0	15
M_S	+2.262	0.040	0.9	8
M_0	+2.476	0.034	0.9	5
M_I	+2.238	0.037	0.9	13

TABLE A.2 SHAGAN RIVER GLM-MAGNITUDES

EVENT	YY/MM/DD	GLM-MAG	σ	#MAGS
1	68/07/19	5.355	0.038	5
2	69/11/30	6.017	0.031	5
3	73/07/23	6.303	0.023	9
4	73/12/14	5.908	0.030	8
5	75/04/27	5.625	0.019	8
6	76/07/04	5.932	0.021	10
7	76/12/07	5.777	0.039	6
8	78/06/11	5.963	0.024	11
9	78/09/15	5.960	0.020	11
10	79/06/23	6.160	0.026	11
11	80/09/14	6.178	0.025	10
12	81/09/13	6.179	0.033	5
13	81/12/27	6.027	0.081	5
14	83/06/12	6.182	0.043	3
15	83/10/26	6.161	0.037	4
16	84/07/14	6.193	0.044	4
17	84/10/27	6.201	0.033	4
18	84/12/16	6.176	0.037	4

APPENDIX B

TABLE B.1a Frequency Dependent Q Model SS

Phase	DOB	TOA=10°	TOA=20°	TOA=30°
$\text{Log}(Pa)$	200	0.402	0.389	0.370
$\text{Log}(Pb)$	200	0.570	0.553	0.531
$\text{Log}(Pc)$	200	0.591	0.553	0.519
$\text{Log}(\frac{Pb}{Pa})$	200	0.168	0.165	0.161
$\text{Log}(\frac{Pc}{Pa})$	200	0.189	0.164	0.149
$\text{Log}(Pa)$	680	0.600	0.595	0.580
$\text{Log}(Pb)$	680	0.791	0.788	0.779
$\text{Log}(Pc)$	680	0.814	0.802	0.794
$\text{Log}(\frac{Pb}{Pa})$	680	0.191	0.192	0.199
$\text{Log}(\frac{Pc}{Pa})$	680	0.214	0.206	0.214

TABLE B.1b Frequency Dependent Q Model TS

Phase	DOB	TOA=10°	TOA=20°	TOA=30°
$\text{Log}(Pa)$	200	0.043	0.029	0.015
$\text{Log}(Pb)$	200	0.178	0.165	0.150
$\text{Log}(Pc)$	200	0.204	0.176	0.154
$\text{Log}(\frac{Pb}{Pa})$	200	0.135	0.136	0.135
$\text{Log}(\frac{Pc}{Pa})$	200	0.161	0.148	0.139
$\text{Log}(Pa)$	680	0.236	0.233	0.221
$\text{Log}(Pb)$	680	0.414	0.414	0.408
$\text{Log}(Pc)$	680	0.455	0.448	0.443
$\text{Log}(\frac{Pb}{Pa})$	680	0.178	0.181	0.188
$\text{Log}(\frac{Pc}{Pa})$	680	0.219	0.215	0.223

TABLE B.1c Frequency Dependent Q Model TT

Phase	DOB	TOA=10°	TOA=20°	TOA=30°
$\text{Log}(Pa)$	200	-0.266	-0.281	-0.295
$\text{Log}(Pb)$	200	-0.151	-0.160	-0.169
$\text{Log}(Pc)$	200	-0.134	-0.159	-0.183
$\text{Log}(\frac{Pb}{Pa})$	200	0.115	0.121	0.126
$\text{Log}(\frac{Pc}{Pa})$	200	0.132	0.122	0.112
$\text{Log}(Pa)$	680	-0.080	-0.083	-0.089
$\text{Log}(Pb)$	680	0.101	0.100	0.096
$\text{Log}(Pc)$	680	0.117	0.118	0.132
$\text{Log}(\frac{Pb}{Pa})$	680	0.181	0.182	0.185
$\text{Log}(\frac{Pc}{Pa})$	680	0.197	0.200	0.221

TABLE B.1d Frequency Independent Q Model ($t^* = 0.5$)

Phase	DOB	TOA=10°	TOA=20°	TOA=30°
$\text{Log}(Pa)$	200	0.047	0.031	0.017
$\text{Log}(Pb)$	200	0.196	0.185	0.174
$\text{Log}(Pc)$	200	0.239	0.216	0.198
$\text{Log}(\frac{Pb}{Pa})$	200	0.151	0.154	0.156
$\text{Log}(\frac{Pc}{Pa})$	200	0.194	0.185	0.180
$\text{Log}(Pa)$	680	0.234	0.231	0.226
$\text{Log}(Pb)$	680	0.440	0.440	0.437
$\text{Log}(Pc)$	680	0.498	0.494	0.497
$\text{Log}(\frac{Pb}{Pa})$	680	0.206	0.208	0.211
$\text{Log}(\frac{Pc}{Pa})$	680	0.214	0.263	0.271

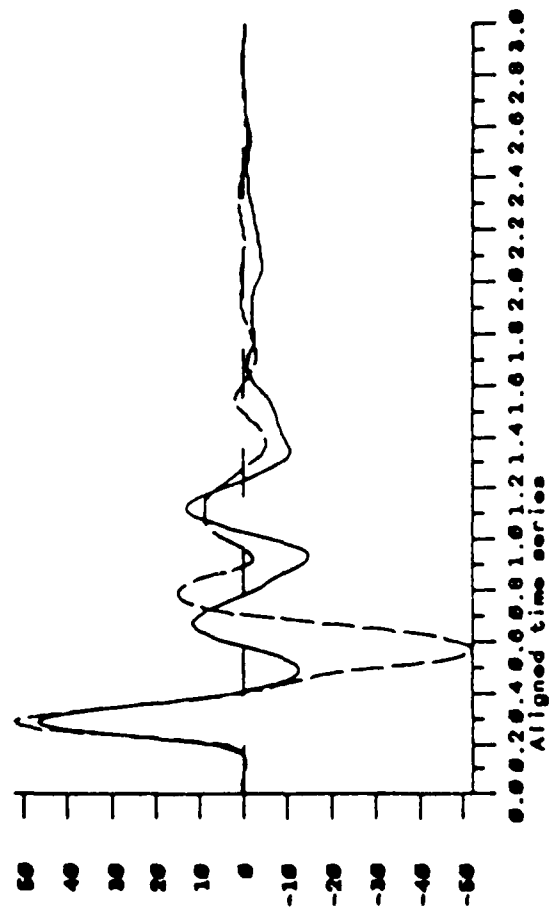
TABLE B.1e Frequency Independent Q Model ($r^* = 0.7$)

Phase	DOB	TOA=10°	TOA=20°	TOA=30°
$\text{Log}(Pa)$	200	-0.237	-0.251	-0.265
$\text{Log}(Pb)$	200	-.097	-0.105	-0.115
$\text{Log}(Pc)$	200	-0.065	-0.091	-0.119
$\text{Log}(\frac{Pb}{Pa})$	200	0.139	0.146	0.150
$\text{Log}(\frac{Pc}{Pa})$	200	0.172	0.160	0.146
$\text{Log}(Pa)$	680	-0.055	-0.058	-0.064
$\text{Log}(Pb)$	680	0.153	0.151	0.147
$\text{Log}(Pc)$	680	0.182	0.190	0.210
$\text{Log}(\frac{Pb}{Pa})$	680	0.208	0.209	0.210
$\text{Log}(\frac{Pc}{Pa})$	680	0.237	0.247	0.273

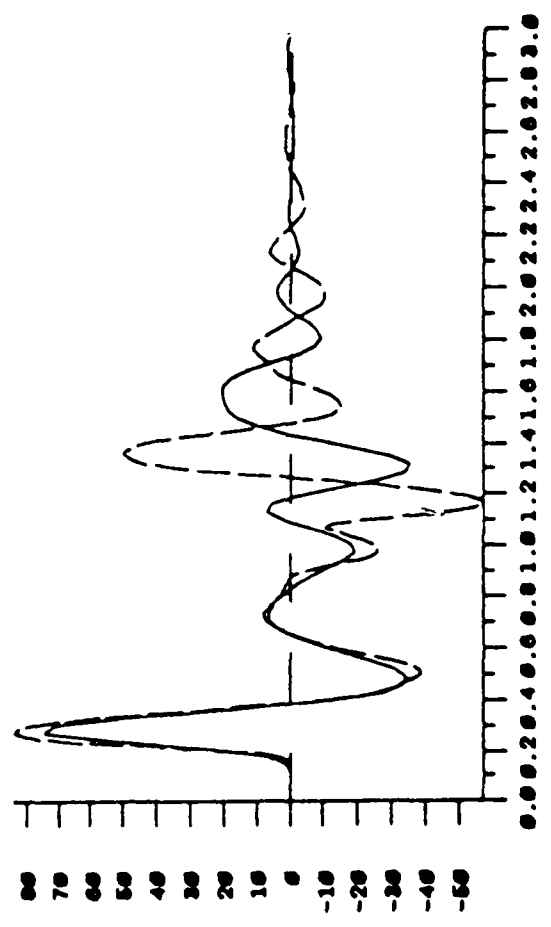
Unfiltered 2d vs 1d solutions at toa20, 3 dob's
Date: 11/2/1988 Time: 10:56:20

Aligned time series

File # 1 : pm200 toa20
File # 2 : pm200 toa20



File # 1 : pm080 toa20
File # 2 : pm080 toa20



Time (sec)

Aligned time series

File # 1 : pm080 toa20
File # 2 : pm080 toa20

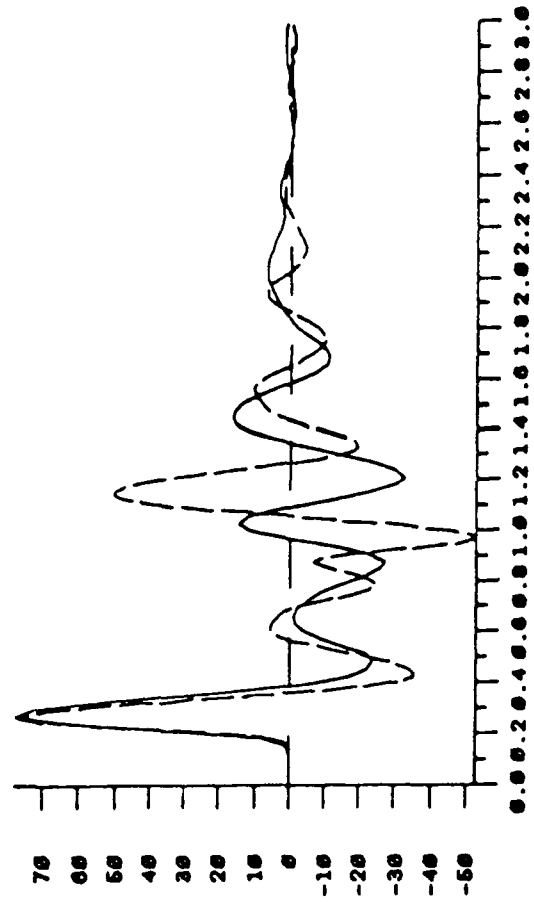
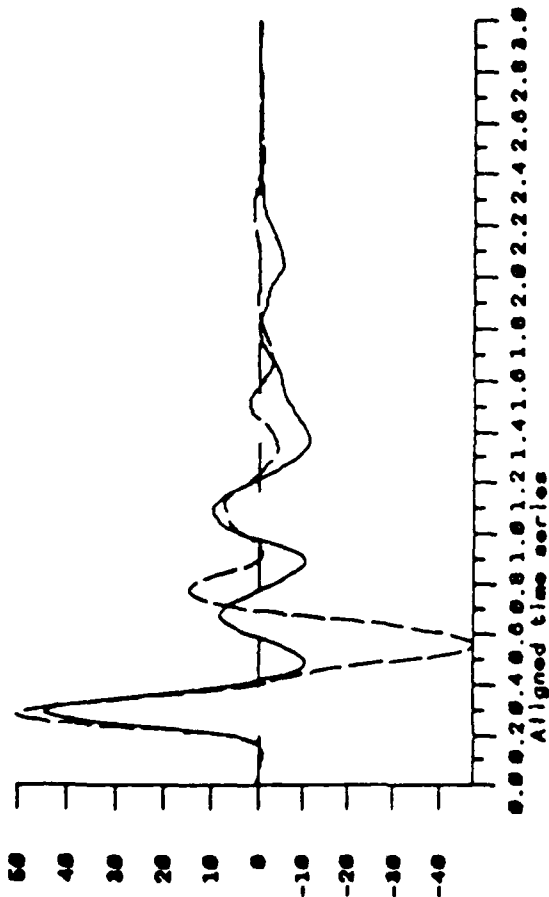


Figure B.1a. Radiated displacement P waveforms for the three 2D Pahute Mesa tuff simulations at 20° takeoff angle compared to the 1D elastic source model.

Unfiltered 2d vs 1d solutions at $t_{\text{max}}=30$, 3 deb's
Date: 11/2/1988 Time: 10:50:53

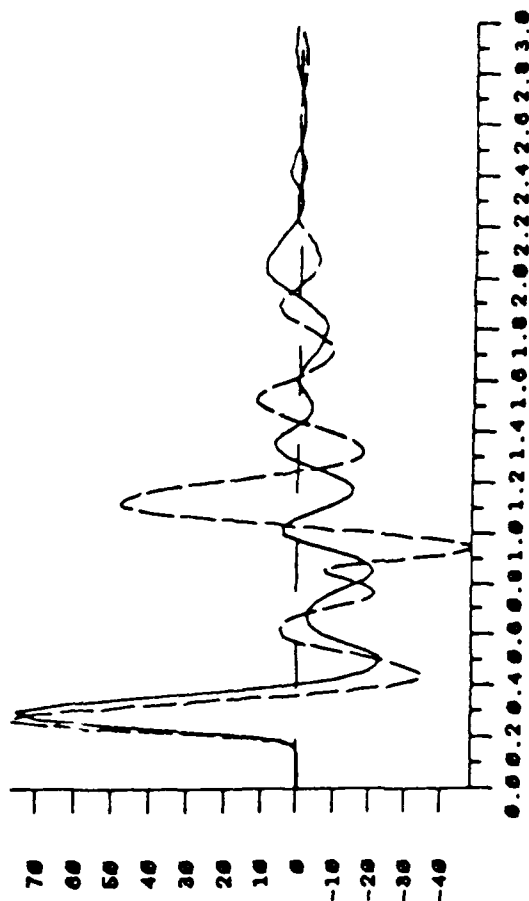
Aligned time series

File # 1 : pm200 toa30
File # 2 : pm200 toa30



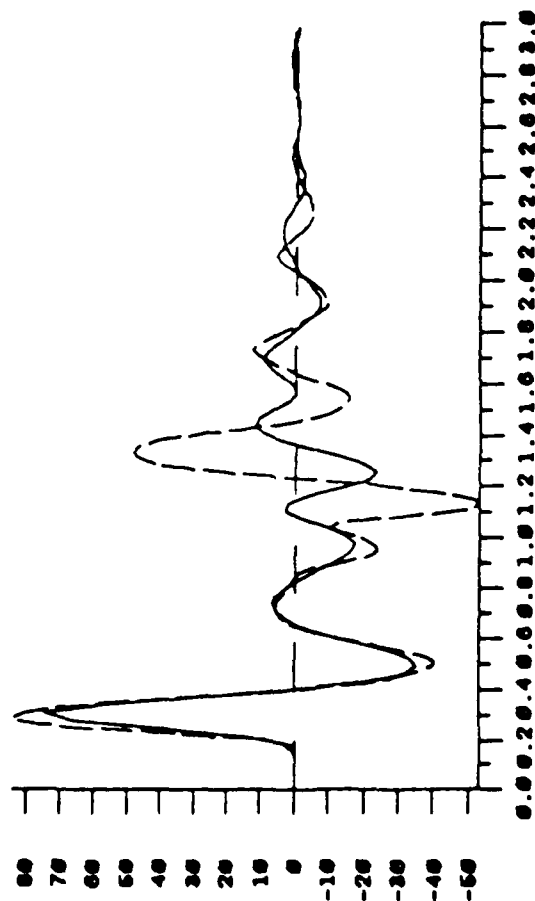
Aligned time series

File # 1 : pm000 toa30
File # 2 : pm000 toa30



B-8

File # 1 : pm000 toa30
File # 2 : pm000 toa30



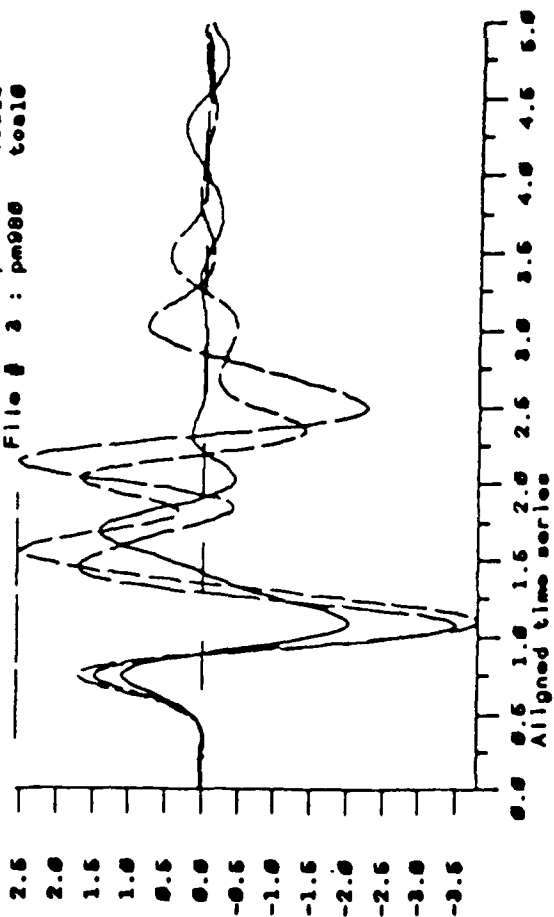
Time (sec)

Figure B.1b. Radiated displacement P waveforms for the three 2D Pahute Mesa tuff simulations at 30° takeoff angle compared to the 1D elastic source model.

2d teleseismograms (tom.5, inst=spwan) versus depth, 3 tom's
 Date: 11/2/1988 Time: 11:32:0

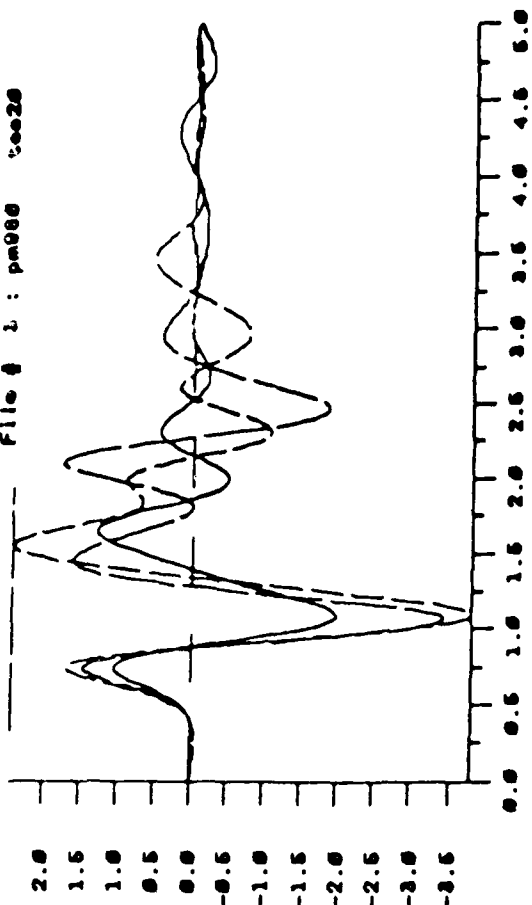
Aligned time series

File # 1 : pm200 tom10
 File # 2 : pm080 tom10
 File # 3 : pm000 tom10



Aligned time series

File # 1 : pm200 tom20
 File # 2 : pm080 tom20
 File # 3 : pm000 tom20



File # 1 : pm200 tom30
 File # 2 : pm080 tom30
 File # 3 : pm000 tom30

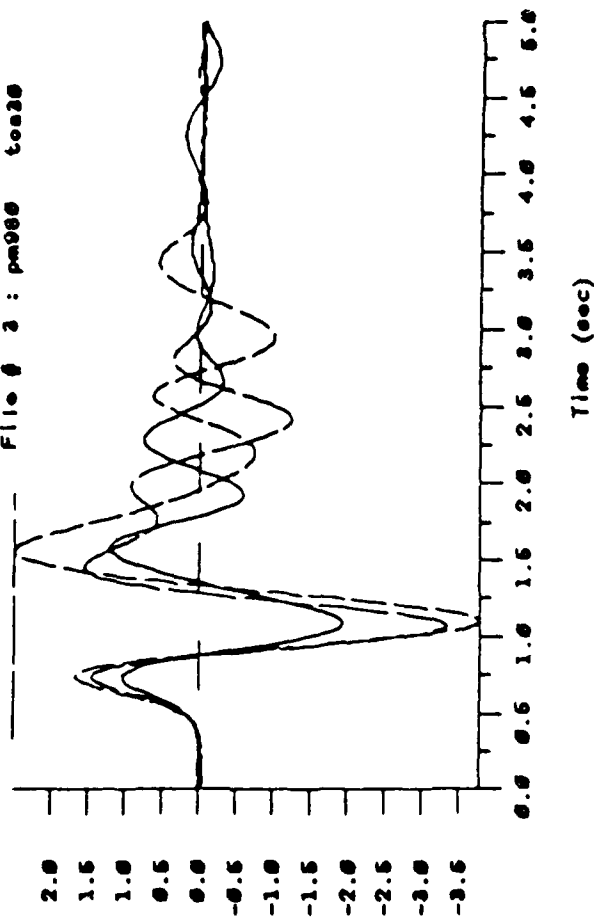
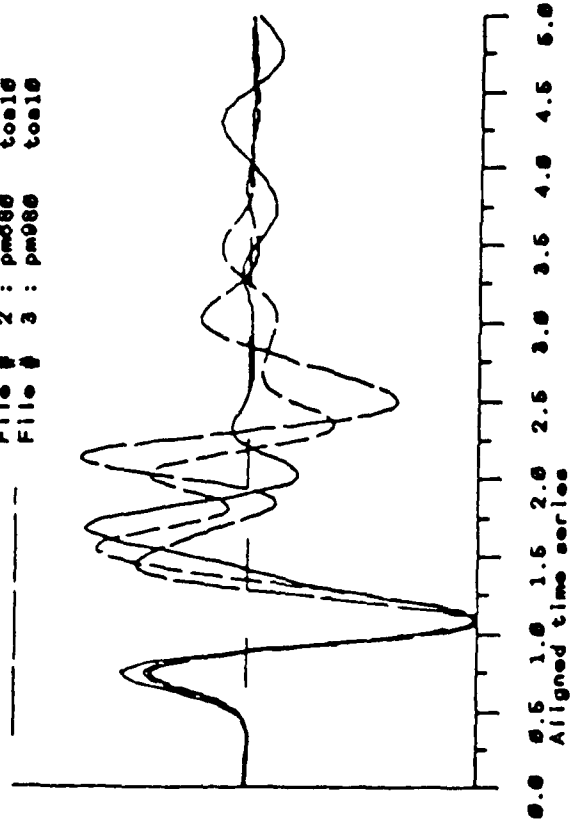


Figure B.2. Same as 4.5b except WWSSN instrument response and attenuation operator ($t^* = 0.5$ s) applied.

pm-acadep: 2d seismograms (tom.5, inst=apwsw) versus depth, 3 toa's
 Date: 11/2/1988 Time: 16:32:38

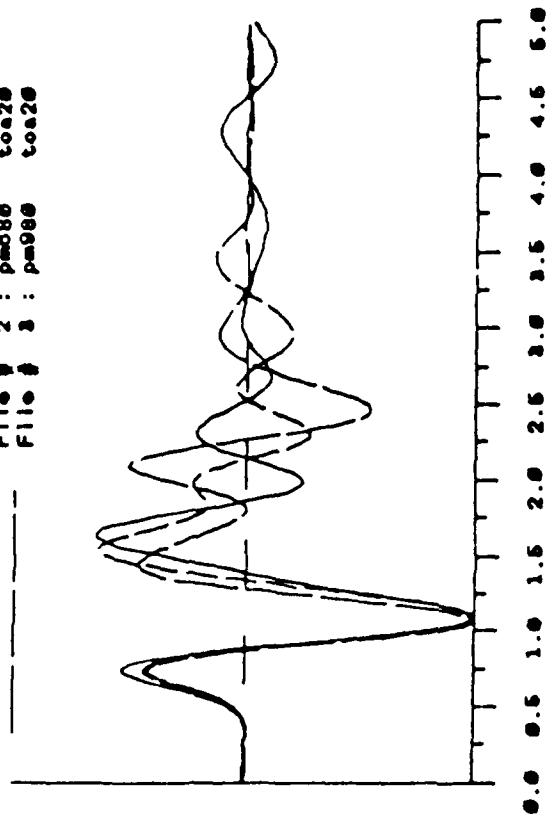
Aligned time series

File # 1 : pm200 toa10
 File # 2 : pm080 toa10
 File # 3 : pm080 toa10

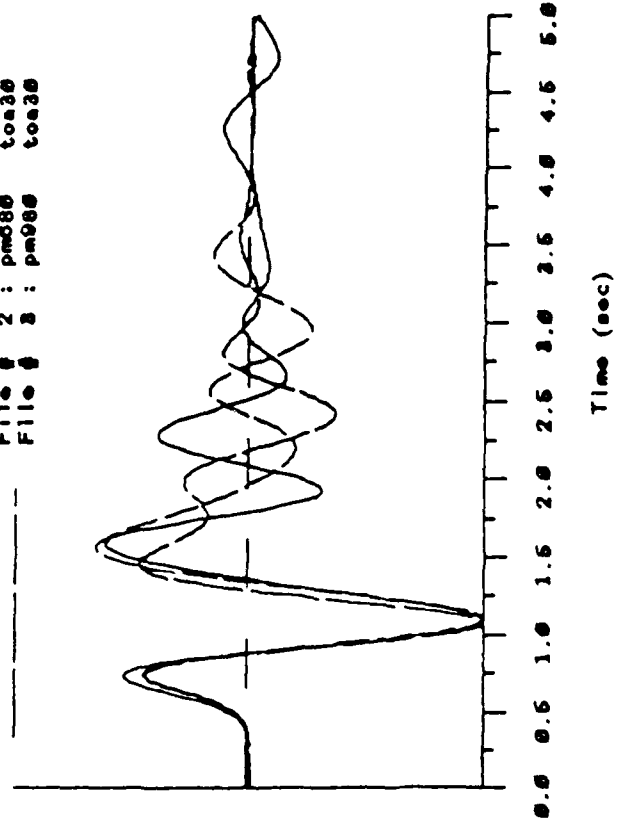


Aligned time series

File # 1 : pm200 toa20
 File # 2 : pm080 toa20
 File # 3 : pm080 toa20



File # 1 : pm200 toa30
 File # 2 : pm080 toa30
 File # 3 : pm080 toa30



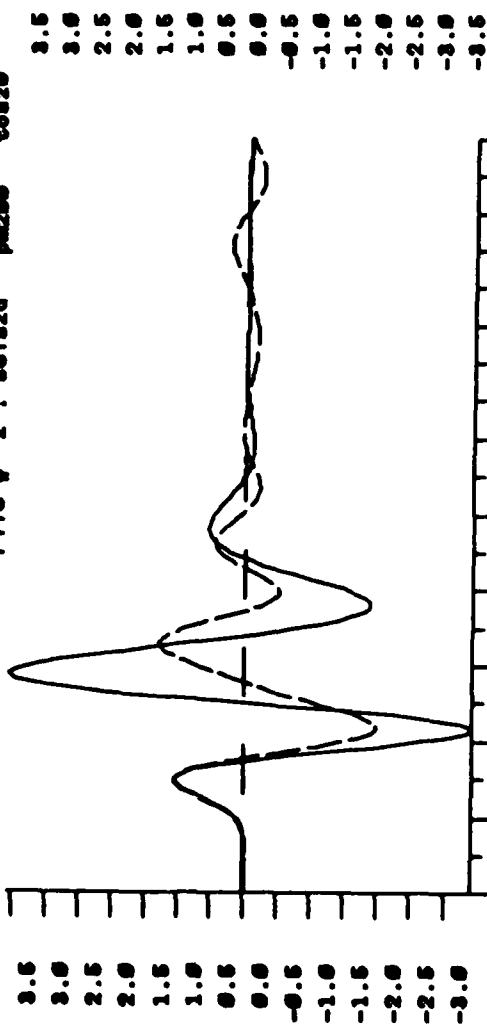
Time (sec)

Figure B.3. Same as B.2 except autoscaled to "b" phase.

2d vs 1d seismograms at toe20, 3 deb's
 Date: 11/ 2/1998 Time: 10: 9:18

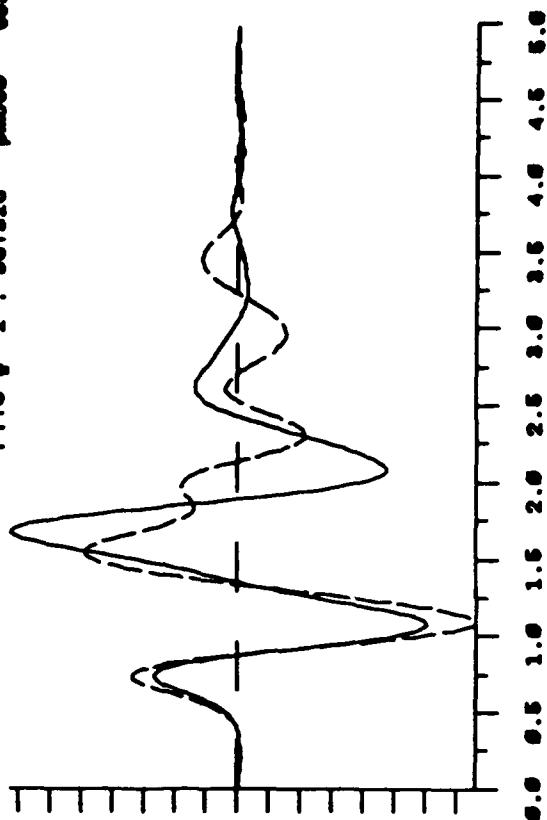
Aligned time series

File # 1 : se1d1d toe20
 File # 2 : se1s2d toe20



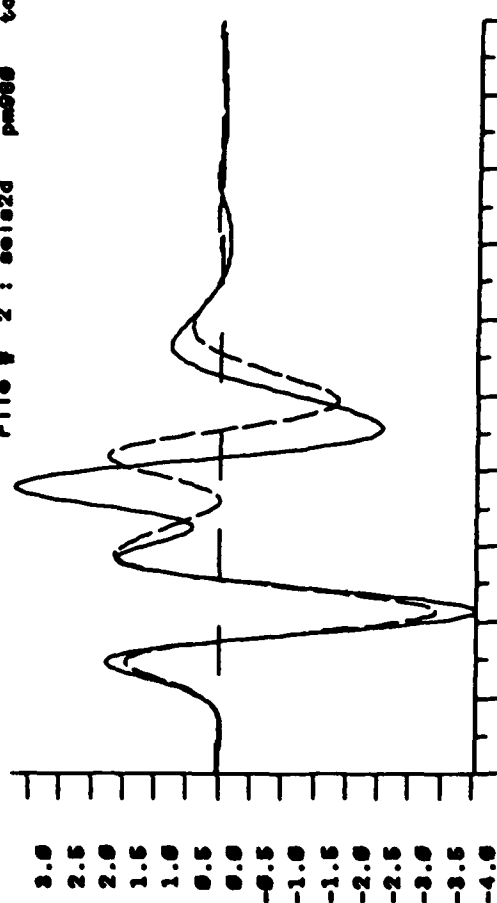
Aligned time series

File # 1 : se1d1d toe20
 File # 2 : se1s2d toe20



B-11

File # 1 : se1d1d toe20
 File # 2 : se1s2d toe20



Time (sec)

Figure B.4a. Same as 4.6 except TOA = 20°.

2d vs 1d seismograms at toa=30, 3 deb's
 Date: 11/ 2/1988 Time: 16: 9:34

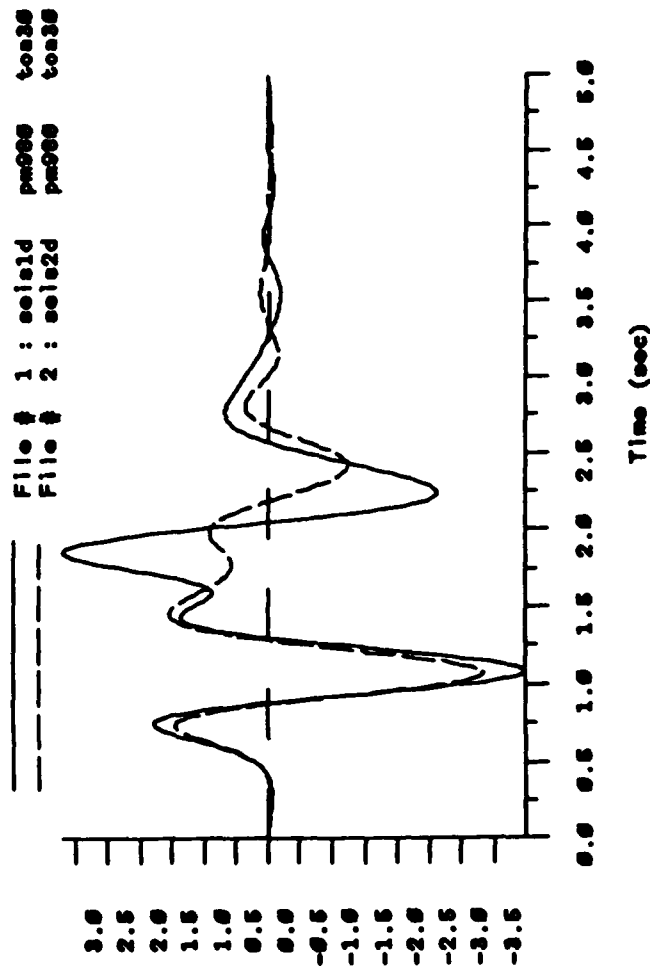
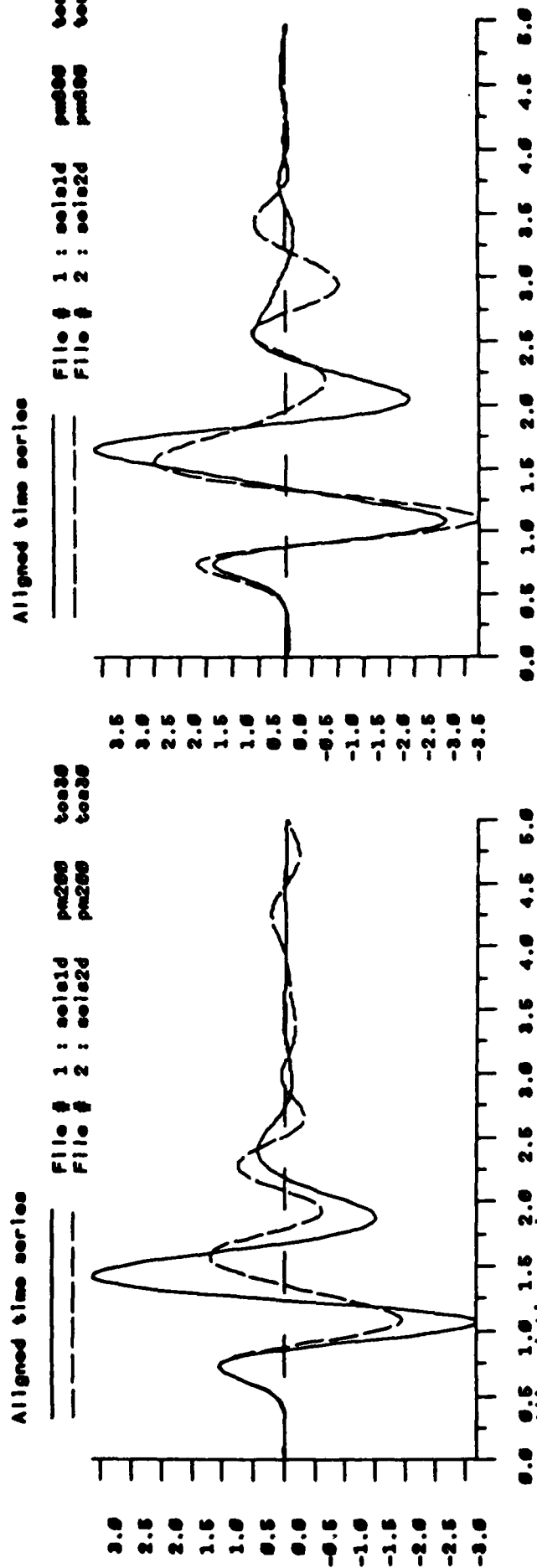
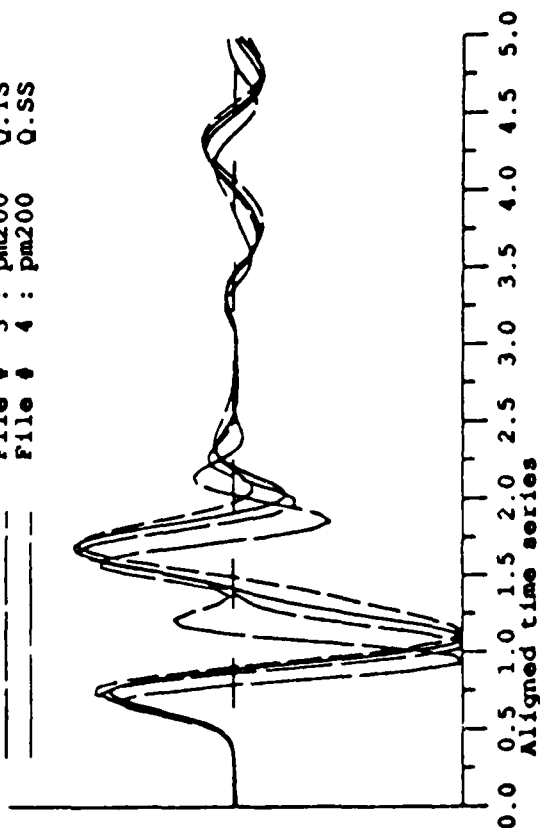


Figure B.4b. Same as 4.6 except TOA = 30°.

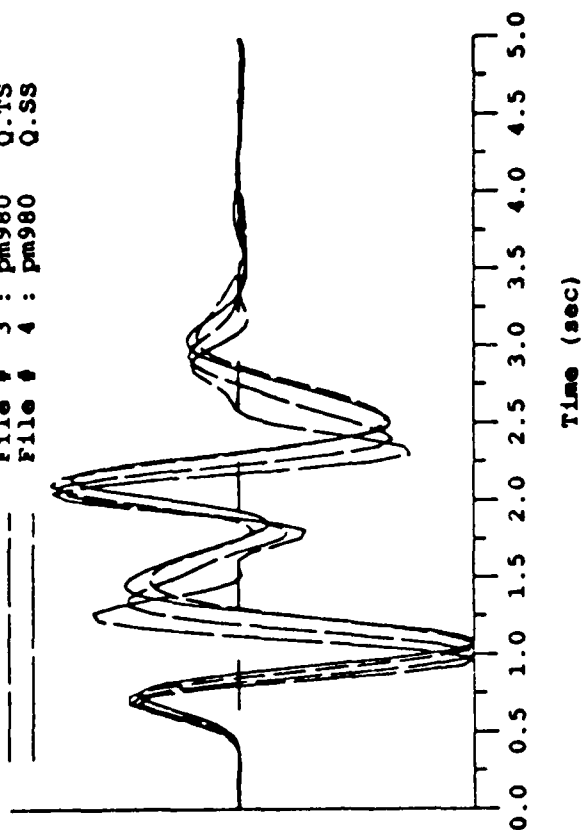
pm.acsQ: 2d seismograms (inst-spwan) versus Q-model, 3 depths, toa=10
 Date: 16/ 2/1988 Time: 10:56: 1

Aligned time series

File # 1 :	pm200	tstar.5
File # 2 :	pm200	Q.TT
File # 3 :	pm200	Q.TS
File # 4 :	pm200	Q.SS



File # 1 :	pm980	tstar.5
File # 2 :	pm980	Q.TT
File # 3 :	pm980	Q.TS
File # 4 :	pm980	Q.SS



Aligned time series

File # 1 :	pm680	tstar.5
File # 2 :	pm680	Q.TT
File # 3 :	pm680	Q.TS
File # 4 :	pm680	Q.SS

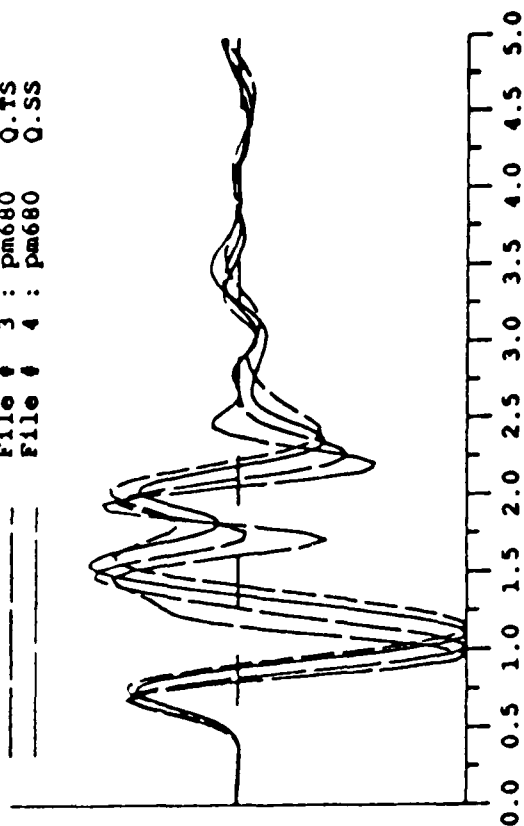


Figure B.4c. 2D synthetic P-waves at takeoff angle 10°, with WSSN instrument, and four different attenuation operators. Traces shown normalized to peak amplitude.

APPENDIX C

**APPLICATION OF THE REPRESENTATION THEOREM AND USE OF THE
"RING-LOAD" GREEN'S FUNCTION FOR REGIONAL SYNTHETIC CALCULATIONS**

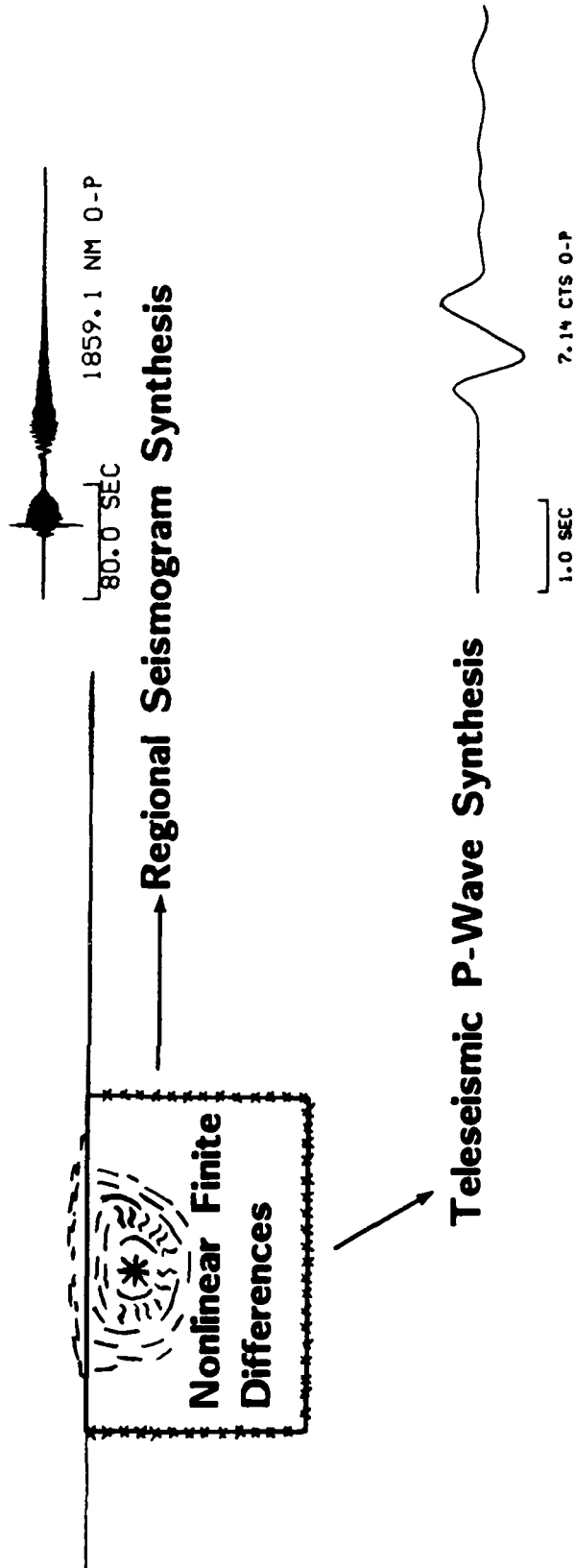
By use of the representation theorem, the results of finite difference simulations may be coupled to Green's functions for regional and teleseismic distances (Figure C.1). The method has been used by Day, *et al.* (1986) with modal summation Green's functions to study surface waves from nonlinear finite difference simulations, and recently by Day, *et al.* (1986b) to calculate teleseismic P waves from finite difference source simulations using teleseismic layered stack propagators. Regional waves are too complicated to be modeled properly with modal summation procedures or with simple far-field Haskell-Thompson propagators.

In practice, we use Green's functions for a layered Earth computed with a wavenumber integration algorithm (see Luco and Apsel, 1983), but the method applies in general to Green's functions computed by other methods. In this way, we simulate complicated nonlinear as well as linear wave propagation in a grid using finite differences and then propagate the wavefields to large distances in a layered Earth. The procedure has a number of applications for seismic scattering problems as well as for use with nonlinear seismic sources.

The representation theorem (Aki and Richards, 1980) states that the displacement field at location \mathbf{x}_0 may be given by an integral over the displacements, $\mathbf{u}(\mathbf{x})$, and tractions, $\boldsymbol{\sigma}_{\mathbf{n}}(\mathbf{x})$, over a closed surface, Σ . In the frequency domain, we can write that,

$$u_i(x_0) = \int_{\Sigma} \hat{n} dS [g_i(\mathbf{x}, \mathbf{x}_0) \cdot \boldsymbol{\sigma}_{\mathbf{n}}(\mathbf{x}) - \mathbf{u}(\mathbf{x}) \cdot \mathbf{C} : \nabla g_i(\mathbf{x}, \mathbf{x}_0)] \quad (1)$$

where $g(\mathbf{x}, \mathbf{x}_0)$ is the displacement at \mathbf{x} due to a point force in the x_i direction applied at \mathbf{x}_0 , \mathbf{C} is the elastic tensor, $\mathbf{u}(\mathbf{x})$ is the displacement at \mathbf{x} from the finite difference simulation, and $\boldsymbol{\sigma}_{\mathbf{n}}(\mathbf{x})$ is the stress tensor on Σ from the finite difference simulation. In



OBJECTIVE:

Formulate a physical basis for discriminants between explosions and earthquakes.

METHODOLOGY:

Using physical models for explosions and numerical wave propagation theory model teleseismic and regional synthetics.

Figure C.1.

2D nonlinear finite difference calculations are used to compute displacements and tractions on a monitoring surface. The motions and forces on the monitoring surface are then used to propagate both regional and teleseismic far-field body waves from the 2D nonlinear sources using the elastodynamic representation theorem.

cylindrical coordinates the integrand becomes,

$$\Gamma(\underline{x}, \underline{x}_0) = g_{ir} \tau_r + g_{iz} \tau_z - M : \nabla g_i \quad (2)$$

and equation (1) becomes

$$u_i(\underline{x}_0) = \int dS_{\underline{x}} \Gamma(\underline{x}, \underline{x}_0) = \int_{\Sigma} r dr dz \int_0^{2\pi} d\phi \Gamma(\underline{x}, \underline{x}_0) \quad (3)$$

where $\tau_r = \hat{r} \cdot \sigma \cdot \hat{n}$, $\tau_z = \hat{z} \cdot \sigma \cdot \hat{n}$, and

$$M = \hat{n} \underline{\underline{u}} \cdot C = \lambda \hat{n} \underline{\underline{u}} + \mu (\hat{n} \underline{\underline{u}} + \underline{\underline{u}} \hat{n}).$$

The integration is performed over a cylindrical surface composed of a surface of constant radius, r , referred to as the "side", and a surface of constant depth, z , referred to as the "bottom". For the side,

$$M = -u_r (\lambda I + 2\mu \hat{r} \hat{r}) - \mu u_z (\hat{r} \hat{z} + \hat{z} \hat{r}),$$

and for the bottom,

$$M = -u_z (\lambda I + 2\mu \hat{z} \hat{z}) - \mu u_r (\hat{r} \hat{z} + \hat{z} \hat{r}).$$

The gradient of the Green's function in cylindrical coordinates becomes,

$$\nabla g_i = \hat{r} \hat{r} \left(\frac{\partial g_{ir}}{\partial r} \right) + \hat{\phi} \hat{\phi} \left(\frac{g_{ir}}{r} \right) + \hat{z} \hat{r} \left(\frac{\partial g_{ir}}{\partial z} \right) + \hat{r} \hat{z} \left(\frac{\partial g_{iz}}{\partial r} \right) + \hat{z} \hat{z} \left(\frac{\partial g_{iz}}{\partial z} \right). \quad (4)$$

By reciprocity, $g_{ir}(\underline{x}, \underline{x}_0)$ can be re-interpreted as the i 'th component of displacement at \underline{x}_0 due to the point source in the \hat{r} direction at \underline{x} . To compute the azimuthal integral in equation (3), note that the displacements and tractions in the integrand are independent of ϕ (axi-symmetric finite difference output) and the integral may be performed over the Green's functions and the derivatives of the Green's functions with respect to depth and range. These functions depend on ϕ by virtue of their dependence on \underline{x}_0 (the receiver location) and we will label the azimuthally integrated Green's function terms as $G_{i\alpha}$ and $\partial_{\beta} G_{i\alpha}$ ($\alpha = r, z$, and $\beta = r, z$). $G_{i\alpha}(r_s, z_s, r_0, z_0)$ is interpreted as

the i 'th displacement at (r_0, z_0) due to the ring loads $f_\alpha(r, z) = \delta(r - r_s) \delta(z - z_s)$ in the $\alpha = r$ and z directions.

Putting equations (2), (3), and (4) together using the azimuthally integrated Green's functions, then the contribution from the side at radius $r=a$ becomes,

$$u_i(r_0, z_0) = a \int [G_{iz} \tau_z + G_{ir} \tau_r] dz \quad (5a)$$

$$+ a \int [(\lambda + 2\mu) u_r \partial_r G_{ir} + \mu u_z (\partial_r G_{iz} + \partial_z G_{ir})] dz$$

and from the bottom at depth z ,

$$u_i(r_0, z_0) = \int [G_{ir} \tau_r + G_{iz} \tau_z] r dr \quad (5b)$$

$$+ \int [\lambda u_z \partial_r G_{ir} + \mu u_r (\partial_r G_{iz} + \partial_z G_{ir}) + u_z ((\lambda + 2\mu) \partial_z G_{iz} + \frac{\lambda}{r} G_{ir})] r dr$$

Monitored displacements and tractions on the cylindrical surface are saved at individual time steps of the finite difference calculation for a plane of constant depth and a set of grid locations of constant radius. The Green's functions and their derivatives are computed for ring loads using a modified version of a wavenumber integration algorithm. The far-field synthetics are then formed from the sum of the appropriate convolutions. The wave-number integration program has been ported to a vector processor computer and substantial improvements have been made since many of the source locations at constant depth share the same wavenumber layer matrix and only differ in range.

The results have been tested against a half-space analytic solution of a point explosion source observed at various take-off angles in the half-space as well as by use of the far-field continuation procedure used in Day, *et al.* (1986) and used in Section IV of this report. Tests have also been done by comparison with a similar program

that computes the excitation of Rayleigh modes and propagates these to the far-field using the output of the finite difference calculations. Additional tests include the systematic removal of monitored finite difference grid locations in the summation procedure. As should be expected, decimation produces the effect that the proper summation begins to break down at high frequencies such that the wavefield becomes spatially aliased.

CONTRACTORS (United States)

Professor Keiiti Aki
Center for Earth Sciences
University of Southern California
University Park
Los Angeles, CA 90089-0741

Professor Charles B. Archambeau
Cooperative Institute for Resch
in Environmental Sciences
University of Colorado
Boulder, CO 80309

Dr. Thomas C. Bache Jr.
Science Applications Int'l Corp.
10210 Campus Point Drive
San Diego, CA 92121 (2 copies)

Dr. Douglas R. Baumgardt
Signal Analysis & Systems Div.
ENSCO, Inc.
5400 Port Royal Road
Springfield, VA 22151-2388

Dr. Jonathan Berger
Institute of Geophysics and
Planetary Physics
Scripps Institution of Oceanography
A-025
University of California, San Diego
La Jolla, CA 92093

Dr. S. Bratt
Science Applications Int'l Corp.
10210 Campus Point Drive
San Diego, CA 92121

Dr. Lawrence J. Burdick
Woodward-Clyde Consultants
P.O. Box 93245
Pasadena, CA 91109-3245 (2 copies)

Professor Robert W. Clayton
Seismological Laboratory/Div. of
Geological & Planetary Sciences
California Institute of Technology
Pasadena, CA 91125

Dr Karl Coyner
N. E. Research
P.O. Box 857
Norwich, VT 05055

Dr. Vernon F. Cormier
Department of Geology & Geophysics
U-45, Room 207
The University of Connecticut
Storrs, Connecticut 06268

Dr. Steven Day
Dept. of Geological Sciences
San Diego State U.
San Diego, CA 92182

Dr. Zoltan A. Der
ENSCO, Inc.
5400 Port Royal Road
Springfield, VA 22151-2388

Professor John Ferguson
Center for Lithospheric Studies
The University of Texas at Dallas
P.O. Box 830688
Richardson, TX 75083-0688

Professor Stanley Flatte'
Applied Sciences Building
University of California,
Santa Cruz, CA 95064

Dr. Alexander Florence
SRI International
333 Ravenswood Avenue
Menlo Park, CA 94025-3493

Professor Steven Grand
Department of Geology
245 Natural History Building
1301 West Green Street
Urbana, IL 61801

Dr. Henry L. Gray
Associate Dean of Dedman College
Department of Statistical Sciences
Southern Methodist University
Dallas, TX 75275

Professor Roy Greenfield
Geosciences Department
403 Deike Building
The Pennsylvania State University
University Park, PA 16802

Professor David G. Harkrider
Seismological Laboratory
Div of Geological & Planetary Sciences
California Institute of Technology
Pasadena, CA 91125

Professor Donald V. Helmberger
Seismological Laboratory
Div of Geological & Planetary Sciences
California Institute of Technology
Pasadena, CA 91125

Professor Eugene Herrin
Institute for the Study of Earth
& Man/Geophysical Laboratory
Southern Methodist University
Dallas, TX 75275

Professor Robert B. Herrmann
Department of Earth & Atmospheric
Sciences
Saint Louis University
Saint Louis, MO 63156

Professor Bryan Isacks
Cornell University
Dept of Geological Sciences
SNEE Hall
Ithaca, NY 14850

Professor Lane R. Johnson
Seismographic Station
University of California
Berkeley, CA 94720

Professor Thomas H. Jordan
Department of Earth, Atmospheric
and Planetary Sciences
Mass Institute of Technology
Cambridge, MA 02139

Dr. Alan Kafka
Department of Geology &
Geophysics
Boston College
Chestnut Hill, MA 02167

Professor Leon Knopoff
University of California
Institute of Geophysics
& Planetary Physics
Los Angeles, CA 90024

Professor Charles A. Langston
Geosciences Department
403 Deike Building
The Pennsylvania State University
University Park, PA 16802

Professor Thorne Lay
Department of Geological Sciences
1006 C.C. Little Building
University of Michigan
Ann Harbor, MI 48109-1063

Dr. Randolph Martin III
New England Research, Inc.
P.O. Box 857
Norwich, VT 05055

Dr. Gary McCartor
Mission Research Corp.
735 State Street
P.O. Drawer 719
Santa Barbara, CA 93102 (2 copies)

Professor Thomas V. McEvilly
Seismographic Station
University of California
Berkeley, CA 94720

Dr. Keith L. McLaughlin
S-CUBED,
A Division of Maxwell Laboratory
P.O. Box 1620
La Jolla, CA 92038-1620

Professor William Menke
Lamont-Doherty Geological Observatory
of Columbia University
Palisades, NY 10964

Professor Brian J. Mitchell
Department of Earth & Atmospheric
Sciences
Saint Louis University
Saint Louis, MO 63156

Mr. Jack Murphy
S-CUBED
A Division of Maxwell Laboratory
11800 Sunrise Valley Drive
Suite 1212
Reston, VA 22091 (2 copies)

Professor J. A. Orcutt
Institute of Geophysics and Planetary
Physics, A-205
Scripps Institute of Oceanography
Univ. of California, San Diego
La Jolla, CA 92093

Professor Keith Priestley
University of Nevada
Mackay School of Mines
Reno, NV 89557

Professor Paul G. Richards
Lamont-Doherty Geological
Observatory of Columbia Univ.
Palisades, NY 10964

Wilmer Rivers
Teledyne Geotech
314 Montgomery Street
Alexandria, VA 22314

Dr. Alan S. Ryall, Jr.
Center of Seismic Studies
1300 North 17th Street
Suite 1450
Arlington, VA 22209-2308 (4 copies)

Professor Charles G. Sammis
Center for Earth Sciences
University of Southern California
University Park
Los Angeles, CA 90089-0741

Professor Christopher H. Scholz
Geological Sciences
Lamont-Doherty Geological Observatory
Palisades, NY 10964

Dr. Jeffrey L. Stevens
S-CUBED,
A Division of Maxwell Laboratory
P.O. Box 1620
La Jolla, CA 92038-1620

Professor Brian Stump
Institute for the Study of Earth & Man
Geophysical Laboratory
Southern Methodist University
Dallas, TX 75275

Professor Ta-liang Teng
Center for Earth Sciences
University of Southern California
University Park
Los Angeles, CA 90089-0741

Dr. Clifford Thurber
State University of New York at
Stony Brooks
Dept of Earth and Space Sciences
Stony Brook, NY 11794-2100

Professor M. Nafi Toksoz
Earth Resources Lab
Dept of Earth, Atmospheric and
Planetary Sciences
Massachusetts Institute of Technology
42 Carleton Street
Cambridge, MA 02142

Professor Terry C. Wallace
Department of Geosciences
Building #11
University of Arizona
Tucson, AZ 85721

Weidlinger Associates
ATTN: Dr. Gregory Wojcik
4410 El Camino Real, Suite 110
Los Altos, CA 94022

Professor Francis T. Wu
Department of Geological Sciences
State University of New York
at Binghamton
Vestal, NY 13901

OTHERS (United States)

Dr. Monem Abdel-Gawad
Rockwell Internat'l Science Center
1049 Camino Dos Rios
Thousand Oaks, CA 91360

Professor Shelton S. Alexander
Geosciences Department
403 Deike Building
The Pennsylvania State University
University Park, PA 16802

Dr. Ralph Archuleta
Department of Geological
Sciences
Univ. of California at
Santa Barbara
Santa Barbara, CA

Dr. Muawia Barazangi
Geological Sciences
Cornell University
Ithaca, NY 14853

J. Barker
Department of Geological Sciences
State University of New York
at Binghamton
Vestal, NY 13901

Mr. William J. Best
907 Westwood Drive
Vienna, VA 22180

Dr. N. Biswas
Geophysical Institute
University of Alaska
Fairbanks, AK 99701

Dr. G. A. Bollinger
Department of Geological Sciences
Virginia Polytechnical Institute
21044 Derring Hall
Blacksburg, VA 24061

Dr. James Bulau
Rockwell Int'l Science Center
1049 Camino Dos Rios
P.O. Box 1085
Thousand Oaks, CA 91360

Mr. Roy Burger
1221 Serry Rd.
Schenectady, NY 12309

Dr. Robert Burridge
Schlumberger-Doll Resch Ctr.
Old Quarry Road
Ridgefield, CT 06877

Science Horizons, Inc.
ATTN: Dr. Theodore Cherry
710 Encinitas Blvd., Suite 101
Encinitas, CA 92024 (2 copies)

Professor Jon F. Claerbout
Professor Amos Nur
Dept. of Geophysics
Stanford University
Stanford, CA 94305 (2 copies)

Dr. Anton W. Dainty
AFGL/LWH
Hanscom AFB, MA 01731

Professor Adam Dziewonski
Hoffman Laboratory
Harvard University
20 Oxford St.
Cambridge, MA 02138

Professor John Ebel
Dept of Geology & Geophysics
Boston College
Chestnut Hill, MA 02167

Dr. Donald Forsyth
Dept. of Geological Sciences
Brown University
Providence, RI 02912

Dr. Anthony Gangi
Texas A&M University
Department of Geophysics
College Station, TX 77843

Dr. Freeman Gilbert
Institute of Geophysics &
Planetary Physics
Univ. of California, San Diego
P.O. Box 109
La Jolla, CA 92037

Mr. Edward Giller
Pacific Seirra Research Corp.
1401 Wilson Boulevard
Arlington, VA 22209

Dr. Jeffrey W. Given
Sierra Geophysics
11255 Kirkland Way
Kirkland, WA 98033

Rong Song Jih
Teledyne Geotech
314 Montgomery Street
Alexandria, Virginia 22314

Professor F.K. Lamb
University of Illinois at
Urbana-Champaign
Department of Physics
1110 West Green Street
Urbana, IL 61801

Dr. Arthur Lerner-Lam
Lamont-Doherty Geological Observatory
of Columbia University
Palisades, NY 10964

Dr. L. Timothy Long
School of Geophysical Sciences
Georgia Institute of Technology
Atlanta, GA 30332

Dr. Peter Malin
University of California at Santa Barbara
Institute for Central Studies
Santa Barbara, CA 93106

Dr. George R. Mellman
Sierra Geophysics
11255 Kirkland Way
Kirkland, WA 98033

Dr. Bernard Minster
Institute of Geophysics and Planetary
Physics, A-205
Scripps Institute of Oceanography
Univ. of California, San Diego
La Jolla, CA 92093

Professor John Nabelek
College of Oceanography
Oregon State University
Corvallis, OR 97331

Dr. Geza Nagy
U. California, San Diego
Dept of Ames, M.S. B-010
La Jolla, CA 92093

Dr. Jack Oliver
Department of Geology
Cornell University
Ithaca, NY 14850

Dr. Robert Phinney/Dr. F.A. Dahlen
Dept of Geological
Geophysical Sci. University
Princeton University
Princeton, NJ 08540 (2 copies)

RADIX Systems, Inc.
Attn: Dr. Jay Pulli
2 Taft Court, Suite 203
Rockville, Maryland 20850

Dr. Norton Rimer
S-CUBED
A Division of Maxwell Laboratory
P.O. 1620
La Jolla, CA 92038-1620

Professor Larry J. Ruff
Department of Geological Sciences
1006 C.C. Little Building
University of Michigan
Ann Arbor, MI 48109-1063

Dr. Richard Sailor
TASC Inc.
55 Walkers Brook Drive
Reading, MA 01867

Thomas J. Sereno, Jr.
Service Application Int'l Corp.
10210 Campus Point Drive
San Diego, CA 92121

Dr. David G. Simpson
Lamont-Doherty Geological Observ.
of Columbia University
Palisades, NY 10964

Dr. Bob Smith
Department of Geophysics
University of Utah
1400 East 2nd South
Salt Lake City, UT 84112

Dr. S. W. Smith
Geophysics Program
University of Washington
Seattle, WA 98195

Dr. Stewart Smith
IRIS Inc.
1616 N. Fort Myer Drive
Suite 1440
Arlington, VA 22209

Rondout Associates
ATTN: Dr. George Sutton,
Dr. Jerry Carter, Dr. Paul Pomeroy
P.O. Box 224
Stone Ridge, NY 12484 (4 copies)

Dr. L. Sykes
Lamont Doherty Geological Observ.
Columbia University
Palisades, NY 10964

Dr. Pradeep Talwani
Department of Geological Sciences
University of South Carolina
Columbia, SC 29208

Dr. R. B. Tittmann
Rockwell International Science Center
1049 Camino Dos Rios
P.O. Box 1085
Thousand Oaks, CA 91360

Professor John H. Woodhouse
Hoffman Laboratory
Harvard University
20 Oxford St.
Cambridge, MA 02138

Dr. Gregory B. Young
ENSCO, Inc.
5400 Port Royal Road
Springfield, VA 22151-2388

OTHERS (FOREIGN)

Dr. Peter Basham
Earth Physics Branch
Geological Survey of Canada
1 Observatory Crescent
Ottawa, Ontario
CANADA K1A 0Y3

Dr. Eduard Berg
Institute of Geophysics
University of Hawaii
Honolulu, HI 96822

Dr. Michel Bouchon - Universite
Scientifique et Medicale de Grenoble
Lab de Geophysique - Interne et
Tectonophysique - I.R.I.G.M-B.P.
38402 St. Martin D'Heres
Cedex FRANCE

Dr. Hilmar Bungum/NTNF/NORSAR
P.O. Box 51
Norwegian Council of Science,
Industry and Research, NORSAR
N-2007 Kjeller, NORWAY

Dr. Michel Campillo
I.R.I.G.M.-B.P. 68
38402 St. Martin D'Heres
Cedex, FRANCE

Dr. Kin-Yip Chun
Geophysics Division
Physics Department
University of Toronto
Ontario, CANADA M5S 1A7

Dr. Alan Douglas
Ministry of Defense
Blacknest, Brimpton,
Reading RG7-4RS
UNITED KINGDOM

Dr. Manfred Henger
Fed. Inst. For Geosciences & Nat'l Res.
Postfach 510153
D-3000 Hannover 51
FEDERAL REPUBLIC OF GERMANY

Dr. E. Husebye
NTNF/NORSAR
P.O. Box 51
N-2007 Kjeller, NORWAY

Ms. Eva Johannisson
Senior Research Officer
National Defense Research Inst.
P.O. Box 27322
S-102 54 Stockholm
SWEDEN

Tormod Kvaerna
NTNF/NORSAR
P.O. Box 51
N-2007 Kjeller, NORWAY

Mr. Peter Marshall, Procurement
Executive, Ministry of Defense
Blacknest, Brimpton,
Reading RG7-4RS
UNITED KINGDOM (3 copies)

Dr. Ben Menaheim
Weizman Institute of Science
Rehovot, ISRAEL 951729

Dr. Svein Mykkeltveit
NTNF/NORSAR
P.O. Box 51
N-2007 Kjeller, NORWAY (3 copies)

Dr. Robert North
Geophysics Division
Geological Survey of Canada
1 Observatory crescent
Ottawa, Ontario
CANADA, K1A 0Y3

Dr. Frode Ringdal
NTNF/NORSAR
P.O. Box 51
N-2007 Kjeller, NORWAY

Dr. Jorg Schlittenhardt
Federal Inst. for Geosciences & Nat'l Res.
Postfach 510153
D-3000 Hannover 51
FEDERAL REPUBLIC OF GERMANY

University of Hawaii
Institute of Geophysics
ATTN: Dr. Daniel Walker
Honolulu, HI 96822

FOREIGN CONTRACTORS

Dr. Ramon Cabre, S.J.
c/o Mr. Ralph Buck
Economic Consular
American Embassy
APO Miami, Florida 34032

Professor Peter Harjes
Institute for Geophysik
Rhur University/Bochum
P.O. Box 102148, 4630 Bochum 1
FEDERAL REPUBLIC OF GERMANY

Professor Brian L.N. Kennett
Research School of Earth Sciences
Institute of Advanced Studies
G.P.O. Box 4
Canberra 2601
AUSTRALIA

Dr. B. Massinon
Societe Radiomana
27, Rue Claude Bernard
7,005, Paris, FRANCE (2 copies)

Dr. Pierre Mechler
Societe Radiomana
27, Rue Claude Bernard
75005, Paris, FRANCE

GOVERNMENT

Dr. Ralph Alewine III
DARPA/NMRO
1400 Wilson Boulevard
Arlington, VA 22209-2308

Dr. Robert Blandford
DARPA/NMRO
1400 Wilson Boulevard
Arlington, VA 22209-2308

Sandia National Laboratory
ATTN: Dr. H. B. Durham
Albuquerque, NM 87185

Dr. Jack Evernden
USGS-Earthquake Studies
345 Middlefield Road
Menlo Park, CA 94025

U.S. Geological Survey
ATTN: Dr. T. Hanks
Nat'l Earthquake Resch Center
345 Middlefield Road
Menlo Park, CA 94025

Dr. James Hannon
Lawrence Livermore Nat'l Lab.
P.O. Box 808
Livermore, CA 94550

Paul Johnson
ESS-4, Mail Stop J979
Los Alamos National Laboratory
Los Alamos, NM 87545

Ms. Ann Kerr
DARPA/NMRO
1400 Wilson Boulevard
Arlington, VA 22209-2308

Dr. Max Koontz
US Dept of Energy/DP 5
Forrestal Building
1000 Independence Ave.
Washington, D.C. 20585

Dr. W. H. K. Lee
USGS
Office of Earthquakes, Volcanoes,
& Engineering
Branch of Seismology
345 Middlefield Rd
Menlo Park, CA 94025

Dr. William Leith
USGS
Mail Stop 928
Reston, VA 22092

Dr. Richard Lewis
Dir. Earthquake Engineering and
Geophysics
U.S. Army Corps of Engineers
Box 631
Vicksburg, MS 39180

Dr. Robert Masse'
Box 25046, Mail Stop 967
Denver Federal Center
Denver, Colorado 80225

Richard Morrow
ACDA/VI
Room 5741
320 21st Street N.W.
Washington, D.C. 20451

Dr. Keith K. Nakanishi
Lawrence Livermore National Laboratory
P.O. Box 808, L-205
Livermore, CA 94550 (2 copies)

Dr. Carl Newton
Los Alamos National Lab.
P.O. Box 1663
Mail Stop C335, Group E553
Los Alamos, NM 87545

Dr. Kenneth H. Olsen
Los Alamos Scientific Lab.
Post Office Box 1663
Los Alamos, NM 87545

Howard J. Patton
Lawrence Livermore National
Laboratory
P.O. Box 808, L-205
Livermore, CA 94550

Mr. Chris Paine
Office of Senator Kennedy
SR 315
United States Senate
Washington, D.C. 20510

AFOSR/NP
ATTN: Colonel Jerry J. Perrizo
Bldg 410
Bolling AFB, Wash D.C. 20332-6448

HQ AFTAC/TT
Attn: Dr. Frank F. Pilotte
Patrick AFB, Florida 32925-6001

Mr. Jack Rachlin
USGS - Geology, Rm 3 C136
Mail Stop 928 National Center
Reston, VA 22092

Robert Reinke
AFWL/NTEG
Kirtland AFB, NM 87117-6008

HQ AFTAC/TGR
Attn: Dr. George H. Rothe
Patrick AFB, Florida 32925-6001

Donald L. Springer
Lawrence Livermore National Laboratory
P.O. Box 808, L-205
Livermore, CA 94550

Dr. Lawrence Turnbull
OSWR/NED
Central Intelligence Agency
CIA, Room 5G48
Washington, D.C. 20505

Dr. Thomas Weaver
Los Alamos Scientific Laboratory
Los Alamos, NM 97544

AFGL/SULL
Research Library
Hanscom AFB, MA 01731-5000 (2 copies)

Secretary of the Air Force (SAFRD)
Washington, DC 20330
Office of the Secretary Defense
DDR & E
Washington, DC 20330

HQ DNA
ATTN: Technical Library
Washington, DC 20305

DARPA/RMO/RETRIEVAL
1400 Wilson Blvd.
Arlington, VA 22209

DARPA/RMO/Security Office
1400 Wilson Blvd.
Arlington, VA 22209

AFGL/XO
Hanscom AFB, MA 01731-5000

AFGL/LW
Hanscom AFB, MA 01731-5000

DARPA/PM
1400 Wilson Boulevard
Arlington, VA 22209

Defense Technical
Information Center
Cameron Station
Alexandria, VA 22314
(5 copies)

Defense Intelligence Agency
Directorate for Scientific &
Technical Intelligence
Washington, D.C. 20301

Defense Nuclear Agency/SPSS
ATTN: Dr. Michael Shore
6801 Telegraph Road
Alexandria, VA 22310

AFTAC/CA (STINFO)
Patrick AFB, FL 32925-6001

Dr. Gregory van der Vink
Congress of the United States
Office of Technology Assessment
Washington, D.C. 20510

Mr. Alfred Lieberman
ACDA/VI-OA'State Department Building
Room 5726
320 - 21st Street, NW
Washington, D.C. 20451

TACTEC
Battelle Memorial Institute
505 King Avenue
Columbus, OH 43201 (Final report only)